Ground-based ISAR imaging of cooperative and non-cooperative sea vessels with 3-D rotational motion

Mohammed Yunus Abdul Gaffar

BScEng(Electronic) University of Natal, MScEng(Electronic) University of Natal

A thesis submitted to the Department of Electrical Engineering, University of Cape Town, in fulfilment of the requirements for the degree of

Doctor of Philosophy

at the

University of Cape Town

December 2009

Declaration

I declare that this thesis is my own, unaided work. It is being submitted for the degree of Doctor of Philosophy at the University of Cape Town. It has not been submitted before for any degree or examination in any other university.

Signature of Author .....

Pretoria
December 2009

Abstract

Inverse Synthetic Aperture Radar (ISAR) images of sea vessels are a rich source of information for radar cross section (RCS) measurement and ship classification. However, ISAR imaging of sea vessels is a challenging task because the 3-D rotational motion of such vessels often gives rise to blurring. Blurry ISAR images are not desirable because they lead to inaccurate parameter estimation, which reduces the probability of correct classification.

The objective of this thesis is to explain how 3-D rotational motion causes blurring in ISAR imagery and to develop effective techniques for imaging cooperative and non-cooperative sea vessels for RCS measurement and ship-classification purposes respectively.

Much research has been done to investigate the effect of 3-D rotational motion on an ISAR image under the assumption that an object's axis of rotation is constant over the coherent processing interval (CPI). In this thesis, a new quaternion-based system model is proposed to characterise the amount of blurring in an ISAR image when a sea vessel possesses 3-D rotational motion over a CPI. Simulations were done to characterise the migration of a scatterer through Doppler cells due to the time-varying nature of the Doppler generating axis of rotation. Simulation results with realistic 3-D rotational motion show substantial blurring in the cross-range dimension of the resulting ISAR image, and this blurring is attributed to the time-varying nature of the angle of the Doppler generating axis of rotation and the object's rotation rate over the CPI.

Sea vessels naturally possess 3-D rotational motion, even in low sea states. However, it is only a component of this motion, referred to as the image-generating Doppler component, that is useful to the ISAR imaging process. The image-generating Doppler components consist of the Doppler generating axis and the effective angle of rotation. This thesis presents a new quaternion-based transformation that converts the measured attitude and position data of a sea vessel into the vessel's Doppler generating axis and effective angular rotation rate. The proposed transformation was thus applied to the measured attitude and GPS position data of a yacht, and the results show that the quaternion-based transformation isolates the component of the 3-D rotational motion that directly influences the ISAR images. Thus, the transformation provides an alternative approach for understanding the blurring caused by 3-D rotational motion in measured ISAR images, as well as for identifying good imaging intervals for applications such as cooperative ISAR for RCS purposes.

In cooperative ISAR applications, the value of the coherent processing time window length (CPTWL) is critical because it should be short enough to limit the blurring caused by the 3-D rotational motion but at the same time long enough to ensure that the desired cross-range resolution is obtained. In this thesis, the motion-aided CPTWL selector (MACS) algorithm is proposed for selecting suitable CPTWLs for ISAR imaging of cooperative sea vessels. The suggested CPTWLs may be used to obtain motion-compensated ISAR images that have the desired medium cross-range resolution and limited blurring due to 3-D rotational motion. The proposed algorithm is applied to the measured motion data of three different classes of sea vessels: a yacht, a fishing trawler, and a survey vessel. Results show that longer CPTWLs are needed for larger vessels in order to obtain ISAR images with the desired cross-range resolution. Experimental results obtained using measured radar data show the effectiveness of the proposed algorithm. Furthermore, the suggested CPTWLs may be used to select an effective initial CPTWL for the maximum-contrast-based automatic time window selection (MC-ATWS) algorithm, proposed by Martorella and Berizzi, when it is applied to measured radar data of small vessels.

In non-cooperative ISAR applications, however, the vessel's motion is unknown and it is a challenging task to isolate focused side-view ISAR images from a long radar recording. This thesis proposes the extended maximum-contrast-based automatic time window selection (EMC-ATWS) algorithm, which is an extension of the MC-ATWS algorithm, to estimate the parameters of multiple optimum imaging intervals that produce focused side-view ISAR images of small non-cooperative vessels. The MC-ATWS algorithm and the proposed EMC-ATWS algorithm were therefore applied to measured radar recordings of two non-cooperative yachts. Results showed that the MC-ATWS estimated the parameters of a single optimum imaging interval that produced a highly focused ISAR image with little Doppler information, which is not desirable for ship classification. Results from the EMC-ATWS algorithm showed that the proposed technique was effective in estimating multiple optimum imaging intervals that generated highly focused side-view ISAR images, which contain useful discriminant information for ship classification.

This thesis is dedicated to my parents,

Yacoob Abdul Gaffar and Shamima Abdul Gaffar,

the loving memory of my grandparents

and,

my wife, Shaaista Khan

Acknowledgements

All praise is due to Allah, the Lord of the worlds, the Compassionate, the Merciful, Master of the Day of Judgment.

I would like to express my sincere thanks to my supervisors, Professor M.R. Inggs at UCT and W.A.J. Nel at CSIR, for their expert guidance and support throughout my study. I have benefitted greatly from their expertise in the theory and practise of radar.

Thanks are also extended to the members of the Radar and Electronic Warfare team at DPSS that assisted with the ISAR measurement trials and members of the Awarenet project for providing a stimulating workgroup. I am grateful to Kumaran Naicker for his work on the calibration of measured HRR profiles and to Professor C. J. Baker for his expert advice during my study.

I also wish to thank the CSIR, Department of Science and Technology and the South African Department of Defence for their financial support.

My heartfelt thanks are owed to my parents, Yacoob and Shamima Abdul Gaffar, for their loving support throughout my life and for motivating me to pursue postgraduate studies. Without their continuous encouragement, this thesis would not be possible.

To my wife, Shaaista, I am thankful for your unconditional love, support and enduring patience during my studies. I would also like to thank my parents-in-law, Riaz and Fatima Khan, for their warm support and for showing keen interest in my work. My sincere appreciation goes out to my sister, Tasneem

Abdul Gaffar, my twin-brother and his wife, Yusuf Abdul Gaffar and Fanny Guillon, and brothers-in-law, Ashraf Ally and Suhail Khan, for their constant support and encouragement. Many thanks are due to my adorable little niece, Zahra, for providing me with endless hours of laughter and enjoyment.

Finally, I would like to thank Reggie Lord for the excellent language editing. Thanks are also owed to Rob Calitz from Armscor and Professor H. Xu from UKZN for encouraging me to study further.

Contents

List of Figures

List of Tables

List of Symbols

$A_{n,m}$	—	Amplitude of the noise and clutter for the m^{th} pulse in the n^{th} burst
a_r	—	Radial acceleration of the center of rotation of an object
B	—	Bandwidth of the effective transmitted signal
B_d	—	Maximum Doppler bandwidth
B_{inst}	—	Instantaneous bandwidth of a frequency stepped pulse
B_{zdm}	—	Doppler bandwidth masking about 0Hz for the calculation of the image contrast with ZDM
B_{zdt}	—	Doppler bandwidth about 0Hz that is used in the LCSIT algorithm
c	—	The speed of light
d_b	—	Allowable Doppler bins of migration
$d_{b,k}$	—	Doppler bins of migration for the k^{th} scatterer
d_k	—	Distance from the k^{th} scatterer to the center of rotation
$\mathbf{e}$	—	Noise and clutter matrix that has n rows and m columns
$e_{n,m}$	—	Clutter and noise component for the m^{th} pulse in the n^{th} burst
e_Ω	—	Allowable cross-range resolution error
f_{BRF}	—	Burst repetition frequency
f_{PRF}	—	Pulse repetition frequency
f_c	—	Carrier frequency
$f_{c,m}$	—	Carrier frequency of the m^{th} pulse
$f_{d,k}$	—	Doppler frequency of the k^{th} scatterer
$f_{d,k,t}$	—	Doppler frequency of the k^{th} scatterer at time t

$f_{d,k,\Delta t(n)}$	—	Doppler frequency of the k^{th} scatterer for the n^{th} discrete rotation
f_s	—	Complex sampling frequency at the radar receiver
$\mathbf{g}_{k,t(n)}$	—	3-D global coordinates of the k^{th} scatterer at time $t(n)$
$I(\eta, \nu; \tau, \Delta\tau)$	—	ISAR image intensity for a CPI with central time τ and CPTWL of $\Delta\tau$
K	—	Number of point scatterers representing an object
l_{cr}	—	Cross-range extent of an object
l_k	—	Lever-arm distance of the k^{th} scatterer
$l_{k,\Delta(n)}$	—	Lever-arm distance of the k^{th} scatterer for $\Delta t(n)$
M	—	Number of pulses in a burst
m	—	Pulse number in a burst
N	—	Number of HRRs used to form an ISAR image
n	—	Burst number
$\mathbf{q}_{b,t(n)}$	—	Quaternion representation of the bank of a vessel at time $t(n)$
$\mathbf{q}_{e,t(n)}$	—	Quaternion representation of the elevation of a vessel at time $t(n)$
$\mathbf{q}_{ep,\Delta t(n)}$	—	Quaternion representation of the effective pitch motion over $\Delta t(n)$
$\mathbf{q}_{er,\Delta t(n)}$	—	Quaternion representation of the effective roll motion over $\Delta t(n)$
$\mathbf{q}_{ey,\Delta t(n)}$	—	Quaternion representation of the effective yaw motion over $\Delta t(n)$
$\mathbf{q}_{gk,t(n)}$	—	Quaternion representation of $\mathbf{g}_{k,t(n)}$
$\mathbf{q}_{hs,t(n)}$	—	Quaternion representation of the heading, which is used in the system model, of a vessel at time $t(n)$
$\mathbf{q}_{ins,t(n)}$	—	Quaternion representing the initial orientation of a vessel with respect to the global axes
$\mathbf{q}_m$	—	Quaternion representating the rotation through an angle of θ_m about an axis $\mathbf{\Omega_m}$
$\mathbf{q}_{rk}$	—	Quaternion representation of $\mathbf{r}_k$
$\mathbf{q}_{tot,t(n)}$	—	Quaternion representation of the incremental rotation

		motion for $\Delta t(n)$
$\mathbf{q}_x(\mathbf{h}, \theta)$	—	Quaternion labelled x that represents the rotation of an angle θ about an axis $\mathbf{h}$
$\mathbf{q}_{\Omega eff, \Delta t(n)}$	—	Quaternion representation of $\mathbf{\Omega}_{eff, \Delta t(n)}$
R_0	—	Initial distance from the radar to the center of rotation of an object
$R_{0,t}$	—	Translation motion of an object
$R_{k,t}$	—	Distance from the radar to the k^{th} scatterer
$R_{k,t(n)}$	—	Distance from the radar to the k^{th} scatterer at time $t(n)$
$R_{\mathbf{x},t}$	—	Distance between the radar and a generate 3-D point $\mathbf{x}$
$\mathbf{RT}$	—	Unit LOS vector from the object's center of rotation to the radar
$\mathbf{RT}_{\perp 1}$	—	Unit vector that is aligned to the V global axis
$\mathbf{RT}_{\perp 2}$	—	Unit vector that is aligned to the W global axis
$\mathbf{r}_k$	—	3-D local coordinates of the k^{th} scatterer
$S_R(f, t)$	—	Complex baseband radar received signal in the time-frequency format
$S_R(\eta, t)$	—	HRR profiles of an object in the time-down-range format
$t(n)$	—	Discrete time of the n^{th} burst
$u_{k,t(n)}$	—	Global u coordinate of the k^{th} scatterer at time $t(n)$
v_1	—	Radial velocity of scatterer 1 to the radar
v_2	—	Radial velocity of scatterer 2 to the radar
$v_{k,t(n)}$	—	Global v coordinate of the k^{th} scatterer at time $t(n)$
v_r	—	Radial velocity of the center of rotation of an object
$w_{k,t(n)}$	—	Global w coordinate of the k^{th} scatterer at time $t(n)$
$\mathbf{x}_n$	—	Unit vector that is aligned to the local X_n axis at time $t(n)$
x_k	—	Local x coordinates for the k^{th} scatterer
$\mathbf{y}_n$	—	Unit vector that is aligned to the local Y_n axis at time $t(n)$
y_k	—	Local y coordinates for the k^{th} scatterer
$\mathbf{z}_n$	—	Unit vector that is aligned to the local Z_n axis at time $t(n)$
z_k	—	Local z coordinates for the k^{th} scatterer
$(X,\ Y,\ Z)$	—	Local coordinate axes
$(U,\ V,\ W)$	—	Global coordinate axes

α_k	—	Complex amplitude representing the RCS of the k^{th} scatterer
$\alpha(\mathbf{x})$	—	Reflectivity of a generic 3-D point $\mathbf{x}$
β_k	—	Angle between $\mathbf{\Omega}_{eff,\Delta t(1)}$ and r_k
γ	—	Overlap factor between two successive CPIs
Δf	—	Frequency step from pulse-to-pulse in a frequency stepped waveform
$\Delta R_{0,t(n)}$	—	Change in the initial range R_0 over time
Δr_c	—	Cross-range resolution
Δr_{cd}	—	Desired cross-range resolution
Δr_d	—	Down-range resolution
s	—	Step size between two successive frames
$\Delta\tau$	—	Coherent Processing Time Window Length
$\Delta t(n)$	—	n^{th} Discrete incremental rotation over the burst
$\Delta\theta$	—	Change in aspect angle of a uniformly rotating object over the CPI
$\Delta\theta_{eff}$	—	Change of an object's aspect angle over the CPI
$\Delta\tau^{(in)}$	—	Initial CPTWL
$\Delta\tau_{opt}$	—	Optimum CPTWL
$\Delta\phi$	—	Change in the Doppler generating axis of rotation over the CPI
ϵ_{LCSIT}	—	Energy difference calculated in the LCSIT algorithm
ϵ_{thres}	—	Energy threshold used in the IT algorithm
η	—	Down-range dimension of an ISAR image
η_{max}	—	Down-range cell with the most Doppler energy in an ISAR image
$\theta_{b,t(n)}$	—	Bank of a vessel at time $t(n)$
$\theta_{br,t(n)}$	—	Bearing of a vessel at time $t(n)$
$\theta_{e,t(n)}$	—	Elevation of a vessel at time $t(n)$
θ_{eff}	—	Effective angle of rotation
$\theta_{h,t(n)}$	—	Heading of a vessel that is measured by an INS system at time $t(n)$
$\theta_{hs,t(n)}$	—	Heading of a vessel that is used in the system model at

		time $t(n)$
$\theta_{RT,\Delta t(n)}$	—	Effective roll angle over $\Delta t(n)$
$\theta_{RT\perp 1,\Delta t(n)}$	—	Effective pitch angle over $\Delta t(n)$
$\theta_{RT\perp 2,\Delta t(n)}$	—	Effective yaw angle over $\Delta t(n)$
$\theta_{r,\Delta t(n)}$	—	Roll angle of a vessel about the local X_{n-1} axis over $\Delta t(n)$
$\theta_{p,\Delta t(n)}$	—	Pitch angle of a vessel about the local Y_{n-1} axis over $\Delta t(n)$
$\theta_{y,\Delta t(n)}$	—	Yaw angle of a vessel about the local Z_{n-1} axis over $\Delta t(n)$
$\theta_{\Delta t(n)}$	—	Angle of rotation angle for the n^{th} discrete rotation
θ_0	—	Initial rotation angle
$\theta_{\Omega eff,\Delta t(n)}$	—	Angle of the Doppler generating axis of rotation from the global W axis
$\theta_{\Omega eff1,\Delta t(n)}$	—	Angle of the Doppler generating axis of rotation from the global V axis
$\dot{\theta}$	—	Angular velocity of an object
$\dot{\theta}_{eff}$	—	Effective angular rotation rate
$\dot{\theta}_{eff,\Delta t(n)}$	—	Effective angular rotation rate during $\Delta t\,(n)$
$\dot{\theta}_m$	—	Rotation rate about the $\mathbf{\Omega}_m$ axis
$\dot{\theta}_{r,\Delta t(n)}$	—	Roll rate of a vessel for the n^{th} discrete rotation over the CPI
$\dot{\theta}_{p,\Delta t(n)}$	—	Pitch rate of a vessel for the n^{th} discrete rotation over the CPI
$\dot{\theta}_{y,\Delta t(n)}$	—	Yaw rate of a vessel for the n^{th} discrete rotation over the CPI
$\dot{\theta}_{\Delta t(n)}$	—	Angular velocity of an object for the n^{th} discrete rotation
$\dot{\theta}_{\Omega eff,\Delta t(n)}$	—	Rotation rate of the angle of the Doppler generating axis of rotation from the global W axis
$\dot{\theta}_{\Omega eff1,\Delta t(n)}$	—	Rotation rate of the angle of the Doppler generating axis of rotation from the global V axis
$\ddot{\theta}$	—	Angular acceleration
λ	—	Wavelength of the transmitted signal
ν	—	Doppler frequency along the cross-range dimension of an ISAR image
τ	—	Central instant of a CPI

τ_{opt}	—	Optimum central instant of the observation time interval
$\Phi_{n,m}$	—	Discretised signal at the radar receiver for pulse number m in burst n
$\Phi^s_{n,m}$	—	Discretised radar received signal without noise
Φ_t	—	Received signal at the radar as a function of time
$\phi_{n,m}$	—	Phase of the noise and clutter for the m^{th} pulse in the n^{th} burst
$\dot{\phi}$	—	Angular velocity of the Doppler generating axis of rotation
$\rho_{x,y,z}$	—	Related to the reflectivity of a scatterer at (x, y, z)
σ_n^2	—	Noise power
σ_s^2	—	Signal power
$\mathbf{\Omega}$	—	Object's axis of rotation
$\mathbf{\Omega}_m$	—	Stationary axis of rotation that lies along the U axis
$\mathbf{\Omega}_{eff}$	—	Doppler generating axis of rotation
$\mathbf{\Omega}_{eff,\Delta t(n)}$	—	Doppler generating axis of rotation for the n^{th} discrete rotation
$\mathbf{\Omega}_{rc}$	—	Direction of the cross-range dimension
$\mathbf{\Omega}_{\Delta t(n)}$	—	Object's axis of rotation for the n^{th} discrete rotation
ω_t	—	Rotational motion as a function of time

Nomenclature

2-D—Two-dimensional

3-D—Three-dimensional

4-D—Four-dimensional

BRF—Burst Repetition Frequency

CPI—Coherent Processing Interval

CPTWL—Coherent Processing Time Window Length

CSIR—Council for Scientific and Industrial Research

DSA—Dominant Scatterer Algorithm

DSTO—Defence Science and Technology Organisation

EEZ—Economic Exclusion Zone

EM—Electromagnetic

EMC-ATWS—Extended Maximum-Contrast-Based Automatic Time Window Selection

EWLE—Extended Window Length Estimator

FT—Fourier Transform

FFT—Fast Fourier Transform

GPS—Global Positioning System

HRR—High Range Resolution

IC—Image Contrast

IFT—Inverse Fourier Transform

INS—Inertial Navigation System

ISAR—Inverse Synthetic Aperture Radar

ISARLAB—ISAR Radar Laboratory

IT—Image Test

JEM—Jet Engine Modulation

JTF—Joint Time-Frequency

LCSIT—Long CPTWL Side-view Image Test

LOS—Line of Sight

MACS—Motion-aided CPTWL Selector

MC-ATWS—Maximum-Contrast-Based Automatic Time Window Selection

MPL—Maximum Position Locator

MUSIC—Multiple Signal Classification

NCTR—Non-cooperative Target Recognition

PO—Physical Optics

PRF—Pulse Repetition Frequency

RCS—Radar Cross Section

SNR—Signal-to-Noise Ratio

WLE—Window Length Estimator

ZDM—Zero Doppler Masking

Chapter 1

Introduction

1.1 Background

Inverse Synthetic Aperture Radar (ISAR) is a radar signal processing technique for imaging objects with high spatial resolution. In this technique, a stationary radar platform illuminates a rotating object with electromagnetic (EM) energy and the backscattered energy from the object is used to form an ISAR image. The intensity of the backscattered energy depends on many factors, which include the properties of the surface (dielectric constant, roughness and slope) and the polarization of the transmitted signal. A typical ISAR image is two-dimensional (2-D) and it illustrates the scattering centres of the object along the down-range and cross-range dimensions. ISAR theory in the context of instrumentation-range measurements was initially discussed by Chen and Andrews [2], Walker [3] and Mensa [4]. In addition, ISAR imaging of aircraft was addressed by Chen and Andrews in [5].

ISAR imaging of rotating objects offers many advantages to optical imaging techniques: high quality images can be obtained in all weather conditions (rain, cloud, haze), at any time (day or night) and at ranges that are beyond the visual range. For these reasons, ISAR is a valuable tool for a wide range of military and civilian applications, which include non-cooperative target recognition

(NCTR) (Bon *et al.* [6], Musman *et al.* [7], Menon *et al.* [8], Botha [9] and Kim *et al.* [10]), radar cross section (RCS) measurement (Jain and Patel [11] and Given and Schmidt [12]), battlefield awareness (Fennel and Wishner [13]), surveillance of ground traffic in airports (Sauer *et al.* [14]), monitoring road traffic (Munoz-Ferreras *et al.* [15]), through-the-wall-imaging (Yoon and Amin [16]) and concealed-object detection (Trischman *et al.* [17]).

1.2 Maritime Applications of ISAR

ISAR imaging of sea vessels has attracted considerable attention from the research and development communities because it provides a rich source of information for maritime surveillance and RCS management. ISAR images contain discriminant information that can be used for classification [6], [7]. In addition, ISAR images may be used to identify scattering centres of high reflectivity for RCS reduction purposes [11], [12].

A few research institutes in the world have developed ISAR systems for maritime applications. Examples of such systems include: the INGARA imaging radar developed by the Defence Science and Technology Organisation (DSTO) in Australia, which is an airborne X-band multi-mode radar with a fully polarimetric collection capability [18]; the P-3 Orion and the S-3B Viking US Navy aircraft that were developed through the joint collaboration of Texas Instruments and the US Naval Research Laboratory. ISAR imaging of maritime vessels from airborne platforms are addressed in papers by Hajduch *et al.* [19], and Barclay and Williams [20].

Recently, South Africa has embarked on the research and development of a maritime surveillance system, referred to as Awarenet by Anderson in [21], to monitor the country's economic exclusion zone (EEZ). The objective of Awarenet is to create a real time, persistent maritime surveillance system that provides situational awareness regarding the presence, classification and possible intent of sea vessels in South Africa's EEZ. This information would be used by the peace, safety and security related agencies to protect the country's borders and peo-

ple from activities such as illegal border crossing, organised crime, illegal fishing and terrorism at sea. Currently, there are two research programmes underway at the Council for Scientific and Industrial Research (CSIR) in South Africa to address some of the challenges of Awarenet; the topics that are current being researched are the field of detection and classification of sea vessels. The research work towards the classification of sea vessels using ISAR techniques has been the responsibility of the candidate and his CSIR supervisor, Willie Nel.

Another important maritime application of ISAR is RCS management, which involves the identification of physical structures of a platform with significant RCS contributions. All Navies require their military sea vessels to be measured, in order to minimise the effect of scattering hotspots. Reducing the absolute RCS of a ship can furthermore reduce the acquisition range of an anti-ship missile as well as improving the performance of a ship's countermeasure against the approaching seeker. The CSIR is responsible for providing this service to the South African Navy. The research work focussing on the RCS management of ships using ISAR has been the responsibility of the candidate, his CSIR supervisor, Willie Nel, and Duncan Stanton.

1.3 ISAR Imaging of Sea Vessels

In an ideal ISAR imaging scenario (see Section 2.2.1), a radar illuminates a controlled 2-D rotating object to obtain a focused 2-D image with high spatial resolution. As only the object is illuminated, there are no artefacts in the image caused by clutter. Furthermore, since the motion of the object is known, the cross-range dimension can be scaled to distance.

ISAR imaging of sea vessels is complex, and there are many challenges that need to be overcome in order to obtain 2-D images with high spatial resolution (see Section 2.3). Some of these include translational (Li *et al.* [22] and references therein) and rotational (Munoz-Ferreras and Perez-Martinez [23]) motion compensation, three-dimensional (3-D) motion (Chen and Miceli [24]), multipath (Berizzi [25]) and cross-range scaling (Prodi [26] and Martorella [27]). The length

of the coherent processing interval (CPI), referred to as the coherent processing time window length (CPTWL), is an important parameter in the ISAR imaging process and it needs to be chosen very carefully, as discussed by Martorella and Berizzi in [28].

An example of successive ISAR images, using the Esperance yacht (see Figure 1.1) is shown in Figure 1.2. Radar recordings were obtained from the Signal Hill 2007 trial (see Appendix A for more information). In this particular recording, the yacht was sailing directly inbound to the radar. The ISAR images were obtained using a CPTWL of 0.8 s, and an overlap factor of 75% between two successive images; translation motion compensation was achieved by using the range alignment technique of Wang and Kasilingam [29] and the autofocus algorithm proposed by Yuan and Casasent [30]. The ISAR images of the yacht corresponds to a radar recording of 2.4 s.

Figure 1.1: Photo of the Esperance yacht

Figure 1.2 shows that many of the ISAR images are blurred. Blurry ISAR images are not desirable because they lead to inaccurate estimation of parameters, which reduces the probability of correct classification, as shown by McFadden and Musman in [31].

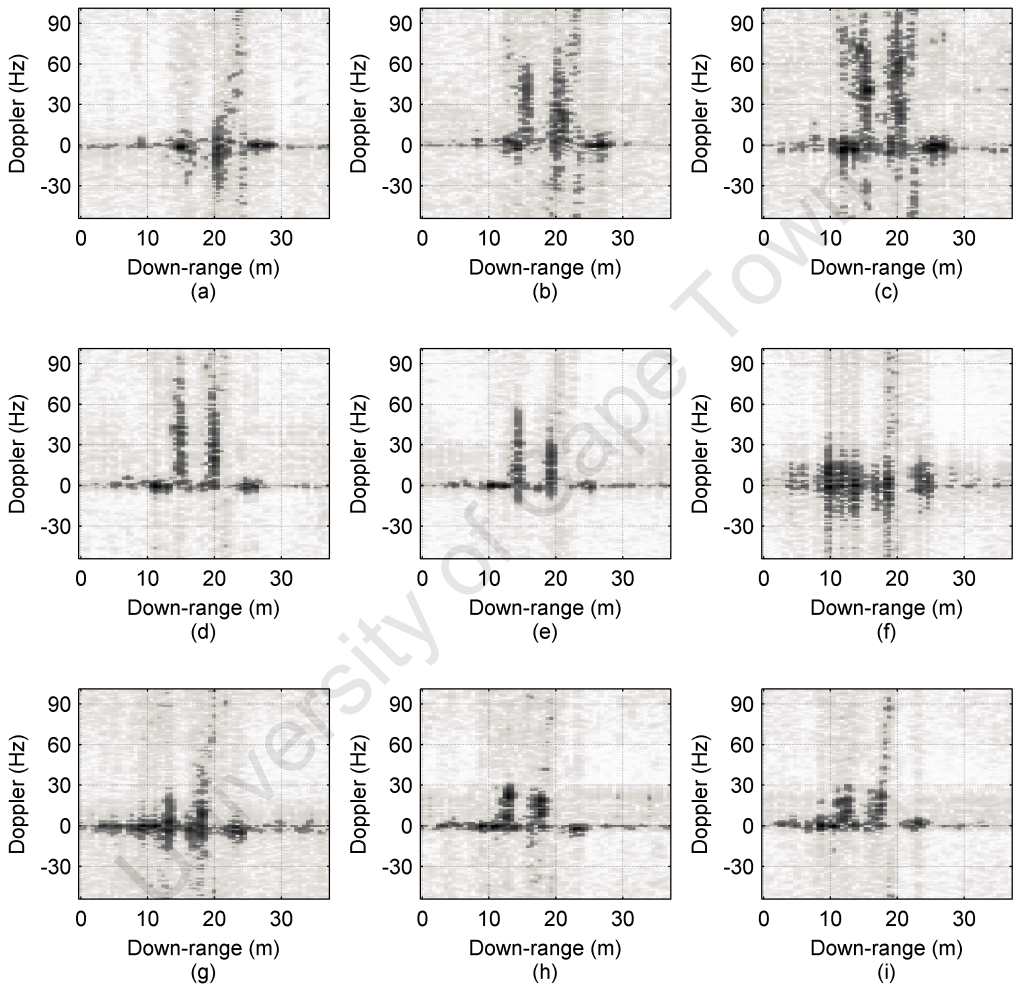

Figure 1.2: Successive motion compensated ISAR images of a yacht obtained with a CPTWL of 0.8 s and an overlap factor of 75%

Occasionally, a side-view image of the yacht is generated, as shown in Figure 1.2(d). During this CPI, the pitch motion of the vessel is dominant (i.e. more significant than the roll and yaw motion), which causes the scatterers along each mast to have different Doppler frequencies. Consequently, the cross-range dimension of the ISAR image is aligned along the height dimension of the vessel and a side-view image is generated. Figure 1.2(f) shows an ISAR image 0.4 s later; during this CPI the 3-D rotational motion of the vessel is significant (i.e. roll, pitch and yaw motion are equally dominant), which causes blurring in the ISAR image.

These ISAR images clearly illustrate that 3-D rotational motion is a major challenge and that it is a research topic that warrants further investigation. Moreover, since a focused side-view ISAR image only occurs occasionally, and for a short time, the choice of the CPTWL and the selection of optimum imaging intervals are important related research topics that need to be addressed. This challenge provides the motivation for the research question and the hypothesis of this thesis.

1.4 Hypothesis and Research Questions

The hypothesis of this thesis is stated as follows:

> "Three-dimensional rotational motion of sea vessels gives rise to blurring in ISAR imagery because it causes the image-generating Doppler components to vary over time. Suitable CPTWLs are selected for cooperative vessels, to obtain ISAR images with limited blurring. For non-cooperative vessels, optimum imaging intervals are estimated to obtain focused side-view ISAR images, which are a rich source of information for ship classification."

The image-generating Doppler components, which consist of the Doppler generating axis of rotation and the effective angular rotation rate, are important to the ISAR imaging process. The Doppler generating axis of rotation influences the

imaging projection plane, and the effective angular rotation rate determines the cross-range resolution of the ISAR image. When the image-generating Doppler components vary over time, it causes scatterers to migrate through cells in the ISAR image; this gives rise to blurring. However, by choosing suitable CPTWLs and optimum imaging intervals where the image-generating Doppler components do not vary significantly over time, ISAR images with limited blurring can be obtained. Such images would be a rich source of information for RCS measurement of cooperative vessels or ISAR-based classification of non-cooperative vessels.

From the hypothesis, the following research questions arise:

- **Research question 1:** Why does a vessel's 3-D rotational motion cause blurring in ISAR imagery?
- **Research question 2:** Is it possible to extract the image-generating Doppler components from the measured motion data of a sea vessel and does the time-varying nature of the image-generating Doppler components cause blurring in ISAR imagery?
- **Research question 3:** Can measured motion data be used to select suitable CPTWLs that would limit the blurring in ISAR imagery of cooperative vessels?
- **Research question 4:** Can optimum imaging intervals, which produce side-view ISAR images, be estimated from only the radar data of a non-cooperative vessel?

Figure 1.3 shows a block diagram that illustrates how the hypothesis, research questions and research objectives are linked to each other. The hypothesis stated in this thesis is supported by four research questions. When all the research questions are answered positively, then the hypothesis is satisfied. Each research question is answered by addressing the corresponding research objective. Figure 1.3 also shows that research objective 1 to research objective 4 are addressed in Chapter 3 to Chapter 6 respectively.

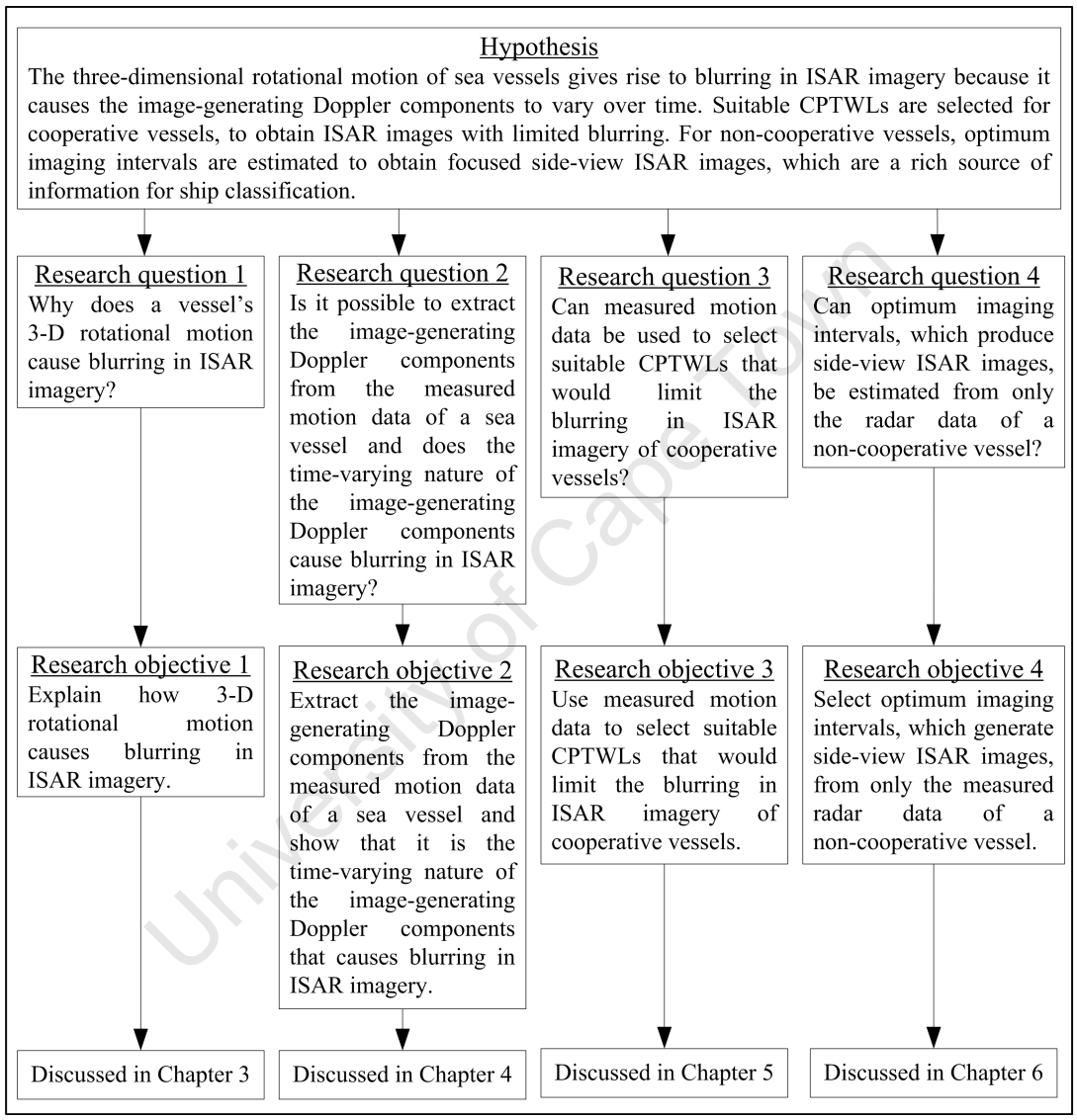

Figure 1.3: Block diagram of the hypothesis, research objectives and research questions of the thesis

The hypothesis stated in this thesis is significant for the ISAR imaging of sea vessels because, assuming that it can be proven to be true, it provides an in-depth understanding of how 3-D rotational motion causes blurring in ISAR imagery. Furthermore, by accurately selecting suitable CPTWLs and optimum imaging intervals for both cooperative and non-cooperative vessels respectively, ISAR images with limited blurring can be generated, which is useful for RCS measurement purposes and ship classification.

1.5 Thesis Objectives

Sea vessels often possess 3-D rotational motion (roll, pitch and yaw). Under this condition it is problematic to form ISAR images of maritime objects, as reported by Rihaczek and Hershkowitz [32], for the following reasons:

- A down-range cell may contain scatterers at different heights and azimuths, which may have very different range histories. As a result, all the scatterers in a down-range cell cannot be focused with a single motion compensation factor. Different motion compensation factors are needed to focus each scatterer separately and it is a challenging task to accurately track the range histories of scatterers.

- For classification purposes, it is desirable to convert the Doppler frequency of ISAR images to cross-range. However, when an inbound vessel possesses 3-D rotational motion, there are two independent rotational motions that cause scatterers to possess Doppler frequencies: pitch motion causes scatterers along the height dimension of the vessel to possess finite Doppler frequencies, whereas yaw motion causes scatterers along the width dimension also to possess Doppler frequencies. Thus, there are two independent cross-range scaling factors that are needed to convert the Doppler frequency on an ISAR image to either the height or width dimension. In order to obtain these two cross-range scaling factors, accurate knowledge of the pitch and yaw motion of the vessel is needed, which is a challenging estimation task for non-cooperative vessels. Furthermore, it is a difficult task to identify if the Doppler frequency of a specific scatterer was caused by the pitch motion of a scatterer with finite height or the yaw motion of a scatterer with finite width, or by both pitch and yaw motion of a scatterer with finite height and width.

- Dominant scattering centres of a complex object like sea vessels are often generated by extended corners and cavities, which are usually irregularly shaped. When the direction of illumination changes, the phase centre of the scattering centre shifts position and there is a larger shift for 3-D rotational

motion than 2-D rotational motion. This spreads a scatterer's response over multiple range and Doppler cells and generates undesirable strong spurious responses in positions away from the scatterer, even with perfect motion compensation.

Thus, it is advantageous to form ISAR images of sea vessels over imaging intervals where the vessel possesses 2-D rotational motion. For this reason, the research in this thesis does not address the problem of forming a focused 2-D or 3-D ISAR image over intervals where the vessel possesses significant 3-D rotational motion.

The aim of the research presented in this thesis is to investigate the effect of 3-D rotational motion on the ISAR imaging process, in order to understand how 3-D rotation motion gives rise to blurring in most ISAR images of sea vessels. In addition, the choice of the CPTWL and the selection of optimum imaging intervals is also discussed, to address the blurring caused by 3-D rotational motion for cooperative and non-cooperative vessels respectively. In summary, this thesis investigates the following aspects of ISAR imaging of sea vessels:

- The effect of a vessel's 3-D rotational motion on the ISAR imaging process
- Extraction of the time-varying image-generating Doppler components from measured motion data
- Using measured motion data to select suitable CPTWLs that would limit the blurring in ISAR imagery of cooperative vessels
- Selecting multiple optimum imaging intervals for non-cooperative sea vessels that produce highly focused side-view ISAR images, which is a rich source of information for ship classification.

These aspects were investigated using measured data from two ISAR measurement campaigns, which were performed at Simon's Town and Signal Hill in May 2007 and November 2007 respectively. During these trials, cooperative sea vessels were instrumented with an Inertial Navigation System (INS)/Global Positioning System (GPS) that recorded the attitude and position of the vessel throughout

the experiment. Radar recordings were obtained using an experimental X-band radar, which generates high range resolution (HRR) profiles using stepped frequency waveforms.

The recorded motion and radar recordings were used to gain a better understanding of how 3-D rotational motion causes blurring, and to assess the performance of algorithms that are proposed in this thesis. The image-generating Doppler components were extracted from the measured motion recordings, and 3-D rotational motion was shown to cause these two components to vary over time. Translation motion compensation algorithms were applied to the radar recording to obtain continuous ISAR images of the sea vessels over time. Most of the motion compensated ISAR images were blurred (see Figure 1.2), because translation motion compensation algorithms incorrectly assume that sea vessels only possess 2-D motion over the CPI. Thus, for sea vessels with 3-D rotational motion it is important to select optimum imaging intervals where the rotation motion is approximately 2-D. These optimum intervals would limit the blurring in the image caused by the roll, pitch and yaw motion of the vessel.

The objectives of this thesis can be summarised as follows:

- To review the principles of ISAR, summarise the major challenges in ISAR and describe the signal processing steps that will generate focused ISAR images for applications such as classification or RCS management. To perform a critical literature review and identify the gaps and limitations of the existing literature, which are addressed in this thesis.

- To review the existing literature that discusses the effect of 3-D motion on the resulting ISAR image. Thereafter, to model the 3-D rotational motion using quaternion algebra. Note that the use of quaterions is motivated in Chapter 2 and Chapter 3. To investigate the effect of a vessel's roll, pitch and yaw motion on the ISAR imaging process. To characterise the amount of blurring that a scatterer experiences when the Doppler generating axis of rotation changes over the CPI.

- To develop a transformation to extract the image-generating Doppler components, which consist of the vessel's Doppler generating axis of rotation and the effective angular rotation rate, from measured motion data. These two components are important to ISAR because the Doppler generating axis of rotation influences the imaging projection plane, and the effective angular rotation rate determines the cross-range resolution of the ISAR image. Furthermore, when these components vary over time, it causes blurring in the resulting ISAR image. To implement the proposed transformation on measured motion data and validate the transformation with measured radar data

- To develop a point scatterer ISAR simulation environment that uses measured motion data to produce simulated ISAR images of a vessel. To validate the simulation using measured radar data.

- To review the current literature regarding the selection of the CPTWL for ISAR imaging of sea vessels. To develop an algorithm that uses measured motion to select suitable CPTWLs that limit the blurring caused by 3-D motion. Furthermore, the suggested CPTWLs should produce ISAR image(s) with the desired cross-range resolution. To apply this algorithm to measured motion data and demonstrate the effectiveness of the suggested CPTWLs using measured radar data.

- To review the current literature on the selection of optimum intervals for ISAR imaging of non-cooperative sea vessels. To propose a technique to select multiple optimum imaging intervals that generates focused side-view ISAR images, which are a rich source of information for ship classification. To apply the proposed algorithm to measured radar data of non-cooperative vessels to demonstrate the effectiveness of the proposed technique.

1.6 Thesis Development

1.6.1 Critical literature survey

Chapter 2 reviews the basic principles of ISAR. A summary of ISAR theory is presented regarding down-range resolution, cross-range resolution, the image projection plane and the image-generating Doppler components. This is followed by a description of the signal processing steps in motion compensation for ISAR. Thereafter, the challenges associated with forming a focused ISAR image of sea vessels are discussed. Lastly, a critical review of the literature is presented to identify the gaps in the literature, which are addressed in this thesis.

1.6.2 Examining the effect of 3-D rotational motion on ISAR imagery

Chapter 3 investigates the effect of 3-D rotational motion on the ISAR imaging process. Results in the literature show that 3-D rotational motion gives rise to blurring in ISAR images, as shown by Chen and Lipps [33] and Li *et al.* [34]. Blurry ISAR images are not desirable for classification purposes [31] because they lead to inaccurate estimation of parameters, which in turn reduces the probability of correct classification. While much research has been done on investigating the effect of 3-D rotational motion on ISAR [24], [35], [36], [37], [38], these papers mainly show results for objects with simulated rotational motion confined to a 2-D plane that is orthogonal to the radar line of sight (LOS) vector i.e. only pitch, roll or yaw motion. Furthermore, matrices are used to model the 3-D rotational motion and this approach is limited because it does not directly and independently model the image-generating Doppler components, whose time-varying nature gives rise to blurring.

In this chapter, a new quaternion-based system model is proposed to investigate the effect of 3-D rotational motion on ISAR imagery. One of the advantages of the system model is that it is flexible enough to incorporate the measured

motion data of a vessel. Quaternions are used to represent the 3-D rotational motion and, while it is equally accurate as using matrices, it offers the advantage of directly and independently modelling the vessels's image-generating Doppler components over the CPI. Since the effect of non-uniform angular rotation has been investigated in [39], Chapter 3 focused on using theory and simulations to understand the effect of a time-varying Doppler generating axis of rotation on the ISAR imaging process.

Point scatterer simulations are performed for three different cases, where the Doppler generating axis of rotation changes in different ways over the CPI. Case 1 considers a side-view ISAR imaging scenario and shows that a uniformly changing yaw perturbation causes the angle of the Doppler generating axis of rotation, denoted by $\theta_{\Omega eff}$, and the object's rotation rate, denoted by $\dot{\theta}$, to vary over time (see Figure 1.4). Consequently, there are certain scatterers along the deck that migrate through cross-range cells, and this gives rise to a blurry ISAR image (see scatterer 1 in Figure 1.5 (a)). Case 2 characterises the migration of scatterer 1 through cross-range cells that is exclusively due to the time-varying nature of the Doppler generating axis of rotation (see Figure 1.5 (b)). Lastly, case 3 considers realistic 3-D rotational motion with time-varying roll, pitch and yaw motion.

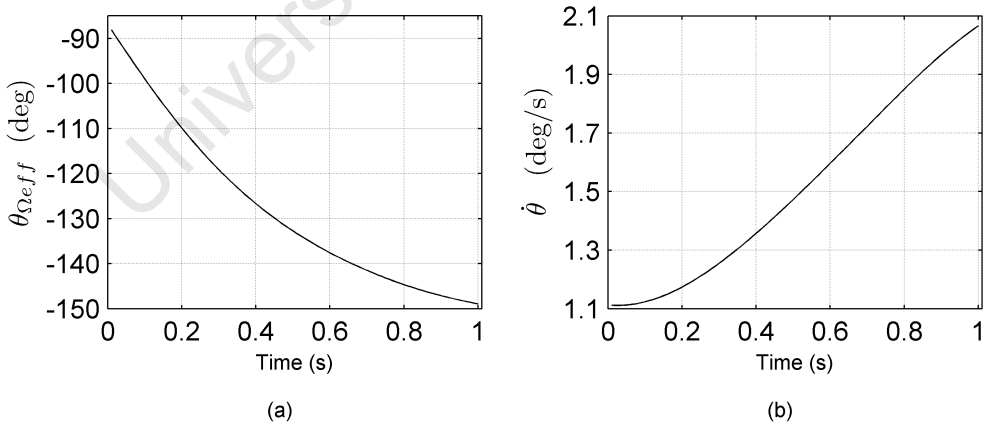

Figure 1.4: (a) Angle of the Doppler generating axis of rotation $\theta_{\Omega eff}$ and (b) angular rotation rate $\dot{\theta}$ over the CPI

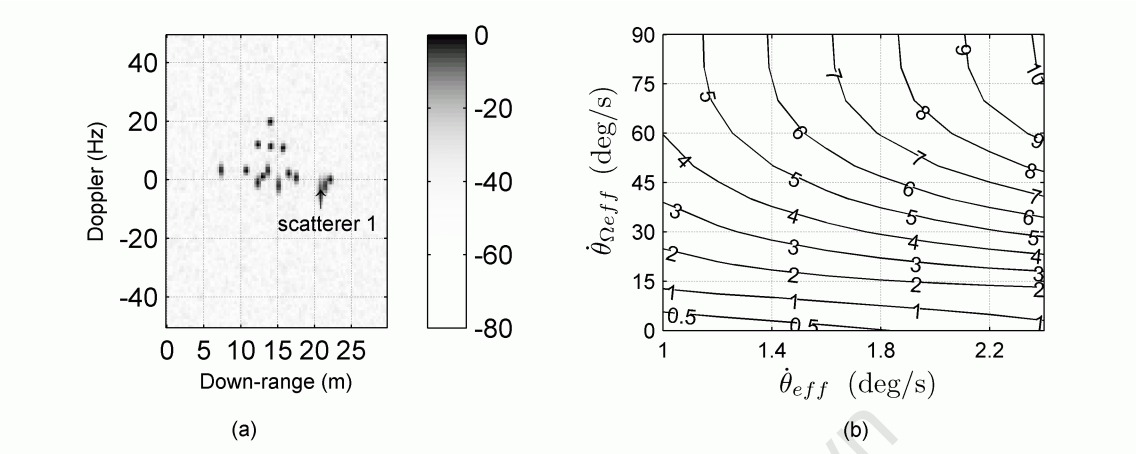

Figure 1.5: (a) ISAR image and (b) contour plot showing the migration through cross-range cells for scatterer 1, for varying $\dot{\theta}_{\Omega eff}$ and $\dot{\theta}_{eff}$

Chapter 3 uses both theory and simulations to show that 3-D rotational motion causes blurring in ISAR imagery. More specifically, Chapter 3 shows that, when an object's Doppler generating axis of rotation varies over the CPI, it causes the Doppler frequency of scatterers to migrate through the cross-range cells of an ISAR image. Consequently, this gives rise to a blurred ISAR imagery.

The results in Chapter 3 show that a time-varying Doppler generating axis of rotation has a significant influence on the blurring in an ISAR image. However, the majority of the results were obtained using theoretical motion and not realistic motion. Thus, it is still necessary to understand how a real sea vessel's Doppler generating axis of rotation changes over time, since this is one of the causes of blurring in measured ISAR images. Another important parameter is the effective angular rotation rate because it influences the cross-range resolution of an ISAR image. Thus, it is important to extract the image-generating Doppler components from the measured motion of a vessel to understand how the time-varying nature of these two components leads to blurring. This problem is addressed in Chapter 4.

1.6.3 Extracting image-generating Doppler components

Maritime vessels and aircraft possess 3-D rotational motion; however, it is only components of this motion, referred to as the image-generating Doppler components, that are useful to the ISAR imaging process. Chapter 4 describes a new transformation that extracts an object's image-generating Doppler components, which consist of the Doppler generating axis of rotation and the effective angular rotation rate, from the measured motion data. These two parameters are important to the ISAR imaging process because the Doppler generating axis of rotation influences the presentation of the vessel, whereas the effective rotation rate affects the cross-range resolution of the resulting ISAR image. In addition, the time-varying nature of these two parameters give rise to blurring in ISAR imagery.

The image-generating Doppler components and their influence on ISAR imaging are described in the literature. A mathematical expression of the continuously varying Doppler generating axis of rotation was derived in papers by Chen and Miceli [24] and Bao *et al.* [38]. However, there is no literature that addresses how to extract both of these image-generating Doppler components from the measured motion data of a vessel.

Chapter 4 proposes a new quaternion-based transformation that calculates both the image-generating Doppler components from measured attitude and the GPS position data of an object. Moreover, a new improved quaternion-based system model is proposed that is computationally more efficient than the system model presented in Chapter 3. The transformation provides the ability of gaining an in-depth understanding of the time-varying nature of these two ISAR related parameters.

The transformation was applied to the measured attitude and GPS position data of a yacht (see photo in Figure 1.1), and the results show that both the angle of the Doppler generating axis of rotation, denoted by $\theta_{\Omega eff,\Delta t(n)}$, and the effective angular rotation rate, denoted by $\dot{\theta}_{eff,\Delta t(n)}$, varied over time (see Figure 1.6 (a) and (b)). However, there are intervals where the image-generating

Doppler components do not vary over time. By choosing radar data that corresponds to these intervals, ISAR images with limited blurring can be obtained, as shown by Figure 1.6 (c). When the CPI corresponds to an interval where the image-generating Doppler components vary over time, the resulting ISAR image contains significant blurring (see Figure 1.6 (d)).

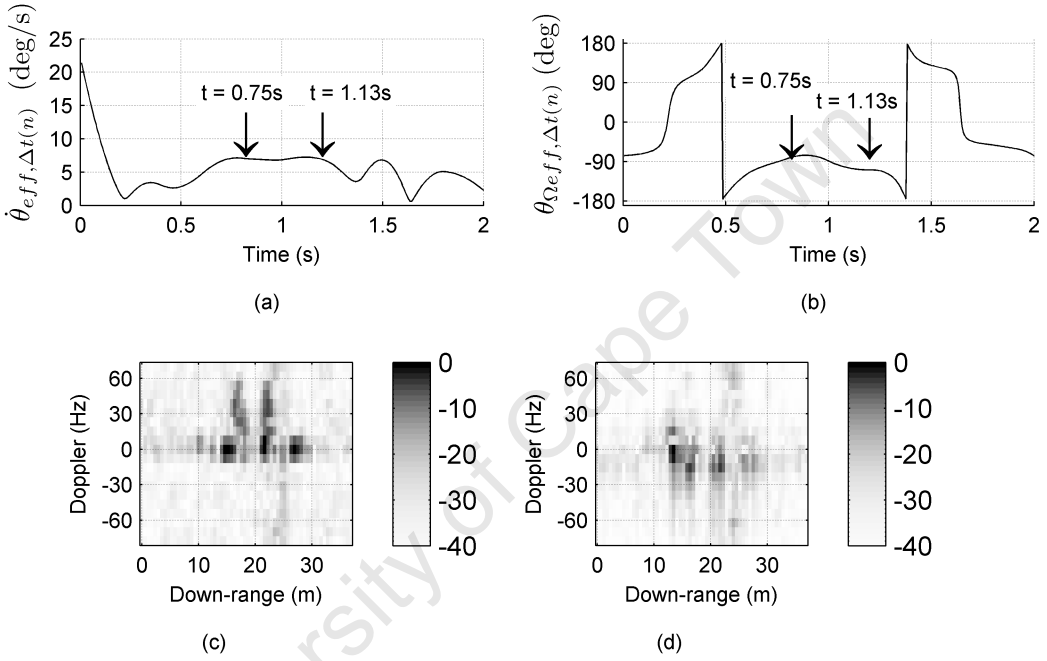

Figure 1.6: (a) Effective angular rotation rate $\dot{\theta}_{eff,\Delta t(n)}$, (b) angle of the Doppler generating axis of rotation $\theta_{\Omega eff,\Delta t(n)}$, (c) measured ISAR image during 0.75 $s \leq t \leq 0.88$ s, and (d) measured ISAR image during 1.65 $s \leq t \leq 1.78$ s

The transformation that is proposed in Chapter 4 shows that it is possible to extract the image-generating Doppler components from measured motion data of sea vessels. Furthermore, results with measured radar data show that, when the image-generating Doppler components vary over time, it causes blurring in ISAR imagery.

Chapter 4 does not provide any information about how to choose a suitable CPTWL when both motion and radar data are available. This is the topic of interest in Chapter 5.

1.6.4 Selecting suitable CPTWLs for cooperative vessels

Results in the literature have shown that 3-D rotation motion gives rise to blurry ISAR imagery. One way of limiting the blurring caused by 3-D rotational motion is to select carefully the duration of the CPI, which is referred to as the CPTWL. The CPTWL should be short enough to limit the blurring caused by 3-D rotational motion and long enough to ensure that the desired cross-range resolution is obtained.

The work of Wehner [40] and Martorella and Berizzi [28] provides some information on selecting CPTWLs for ISAR imaging of ships. However, the suggested range in [40] is too broad, as it spans more than an order of magnitude. Moreover, Wehner gives no information on how this suggested range changes for different classes of sea vessels. An optimum imaging selection algorithm proposed in [28] shows how the optimum central instant of the processing interval should be estimated, as well as how to ascertain the optimum CPTWL that provides an ISAR image with the highest focus. However, this algorithm does not show how the initial CPTWL for a specific recording should be chosen, and the suitability of this technique for small ships with chaotic motion has not been investigated. Moreover, it does not take advantage of motion data from instrumented vessels that may be available during measurement trials for RCS measurement purposes.

Chapter 5 proposes a technique, referred to as the motion-aided CPTWL selector (MACS) algorithm that uses measured motion data to select suitable CPTWLs for ISAR imaging of sea vessels. The suggested CPTWLs produces ISAR image(s) with the desired cross-range resolution and limited blurring due to 3-D rotational motion.

The MACS algorithm was applied to motion datasets of three different classes of vessels: a yacht, a fishing trawler and a survey vessel. The suggested CPTWLs indicate that a longer CPTWL is needed for larger vessels. The MACS algorithm suggested a suitable CPTWL range of $\{0.55\text{ s},\ 0.85\text{ s}\}$, $\{1.6\text{ s},\ 1.8\text{ s}\}$ and $\{1.2\text{ s},\ 2\text{ s}\}$ for the yacht, fishing trawler and survey vessel respectively. The effectiveness of the suggested range of CPTWLS for the yacht was demonstrated

using measured radar data. Figure 1.7 shows three ISAR images of the yacht that were obtained using a CPTWL, denoted by $\Delta\tau$, of 0.2 s, 0.8 s and 1.6 s. A photo of the yacht is shown in Figure 1.1.

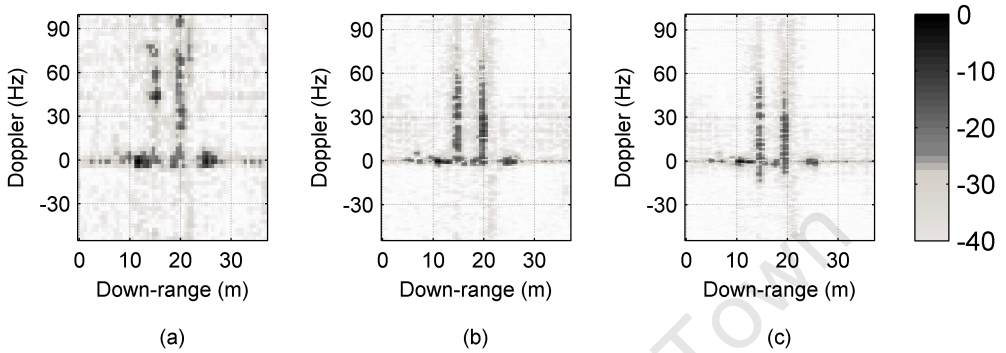

Figure 1.7: ISAR images of the yacht for a CPTWL of (a) $\Delta\tau = 0.2$ s, (b) $\Delta\tau = 0.8$ s and (c) $\Delta\tau = 1.6$ s

When the CPTWL is too short (see Figure 1.7 (a)), the cross-range resolution of the resulting image is poor. Conversely, when the CPTWL is too long (see Figure 1.7 (c)), the 3-D rotational motion of the vessel is significant and gives rise to a blurry ISAR image, where the heights of the yacht's two masts do not appear to be equal. These limitations are overcome when the CPTWL is chosen from the suggested range of CPTWLs, and Figure 1.7 (b) shows the resulting ISAR image for a CPTWL of 0.8 s. The cross-range resolution is superior to that of Figure 1.7 (a) and the two masts are clearly discernible. This demonstrates the effectiveness of the suggested CPTWL range to generate ISAR images with sufficient cross-range resolution and limited blurring due to 3-D rotational motion.

The MACS algorithm proposed in Chapter 5 shows that measured motion data of sea vessels can be used to select suitable CPTWLs that would limit the blurring in the ISAR imagery of cooperative vessels. Moreover, it ensures that the CPTWLs are long enough to obtain ISAR images with the desired cross-range resolution.

When both motion and radar data are available, the MACS algorithm may be used to obtain ISAR images for cooperative sea vessels for RCS measurement purposes. However, motion data is not available for non-cooperative vessels, and

Chapter 5 does not show how optimum imaging intervals should be selected for this case. This research topic is addressed in Chapter 6, and it is an important area of research for ISAR-based classification of non-cooperative sea vessels.

1.6.5 Selecting optimum imaging intervals for non-cooperative vessels

In maritime surveillance applications, ISAR images of sea vessels are used for ship classification. The literature has shown that side-view ISAR images contain discriminant information that is useful for classification. However, it is a challenging task to isolate focused side-view ISAR images of a non-cooperative vessel from a long radar recording, because a vessel's roll, pitch and yaw motion affects the presentation of the vessel in the ISAR image and the 3-D rotational motion also caused blurring in many ISAR images.

Many algorithms have been proposed in the literature to identify optimum imaging intervals for ISAR imaging of non-cooperative sea vessels. These algorithms can be grouped into frame selection techniques and joint frame and optimum CPTWL selection techniques. Examples of the former include papers by Hajduch *et al.* [19], Rihaczek and Hershkowitz [32], Li *et al.* [34] and Pastina and Spina [41], whereas an example of the latter is the MC-ATWS algorithm proposed by Martorella and Berizzi [28].

Frame selection techniques are limited because they do not show how an effective initial CPTWL should be chosen and because they assume that the initial CPTWL is approximately equal to the duration of all the optimum ISAR imaging intervals in the radar recording. Furthermore, these algorithms are problematic to implement with real data because they require accurate phase unwrapping and because a few techniques assume accurate tracking of a scatterer at the bow and the stern of the ship that are the same width and height position, which is difficult to achieve in practice.

Joint frame and optimum CPTWL selection techniques, such as the maximum-contrast-based automatic time window selection (MC-ATWS) algorithm pro-

posed by Martorella and Berizzi in [28], also possess several limitations: the algorithm only estimates the parameters of a single imaging interval and ignores other optimum imaging intervals that may exist in a long radar recording; when the algorithm is applied to radar recordings of small sea vessels, the algorithm's performance is dependent on the value of the initial CPTWL; furthermore, the highly focused ISAR image that is generated from the optimum imaging interval does not always correspond to a side-view ISAR image, which is desired for ship classification.

Chapter 6 proposes a new algorithm, referred to as the extended maximum-contrast-based automatic time window selection (EMC-ATWS) algorithm, which identifies multiple optimum imaging intervals for small non-cooperative sea vessels. The proposed technique is superior to the original MC-ATWS algorithm because it uses a range of initial CPTWLs, which means that the proposed algorithm's performance is not dependent on a single initial CPTWL. Furthermore, the EMC-ATWS algorithm offers the advantage of extracting more than a single optimum imaging interval from a radar recording. Lastly, the imaging intervals that are found give rise to focused side-view ISAR images, which are a rich source of information for operator assisted ship classification.

Both the MC-ATWS and the EMC-ATWS algorithms were applied to measured radar recordings of two inbound non-cooperative yachts. Results in Figure 1.8 show that the MC-ATWS algorithm estimates the parameters of a single optimum imaging interval that produces a highly focused ISAR image with very little Doppler information, which is undesirable for operator assisted ship classification. In contrast, Figure 1.9 shows that the EMC-ATWS algorithm estimated the parameters of multiple optimum imaging intervals that each generated a highly focused side-view ISAR image.

Thus, results from measured radar show that the proposed EMC-ATWS algorithm is an effective algorithm for estimating multiple optimum imaging intervals for small non-cooperative vessels.

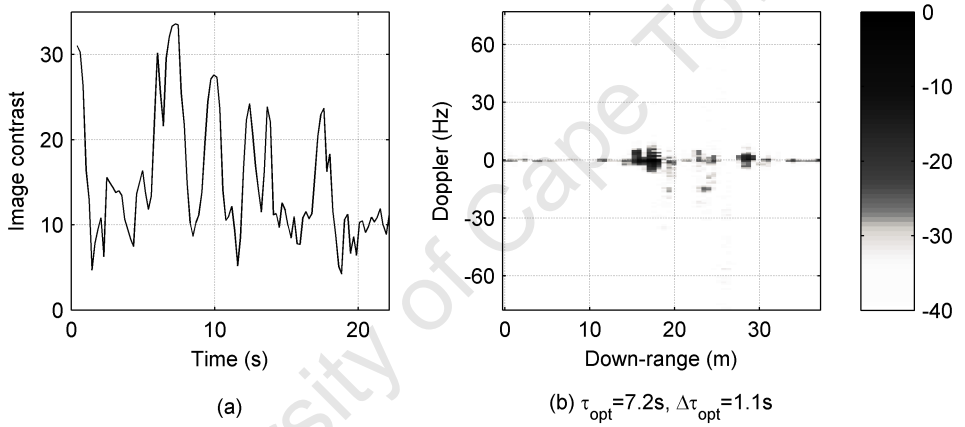

Figure 1.8: Results from applying the MC-ATWS algorithm to the radar recording of the Esperance: (a) IC versus time, (b) motion compensated ISAR image obtained from the optimum imaging interval with $\tau_{opt} = 7.2$ s and $\Delta\tau_{opt} = 1.1$ s

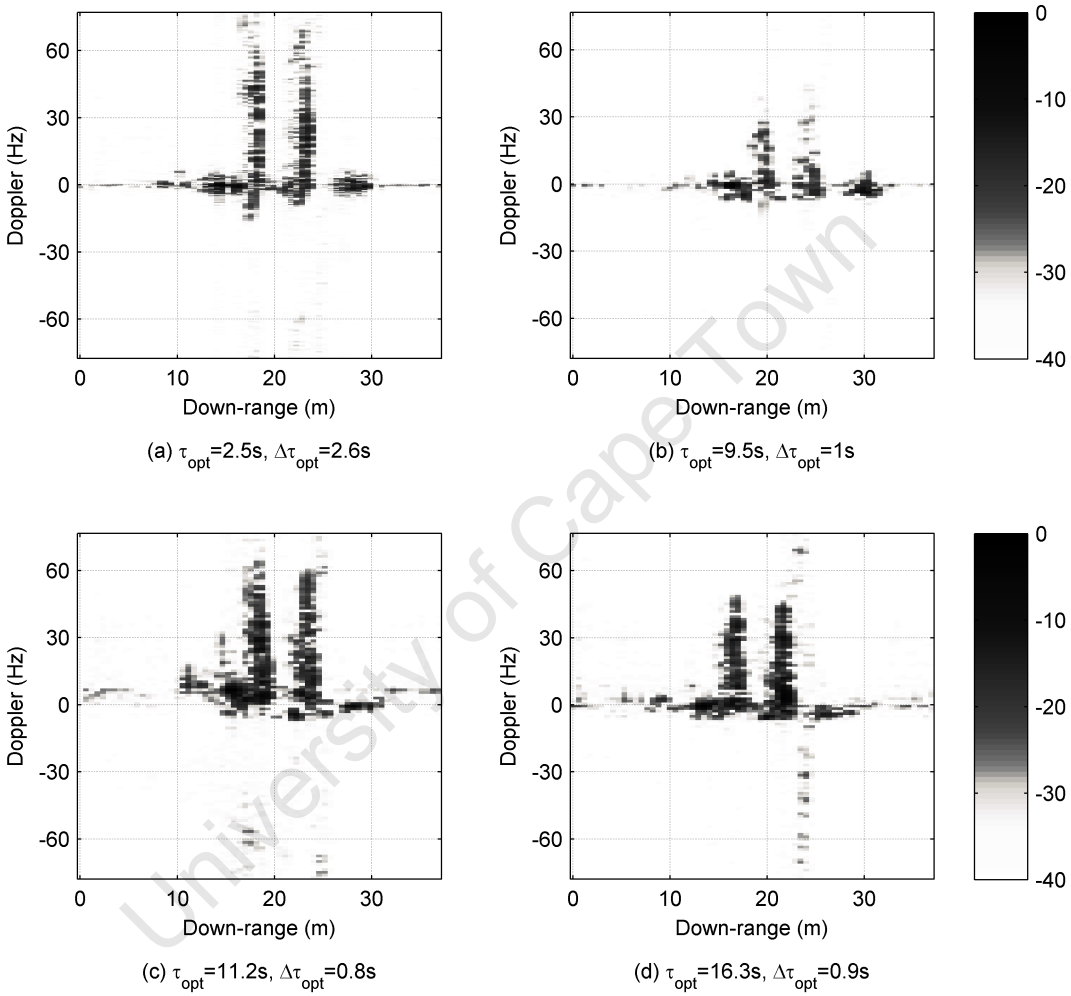

Figure 1.9: Results from applying the EMC-ATWS algorithm to the radar recording of the Esperance: motion compensated ISAR images obtained from the optimum imaging intervals with parameters (a) $\tau_{opt} = 2.5$ s and $\Delta\tau_{opt} = 2.6$ s , (b) $\tau_{opt} = 9.5$ s and $\Delta\tau_{opt} = 1$ s , (c) $\tau_{opt} = 11.2$ s and $\Delta\tau_{opt} = 0.8$ s , (d) $\tau_{opt} = 16.3$ s and $\Delta\tau_{opt} = 0.9$ s

1.6.6 Conclusions

Conclusions and recommendations for future work are summarised in Chapter 7.

1.7 Statement of Originality

The original contributions made in this thesis can be summarised as follows:

- Chapter 3 (effect of 3-D rotational motion on ISAR imagery) — In this chapter, a new system model is proposed that uses quaternion mathematics to represent the 3-D rotational motion of a vessel. The application of quaternions to the field of ISAR has not been documented in the literature thus far. The new system model is used to characterise the effect of a target's time varying Doppler generating axis of rotation on the migration of a scatterer through Doppler cells, which has also not been addressed in the literature. Portions of this work have been presented at the IET International Radar Conference in Edinburgh, Scotland in 2007 [42].

- Chapter 4 (extraction of image-generating Doppler components) — A new transformation is proposed to extract the image-generating Doppler components from measured motion data. In addition, this chapter describes a new point scatterer ISAR environment that uses quaternions to represent a vessel's 3-D rotational motion. The development, coding, application of the transform to measured motion data, simulation and validation with measured radar data are all the candidate's own work. This work has been published in the IEEE Geoscience and Remote Sensing Letters Journal [43].

- Chapter 5 (selecting suitable CPTWLs for cooperative vessels) — This chapter presents a novel technique, referred to as the MACS algorithm, that selects suitable CPTWLs for ground-based ISAR imaging of sea vessels. The concept of this algorithm, its coding, application to measured motion data and the effectiveness of the suggested CPTWLs to measured radar

data are the candidate's own work. This work has been published in the IEEE Transactions on Geoscience and Remote Sensing Journal [44].

- Chapter 6 (selecting optimum imaging intervals for non-cooperative vessels) — A new technique, referred to as the EMC-ATWS algorithm, is proposed for selecting multiple optimum imaging intervals that generates focused side-view ISAR images of small non-cooperative vessels, which is a rich source of information for operator assisted ship classification. The concept of this algorithm, its coding and application to measured radar data are the candidate's own work. This work has been submitted to the IEEE Geoscience and Remote Sensing Letters Journal [45].

Chapter 2

Literature Review

2.1 Introduction

ISAR imaging of maritime objects has been an active topic of research for many decades, as described by Wehner [40]. Much of the research effort in the application of ISAR has focused on classification, as shown in papers by Bon *et al.* [6], Musman *et al.* [7] and Yuan and Casasent [30].

ISAR imaging of sea vessels can provide more information about a maritime object than conventional radar techniques, which traditionally estimate the distance, radial velocity, azimuth angle and elevation angle of a vessel. A typical 2-D ISAR image represents the backscattered EM energy from an object in the down-range and cross-range dimensions. Literature has shown that side-view and top-view ISAR images of sea vessels are a rich source of information for classification purposes [7]. High down-range resolution is obtained using a waveform with a large effective transmit bandwidth, and cross-range information of a rotating object is obtained from the Doppler frequency of the moving scatterers.

An example of how ISAR provides cross-range information is shown in Figure 2.1. In this diagram, a sea vessel is sailing directly inbound to the radar, a vector from the sea vessel's centre of rotation to the radar is denoted by **RT**, and the

two orthogonal vectors are expressed by $\mathbf{RT}_{\perp 1}$ and $\mathbf{RT}_{\perp 2}$. In this example, the rotational motion of the sea vessel is represented by an angular velocity of $\dot{\theta}$ about a vector $\mathbf{\Omega}$, which is along the $\mathbf{RT}_{\perp 1}$ vector; in essence, the vessel possesses pure pitch motion.

Side-view ISAR imaging of sea vessels operates on the principle that, when an inbound vessel possesses pure pitch motion, the scatterers along each mast have cross-range dependent Doppler frequencies. Thus, cross-range information is obtained by simply separating scatterers according to their Doppler frequency. The difference in radial velocities of two scatterers along a mast is shown in Figure 2.1, where the radial velocity of the scatterer higher up mast 1, denoted by v_1, is greater than the radial velocity of the scatterer lower down, which is expressed by v_2. In this example the cross-range dimension is along the $\mathbf{RT}_{\perp 2}$ direction, because this vector is orthogonal to the plane spanned by the $\mathbf{RT}$ vector and the vessel's Doppler generating axis of rotation. A more generalised formulation of the direction of the cross-range dimension is given in Section 2.2.4.

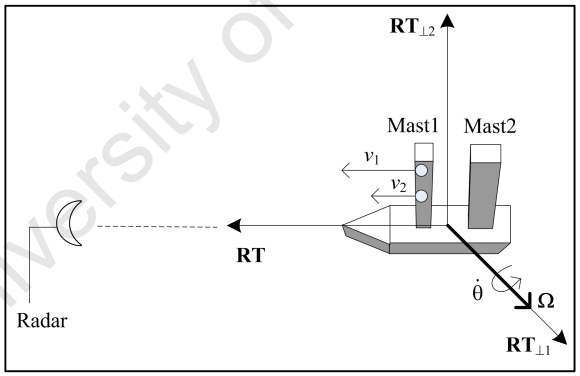

Figure 2.1: An example illustrating how ISAR uses rotational motion to provide cross-range information

A mathematical description of the theory of ISAR is given in Section 2.2. In that section, the conventional ISAR system model is formulated in Section 2.2.1, properties of the down-range and cross-range dimensions of an ISAR image are discussed in Section 2.2.2 and Section 2.2.3 respectively, the image projection plane and the image-generating Doppler components are described in Section 2.2.4, and the signal processing steps in motion compensation are outlined in

Section 2.2.5. The ISAR theory that is presented in Section 2.2 is in no sense novel, but it provides the foundation for understanding the challenges in ISAR, discussed in Section 2.3. It also provides the necessary background for performing a critical review of the literature pertaining to the field of ISAR imaging of sea vessels with 3-D rotational motion (see Section 2.4).

2.2 ISAR Theory

This section provides a mathematical description of the theory of ISAR. It summarises the principles of ISAR and derives the conventional mathematical system model that is used in the ISAR literature. Furthermore, it discusses the sampling requirements that need to be met, in order to prevent ambiguity in the down-range and cross-range dimensions of an ISAR image. The other topics discussed are the image projection plane, the image-generating Doppler components and the signal processing steps that are required for ISAR motion compensation.

2.2.1 The conventional ISAR system model

ISAR uses the relative change in aspect angle between the radar and an object to provide cross-range information. There are two components of motion that cause changes in the relative aspect angle: translation motion and 3-D rotational motion. For fast moving airborne objects, translation motion is the major component of motion that causes changes in the relative aspect angle over a CPI. However, for maritime objects, translation motion is a minor component of motion and it is the 3-D rotational motion that gives rise to major relative changes in aspect angle over a CPI. In cases where both the translation and rotation motion of an object give rise to cross-range information, an algorithm to compensate for the effective translation motion was proposed by Aprile *et al.* in [46].

The conventional system model of a ground-based radar illuminating a 2-D rotating sea vessel is illustrated in Figure 2.2. The rotational motion of a sea vessel

is essential for ISAR imaging because it provides cross-range information. Translational motion is not useful and it needs to be compensated from the radar's received signal.

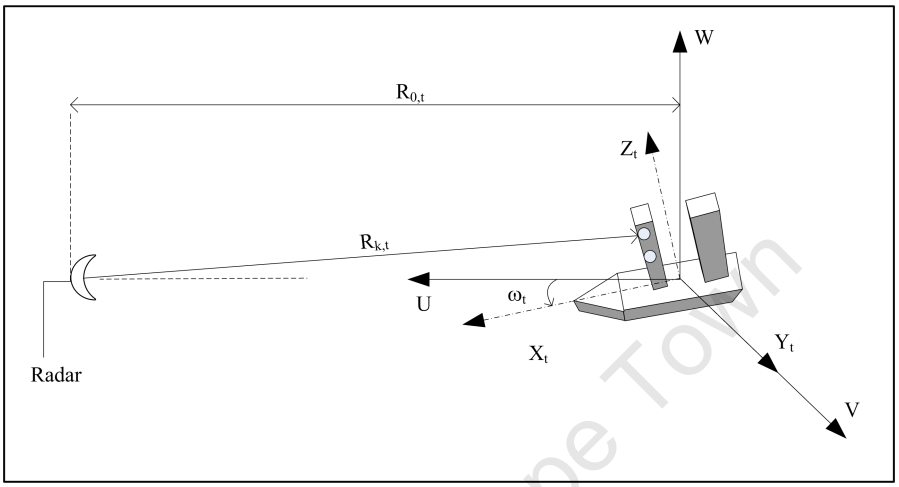

Figure 2.2: Conventional ground-based ISAR imaging system model showing a radar illuminating a sea vessel with pure pitch motion

In Figure 2.2, two axes are defined around the centre of rotation of the sea vessel: the global axes (U, V, W), which are fixed, and the local axes (X_t, Y_t, Z_t) at time t, which change as the vessel experiences rotational motion. It should be noted that $\mathbf{RT}$, $\mathbf{RT}_{\perp 1}$ and $\mathbf{RT}_{\perp 2}$ shown in Figure 2.1 are unit vectors along the global axes U, V and W respectively. In this diagram, $R_{0,t}$ represents the translation motion, $R_{k,t}$ expresses the distance from the radar to the k^{th} scatterer and ω_t is the angular rotation rate; all of these variables vary over time. The translational motion component, denoted by $R_0(t)$, is a function of the initial range R_0, the radial velocity v_r and the radial acceleration a_r of the sea vessel. The rotation angle at time t, denoted by ω_t, may be expressed in terms of the initial rotational angle (in radians) θ_0, the angular velocity $\dot{\theta}$ and the angular acceleration $\ddot{\theta}$. These expressions can be mathematically stated as follows:

$$R_{0,t} = R_0 + v_r t + \frac{1}{2} a_r t^2 \tag{2.1}$$

$$\omega_t = \theta_0 + \dot{\theta} t + \frac{1}{2} \ddot{\theta} t^2 \tag{2.2}$$

When the initial range R_0 is much greater than the physical dimensions of the sea vessel, the distance between the radar and the k^{th} scatterer, denoted by $R_{k,t}$, can be approximated as:

$$R_{k,t} = R_{0,t} + z_k \sin(\omega_t) - x_k \cos(\omega_t) \tag{2.3}$$

where (x_k, y_k, z_k) is the local coordinates of the k^{th} scatterer. The full derivation of (2.3) is described by Chen and Qian in [47]. The simplified expression of $R_{k,t}$ in (2.3) is used to formulate the conventional mathematical system model, which is also used in [47], of the radar's received signal Φ_t:

$$\Phi_t = \int_{-\infty}^{\infty}\int_{-\infty}^{\infty}\int_{-\infty}^{\infty} \rho_{x,y,z} e^{-j\left(2\pi f_c \frac{2R_{k,t}}{c}\right)} \mathrm{d}x\ \mathrm{d}y\ \mathrm{d}z \tag{2.4}$$

where $\frac{2R_{k,t}}{c}$ is the return time of the radar signal to the k^{th} scatterer, c is the speed of light, f_c is the carrier frequency and $\rho_{x,y,z}$ is related to the reflectivity of the k^{th} scatterering centre at local coordinates (x_k, y_k, z_k).

Substituting (2.3) into (2.4) gives:

$$\Phi_t = e^{-j\left(2\pi f_c \frac{2R_{0,t}}{c}\right)} \int_{-\infty}^{\infty}\int_{-\infty}^{\infty}\int_{-\infty}^{\infty} \rho_{x,y,z} e^{-j\left(\frac{4\pi f_c}{c}\left(z_k \sin(\omega_t) - x_k \cos(\omega_t)\right)\right)} \mathrm{d}x\ \mathrm{d}y\ \mathrm{d}z \tag{2.5}$$

For a radar that uses a stepped frequency waveform to synthesise a large effective transmit bandwidth, the discretised signal at the radar receiver can be written as:

$$\Phi_{n,m} = \underbrace{e^{-j\left(4\pi f_{c,m} \frac{\Delta R_{0,t(n)}}{c}\right)}}_{\text{translational motion}} \underbrace{\left\{\sum_{k=1}^{K} \alpha_k e^{-j\left(\frac{4\pi f_{c,m}}{c}\left(z_k \sin\left(\omega_{t(n)}\right) - x_k \cos\left(\omega_{t(n)}\right)\right)\right)}\right\}}_{\text{rotational motion}} + e_{n,m} \tag{2.6}$$

where the first term shows the change of phase due to translational motion, the second term shows the change of phase due to rotational motion and the rest of

the symbols are defined as follows:

K – number of point scatterers representing an object

α_k – amplitude, which represents the RCS of the k^{th} scatterer

m – pulse number in a burst of M pulses, $0 \leq m \leq M-1$

n – burst number in a total of N bursts in an ISAR image, $0 \leq n \leq N-1$

$f_{c,m}$ – carrier frequency of the m^{th} pulse

$t(n)$ – discrete time from burst to burst

$\Delta R_{0,t(n)}$ – change in the initial range from burst to burst, given by $v_r t(n) + \frac{1}{2} a_r t(n)^2$

$e_{n,m}$ – clutter and noise for the m^{th} pulse, and the n^{th} burst

A detailed study of stepped frequency waveforms is given in Mahafza [48] and Wehner [40], as are the challenges associated with using stepped frequency waveforms to generate HRR profiles.

The mathematical formulation of the radar's received signal using stepped frequency waveforms in (2.6) is a conventional system model, which is widely used in the ISAR literature. Some examples include papers by Li *et al.* [22], Munoz-Ferreras and Perez-Martinez [23] and Wehner [40]. This system model may be used to obtain simulated HRR profiles and simulated ISAR images of a point-scatterer model. The following assumptions are made in the derivation of (2.6):

- The object has 2-D rotational motion, which is characterised by a fixed axis of rotation over the CPI.
- The object can be represented as a fixed number of point scatterers and the RCS of each scatterer is fixed over the CPI.

Stepped frequency waveforms use M pulses to form a single HRR profile and N HRR profiles are used to obtain an ISAR image. An ISAR image is formed by stacking HRR profiles as columns of a matrix, and applying the fast Fourier Transform (FFT) along the row dimension. A detailed description of the signal

processing steps needed to form an ISAR image is given in [40]. ISAR imaging of 2-D rotating objects for large rotation angles, which give rise to cross-range migration, and non-uniform rotation is addressed by Berger *et al.* in [49]. However, when an object has translation motion or significant rotational motion, motion compensation is needed to focus the image (see Section 2.2.5).

A typical 2-D ISAR sampling grid with a finite resolution of Δr_d and Δr_c respectively, is illustrated in Figure 2.3. The total dimension of the down-range and cross-range extent of an ISAR image and the related sampling requirements are dependent on the parameters of the stepped-frequency waveform. This is discussed in more detail in the next two sections.

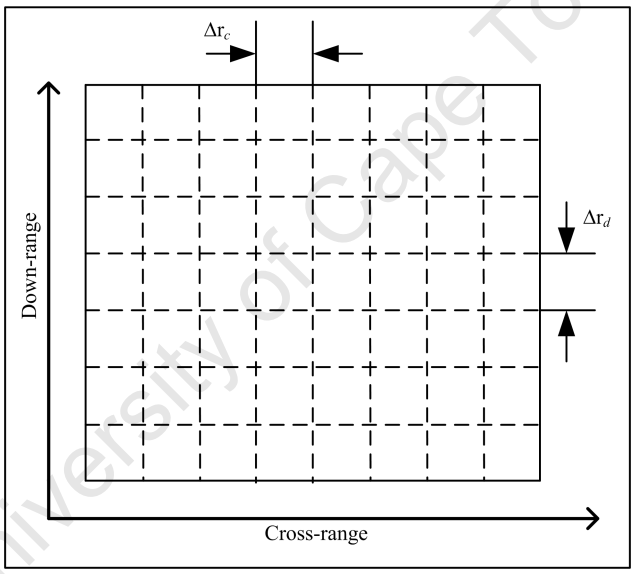

Figure 2.3: A typical 2-D ISAR sampling grid with finite down-range and cross-range resolution

2.2.2 Down-range resolution, sampling and ambiguity

The down-range resolution Δr_d of an ISAR image is a function of the bandwidth B of the effective transmitted signal. Mathematically, the down-range resolution is approximately given by:

$$\Delta r_d = \frac{c}{2B} \tag{2.7}$$

In stepped-frequency waveforms, the carrier frequency of the transmitted pulse is increased from pulse-to-pulse. Various methods have been proposed to combine the pulses to form a HRR profile. It can be performed in the time domain (Lord and Inggs [50]) or the frequency domain (Wilkinson *et al.* [51] and French [52]). As a result, a larger effective transmit bandwidth is synthesised, which is given by:

$$B = M\Delta f \tag{2.8}$$

where Δf is the frequency step from pulse to pulse, which is equal to the instantaneous bandwidth of each pulse B_{inst} to prevent overlap between successive subspectra.

The radar receiver's complex sampling frequency f_s needs to be greater than the Nyquist rate, given by B_{inst}, to prevent aliasing:

$$f_s \geq B_{inst} \tag{2.9}$$

However, down-range ambiguity is common for stepped-frequency waveforms since the unambiguous range window, defined by Mahafza in [48], r_d is dependent on Δf in the following way:

$$r_d = \frac{c}{2\Delta f} \tag{2.10}$$

For example, an X-band radar with a frequency step of 10 MHz has an unambiguous range window of approximately 15 m.

Stepped-frequency waveforms have the disadvantage of using many pulses to form a single HRR profile. For fast moving objects, scatterers migrate through down-range cells and give rise to blurred HRR profiles. Algorithms to compensate for the translation motion of an object within the stepped-frequency burst have been proposed by Gao *et al.* [53] and Jeong *et al.* [54].

More details about the characteristics of stepped-frequency waveforms for generating HRR profiles can be found in Wehner [40]. In this thesis, it is assumed that the parameters of the stepped-frequency waveform are carefully selected so that backscattered energy from a vessel falls within the radar's measurement

gates and that the down-range ambiguity is large enough to cover the maximum down-range extent of the vessel.

2.2.3 Cross-range resolution and sampling considerations

Cross-range resolution Δr_c refers to the spatial distance of each cross-range cell of an ISAR image, and in Wehner [40] it is approximately given by:

$$\Delta r_c = \frac{\lambda}{2\Delta\theta} \tag{2.11}$$

where λ is the wavelength of the transmitted signal, and $\Delta\theta$ is the change in aspect angle (in radians) of a uniformly rotating object over the CPI. A detailed derivation of the cross-range resolution, as well as the assumptions that are made, can be found in Section 5.4.

The cross-range dimension of an ISAR image fundamentally represents the Doppler frequency of the rotating scatterers of an object. To satisfy the Nyquist rate, the sampling frequency in the cross-range dimension must be greater than the maximum Doppler bandwidth B_d of a rotating object, which is given by:

$$B_d = \frac{2\dot{\theta} l_{cr}}{\lambda} \tag{2.12}$$

where l_{cr} is the maximum cross-range extent of a uniformly rotating object with an angular velocity of $\dot{\theta}$. For stepped-frequency waveforms, the cross-range sampling frequency is given by the burst repetition frequency (BRF) f_{BRF}:

$$f_{BRF} = \frac{f_{PRF}}{M} \tag{2.13}$$

where f_{PRF} represents the pulse repetition frequency (PRF) of the radar waveform. Thus, to prevent aliasing in a complex sampling system, the BRF must be greater than the maximum Doppler bandwidth:

$$f_{BRF} \geq B_d \tag{2.14}$$

Once the cross-range dimension has been scaled from Doppler to distance using (2.11), the maximum cross-range extent of an ISAR image, denoted by r_c, is given by:

$$r_c = N\Delta r_c \tag{2.15}$$

A 2-D ISAR image represents the projection of a 3-D object onto a 2-D image projection plane. When an object has 2-D rotational motion, as illustrated in Figure 2.1, the image projection plane is stationary over the CPI. However, when an object possesses 3-D rotational motion, it causes the image projection plane to vary over time. A mathematical description of the image projection plane is presented in the next section.

2.2.4 The image projection plane and the image-generating Doppler components

Figure 2.4 illustrates an example of a 3-D rotating object together with its image projection plane. The 3-D rotational motion is represented by an angular velocity of $\dot{\theta}$ about an axis $\mathbf{\Omega} = [u_\Omega \;\; v_\Omega \;\; w_\Omega]$, where u_Ω, v_Ω and w_Ω are non-zero values. In order to express the 2-D image projection plane mathematically, the component of the 3-D rotational motion that gives rise to cross-range information needs to be defined.

In this thesis, the components of the 3-D rotational motion that generates cross-range information are referred to as the image-generating Doppler components and they consist of a vessel's Doppler generating axis of rotation $\mathbf{\Omega}_{eff}$ and effective angular rotation rate $\dot{\theta}_{eff}$. The Doppler generating axis of rotation is the projection of $\mathbf{\Omega}$ onto the 2-D plane that is orthogonal to the LOS vector $\mathbf{RT}$ (Chen and Miceli [24], Bao *et al.* [38] and Martorella *et al.* [55]). Stated mathematically: $\mathbf{\Omega}_{eff}$ is the projection of $\mathbf{\Omega}$ onto the plane spanned by the V-W axes, where $v_{\Omega eff} = v_\Omega$, $w_{\Omega eff} = w_\Omega$ and $u_{\Omega eff} = 0$. The effective angular rotation is the component of rotation that provides cross-range information, and $\dot{\theta}_{eff}$ is used to obtain the cross-range resolution (see (2.11)).

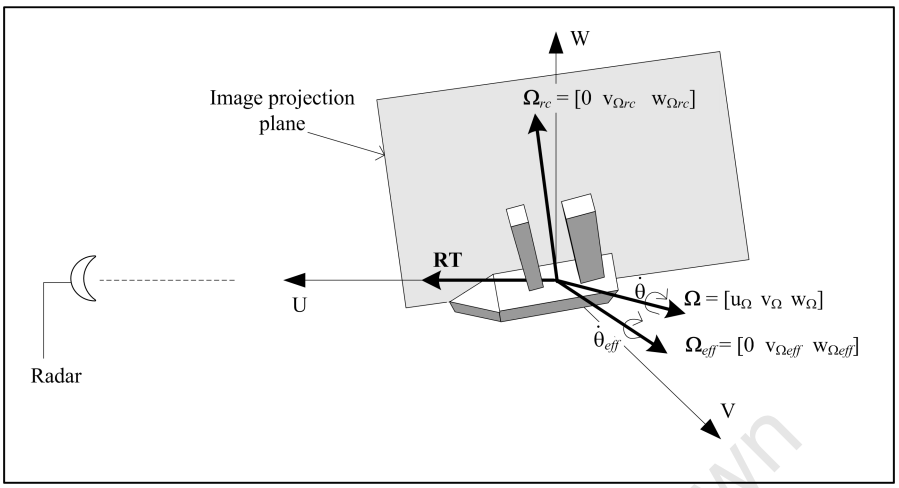

Figure 2.4: Illustration of the image-generating Doppler components: $\mathbf{\Omega}_{eff}$ and $\dot{\theta}_{eff}$

Finally, the 2-D image projection plane can be mathematically formulated as the span of two vectors: the Doppler generating axis of rotation $\mathbf{\Omega}_{eff}$ and the cross-range vector $\mathbf{\Omega}_{rc}$, which is given by:

$$\mathbf{\Omega}_{rc} = \mathbf{RT} \times \mathbf{\Omega}_{eff} \tag{2.16}$$

where $\times$ denotes the cross product.

2.2.5 Motion compensation

Motion compensation removes the effect of translation and large rotational motion on a radar's received signal, in order to obtain a focused ISAR image. The signal processing steps that are required are illustrated in Figure 2.5. A brief description of each step is given below:

1. **Range alignment** - aligns all the HRR profiles so that each scatterer remains in the same down-range cell over the CPI

2. **Autofocus** - compensates for the fine phase errors along the cross-range dimension that cannot be compensated for by range alignment algorithms

3. **Polar reformatting** - compensates for the migration of scatterers through range-Doppler cells for objects with large rotational rates or ISAR images with high down-range and cross-range resolution

4. **Doppler processing** - provides cross-range information by separating scatterers according to their Doppler frequency. Frequency estimation algorithms can be used to estimate the Doppler frequency of the scatterers in each down-range cell. Some examples of frequency estimation algorithms include the Fourier Transform, wavelets Multiple Signal Classification (MUSIC) and joint time-frequency (JTF) transforms. An introduction to frequency estimation algorithms is given by Moon and Stirling in [56]. Different frequency estimation algorithms have been applied to form ISAR images of objects: the Fourier Transform was used by Chen and Andrews in [5], wavelets were used by by Thomas *et al.* in [57], MUSIC was used by Yoon and Amin [16] and Odendaal *et al.* [58], and JTF transforms were used by Chen and Qian in [47] to obtain many ISAR images over a single CPI.

The field of translation and rotation motion compensation in ISAR has been an active area of research for a few decades. This field of research has produced numerous publications in international journals, conferences and books.

Translation motion compensation is performed using range alignment [5] [29], [59], [60], [61], [62] and autofocus [30], [62], [63], [64], [65], [66] techniques. Martorella *et al.* [67] show that a better estimate of the phase error for autofocus can be obtained from full polarimetric measurements of sea vessels. An object's translation motion can also be compensated for by using a joint range alignment and autofocus technique such as AUTOCLEAN, which was proposed by Li *et al.* in [22]. Algorithms that compensate for the higher order phase terms were proposed by Thayaparan *et al.* [68], Wang and Jiang [69] and Li *et al.* [70]. A compututationally efficient algorithm for translation motion compensation for real-time ISAR application was proposed by Aprile *et al.* in [71].

Rotation motion compensation techniques for uniformly rotating objects include algorithms proposed by Aprile *et al.* [72], Kong and Edwards [73] and Lu and Bao [74] for cooperative vessels, and Munoz-Ferreras and Perez-Martinez [23],

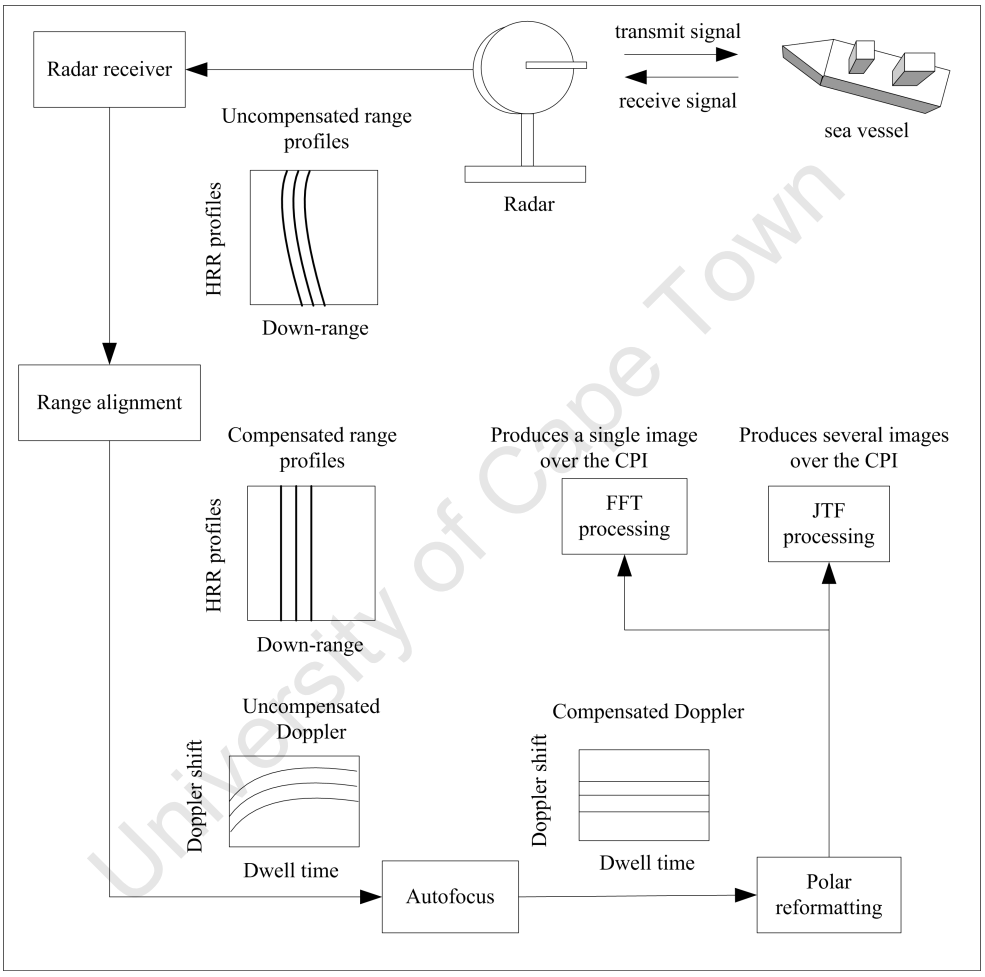

Figure 2.5: Block diagram showing the signal processing steps for motion compensation in ISAR

Pastina [75] and Wang and Jiang [76] for non-cooperative vessels. Rotation motion compensation is also referred to as polar reformatting, which is discussed in papers by Xing *et al.* [77] and Lipps and Kerr [78]. For objects with non-uniform rotation, JTF transforms can be used to produce more focused images, as shown by Xing *et al.* [79] and Zhu *et al.* [80].

A limited amount of research has been done on the comparison of various motion compensation algorithms: Trishman [81] analysed the strengths and weaknesses of different range alignment algorithms; a survey of a few autofocus techniques was done by Berizzi *et al.* [82]; Munoz-Ferreras and Perez-Martinez performed a comparison of two polar reformatting techniques [23]; existing JTF transforms in the literature were discussed by Qian and Chen [83]; and the application of different JTF transforms to ISAR was done by Chen and Ling [84].

The introduction to ISAR that is presented in this chapter is not intended to be a comprehensive overview of the field of motion compensation for ISAR. However, the introduction provides the necessary foundation for understanding the critical analysis of the literature discussed in Section 2.4. The basic principles of ISAR are discussed by Mensa [4], Wehner [40], Prickett and Chen [85], Rihaczek and Hershkowitz [86], Borden [87] and Ausherman *et al.* [88]. Advanced motion compensation algorithms are discussed by Jae Sok Son *et al.* [89], and Chen and Ling [90], which also provides an overview of the application of JTF transforms to ISAR. Lastly, the topic of polar reformatting is addressed by Carrara *et al.* [91] and Borden [92].

2.3 Challenges in ISAR

There are many challenges that need to be overcome, in order to obtain focused ISAR images of sea vessels or aircraft without blurring or artefacts. Some of these challenges include:

- **Motion compensation** - The motion of real objects can be broken down into translational and rotational motion. The rotational motion is essential

for ISAR, whereas the translation motion needs to be compensated for. For ISAR images with high cross-range resolution, the rotational motion causes scatterers to migrate through resolution cells and this also needs to be compensated for. A detailed dicussion of this topic can be found in Section 2.2.5.

- **3-D rotational motion** - when an object possesses 3-D rotational motion, it causes blurring in the ISAR image as illustrated by Figure 1.2. The effect of 3-D rotational motion on the ISAR imaging has been investigated by Bao *et al.* [38], Chen and Miceli [24], [35], [36] and Berizzi and Diani [37]. 3-D rotational motion of vessels can be overcome by selecting optimum imaging intervals, as shown by Rihaczek and Hershkowitz [32] and Pastina *et al.* [93].

- **Multipath** - when a radar illuminates an object at low elevation angles, the received signal at the radar is made up of two components: the direct path and the indirect path, which is the reflection due to the Earth or sea surface. The two components both add constructively and destructively, and this produces an amplitude and phase variation at the radar's received signal.

  Further details about the effect of multipath on ISAR can be found in papers by Berizzi [25], Gao *et al.* [94] and Berizzi and Diani [95]. Moreover, the effect of multipath on 3-D ISAR imaging of sea vessel was investigated by Lord *et al.* [96]. Lastly, Gao *et al.* [97] proposed an algorithm to remove the artefacts caused by multipath.

  It is hypothesised that multipath does not significantly contribute to the blurring of measured ISAR imagery of sea vessels considered in this thesis.

- **Non-point like scattering** - when an EM wave travels inside a cavity, the signal is delayed in time before it is sent back to the radar. This creates a typical ghost trail as shown by Trintinalia and Ling in [98]. A technique for reducing the radar image artefacts caused by inlets and cavities was proposed by Borden [99].

- **Doppler modulation** - Doppler modulation is a phenomenon caused by rotating objects on a platform, such as a rotating antenna onboard a ship. Doppler modulation has the effect of corrupting the geometrical features of a rotating object along the cross-range dimension of an ISAR image. A related topic is jet engine modulation (JEM) and a discussion on this topic is given by Li in [100]. Doppler modulation is also referred to as Micro-Doppler, as discussed in literature by Ghaleb *et al.* [101].

- **Walking scatterers** - when a radar illuminates a curved surface, the specular point of reflection changes with aspect angle, as illustrated by Figure 2.6. This phenomenon causes the specular reflection point to migrate through resolution cells, and it leads to blurring in ISAR images with high cross-range resolution. The problem of walking scatterers in the context of identifying scatterer centre locations was addressed by Jonsson *et al.* in [102].

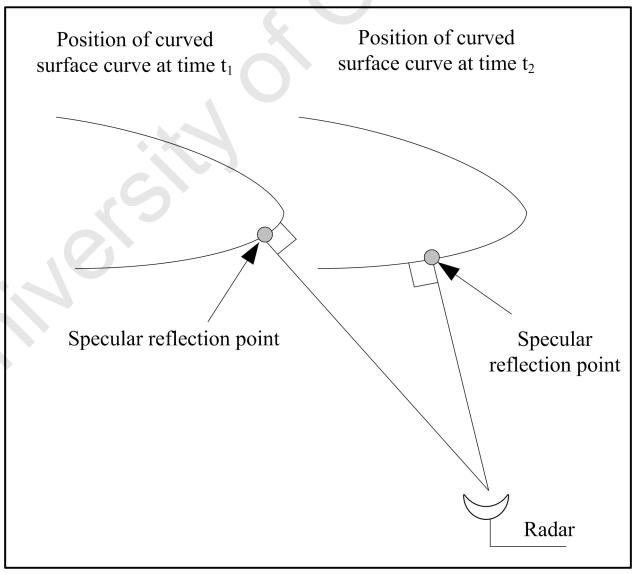

Figure 2.6: Diagram illustrating the migration of the specular point of reflection for curved surfaces

When all the challenges associated with forming ISAR images have been addressed, focused images can be obtained. These images may be useful for classification or RCS management purposes.

The field of ISAR is not yet mature, as there are research topics that are not well understood, such as the correction of image blurring caused by the time-varying nature of the axis of rotation, which was described by Chadwick and Williams in [103]. New algorithms being developed need to be tested on radar data and it is expensive to perform field measurements for different classes of sea vessels in varying environmental conditions. Simulations are often used to produce realistic synthetic radar data of sea vessels for different conditions: ISAR simulation environments for sea vessels have been developed by Karakasiliotis *et al.* [104], Kostis [105] and Haywood *et al.* [106]. The simulation environment proposed in [106] is referred to as ISAR Radar Laboratory (ISARLAB).

Many algorithms have been proposed to address the various challenges with ISAR, but they have limitations: assumptions are made in the system model, which are not always satisfied in measured data. Furthermore, algorithms in the literature typically tackle one problem at a time and ignore the other challenges. For example: the literature that investigates the effect of walking scatterers, does not model other challenges, such as multipath, 3-D rotational motion or translation motion; a simplified system model is presented to reduce the complexity of the problem. These papers assume that all the other challenges have been perfectly compensated for and they do not investigate the effect of imperfect compensation on the problem at hand. These are important research topics that need to be addressed for operational ISAR imaging systems. An overview of recent papers in the field of ISAR relating to motion compensation, image formation and target recognition was discussed by Martorella *et al.* in [107].

The sequential steps that are needed for an operational ISAR imaging system for sea vessels is shown in Figure 2.7. This diagram is the candidate's view of the signal processing challenges that need to be overcome in order to create focused ISAR images for classification and RCS management purposes. Firstly, the radar waveform parameters need to be carefully selected so that they are suited to the vessel of interest. Once the HRR profiles of the vessel are obtained, artefacts caused by multipath and other non-point like scattering mechanisms need to be removed. Thereafter, optimum imaging intervals need to be estimated in order to select subsets of radar data where the vessel has a low degree of 3-

D motion. Translation and rotation motion compensation are applied to these subsets of data to obtain focused ISAR images. This is followed by cross-range scaling of the ISAR image(s) to transform the cross-range dimension to distance (Martorella [27]). The ISAR image may now be used for maritime applications, such as classification or RCS management.

ISAR images provide a rich source of information for the classification of sea vessels, as shown by Bon *et al.* [6], Musman *et al.* [7], Cooke *et al.* [108], Maki *et al.* [109], and Melendez and Bennett [110]. Features that may be extracted from a side-view ISAR image for classification purposes include a vessel's down-range extent (McFadden and Musman [31] and Pastina and Spina [111]), locations of superstructure breaks (Musman *et al.* [7] and Pastina and Spina [111]), ship silhouette (Pastina and Spina [111], upright locations as a percentage of the range extent (Musman *et al.* [7]) and scattering centres (Martorella *et al.* [55] and Shin and Myung [112]).

Bon *et al.* [6] suggests that the discriminant features for ISAR based ship classification are the ship's length, its height, the height-normalised ISAR profile and the ten Fourier descriptors of its contour. Other ISAR-based approaches focus on profiling the height structure of the ship (Maki *et al.* [113]) and on forming a polar grid ISAR image, which is reported to be invariant to rotation and scale, as described by Kim *et al.* in [10]. Recent work by Martorella *et al.* [114] show that full polarimetric data of sea vessels can be used to improve classification performance compared to using a single polarisation.

The most popular pattern recognition algorithms that are used for classification of sea vessels are template matching (Maki *et al.* [113]), invariant feature extraction (Kim *et al.* [10]) and model based techniques (Rice *et al.* [115]).

There are many research topics in the field of ISAR, and a few of the important topics were discussed in this section. The next section presents a critical review of the literature to identify the gaps that exist.

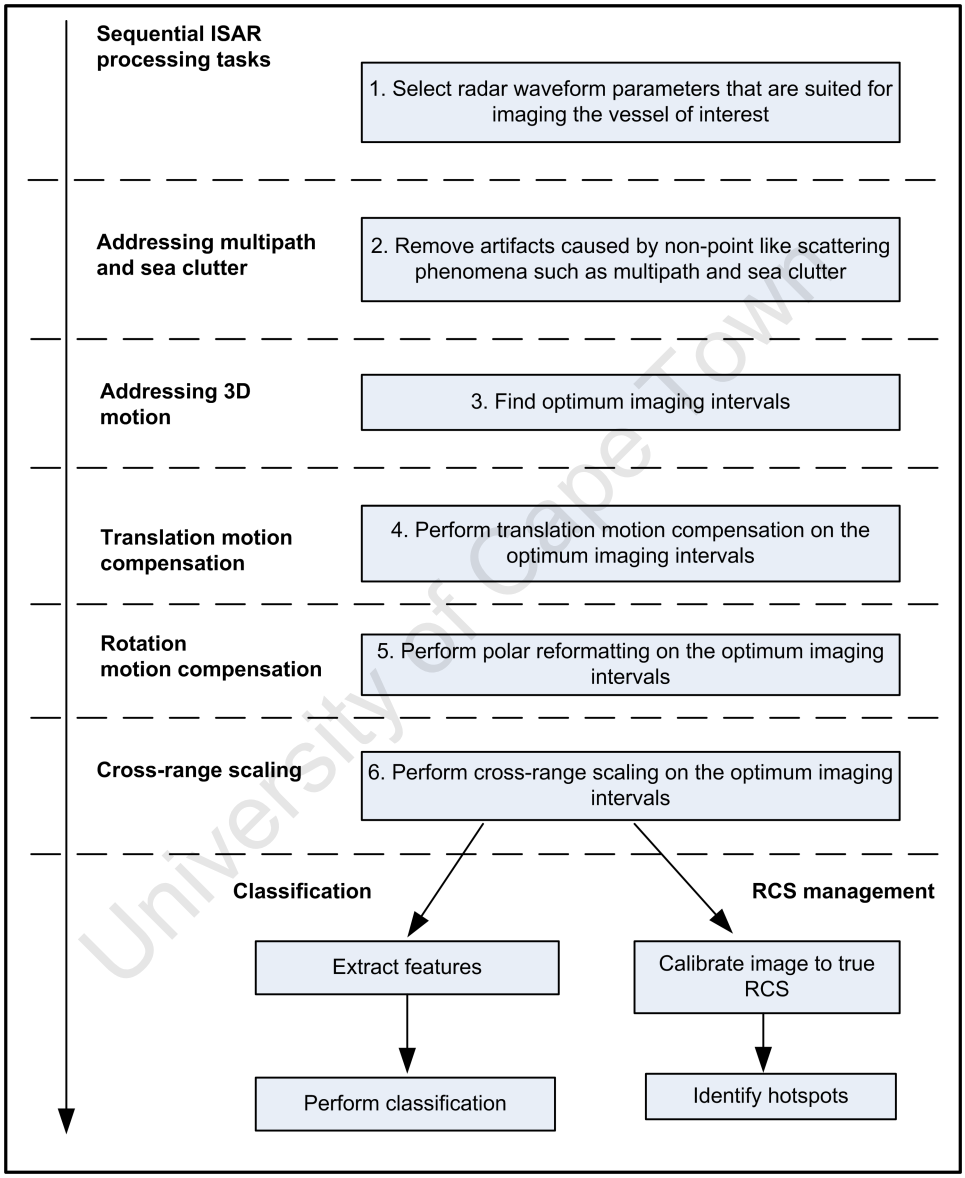

Figure 2.7: Block diagram for ISAR imaging of sea vessels

2.4 A Critical Literature Review

This section presents a critical review of the application of current algorithms to the topic of ISAR imaging of sea vessels with 3-D rotational motion. The strengths and weaknesses of the algorithms in the literature are identified by comparing the properties of the system models. The critical review aims to identify the gaps in the literature and to highlight the novel aspects of the research objectives stated in Section 1.4. The comparison of eight ISAR related algorithms is summarised in Table 2.1. The following observations can be made:

- **Observation 1 - Motion compensation algorithms assume that objects possess 2-D rotational motion:** The translation and rotation motion compensation algorithms shown in Table 2.1 use the conventional system model described in Section 2.2.1, which assume that the rotational motion of an object is two-dimensional (see 1. in Table 2.1). The 2-D rotational motion is modelled as a fixed Doppler generating axis of rotation with a constant angular rotation rate (see 2. in Table 2.1). This assumption is also made by other motion compensation algorithms in the literature, which include: range alignment algorithms proposed by Chen and Andrews [5], Wang and Kasilingam [29], Yuan and Casasent [30], Xi *et al.* [62] and Qiu and Zhao [116]; autofocus algorithms proposed by Wahl *et al.* [65], Steinberg [66], Jackowats and Wahl [117], Wang *et al.* [118] and Zhaodo *et al.* [119]; joint range alignment and autofocus algorithms developed by Li *et al.* [22] and Liu and Zhang [120]; polar reformatting techniques developed by Kong and Edwards [73], Carrara *et al.* [91] and Lu and Bao [121].

  When an object possess 3-D rotational motion, applying conventional motion compensation algorithms often gives rise to blurry ISAR images. Since conventional motion compensation algorithms assume that the object of interest possesses 2-D rotation, it is important to select optimum imaging intervals where the object's motion is approximately 2-D. After estimating optimum imaging intervals, focused ISAR images can be obtained by applying conventional translation motion compensation algorithms to the

HRR profiles corresponding to the optimum imaging intervals. These focused ISAR images would be a rich source of information for classification purposes.

- **Observation 2 - Most current system models do not directly model the Doppler generating axis of rotation, and this parameter cannot be independently changed over the CPI:** In most of the current literature, rotational matrices are used to model the 3-D rotational motion (roll, pitch and yaw) of a sea vessel [24], [32], [33], [93]. This approach is limited, because it does not independently model both the image-generating Doppler components (see 3. in Table 2.1). When the image-generating Doppler components vary over time, it causes blurring in an ISAR image. Most current mathematical system models are unable to model directly the Doppler generating axis of rotation and they are also unable to characterise the amount of blurring that is caused by the time-varying nature of the Doppler generating axis of rotation. This limitation is the focus of research objective 1 (see Section 1.4), which is addressed in Chapter 3.

  It should be noted that the differential equation based system model proposed by Scaglione and Barbarossa in [122], and later used by Berizzi *et al.* in [1], can be used to change the 3-D rotational motion over the CPI. In this thesis, an alternative quaternion-based model that directly models the axis of rotation is used to change the 3-D rotational motion over the CPI. It can be demonstrated, under certain conditions, the expression of the Doppler frequency of a scatterer by the model proposed in [122] is equivalent to the quaternion-based system model proposed in this thesis (see Appendix B for more details).

- **Observation 3 - The current literature is unable to explain how 3-D rotational motion of ships causes blurring in most measured ISAR images of sea vessels:** Results in the literature show that measured 3-D rotational motion (see 4. in Table 2.1) causes blurring in ISAR images [24], [33]. Furthermore, there are system models in the literature that analytically express the Doppler generating axis of rotation (see 5.

in Table 2.1). However, there is no literature that shows how the image-generating Doppler components should be extracted from measured motion data. The time-varying nature of these components may be used to explain why most motion compensated ISAR images of real ships contain blurring. This limitation is the focus of research objective 2 (see Section 1.4), which is addressed in Chapter 4.

The critical review of the literature shows that the effect of 3-D rotational motion on ISAR imaging has not been fully investigated. While the effect of non-uniform rotation rate has been addressed by [39], there is no work that investigates the effect of a time-varying Doppler generating axis of rotation on an ISAR image (see observation 2). In addition, there is no work in the literature that shows how the image-generating Doppler components can be extracted from the measured motion data, which can be used to explain why 3-D rotational motion gives rise to blurring in most measured ISAR images of sea vessels (see observation 3). Lastly, motion compensation algorithms in the literature only model 2-D rotational motion, and for this reason it is important to select intervals that have a low degree of 3-D rotational motion in order to obtain focused ISAR images of cooperative and non-cooperative sea vessels (see observation 1).

Little work has been published on how to choose a suitable CPTWL for ISAR imaging of cooperative vessels, which would minimise the blurring caused by a vessel's 3-D rotational motion. If the CPTWL is too short, the desired cross-range resolution may not be achieved. Conversely, if the CPTWL is too long, the 3-D rotational motion of the vessel causes blurring in most ISAR images. It is reported in Wehner [40] that the optimum CPTWL for unfocused ISAR images lies between 0.025 s and 0.5 s for X-band measurements of ships. The disadvantage with this suggested range is that it is too broad and in the case of cooperative vessels, it does not take advantage of measured motion data that may be available. Thus, there is a need to develop a new technique to overcome these limitations in the literature for selecting suitable CPTWLs for ISAR imaging of cooperative vessels. This topic is the focus of research objective 3, and thus a new algorithm for selecting suitable CPTWLs is proposed in Chapter 5.

Table 2.1: Comparison of the properties of various ISAR related system models in the literature

	Algorithms in the literature							
Property of the system model	[60]† RA	[123]† AF	[23]† PR	[33] ISV3D	[39] Inv3D	[24] Inv3D	[32] OpInt	[93] OpInt
1. Does the object have 3-D rotational motion?	No	No	No	Yes	No	Yes	Yes	Yes
2. Is the rotational motion modelled as a fixed Doppler generating axis of rotation with a constant angular rotation rate?	Yes	Yes	Yes	No	No	No	No	No
3. Does the system model use rotational matrices to model 3-D rotational motion?	N/A	N/A	N/A	Yes	N/A	Yes	Yes	Yes
4. If 3-D rotational motion is modelled, can the system model incorporate measured 3-D rotational motion of a vessel?	N/A	N/A	N/A	Yes	N/A	Yes	Yes	Yes
5. If 3-D rotational motion is modelled, does the model directly model the Doppler generating axis of rotation?	N/A	N/A	N/A	Yes	N/A	Yes	No	No

RA - Range alignment, AF - Autofocus, PR - Polar reformatting, ISV3D - ISAR imaging of vessels with 3-D rotational motion, Inv3D - Investigating the effect of 3-D rotational motion on the ISAR imaging process, OpInt - Selecting optimum imaging intervals

† The mathematical system model is based on (2.6)

Many algorithms have been proposed in the literature to identify optimum imaging intervals for ISAR imaging of non-cooperative sea vessels. However, the algorithms proposed by Rihaczek and Hershkowitz [32], Li *et al.* [34] and Pastina and Spina [41] are problematic to implement with real data because they require accurate phase unwrapping, and because algorithms in [32] and [41] assume accurate tracking of a scatterer at the bow and one at the stern of the ship, with both being of the same width and height position, which is difficult to achieve in practice. The algorithm proposed by Martorella and Berizzi in [28] also has several limitations: the algorithm only estimates the parameters of a single imaging interval and ignores other optimum imaging intervals that may exist in a long radar recording; when the algorithm is applied to radar recordings of small sea vessels, the algorithm's performance is dependent on the value of the initial CPTWL, as shown by Abdul Gaffar *et al.* in [44]; furthermore, the highly focused ISAR image that corresponds to the optimum imaging interval does not always correspond to a side-view ISAR image, which is desired for ship classification. For these reasons, there is a need to develop a new algorithm that overcomes these limitations in the literature regarding the selection of optimum imaging intervals for ISAR imaging of non-cooperative vessels. This topic is the focus of research objective 4, and a new algorithm for selecting optimum imaging intervals for non-cooperative vessels is therefore proposed in Chapter 5.

Observations 1, 2 and 3 clearly outline the gaps in the literature. These limitations are overcome by satisfying the research objectives stated in Section 1.4. Moreover, addressing these research objectives provides answers to the research questions stated in Section 1.4, and when these research questions are answered positively, the thesis hypothesis is satisfied.

2.5 Review and Summary

In this chapter, the basic theory of ISAR has been presented with a special focus on ISAR imaging of sea vessels with 3-D rotational motion. The conventional ISAR system model in the literature was derived and the assumptions

that are made in this model were highlighted. A mathematical description of the down-range properties of an ISAR image was formulated for stepped frequency waveforms. This was followed by a mathematical description of the cross-range properties of an ISAR image for a uniformly rotating object. The image projection plane and the image-generating Doppler components in ISAR were discussed, as well as the need for motion compensation. Some of the challenges in ISAR were described with reference to literature that aims to address some of these challenges. Lastly, a selective critical literature review was presented to identify the gaps in the literature and to highlight the novel aspects of the research objectives stated in Section 1.4.

In the following chapter, a new mathematical system model is presented that makes it possible to characterise the effect of a time-varying Doppler generating axis of rotation on the migration of a scatterer through the cross-range cells of an ISAR image.

Chapter 3

The Effect of 3-D Rotational Motion on ISAR Imagery

3.1 Introduction

The previous chapter discussed the various challenges associated with forming a focused ISAR image and highlighted the importance of understanding the effect of 3-D rotational motion on an ISAR image. Results in the literature show that 3-D rotational motion gives rise to blurring in ISAR images [33], [34]. This result can also be observed in the measured ISAR images of a yacht, shown in Figure 1.2. Blurry ISAR images are not desired for classification purposes [31] because they lead to inaccurate estimation of parameters, which reduces the probability of correct classification.

Much research has been done on investigating the effect of 3-D rotational motion on ISAR [24], [35], [36], [37], [38]. Chen and Miceli [36] mathematically expressed the Doppler frequency of an individual scatterer when an object has pure roll, pitch or yaw motion. Results in [36] show that, even if the rotational rate (roll, pitch or yaw rate) is constant, the motion induced Doppler frequency is still time-varying, due to the large change in aspect angle over the CPI. In further work by Chen and Miceli [24], the Doppler generating axis of rotation is mathematically

formulated in terms of the object's axis of rotation and the radar LOS vector. This formulation is used to explain that 3-D rotational motion causes the image projection plane to vary over time, which gives rise to blurring. In work by Berizzi and Diani [37], the impulse response of an imaging system is presented and the conditions under which pitch, roll and yaw motion have negligible effect on image focus are evaluated.

However, the results in the current literature are limited because they only investigate the blurring caused by objects with rotational motion confined to a 2-D plane that is orthogonal to the radar LOS vector, i.e. only pitch, roll or yaw motion. Furthermore, current system models use matrices to model the 3-D rotational motion, and this approach is limited because it does not directly and independently model both of the image-generating Doppler components, which consist of the Doppler generating axis of rotation and the effective angular rotation rate. Hence, current system models are unable to characterise the amount of blurring in an ISAR image that is caused by the time-varying nature of each of the image-generating Doppler components.

Since the effect of the time-varying nature of the effective angular rotation rate has been investigated by Wong *et al.* in [39], this chapter focuses on the effect of a time-varying Doppler generating axis of rotation on ISAR imaging. A new quaternion-based system model is proposed where quaternions are used to represent an object's 3-D rotational motion; because quaternions are equally as accurate as matrices, they offer the advantage of directly and independently modelling a vessel's image-generating Doppler components over the CPI. These two components are particularly important to ISAR because the Doppler generating axis of rotation is used to obtain the image projection plane and the effective angular rotation rate influences the cross-range resolution of an ISAR image. This chapter is a more complete and accurate study of the investigation, which was initially performed in [42]. The new contributions made are summarised as follows:

- A mathematical formulation of the instantaneous Doppler frequency of an object's scatterer using quaternion algebra to model the image-generating Doppler components

- Characterisation of an object's time-varying Doppler generating axis of rotation on migration of the k^{th} scatterer through cross-range cells.

A new quaternion-based system model is formulated in Section 3.2. The mathematical analysis of an object's time-varying Doppler generating axis of rotation is presented in Section 3.3. The simulation setup for three different types of motion is described in Section 3.4, and the simulation results for a point-scatterer model are shown in Section 3.5. Lastly, conclusions are summarised in Section 3.6.

3.2 System Model

In this section, a quaternion-based system model is derived for a point scatterer model. The mathematical formulation of the radar's received signal can be used to obtain simulated ISAR images of an object with arbitrary 3-D rotational motion. Since the proposed system model directly models an object's incremental 3-D rotational motion from burst-to-burst, the Doppler generating axis of rotation can be directly and independently changed over the CPI. Consequently, the system model provides the ability of investigating the effect of a time-varying Doppler generating axis of rotation on ISAR imaging. Moreover, if motion data of a vessel are available, the mathematical formulae derived in Section 3.2.7 can be used to calculate a vessel's Doppler generating axis of rotation and rotation rate over the CPI. It should be noted that this derivation has not yet been formulated in the ISAR literature.

3.2.1 The quaternion as a rotational operator

The concept of quaternions was introduced by Hamilton in 1843 as a non-commutative extension of complex numbers [124]. Quaternions have been used in the field of theoretical and applied mathematics, and are popularly used to represent 3-D rotational motion in 3-D computer graphics (Daniel [125]) and robotics (Funda and Paul [126]) applications. A comparison of matrices and quaternions as rotational operators as well as a detailed study of quaternion algebra is given by Kuipers in [127]. This section gives a brief introduction to quaternion algebra and describes how quaternions can be used to represent 3-D rotational motion.

A quaternion, arbitrarily labelled x, denoted by $\mathbf{q}_x$, is defined as a mathematical expression with four parameters:

$$\mathbf{q} = q_x^1 + iq_x^2 + jq_x^3 + kq_x^4 \tag{3.1}$$

where q_x^1, q_x^2, q_x^3, q_x^3 are scalar elements and i, j, k are mutually orthogonal complex quantities that satisfy the following quaternion multiplicative identities:

$$i^2 = j^2 = k^2 = ijk = -1 \tag{3.2}$$

In this chapter, and in the rest of the thesis, the notation in (3.1) is abbreviated to

$$\mathbf{q}_x = \begin{bmatrix} q_x^{\{1\}} & q_x^{\{2\}} & q_x^{\{3\}} & q_x^{\{4\}} \end{bmatrix} \tag{3.3}$$

where the superscripts $\{1\}$, $\{2\}$, $\{3\}$ and $\{4\}$ are used to denote the respective scalar elements of $\mathbf{q}_x$. The conjugate $\mathbf{q}_x^*$, norm $\|\mathbf{q}_x\|$ and inverse $\mathbf{q}_x^{-1}$ are defined as follows:

$$\mathbf{q}_x^* = \begin{bmatrix} q_x^{\{1\}} & -q_x^{\{2\}} & -q_x^{\{3\}} & -q_x^{\{4\}} \end{bmatrix} \tag{3.4}$$

$$\|\mathbf{q}_x\| = \sqrt{\left(q_x^{\{1\}}\right)^2 + \left(q_x^{\{2\}}\right)^2 + \left(q_x^{\{3\}}\right)^2 + \left(q_x^{\{4\}}\right)^2} \tag{3.5}$$

$$\mathbf{q}_x^{-1} = \frac{\mathbf{q}_x^*}{\|\mathbf{q}_x\|^2} \tag{3.6}$$

A 3-D point in space, denoted by $\mathbf{p} = [x_p \;\; y_p \;\; z_p]$, can be transformed into a four-dimensional (4-D) quaternion $\mathbf{q_p}$ as follows:

$$\mathbf{q_p} = [0 \;\; \mathbf{p}] \tag{3.7}$$

A rotation through an angle θ about an axis $\mathbf{h} = [h_1 \;\; h_2 \;\; h_3]$ can be mathematically represented by a unit quaternion $\mathbf{q}_x(\mathbf{h}, \theta)$ as follows:

$$\mathbf{q}_x(\mathbf{h}, \theta) = \left[\cos\left(\frac{\theta}{2}\right) \quad \mathbf{h}\sin\left(\frac{\theta}{2}\right)\right] \tag{3.8}$$

$$\mathbf{q}_x(\mathbf{h}, \theta) = \left[\cos\left(\frac{\theta}{2}\right) \quad h_1\sin\left(\frac{\theta}{2}\right) \quad h_2\sin\left(\frac{\theta}{2}\right) \quad h_3\sin\left(\frac{\theta}{2}\right)\right] \tag{3.9}$$

Let $\mathbf{q}_a = [0 \;\; \mathbf{a}]$ and $\mathbf{q}_b = [0 \;\; \mathbf{b}]$ denote the 4-D quaternion representation of two 3-D points, expressed as $\mathbf{a} = [x_a \;\; y_a \;\; z_a]$ and $\mathbf{b} = [x_b \;\; y_b \;\; z_b]$. The quaternion rotational operator that rotates point $\mathbf{a}$ about an axis $\mathbf{h}$ clockwise through an angle θ onto point $\mathbf{b}$ is given by:

$$\mathbf{q}_b = \mathbf{q}_x(\mathbf{h}, \theta)^* \otimes \mathbf{q}_a \otimes \mathbf{q}_x(\mathbf{h}, \theta) \tag{3.10}$$

where $\otimes$ denotes quaternion multiplication and $\mathbf{b}$ is given by:

$$\mathbf{b} = \left[q_b^{\{2\}} \quad q_b^{\{3\}} \quad q_b^{\{4\}}\right] \tag{3.11}$$

The next section shows how quaternions may be used to transform a point scatterer in the system model from the local coordinates to the global coordinates.

3.2.2 Transformation from the local to the global coordinate frame

The system model illustrated in Figure 3.1 considers a sea vessel with only 3-D rotational motion and assumes that any translation motion has been compensated for. Two coordinate axes are defined: the radar coordinate axes (U, V, W),

which are fixed, and the local coordinate axes (X_n, Y_n, Z_n) at time $t(n)$, which change as the vessel experiences rotational motion. In this diagram, $R_{k,t(n)}$ denotes the distance from the radar to the k^{th} scatterer of the vessel for time $t(n)$ and R_0 represents the distance from the radar to the vessel's centre of rotation. The time interval during each discrete rotation is given by Δt, where $\Delta t(n) = t(n) - t(n-1)$. It should be noted that there are $N-1$ discrete rotations over the CPI. Consequently,

$$\Delta t(n) \in \{\Delta t(1),\ \Delta t(2),\ \cdots,\Delta t(N-1)\} \tag{3.12}$$

and

$$t(n) \in \{t(0),\ t(1),\ \cdots,t(N-1)\} \tag{3.13}$$

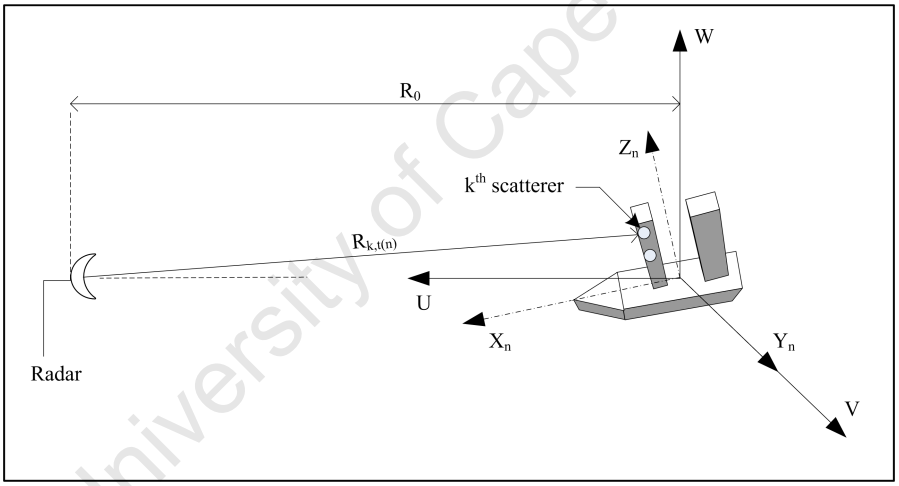

Figure 3.1: System model showing the global coordinates (U, V, W) that are fixed and the local coordinates (X_n, Y_n, Z_n) at time $t(n)$

The 4-D quaternion representation of the local coordinates of the k^{th} scatterer is expressed as $\mathbf{q}_{rk} = [0 \ \ \mathbf{r}_k]$, where $\mathbf{r}_k = [x_k \ \ y_k \ \ z_k]$. However, it is the global coordinates of the k^{th} scatterer, denoted by $\mathbf{g}_{k,t(n)} = \left[u_{k,t(n)} \ \ v_{k,t(n)} \ \ w_{k,t(n)}\right]$, that determine the phase at the radar receiver.

Assume that the radar continuously tracks the vessel so that its centre of rotation always lies on the global U axis and the physical dimensions of the vessel are much less than R_0. Furthermore, let $\mathbf{q}_{gk,t(n)}$ denote the quaternion representation

of the global coordinates $\mathbf{g}_{k,t(n)}$ of the k^{th} scatterer at $t(n)$. Then, after the first discrete rotation, $\mathbf{q}_{gk,t(1)}$ and $\mathbf{g}_{k,t(1)}$ is given by:

$$\mathbf{q}_{gk,t(1)} = \left(\mathbf{q}_{tot,\Delta t(1)}\right)^* \otimes \left(\left(\mathbf{q}_{ins,t(0)}\right)^* \otimes \mathbf{q}_{rk} \otimes \left(\mathbf{q}_{ins,t(0)}\right)\right) \otimes \left(\mathbf{q}_{tot,\Delta t(1)}\right) \quad (3.14)$$

and

$$\mathbf{g}_{k,t(1)} = \begin{bmatrix} q^{\{2\}}_{gk,t(1)} & q^{\{3\}}_{gk,t(1)} & q^{\{4\}}_{gk,t(1)} \end{bmatrix} \quad (3.15)$$

After n discrete rotations, the global coordinates of the k^{th} scatterer at time $t(n)$ can be expressed as:

$$\begin{aligned} \mathbf{q}_{gk,t(n)} \quad = \quad & \left(\mathbf{q}_{tot,\Delta t(n)}\right)^* \otimes \cdots \left(\mathbf{q}_{tot,\Delta t(1)}\right)^* \otimes \left(\left(\mathbf{q}_{ins,t(0)}\right)^* \otimes \mathbf{q}_{rk} \otimes \mathbf{q}_{ins,t(0)}\right) \cdots \\ & \cdots \otimes \mathbf{q}_{tot,\Delta t(1)} \cdots \otimes \mathbf{q}_{tot,\Delta t(n)} \end{aligned} \quad (3.16)$$

and

$$\mathbf{g}_{k,t(n)} = \begin{bmatrix} q^{\{2\}}_{gk,t(n)} & q^{\{3\}}_{gk,t(n)} & q^{\{4\}}_{gk,t(n)} \end{bmatrix} \quad (3.17)$$

where $\mathbf{q}_{ins,t(0)}$ is the quaternion that represents the initial orientation of the vessel with respect to the global axes, and $\mathbf{q}_{tot,\Delta t(n)}$ represents the incremental rotational motion over $\Delta t(n)$ caused by the roll, pitch and yaw motion of the sea vessel. Stated mathematically:

$$\mathbf{q}_{ins,t(0)} = \mathbf{q}_{hs,t(0)}\left(\mathbf{RT}_{\perp 2}, \theta_{hs,t(0)}\right) \otimes \mathbf{q}_{e,t(0)}\left(\mathbf{RT}_{\perp 1}, \theta_{e,t(0)}\right) \otimes \mathbf{q}_{b,t(0)}\left(\mathbf{RT}, \theta_{b,t(0)}\right) \quad (3.18)$$

$$\mathbf{q}_{tot,\Delta t(n)} = \mathbf{q}_{y,\Delta t(n)}\left(\mathbf{z}_{n-1}, \theta_{y,\Delta t(n)}\right) \otimes \mathbf{q}_{p,\Delta t(n)}\left(\mathbf{y}_{n-1}, \theta_{p,\Delta t(n)}\right) \otimes \mathbf{q}_{r,\Delta t(n)}\left(\mathbf{x}_{n-1}, \theta_{r,\Delta t(n)}\right) \quad (3.19)$$

where $\mathbf{x}_{n-1}$, $\mathbf{y}_{n-1}$ and $\mathbf{z}_{n-1}$ are unit vectors that are aligned to the local coordinate axes X_{n-1}, Y_{n-1} and Z_{n-1} respectively, at time $t(n-1)$ (see Section 3.2.3 for more details). The unit vectors $\mathbf{RT}$, $\mathbf{RT}_{\perp 1}$ and $\mathbf{RT}_{\perp 2}$ are aligned to the global coordinate axes U, V and W respectively. The heading $\theta_{hs,t(0)}$, elevation $\theta_{e,t(0)}$ and bank $\theta_{b,t(0)}$ angles define the initial orientation of the vessel, and the yaw $\theta_{y,\Delta t(n)}$, pitch $\theta_{p,\Delta t(n)}$ and roll $\theta_{r,\Delta t(n)}$ angles represent the n^{th} incremental rotational motion about a vessel's local axes. This definition of the rotational motion corresponds to the convention adopted by Kuipers in [127].

The heading $\theta_{hs,t(n)}$, elevation $\theta_{e,t(n)}$ and bank $\theta_{b,t(n)}$ can be used to calculate the vessel's incremental 3-D rotational motion, which consists of the roll rate $\dot{\theta}_{r,\Delta t(n)}$, pitch rate $\dot{\theta}_{p,\Delta t(n)}$ and yaw rate $\dot{\theta}_{y,\Delta t(n)}$, as follows:

$$\dot{\theta}_{r,\Delta t(n)} = \frac{\theta_{b,t(n)} - \theta_{b,t(n-1)}}{\Delta t} \tag{3.20}$$

$$\dot{\theta}_{p,\Delta t(n)} = \frac{\theta_{e,t(n)} - \theta_{e,t(n-1)}}{\Delta t} \tag{3.21}$$

$$\dot{\theta}_{y,\Delta t(n)} = \frac{\theta_{hs,t(n)} - \theta_{hs,t(n-1)}}{\Delta t} \tag{3.22}$$

3.2.3 Calculation of the unit vectors along the local coordinate axis

The unit vectors $\mathbf{z}_n$, $\mathbf{y}_n$ and $\mathbf{x}_n$ are aligned to the local coordinate axes X_n, Y_n and Z_n respectively, at time $t(n)$. In this system model, the rotational sequence of the vessel is assumed to be heading, elevation and then bank. Consequently, $\mathbf{z}_n$, $\mathbf{y}_n$ and $\mathbf{x}_n$ can be calculated by using the following five steps:

1. Initialise the unit vectors of the local coordinate system to the unit vectors about the global coordinate system:

$$\mathbf{x}_{n,\text{initial}} = \mathbf{RT} \tag{3.23}$$

$$\mathbf{y}_{n,\text{initial}} = \mathbf{RT}_{\perp 1} \tag{3.24}$$

$$\mathbf{z}_{n,\text{initial}} = \mathbf{RT}_{\perp 2} \tag{3.25}$$

2. Rotate the roll and the pitch axes, expressed as $\mathbf{x}_{n,\text{initial}}$ and $\mathbf{y}_{n,\text{initial}}$ respectively, about the yaw axis $\mathbf{z}_{n,\text{initial}}$ through the heading angle of $\theta_{hs,t(n)}$:

$$\mathbf{q}_{xn,\text{initial}} = [0 \quad \mathbf{x}_{n,\text{initial}}] \tag{3.26}$$

$$\mathbf{q}_{yn,\text{initial}} = [0 \quad \mathbf{y}_{n,\text{initial}}] \tag{3.27}$$

$$\mathbf{q}_{xn,temp} = \left(\mathbf{q}_{hs,t(n)}\left(\mathbf{z}_{n,\text{initial}}, \theta_{hs,t(n)}\right)\right)^{*} \otimes \mathbf{q}_{xn,\text{initial}} \otimes \mathbf{q}_{hs,t(n)}\left(\mathbf{z}_{n,\text{initial}}, \theta_{hs,t(n)}\right) \tag{3.28}$$

$$\mathbf{q}_{yn,temp} = \left(\mathbf{q}_{hs,t(n)}\left(\mathbf{z}_{n,\text{initial}}, \theta_{hs,t(n)}\right)\right)^{*} \otimes \mathbf{q}_{yn,\text{initial}} \otimes \mathbf{q}_{hs,t(n)}\left(\mathbf{z}_{n,\text{initial}}, \theta_{hs,t(n)}\right) \tag{3.29}$$

3. Rotate the roll and yaw axes, expressed as $\mathbf{x}_{n,\text{temp}}$ and $\mathbf{z}_{n,\text{initial}}$ respectively, about the pitch axis $\mathbf{y}_{n,\text{temp}}$ through the elevation angle of $\theta_{e,t(n)}$:

$$\mathbf{q}_{xn,\text{temp}} = [0 \quad \mathbf{x}_{n,\text{temp}}] \tag{3.30}$$

$$\mathbf{q}_{zn,\text{initial}} = [0 \quad \mathbf{z}_{n,\text{initial}}] \tag{3.31}$$

$$\mathbf{q}_{xn} = \left(\mathbf{q}_{e,t(n)}\left(\mathbf{y}_{n,\text{temp}}, \theta_{e,t(n)}\right)\right)^{*} \otimes \mathbf{q}_{xn,\text{temp}} \otimes \mathbf{q}_{e,t(n)}\left(\mathbf{y}_{n,\text{temp}}, \theta_{e,t(n)}\right) \tag{3.32}$$

$$\mathbf{q}_{zn,temp} = \left(\mathbf{q}_{e,t(n)}\left(\mathbf{y}_{n,\text{temp}}, \theta_{e,t(n)}\right)\right)^{*} \otimes \mathbf{q}_{zn,\text{initial}} \otimes \mathbf{q}_{e,t(n)}\left(\mathbf{y}_{n,\text{temp}}, \theta_{e,t(n)}\right) \tag{3.33}$$

4. Rotate the pitch and yaw axes, expressed as $\mathbf{y}_{n,\text{temp}}$ and $\mathbf{z}_{n,\text{temp}}$ respectively, about the roll axis $\mathbf{x}_n$ through the bank angle of $\theta_{b,t(n)}$:

$$\mathbf{q}_{yn,\text{temp}} = [0 \quad \mathbf{y}_{n,\text{temp}}] \tag{3.34}$$

$$\mathbf{q}_{zn,\text{temp}} = [0 \quad \mathbf{z}_{n,\text{temp}}] \tag{3.35}$$

$$\mathbf{q}_{yn} = \left(\mathbf{q}_{b,t(n)}\left(\mathbf{x}_{n}, \theta_{b,t(n)}\right)\right)^{*} \otimes \mathbf{q}_{yn,\text{temp}} \otimes \mathbf{q}_{b,t(n)}\left(\mathbf{x}_{n}, \theta_{b,t(n)}\right) \tag{3.36}$$

$$\mathbf{q}_{zn} = \left(\mathbf{q}_{b,t(n)}\left(\mathbf{x}_{n}, \theta_{b,t(n)}\right)\right)^{*} \otimes \mathbf{q}_{zn,\text{temp}} \otimes \mathbf{q}_{b,t(n)}\left(\mathbf{x}_{n}, \theta_{b,t(n)}\right) \tag{3.37}$$

5. Obtain the local coordinates $\mathbf{x}_n$, $\mathbf{y}_n$ and $\mathbf{z}_n$:

$$\mathbf{x}_n = \begin{bmatrix} q_{xn}^{\{2\}} & q_{xn}^{\{3\}} & q_{xn}^{\{4\}} \end{bmatrix} \tag{3.38}$$

$$\mathbf{y}_n = \begin{bmatrix} q_{yn}^{\{2\}} & q_{yn}^{\{3\}} & q_{yn}^{\{4\}} \end{bmatrix} \tag{3.39}$$

$$\mathbf{z}_n = \begin{bmatrix} q_{zn}^{\{2\}} & q_{zn}^{\{3\}} & q_{zn}^{\{4\}} \end{bmatrix} \tag{3.40}$$

The next section shows how the global coordinates of a scatterer may be used to formulate mathematically the signal at the radar receiver.

3.2.4 Signal received at the radar

When the variation of the aspect angle between the radar and the vessel is small during the CPI, the vessel can be viewed as consisting of point scatterers with constant RCSs and fixed locations in the local coordinate system [5]. Thus, assume that a vessel can be represented by K point scatterers. Further assume that the radar transmits a stepped frequency waveform and that the motion of the vessel is stationary over the burst[1]. Then, the radar's received signal for the m^{th} pulse and the n^{th} burst, denoted by $\Phi_{n,m}$, is given by:

$$\Phi_{n,m} = \sum_{k=1}^{K} \alpha_k \, e^{\left(-j2\pi f_{c,m} \frac{2R_{k,t(n)}}{c}\right)} + e_{n,m} \tag{3.41}$$

where $f_{c,m}$ represents the centre frequency of the m^{th} transmitted pulse within a burst, where a burst of M pulses is compressed to form a high resolution range profile, n represents the burst number, α_k is the RCS of the k^{th} scatterer, c is the speed of light, $e_{n,m}$ denotes the clutter and noise for the m^{th} pulse in the n^{th} burst and $R_{k,t(n)}$ denotes the range of the k^{th} scatterer and it is given by:

$$R_{k,t(n)} = \sqrt{\left(R_0 - u_{k,t(n)}\right)^2 + \left(v_{k,t(n)}\right)^2 + \left(w_{k,t(n)}\right)^2} \tag{3.42}$$

The mathematical formulation of the received signal may be used to obtain simulated ISAR images of a sea vessel, for arbitrary incremental 3-D rotational motion represented by $\mathbf{q}_{tot,\Delta t(n)}$ over an ISAR burst.

[1]This implies that the distance traversed by an object over an ISAR burst is much less than the down-range resolution of the high range resolution profile. This assumption is valid for imaging low speed objects, such as sailing yachts, with medium resolution, when the burst repetition frequency is greater than or equal to 100 Hz

3.2.5 Signal-to-noise ratio

The mean signal-to-noise ratio (SNR) of an ISAR image is defined as the ratio of the signal power σ_s^2 to the noise power σ_n^2:

$$\text{SNR} = 10 \log_{10} \left(\frac{\sigma_s^2}{\sigma_n^2} \right) \tag{3.43}$$

For simulation purposes, the SNR of an image can be set using the following four steps:

1. Calculate the signal power σ_s^2 of the simulated ISAR image as follows:

$$\sigma_s^2 = \frac{1}{MN} \sum_{m=0}^{M-1} \sum_{n=0}^{N-1} \left| \Phi_{n,m}^s \right|^2 \tag{3.44}$$

   where $\Phi_{n,m}^s$ is the radar received signal without noise, and it is given by:

$$\Phi_{n,m}^s = \sum_{k=1}^{K} \alpha_k \, e^{\left(-j2\pi f_{c,m} \frac{2R_{k,t(n)}}{c} \right)} \tag{3.45}$$

2. Calculate the required noise power σ_n^2 using the following formula:

$$\sigma_n^2 = \sigma_s^2 10^{\frac{-\text{SNR}}{10}} \tag{3.46}$$

3. Generate the noise matrix $\mathbf{e}$ that has n rows and m columns, where each element $e_{n,m}$ is a complex value with an amplitude of $A_{n,m}$ and a phase of $\phi_{n,m}$:

$$e_{n,m} = |A_{n,m}| \, e^{-j\phi_{n,m}} \tag{3.47}$$

   The amplitude $A_{n,m}$ is chosen from a Gaussian distribution with a mean of zero and a variance of σ_n^2, and the phase $\phi_{n,m}$ is chosen from a uniform distribution that has a range of zero to 2π.

4. Lastly, the received signal at the radar, denoted by $\Phi_{n,m}$, is given by:

$$\Phi_{n,m} = \Phi^{s}_{n,m} + e_{n,m} \tag{3.48}$$

3.2.6 Doppler frequency associated with the k^{th} scatterer

When a sea vessel experiences 3-D rotational motion, the distance from the radar to the k^{th} scatterer $R_{k,t(n)}$ changes over time, as it is mathematical shown in (3.42). As a result, the Doppler frequency $f_{d,k,\Delta t(n)}$ of the k^{th} scatterere can be expressed in discrete form as:

$$f_{d,k,\Delta t(n)} = \frac{2}{\lambda}\left(\frac{R_{k,t(n)} - R_{k,t(n-1)}}{\Delta t}\right) \tag{3.49}$$

However, for objects with arbitrary 3-D rotational motion, it is only a component of the rotational motion that gives rise to cross-range dependent Doppler frequencies [24]. The useful component of the rotational motion is referred to as the image-generating Doppler components (see Section 2.2.4 for a detailed description), which consist of the Doppler generating axis of rotation $\mathbf{\Omega}_{eff,\Delta t(n)}$ and the effective angular rotation rate $\dot{\theta}_{eff,\Delta t(n)}$.

3.2.7 Object's rotation and the image-generating Doppler components

Figure 3.2 illustrates the rotational components of an object for the simple and ideal case, where the components do not vary over time. In this example, the object's 3-D rotational motion (roll, pitch and yaw) can be represented as a rotation about an axis of rotation $\mathbf{\Omega}$ at an angular rotation rate of $\dot{\theta}$. The image-generating Doppler components are illustrated as the Doppler generating axis of rotation $\mathbf{\Omega}_{eff}$ and the effective angular rotation rate $\dot{\theta}_{eff}$. Consequently, the

Doppler frequency of the k^{th} scatterer can also be expressed as:

$$f_{d,k} = \frac{2}{\lambda}\left(l_k \dot{\theta}_{eff}\right) \tag{3.50}$$

where l_k is the distance from the Doppler generating axis of rotation to the k^{th} scatterer.

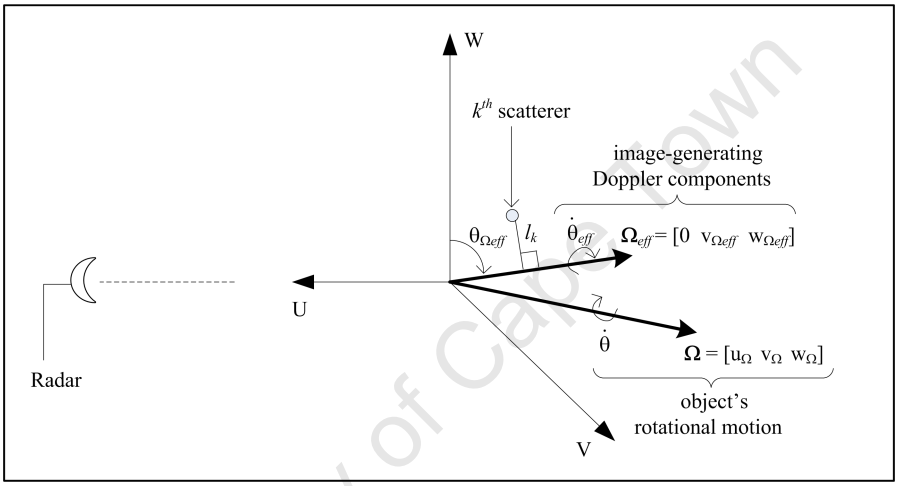

Figure 3.2: Diagram illustrating an object's rotational motion and the image-generating Doppler components

Equation (3.50) shows that if the lever-arm distance l_k or the effective rotation rate $\dot{\theta}_{eff}$ changes over the CPI, it induces a time-varying Doppler frequency for the k^{th} scatterer. If the Doppler variation of a scatterer is greater than the Doppler resolution, the scatterer will experience migration through Doppler cells or cross-range cells of an ISAR image.

For objects that possess time-varying roll, pitch and yaw motion, the important rotational parameters for ISAR consist of the Doppler generating axis of rotation $\boldsymbol{\Omega}_{eff,\Delta t(n)}$, the angle of the Doppler generating axis of rotation $\theta_{\Omega eff,\Delta t(n)}$ and the object's rotation rate $\dot{\theta}_{\Delta t(n)}$. These parameters can be calculated by using the following steps:

1. Calculate the incremental rotational motion $\mathbf{q}_{tot,\Delta t(n)}$ using (3.19):

$$\mathbf{q}_{tot,\Delta t(n)} = \mathbf{q}_{y,\Delta t(n)}\left(\mathbf{z}_{n-1}, \theta_{y,\Delta t(n)}\right) \otimes \mathbf{q}_{p,\Delta t(n)}\left(\mathbf{y}_{n-1}, \theta_{p,\Delta t(n)}\right) \cdots \\ \cdots \otimes \mathbf{q}_{r,\Delta t(n)}\left(\mathbf{x}_{n-1}, \theta_{r,\Delta t(n)}\right) \tag{3.19}$$

2. Extract the angle of rotation $\theta_{\Delta t(n)}$

$$\theta_{\Delta t(n)} = 2\arccos\left(q^{\{1\}}_{tot,\Delta t(n)}\right) \tag{3.51}$$

3. Consequently, the object's axis of rotation $\mathbf{\Omega}_{\Delta t(n)}$ is given by:

$$\mathbf{\Omega}_{\Delta t(n)} = \frac{1}{\sin\left(0.5\theta_{\Delta t(n)}\right)}\begin{bmatrix} q^{\{2\}}_{tot,\Delta t(n)} & q^{\{3\}}_{tot,\Delta t(n)} & q^{\{4\}}_{tot,\Delta t(n)} \end{bmatrix} \tag{3.52}$$

4. The object's rotation rate $\dot{\theta}_{\Delta t(n)}$ is given by:

$$\dot{\theta}_{\Delta t(n)} = \frac{\theta_{\Delta t(n)}}{\Delta t} \tag{3.53}$$

The Doppler generating axis of rotation $\mathbf{\Omega}_{eff,\Delta t(n)}$ is given by the projection of the object's axis of rotation $\mathbf{\Omega}_{\Delta t(n)}$ onto the $V - W$ plane. The angle of the Doppler generating axis of rotation $\mathbf{\Omega}_{eff,\Delta t(n)} = \begin{bmatrix} 0 & v_{\Omega eff,\Delta t(n)} & w_{\Omega eff,\Delta t(n)} \end{bmatrix}$ with respect to the global W axis, denoted by $\theta_{\Omega eff,\Delta t(n)}$, is defined as:

$$\theta_{\Omega eff,\Delta t(n)} = \arctan 2\left(v_{\Omega eff,\Delta t(n)}, w_{\Omega eff,\Delta t(n)}\right) \tag{3.54}$$

where $\arctan 2$ is a two-argument function that computes the arctangent with a range of $(-180°, 180°]$. The rate of change of $\theta_{\Omega eff,\Delta t(n)}$ is given by:

$$\dot{\theta}_{\Omega eff,\Delta t(n)} = \frac{\theta_{\Omega eff,\Delta t(n)} - \theta_{\Omega eff,\Delta t(n-1)}}{\Delta t} \tag{3.55}$$

The effective rotation rate $\dot{\theta}_{eff,\Delta t(n)}$ is the component of the object's rotation rate $\dot{\theta}_{\Delta t(n)}$ that gives rise to Doppler information, as shown by (3.50). The calculation of the effective rotation rate $\dot{\theta}_{eff,\Delta t(n)}$ from measured motion data has not been

addressed in the literature. A technique for calculating $\dot{\theta}_{eff,\Delta t(n)}$ from measured motion data is proposed in Chapter 4.

The next section presents a mathematical analysis that supports the hypothesis that the time-varying Doppler generating axis of rotation induces a time-varying Doppler frequency that causes scatterers to migrate through the cross-range cells of an ISAR image.

3.3 Time-varying Doppler Generating Axis of Rotation

Figure 3.3 considers the case where the angle of the Doppler generating axis of rotation $\mathbf{\Omega}_{eff,\Delta t(n)}$ changes uniformly at a rate of $\dot{\phi}$ over the CPI. The following symbols are defined in order to express the Doppler frequency of the k^{th} scatterer over time:

$\dot{\theta}_{eff}$ – effective rotation rate, which is constant over the CPI

d_k – distance from the object's centre of rotation to the k^{th} scatterer

$l_{k,\Delta t(n)}$ – lever-arm distance from the k^{th} scatterer to $\mathbf{\Omega}_{eff,\Delta t(n)}$ for the n^{th} discrete rotation

β_k – angle between $\mathbf{\Omega}_{eff,\Delta t(1)}$ and r_k

$\Delta\phi$ – change in the angle of the Doppler generating axis of rotation over the CPI, which changes uniformly at a rate of $\dot{\phi}$ through the CPI

In this example, the Doppler frequency of the k^{th} scatter can be expressed in discrete form as:

$$\begin{aligned} f_{d,k,\Delta t(n)} &= \frac{2}{\lambda}\left(l_{k,\Delta t(n)}\dot{\theta}_{eff}\right) \\ &= \frac{2}{\lambda}\left(d_k \sin\left(\beta_k + \dot{\phi}t(n)\right)\dot{\theta}_{eff}\right) \end{aligned} \tag{3.56}$$

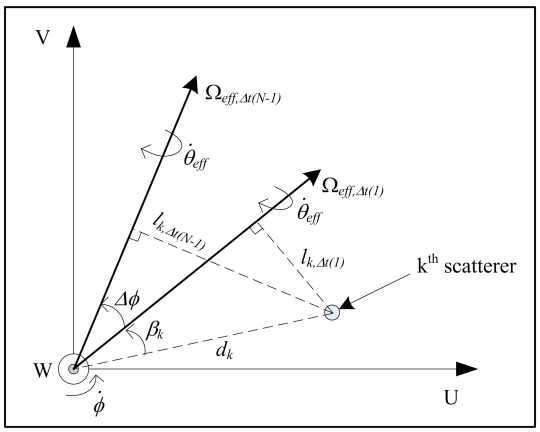

Figure 3.3: Illustration of a time-varying Doppler generating axis of rotation over the CPI

or in continuous form as:

$$\begin{aligned} f_{d,k,t} &= \frac{2}{\lambda}\Big(d_k \sin\left(\beta_k + \dot{\phi}t\right)\dot{\theta}_{eff}\Big) \\ &= \frac{2d_k\dot{\theta}_{eff}}{\lambda}\Big(\sin\left(\beta_k\right)\cos\left(\dot{\phi}t\right) + \cos\left(\beta_k\right)\sin\left(\dot{\phi}t\right)\Big) \end{aligned} \tag{3.57}$$

When $\Delta\phi \leq \frac{\pi}{4}$, the Taylor series expansion can be applied to (3.57) to express $f_{d,k,t}$ directly as a function of t:

$$\begin{aligned} f_{d,k,t} &= \frac{2d_k\dot{\theta}_{eff}}{\lambda}\left(\sin\left(\beta_k\right)\left(1 - \frac{(\dot{\phi}t)^2}{2!}\right) + \cos\left(\beta_k\right)\left((\dot{\phi}t) - \frac{(\dot{\phi}t)^3}{3!}\right)\right) \\ &= \frac{2d_k\dot{\theta}_{eff}}{\lambda}\left(\sin\left(\beta_k\right) + \left(\cos\left(\beta_k\right)\dot{\phi}\right)t - \left(\sin\left(\beta_k\right)\frac{\dot{\phi}^2}{2}\right)t^2 - \left(\cos\left(\beta_k\right)\frac{\dot{\phi}^3}{6}\right)t^3\right) \end{aligned} \tag{3.58}$$

Thus, when the angle of the Doppler generating axis changes over the CPI, (3.58) shows that the Doppler frequency of the k^{th} scatterer $f_{d,k,t}$ is a function of time. As a result, when traditional Fourier Transform processing is used to separate scatterers according to their Doppler frequency, scatterers migrate through cross-range cells due to the existence of the quadratic and higher order terms.

In addition, a time-varying Doppler generating axis of rotation causes the lever-arm distance $l_{k,\Delta t(n)}$ of the k^{th} scatterer to vary over time, as shown by (3.56). In effect, this induces a time-varying Doppler frequency.

To the candidate's knowledge, there is no literature that characterises the effect of a time-varying Doppler generating axis of rotation on ISAR imaging. The system models in the literature are limited because matrices are used to model 3-D rotational motion. Since rotational matrices do not directly and independently model the Doppler generating axis of rotation, this approach cannot be used to investigate this topic in great detail.

However, the quaternion-based system model presented in Section 3.2.2 is flexible enough to investigate the effect of a time-varying Doppler generating axis of rotation on ISAR imaging because it directly models the 3-D rotational motion in terms of an object's axis of rotation and angle of rotation for each discrete rotation over the CPI. Furthermore, by expressing the rotational motion in terms of the image-generating Doppler components, it makes it possible to vary the Doppler generating axis of rotation over the CPI directly and independently. Simulations were done, using a point scatterer model, to investigate this approach in greater detail. The simulation setup that was used is described in the next section.

3.4 Simulation Setup

This section considers a point scatterer model of a yacht and investigates three cases in which the yacht's Doppler generating axis of rotation varies over the CPI. The model of the yacht is illustrated in Figure (3.4) where point scatterers were arbitrarily placed at different mast heights and positions to show the outline of the vessel.

Case 1 considers an inbound vessel with constant pitch rate, and investigates the effect of a yaw perturbation on a side-view ISAR image. Case 2 investigates the number of Doppler cells of migration that the k^{th} scatterer experiences, when the

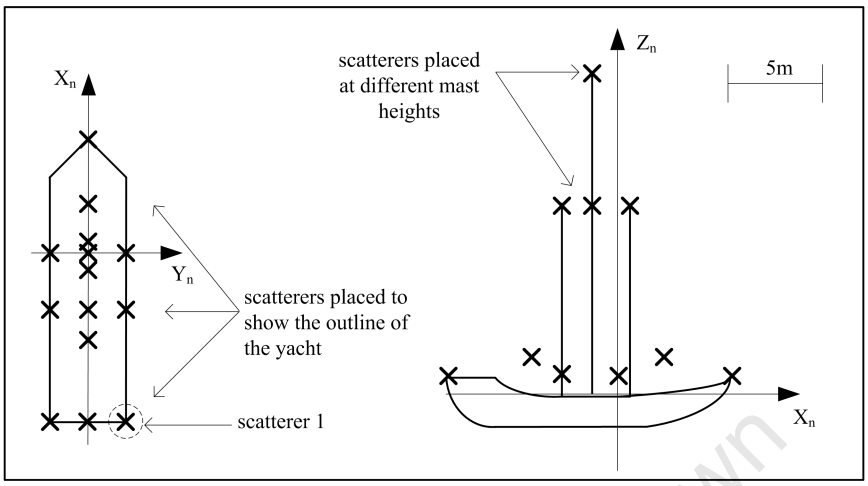

Figure 3.4: A simple point scatterer model of an arbitrary yacht

angle of the Doppler generating axis of rotation changes uniformly, at different rates, over the CPI. In this case, the effective rotation rate $\dot{\theta}_{eff}$ is kept constant over the CPI, so that the cause of the migration is only due to the time-varying nature of the Doppler generating axis of rotation. Lastly, case 3 considers the measured 3-D rotational motion of an instrumented yacht.

3.4.1 Case 1: Description

Case 1 investigates the effect of a yaw perturbation on a side-view ISAR image of a sea vessel. In this case, the pitch rate of an inbound vessel is constant, and this pitch motion is used to generate a side-view ISAR image. However, the vessel also possesses a time-varying yaw component that induces a perturbation to the imaging process. The yaw motion induces a time-varying Doppler generating axis of rotation over the CPI, which leads to blurring in the ISAR image.

3.4.2 Case 2: Description

Case 2 considers the scenario where the the angle of the Doppler generating axis of rotation changes uniformly over the CPI. In this case, the Doppler generating

axis of rotation is aligned to the global V axis at the start of the CPI, to ensure that the rotational motion is ideally suited to the side-view imaging case. In effect, the lever-arm distance of the k^{th} scatterer changes over the CPI and this gives rise to the migration of scatterers through Doppler cells. This example corresponds to a typical side-view ISAR imaging scenario with a perturbation that causes the angle of the Doppler generating axis of rotation to change uniformly over the CPI.

The considered simulation setup is shown in Figure 3.5. The symbols used in the diagram are defined as follows:

$\boldsymbol{\Omega}_{eff,\Delta t(n)}$ – Doppler generating axis of rotation for the n^{th} discrete rotation

$\theta_{\Omega eff,\Delta t(n)}$ – angle of $\boldsymbol{\Omega}_{eff,\Delta t(n)}$ from the W axis, for the n^{th} discrete rotation

$\dot{\theta}_{eff}$ – effective angular rotation rate about $\boldsymbol{\Omega}_{eff,\Delta t(n)}$

$\boldsymbol{\Omega}_m$ – a stationary axis of rotation that lies along the U axis

$\dot{\theta}_m$ – angular rotation rate about $\boldsymbol{\Omega}_m$

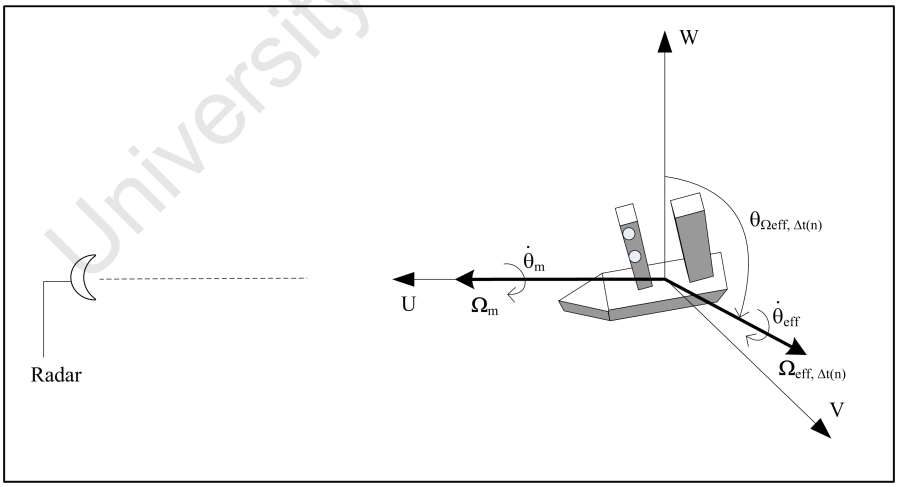

Figure 3.5: Simulation setup for case 1

In the simulation, the sea vessel's 3-D rotational motion is represented by an effective angular rotation rate of $\dot{\theta}_{eff}$ about a Doppler generating axis of rotation

$\mathbf{\Omega}_{eff,\Delta t(n)}$. The angle of rotation during each discrete rotation θ_{eff} is given by:

$$\theta_{eff} = \dot{\theta}_{eff}\Delta t \tag{3.59}$$

During the CPI, the Doppler generating axis of rotation rotates about a fixed axis of rotation $\mathbf{\Omega}_m$, at an angular rate of $\dot{\theta}_m$. As a result, the angle of the Doppler generating axis of rotation $\theta_{\Omega eff,\Delta t(n)}$ changes uniformly over the CPI. The number of Doppler cells of migration that is experienced by the k^{th} scatterer, denoted by $d_{b,k}$, is calculated by using the following steps:

1. **Initialisation**: Initialise the initial Doppler generating axis of rotation at the start of the CPI, which is denoted as $\mathbf{\Omega}_{eff,\Delta t(0)}$. Set $n = 1$.

2. **Obtain the Doppler generating axis of rotation for the n^{th} rotation**: Let $\mathbf{q}_{\Omega eff,\Delta t(n-1)} = \begin{bmatrix} 0 & \mathbf{\Omega}_{eff,\Delta t(n-1)} \end{bmatrix}$ denote the 4-D quaternion representation of $\mathbf{\Omega}_{eff,\Delta t(n)}$ for the $(n-1)^{th}$ discrete rotation. Then, $\mathbf{q}_{\Omega eff,\Delta t(n)}$ for the n^{th} discrete rotation can be expressed as:

$$\mathbf{q}_{\Omega eff,\Delta t(n)} = \Big(\mathbf{q}_m(\mathbf{\Omega}_m, \theta_m)\Big)^* \otimes \mathbf{q}_{\Omega eff,\Delta t(n-1)} \otimes \mathbf{q}_m(\mathbf{\Omega}_m, \theta_m) \tag{3.60}$$

   where $\theta_m = \dot{\theta}_m \Delta t$, and $\mathbf{\Omega}_{eff,\Delta t(n)}$ is given by:

$$\mathbf{\Omega}_{eff,\Delta t(n)} = \begin{bmatrix} q^{\{2\}}_{\Omega eff,\Delta t(n)} & q^{\{3\}}_{\Omega eff,\Delta t(n)} & q^{\{4\}}_{\Omega eff,\Delta t(n)} \end{bmatrix} \tag{3.61}$$

3. **Calculate the incremental motion for the n^{th} rotation**: Since the Doppler generating axis of rotation changes over the the CPI, the quaternion that represents the incremental motion for the n^{th} rotation, denoted by $\mathbf{q}_{tot,\Delta t(n)}\left(\mathbf{\Omega}_{eff,\Delta t(n)}, \theta_{eff}\right)$, is different to the $(n-1)^{th}$ rotation. It can be expressed as:

$$\mathbf{q}_{tot,\Delta t(n)}\left(\mathbf{\Omega}_{eff,\Delta t(n)}, \theta_{eff}\right) = \left[\cos\left(\frac{\theta_{eff}}{2}\right) \quad \mathbf{\Omega}_{eff,\Delta t(n)} \sin\left(\frac{\theta_{eff}}{2}\right)\right] \tag{3.62}$$

4. **Obtain the Doppler frequency for the k^{th} scatterer $f_{d,k,\Delta t(n)}$ for $\Delta t(n)$**: Calculate the global coordinates of the k^{th} scatterer using 3.16 and

3.17. Thereafter, calculate the range of the k^{th} scatterer from the radar using 3.42. Lastly, obtain the Doppler frequency $f_{d,k,\Delta t(n)}$ using 3.49.

5. **Obtain the Doppler frequency for the k^{th} scatterer for all $(N-1)$ discrete rotations**: Increment n and repeat steps 1, 2 and 3 until all $N-1$ discrete rotations are completed.

6. **Calculate the number of Doppler cells of migration that the k^{th} scatterer experiences over the CPI**: Calculate the number of Doppler cells of migration that the k^{th} scatterer experiences over the CPI, denoted by $d_{b,k}$, using the following:

$$d_{b,k} = \frac{1}{(N-1)\,\Delta t}\left(\max_{n\in\{1,2,N-1\}}\left(f_{d,k,\Delta t(n)}\right) - \min_{n\in\{1,2,N-1\}}\left(f_{d,k,\Delta t(n)}\right)\right) \quad (3.63)$$

3.4.3 Case 3: Description

Case 3 investigates the effect of realistic 3-D rotational motion on ISAR imaging. It considers the case where an inbound vessel experiences time-varying roll, pitch and yaw motion that is based on measured data.

3.5 Simulation Results

This section presents the simulation results of the three cases described in Section 3.4. In all three cases, a stepped frequency radar waveform is used to obtain simulated HRR profiles of the point scatterer sea vessel shown in Figure 3.4. The range from the radar to the vessel's centre of rotation R_0 is 10 km. The radar parameter values that are used in the simulations are summarised in Table 3.1. Note that the duration of the CPI is referred to as the CPTWL, which is denoted by $\Delta\tau$.

Table 3.1: Radar parameter values used in the simulation

Parameter description	Symbol	Value
Pulse repetition frequency	f_{PRF}	10 kHz
Number of pulses in a burst	M	100
Frequency step	Δf	5 MHz
Number of bursts	N	100
Burst repetition frequency	f_{BRF}	100 Hz
Carrier frequency of the 1st pulse	$f_{c,0}$	9.5 GHz
Time period between discrete rotations	Δt	0.01 s
CPTWL	$\Delta\tau$	1 s

3.5.1 Case 1: Results and discussion

Case 1 investigates the blurring in side-view ISAR imagery for two different scenarios: case 1a considers the ideal situation where a vessel possesses uniformly changing pitch motion, and case 1b considers the ideal situation with a yaw perturbation.

The 3-D rotational motion of the sea vessel in case 1a and case 1b is shown in Figure 3.6. The bank, elevation and heading of the vessel are parameters that are typically measured by an INS/GPS system. The roll rate, pitch rate and yaw rate are calculated by using (3.20), (3.21) and (3.22) respectively. It should be noted that both case 1a and case 1b consider idealised motion, in order to investigate the effect of uniformly changing yaw perturbation on a side-view ISAR image.

In case 1, the radar illuminates the point scatterer model of the yacht (see Figure 3.4) undergoing the 3-D rotational motion shown in Figure 3.6, and the system model in Section 3.2 was used to obtain the radar's received signal. The normalised ISAR images that were obtained for case 1a and case 1b are illustrated in Figure 3.7(a) and (b) respectively. In the simulation, the amplitudes of all the point scatterers were equal and the SNR of the ISAR image was fixed to 15 dB.

When the vessel possessed uniformly changing pitch motion, corresponding to case 1a, all the point scatterers in the ISAR image were focused. However, when the vessel also possessed a uniformly changing yaw perturbation, scatterers along

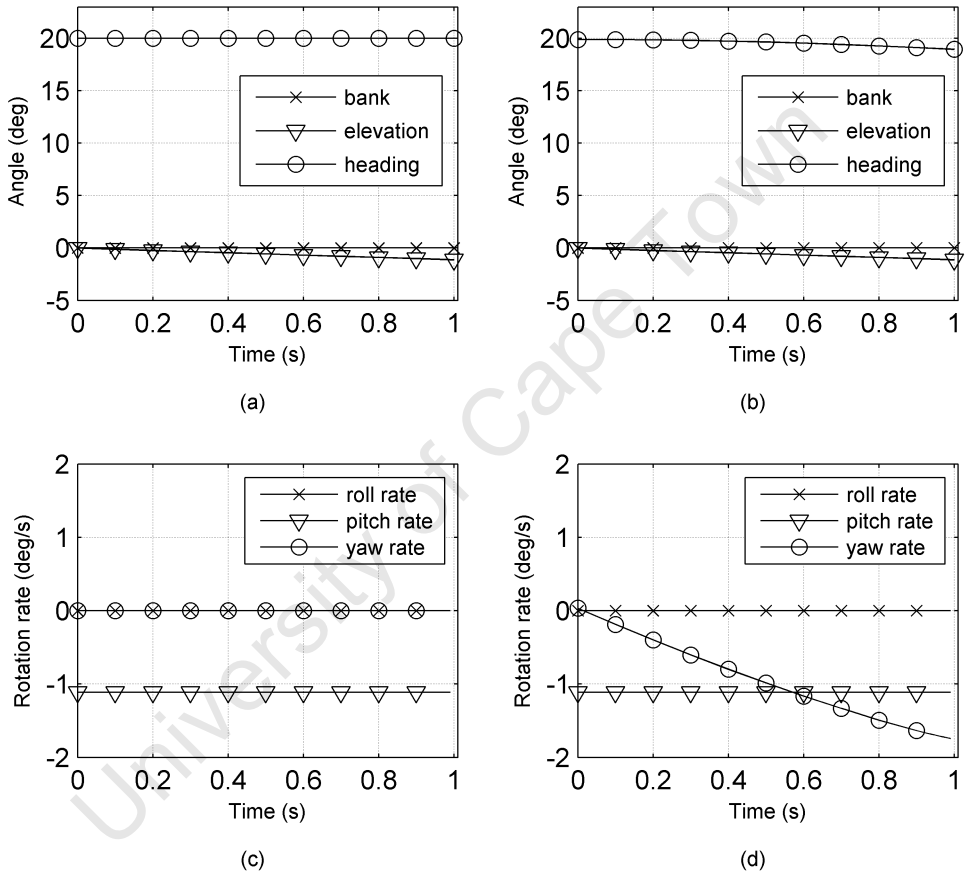

Figure 3.6: Motion data of the sea vessel: bank, elevation and heading for (a) case 1a and (b) case 1b, and roll, pitch and yaw for (c) case 1a and (d) case 1b

the bow and deck of the vessel migrated through cross-range cells, which led to blurring in the ISAR image. This is clearly illustrated by scatterer 1, which is located at the stern of the vessel (see Figure 3.4). Figure 3.7(d) shows that the Doppler frequency of scatterer 1 ranges from 0 Hz to approximately 9 Hz over the CPI. Since the CPI is 1 s, this gives a Doppler resolution of 1 Hz. Thus, scatterer 1 migrates through approximately 9 cross-range cells in the ISAR image.

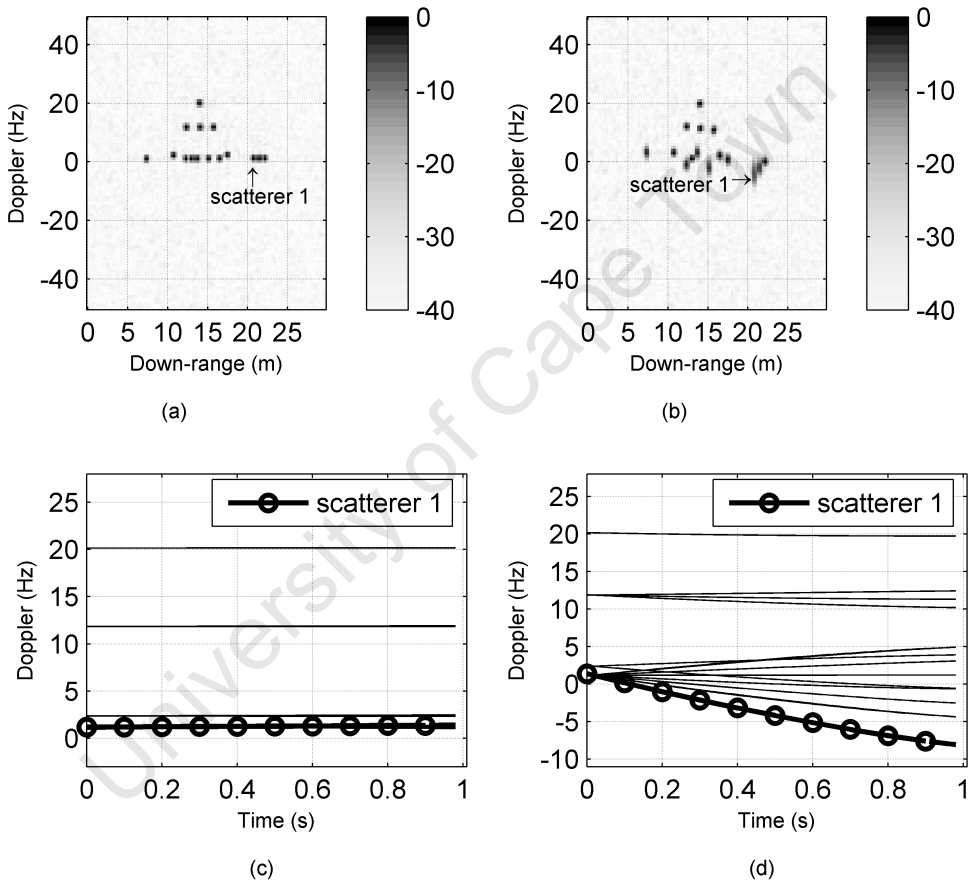

Figure 3.7: ISAR image of the point scatterer model of the yacht for (a) case 1a and (b) case 1b, and the Doppler frequency of all the point scatterers for (c) case 1a and (d) case 1b

The cause of migration can be explained by understanding that the cross-range dimension of an ISAR image fundamentally represents Doppler frequency. Equation (3.50) shows that the Doppler frequency of the k^{th} scatterer is dependent on

the lever-arm extent l_k of the k^{th} scatterer and the effective rotation rate $\dot{\theta}_{eff}$. Thus, if l_k or $\dot{\theta}_{eff}$ changes over the CPI, it induces a time-varying Doppler frequency, which gives rise to migration through the Doppler cells or the cross-range cells of an ISAR image.

Figure 3.8 analyses case 1b in greater detail by showing the angle of the Doppler generating axis of rotation $\theta_{\Omega eff}$ and the rotation rate $\dot{\theta}$ of the vessel; these parameters can be calculated by using (3.54) and (3.53) respectively. It can be observed that $\theta_{\Omega eff}$ changes by approximately 60° and $\dot{\theta}$ by nearly a factor of two over the CPI. Thus, it is concluded that a uniformly changing yaw perturbation causes the angle of the Doppler generating axis of rotation and the vessel's rotation rate to vary over the CPI.

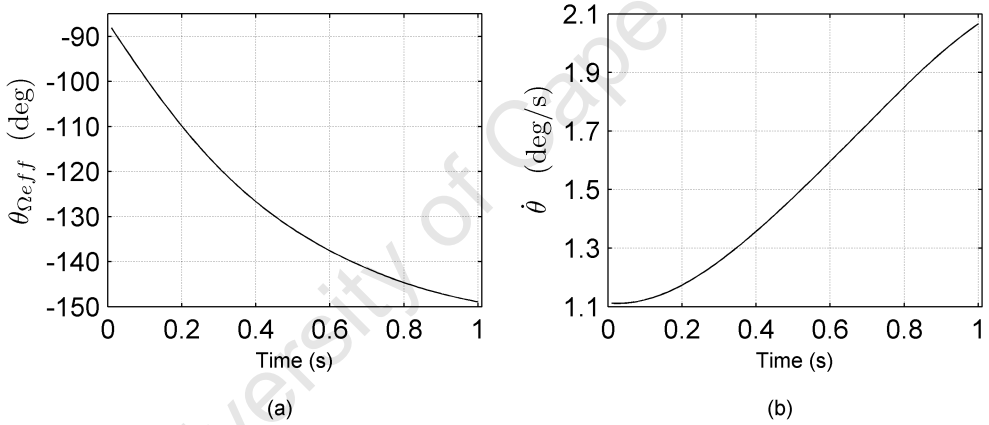

Figure 3.8: Rotational motion components for case 1b showing the (a) angle of Doppler generating axis of rotation $\theta_{\Omega eff}$ and the (b) rotation rate $\dot{\theta}$, over the CPI

When the angle of the Doppler generating axis of rotation changes over the CPI, it causes the lever-arm distance l_k of the k^{th} scatterer to vary over time, which induces a time-varying Doppler frequency. Similarly, for a time-varying $\dot{\theta}$, it causes a time-varying $\dot{\theta}_{eff}$, which also induces a time-varying Doppler frequency. In summary, the two main causes of blurring are the time-varying nature of the angle of the Doppler generating axis of rotation and the effective rotation rate. In case 1b, scatterer 1 migrates through approximately 9 Doppler cells due to the time-varying nature of both $\theta_{\Omega eff}$ and $\dot{\theta}$.

Case 2 investigates how to estimate the number of cells of migration that scatterer 1 experiences exclusively due to the time-varying nature of $\theta_{\Omega eff}$.

3.5.2 Case 2: Results and discussion

Case 2 considers the idealised case where the angle of the Doppler generating axis of rotation changes uniformly over the CPI, and the effective rotation rate of the vessel is constant. Thereafter, $d_{b,k}$ is calculated and this result may be used to predict the number of Doppler cells of migration that a scatterer experiences purely due to the time-varying nature of the Doppler generating axis of rotation. In addition, case 2 considers scatterer 1 in Figure 3.4, so that the results may be used to estimate the number of Doppler cells of migration that are exclusively due to the time-varying nature of the angle of the Doppler generating axis of rotation, for case 1b.

The simulation parameter values for case 2 are summarised in Table 3.2 and the radar parameter values are contained in Table 3.1. In this example, scatterer 1 rotates about the Doppler generating axis of rotation at a constant rotation rate of $\dot{\theta}_{eff}$. At the start of the CPI, the Doppler generating axis of rotation $\mathbf{\Omega}_{eff,\Delta t(0)}$ is aligned to the global V axis. Consequently, the initial 3-D rotational motion of the vessel corresponds to uniformly changing pitch motion. During the CPI, the Doppler generating axis of rotation $\mathbf{\Omega}_{eff,\Delta t(n)}$ rotates about the fixed axis of rotation $\mathbf{\Omega}_m$ at a rate of $\dot{\theta}_m$. The number of Doppler cells of migration for scatterer 1, denoted by $d_{b,1}$, is calculated by using the steps described in Section 3.4.2.

Table 3.2: Simulation parameter values for case 2

Parameter description	Symbol	Value
Local coordinates of scatterer 1	$\mathbf{r}_1$	$[9 \;\; 2 \;\; 1]$
Initial Doppler generating axis of rotation	$\mathbf{\Omega}_{eff,\Delta t(0)}$	$[0 \;\; 1 \;\; 0]$
Effective angular rotation rate	$\dot{\theta}_{eff}$	$\in \{1, 1.2, \cdots, 2.4\}^\circ/s$
Fixed axis of rotation	$\mathbf{\Omega}_m$	$[1 \;\; 0 \;\; 0]$
Angular rotation rate about $\mathbf{\Omega}_m$	$\dot{\theta}_m$	$\in \{0, 10, \cdots, 90\}^\circ/s$

Case 2 calculates $d_{b,1}$ for different rotation rates $\dot{\theta}_m$ and $\dot{\theta}_{eff}$, as shown in Table 3.2. In this example, $\dot{\theta}_m$ also corresponds to the rotation rate of the angle of the Doppler generating axis of rotation $\dot{\theta}_{\Omega eff}$. Thus, Figure 3.9 illustrates a contour plot of $d_{b,1}$ for various effective rotation rates of $\dot{\theta}_{eff}$ and different rates of $\dot{\theta}_{\Omega eff}$. For example, if $\dot{\theta}_{eff}$ was $1.8°/s$ and $\dot{\theta}_{\Omega eff}$ was $15°/s$ over the CPI, then scatterer 1 migrates through two cross-range cells of the resulting ISAR image.

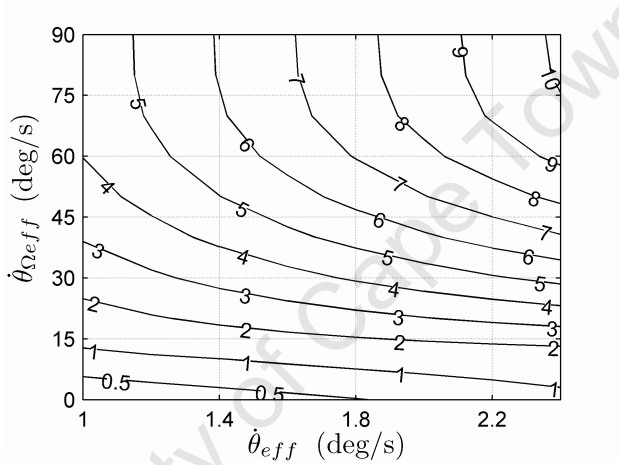

Figure 3.9: Contour plot showing the migration through cross-range cells for scatterer 1 when the angle of the Doppler generating axis of rotation, $\theta_{\Omega eff}$ and the effective rotation rate $\dot{\theta}_{eff}$ change at different rates

In case 1b, the angle of the Doppler generating axis of rotation changed by 60° and the average rotation rate $\dot{\theta}$ was approximately $1.5°/s$ over the CPI (see Figure 3.8). Since the angle of the Doppler generating axis of rotation changed linearly over the CPI of 1s, then $\dot{\theta}_{\Omega eff} = 60°/s$. Furthermore, the average rotation rate corresponded to the average effective rotation rate over the CPI; thus, $\dot{\theta}_{eff} = 1.5°/s$. Then Figure 3.9 shows that scatterer 1 experiences approximately 6 cells of migration due to the time-varying nature of the Doppler generating axis of rotation. The rest of the blurring can be attributed to the time-varying nature of the effective rotation rate over the CPI.

3.5.3 Case 3: Results and discussion

Case 3 investigates the effect of realistic 3-D rotational motion on ISAR imagery. The motion data is based on real data of a yacht that was smoothed by using a third order polynomial fit. Motion measurements were obtained in relatively calm sea condition, i.e. a sea state of 2. During the recording, the vessel sailed inbound with respect to the radar at a heading of approximately 20° (see Figure 3.10 (a)). If the vessel possessed pure pitch motion, a focused side-view ISAR image would be obtained. However, in this example, the yacht possesses time-varying roll, pitch and yaw motion as illustrated by Figure 3.10 (b).

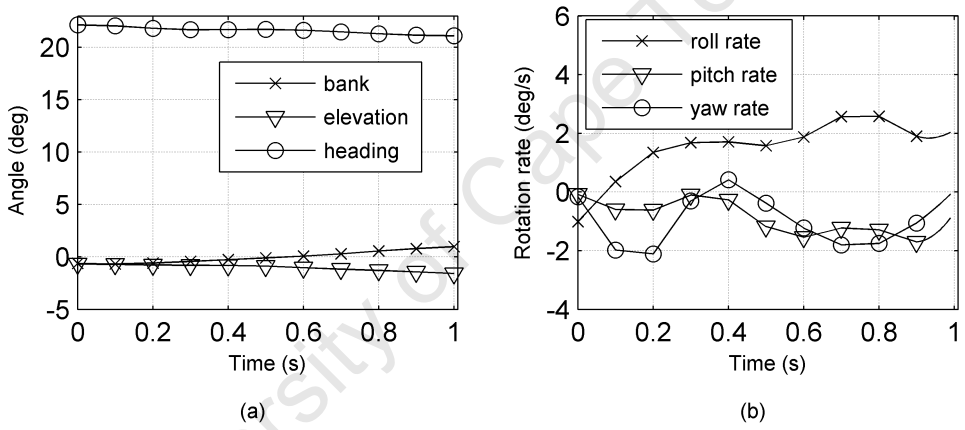

Figure 3.10: Motion data for case 3, showing the (a) bank, elevation and heading, and (b) roll, pitch and yaw rate of the sea vessel

The resulting ISAR image is shown in Figure 3.11(a); a significant amount of blurring can clearly be observed. This blurring is caused by the time-varying roll, pitch and yaw motion that induces a time-varying Doppler frequency for all the point scatterers, as shown by Figure 3.11 (b). Furthermore, the blurring can also be explained by observing the variation of $\theta_{\Omega eff}$ and $\dot{\theta}$ over the CPI, which is illustrated in Figure 3.12(a) and (b) respectively.

In order to generate a focused side-view ISAR image, $\theta_{\Omega eff} = \pm 90°$ and $\dot{\theta}$ should be constant over the CPI. However, in case 3, both $\theta_{\Omega eff}$ and $\dot{\theta}$ vary over time and this leads to scatterers migrating through the cross-range cells of the ISAR

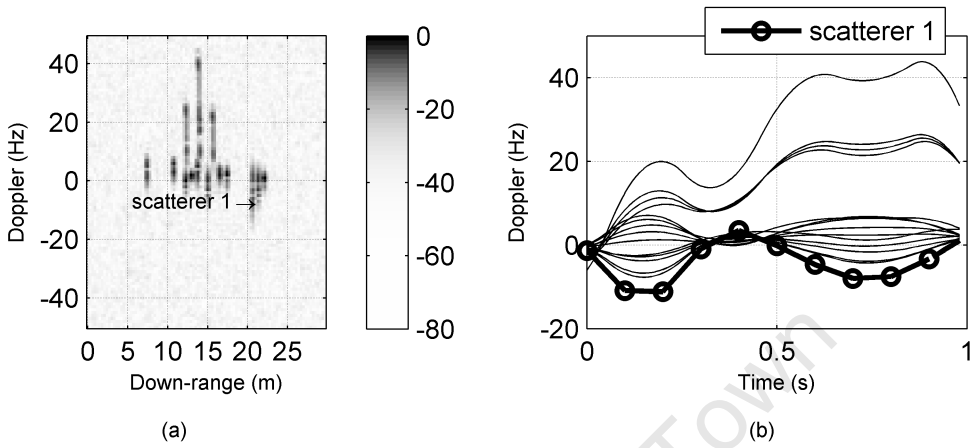

Figure 3.11: (a) ISAR image of the point scatterer model of the yacht and (b) Doppler frequencies of all the scatterers over the CPI, for case 3

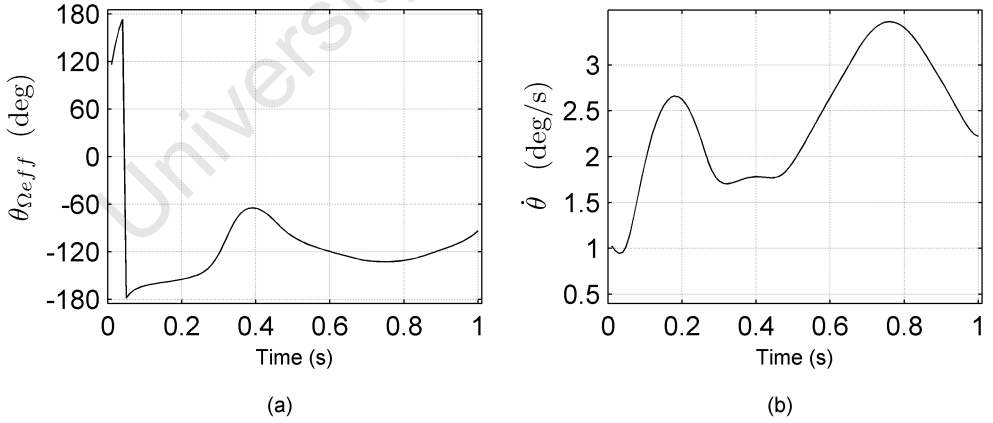

Figure 3.12: Rotational motion components for case 3 showing (a) the angle of Doppler generating axis of rotation $\theta_{\Omega eff}$ and (b) the rotation rate of the vessel $\dot{\theta}$ over the CPI

image. This type of scatterer migration cannot be compensated for by standard translation motion compensation or polar reformatting algorithms because these algorithms assume that $\theta_{\Omega eff}$ and $\dot{\theta}$ are constant over the CPI.

One way of limiting the migration of scatterers is to choose carefully the length of the CPI, or the CPTWL, so that the angle of the Doppler generating axis of rotation and the effective rotation rate are approximately constant. This concept is explored in greater detail in Chapter 5.

3.6 Conclusions

This chapter provided an in-depth understanding of how 3-D rotational motion causes blurring in an ISAR image. Furthermore, it focused on the effect of a vessel's time-varying Doppler generating axis of rotation on ISAR imaging. The current ISAR literature uses matrices to represent the 3-D rotational motion of an object, which makes it difficult to manipulate, directly and independently, the direction of the Doppler generating axis of rotation over the CPI. In this work, the rotational motion of the object was alternatively represented using quaternions, which made it possible to model and manipulate directly the object's axis of rotation and angle of rotation, for each discrete rotation.

In this chapter, a new quaternion-based system model was also presented that was flexible enough to accept the measured motion data of a vessel. Furthermore, the mathematical formulations of a few key motion parameters were presented, which included the object's axis of rotation $\mathbf{\Omega}_{\Delta t(n)}$, the Doppler generating axis of rotation $\mathbf{\Omega}_{eff,\Delta t(n)}$, the angle of the Doppler generating axis of rotation $\theta_{\Omega eff,\Delta t(n)}$ and the object's rotation rate $\dot{\theta}_{\Delta t(n)}$. These parameters are important to ISAR imaging because the Doppler generating axis of rotation determines the imaging projection plane; a component of the object's rotation rate, referred to as the effective rotation rate $\dot{\theta}_{eff,\Delta t(n)}$, is used to estimate the cross-range resolution of an ISAR image. In addition, the time-varying nature of $\theta_{\Omega eff,\Delta t(n)}$ and $\dot{\theta}_{eff,\Delta t(n)}$ causes scatterers to migrate through the cross-range cells of an ISAR image.

Simulations were performed for three different cases, where the Doppler generating axis of rotation changed in different ways over the CPI. Case 1 considered a side-view ISAR imaging scenario and showed that a uniformly changing yaw perturbation causes the angle of the Doppler generating axis of rotation and the object's rotation rate to vary over time. Case 2 characterised the migration of a scatterer through Doppler cells that was exclusively due to the time-varying nature of the Doppler generating axis of rotation. Lastly, case 3 considered realistic 3-D rotational motion with time-varying roll, pitch and yaw motion. This case showed that the resulting ISAR image contains substantial blurring, because the angle of the Doppler generating axis of rotation and the object's rotation rate varied significantly over the CPI.

In summary, Chapter 3 showed that 3-D rotational motion causes blurring in ISAR imagery. More specifically, theory and simulations were used to show that an object's time-varying Doppler generating axis of rotation gives rise to blurring in an ISAR image.

In the following chapter, the mathematical formulation of the effective rotation rate is discussed; this issue has not been addressed in this chapter. In addition, a new simplified system model is presented that removes the need for calculating the unit vectors along the local coordinate axes for each discrete rotation (see Section 3.2.3).

Chapter 4

Extraction of the Image-generating Doppler Components

4.1 Introduction

As explained in Chapter 1, ISAR is an imaging technique that is dependent on an object's rotational motion over the CPI. Maritime vessels and aircraft possess 3-D rotational motion; however, it is only two components of this motion, referred to as the image-generating Doppler components, that are useful to the ISAR imaging process (see Section 2.2.4). The image-generating Doppler components consist of the Doppler generating axis of rotation and the effective angular rotation rate. These two parameters are important to the ISAR imaging process because the Doppler generating axis of rotation influences the presentation[1] of the vessel and the effective angular rotation rate determines the resulting cross-range resolution. In addition, the time-varying nature of these two parameters gives rise to blurring in an ISAR image, as illustrated in Section 3.5.3.

[1] Presentation refers to the orientation of the vessel in an ISAR image, as defined by Musman *et al.* in [7].

The image-generating Doppler components and their influence on ISAR imaging are described in the current literature. A mathematical expression of the continuously varying Doppler generating axis of rotation was derived in papers by Chen and Miceli [24] and Bao *et al.* [38]. The effect of the time-varying effective angular rotation rate was characterised by Wong *et al.* [39]. The effect of the time-varying Doppler generating axis of rotation was investigated by the candidate in Chapter 3. However, there is no literature that addresses how both of the image-generating Doppler components can be extracted from measured motion data.

The previous chapter showed how the key motion parameters of an object (see Section 3.2.7) can be calculated, these parameters included the object's axis of rotation $\mathbf{\Omega}_{\Delta t(n)}$, the Doppler generating axis of rotation $\mathbf{\Omega}_{eff,\Delta t(n)}$, the angle of the Doppler generating axis of rotation $\theta_{\Omega eff,\Delta t(n)}$ and the object's rotation rate $\dot{\theta}_{\Delta t(n)}$. However, the calculation of the effective angular rotation rate $\dot{\theta}_{eff,\Delta t(n)}$ was not discussed, because this formulation has not been addressed in the literature. Furthermore, the formulation of $\mathbf{\Omega}_{eff,\Delta t(n)}$ was expressed in terms of the incremental motion about the local coordinate axis (see (3.19)), which is computationally expensive because it requires the calculation of the unit vectors along the local coordinate axis at time $t(n-1)$ (see Section 3.2.3).

This chapter proposes a new quaternion-based transformation that calculates both of the image-generating Doppler components from the measured attitude and GPS position data of an object. In addition, a new derivation for $\mathbf{\Omega}_{eff,\Delta t(n)}$ is presented, where the incremental motion over the discrete rotation is expressed about unit vectors along the global coordinate axes. This approach is computationally less expensive than the derivation in Chapter 3 because it does not require the calculation of the unit vectors along the local coordinate for time $t(n-1)$.

The calculation of the image-generating Doppler components makes it possible to gain an in-depth understanding of the time-varying nature of these two ISAR related parameters. Thus, the proposed transformation provides a rich source of information for ISAR imaging purposes rather than simply attitude and bearing

data themselves. The time-varying nature of the image-generating Doppler components can be used to explain the causes of the blurring in most ISAR images of sea vessels that possess 3-D rotational motion. Furthermore, the proposed transformation can be used as an alternative method for identifying good imaging intervals with a low degree of 3-D motion for applications such as cooperative ISAR for radar cross section measurement purposes. This is a useful engineering problem, since many Navies require their vessels to be measured in order to minimise the effect of scattering hotspots.

A description of the system model that is considered in this chapter is given in Section 4.2. The mathematical derivation of the new quaternion-based transformation is presented in Section 4.3. The proposed transformation was applied to the measured motion data of a yacht, and the results that were obtained are given in Section 4.4. Moreover, the measured radar data of the yacht were obtained using an experimental X-band radar, and a technique of using the image-generating Doppler components to identify good imaging intervals is also discussed in Section 4.4. Lastly, conclusions are summarised in Section 4.5.

4.2 System Model

In the system model, a rotation through an angle θ about an axis $\mathbf{h} = [h_1 \quad h_2 \quad h_3]$ is represented by a quaternion $\mathbf{q}_x(\mathbf{h}, \theta)$, arbitrarily labelled x, in vector form as:

$$\mathbf{q}_x(\mathbf{h}, \theta) = \left[\cos\left(\frac{\theta}{2}\right) \quad \mathbf{h}\sin\left(\frac{\theta}{2}\right)\right] \tag{4.1}$$

or in scalar form[2] as:

$$\mathbf{q}_x(\mathbf{h}, \theta) = \left[\cos\left(\frac{\theta}{2}\right) \quad h_1\sin\left(\frac{\theta}{2}\right) \quad h_2\sin\left(\frac{\theta}{2}\right) \quad h_3\sin\left(\frac{\theta}{2}\right)\right] \tag{4.2}$$

$$= \left[q_x^{\{1\}} \quad q_x^{\{2\}} \quad q_x^{\{3\}} \quad q_x^{\{4\}}\right] \tag{4.3}$$

[2] It should be noted that the superscripts {1}, {2}, {3} and {4} are used to denote the respective scalar elements of the quaternion.

The system model is illustrated in Figure 4.1; it considers a vessel with only rotational motion and assumes that any translation motion has been compensated for. Two coordinate axes are defined: the radar coordinate axes (U, V, W), which are fixed, and the local coordinate axes (X_n, Y_n, Z_n), which change as the vessel experiences 3-D rotational motion. In this diagram, $R_{k,t(n)}$ denotes the distance from the radar to the k^{th} scatterer of the vessel for time $t(n)$, and R_0 represents the distance from the radar to the vessel's centre of rotation.

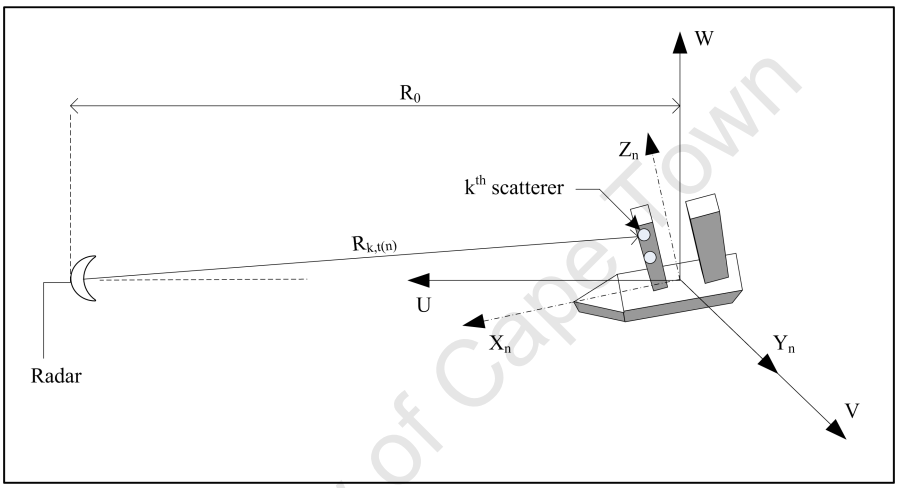

Figure 4.1: System model of the radar and the vessel showing the global and local coordinate axes

The 4-D quaternion representation of the local coordinates of the k^{th} scatterer is expressed as $\mathbf{q}_{rk} = [0 \;\; \mathbf{r}_k]$, where $\mathbf{r}_k = [x_k \;\; y_k \;\; z_k]$. However, it is the global coordinates of the k^{th} scatterer, denoted by $\mathbf{g}_{k,t(n)} = \begin{bmatrix} u_{k,t(n)} & v_{k,t(n)} & w_{k,t(n)} \end{bmatrix}$, that determine the phase at the radar receiver. Assume that the radar continuously tracks the vessel so that the vessel's centre of rotation always lies on the global U axis and that the physical dimensions of the vessel are much less than R_0. Then, the global coordinates of the k^{th} scatterer at $t(n)$, which is denoted by $\mathbf{q}_{gk,t(n)}$ in 4-D quaternion notation and $\mathbf{g}_{k,t(n)}$ in 3-D form, can be expressed as:

$$\mathbf{q}_{gk,t(n)} = (\mathbf{q}_{tot,\Delta t(n)})^* \otimes \Big((\mathbf{q}_{ins,t(n-1)})^* \otimes \mathbf{q}_{rk} \otimes (\mathbf{q}_{ins,t(n-1)}) \Big) \otimes (\mathbf{q}_{tot,\Delta t(n)}) \quad (4.4)$$

and

$$\mathbf{g}_{k,t(n)} = \begin{bmatrix} q^{\{2\}}_{gk,t(n)} & q^{\{3\}}_{gk,t(n)} & q^{\{4\}}_{gk,t(n)} \end{bmatrix} \quad (4.5)$$

where $\otimes$ represents quaternion multiplication, $\mathbf{q}_{ins,t(n-1)}$ is the quaternion that represents the combined 3-D rotation of heading $\theta_{hs,t(n-1)}$, elevation $\theta_{e,t(n-1)}$ and bank $\theta_{b,t(n-1)}$ for time $t(n-1)$, and $\mathbf{q}_{tot,\Delta t(n)}$ denotes the vessel's incremental rotational motion over $\Delta t(n)$. Stated mathematically:

$$\mathbf{q}_{ins,t(n-1)} = \mathbf{q}_{hs,t(n-1)}\left(\mathbf{RT}_{\perp 2}, \theta_{hs,t(n-1)}\right) \otimes \mathbf{q}_{e,t(n-1)}\left(\mathbf{RT}_{\perp 1}, \theta_{e,t(n-1)}\right) \otimes \cdots \\ \cdots \mathbf{q}_{b,t(n-1)}\left(\mathbf{RT}, \theta_{b,t(n-1)}\right) \tag{4.6}$$

$$\mathbf{q}_{tot,\Delta t(n)} = \mathbf{q}_{y,\Delta t(n)}\left(\mathbf{z}_n, \theta_{y,\Delta t(n)}\right) \otimes \mathbf{q}_{p,\Delta t(n)}\left(\mathbf{y}_n, \theta_{p,\Delta t(n)}\right) \otimes \mathbf{q}_{r,\Delta t(n)}\left(\mathbf{x}_n, \theta_{r,\Delta t(n)}\right) \tag{4.7}$$

where the unit vectors $\mathbf{z}_n$, $\mathbf{y}_n$ and $\mathbf{x}_n$ are defined about the local coordinate axes X_n, Y_n and Z_n respectively, at time $t(n)$. The unit vectors $\mathbf{RT}$, $\mathbf{RT}_{\perp 1}$ and $\mathbf{RT}_{\perp 2}$ are defined about the global coordinate axes U, V and W respectively. The heading $\theta_{hs,t(n-1)}$, elevation $\theta_{e,t(n-1)}$ and bank $\theta_{b,t(n-1)}$ angles define the orientation of the vessel at $t(n-1)$, as shown by Figure 4.2. The yaw $\theta_{y,\Delta t(n)}$, pitch $\theta_{p,\Delta t(n)}$ and roll $\theta_{r,\Delta t(n)}$ angles represent the n^{th} incremental rotational motion about a vessel's local axes, as illustrated by Figure 4.3. This definition corresponds to the convention adopted by Kuipers in [127]. In this system model, the rotational sequence is assumed to be heading, elevation and then bank.

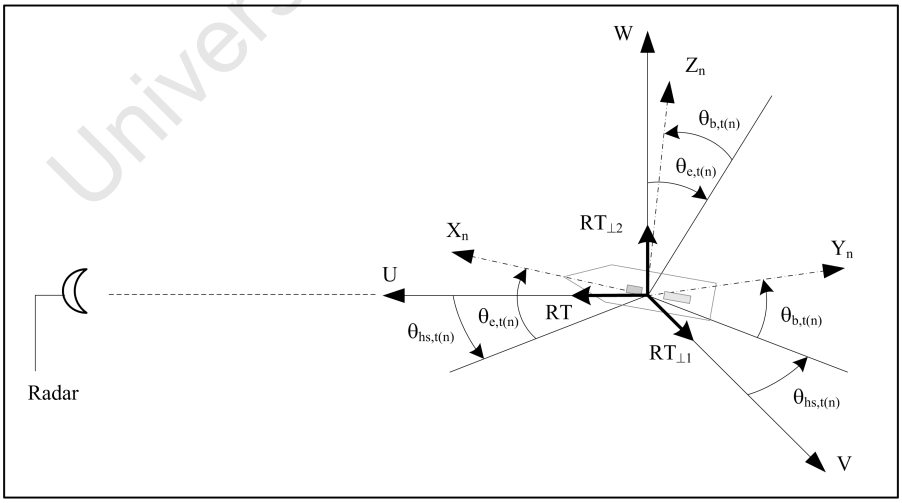

Figure 4.2: System model illustrating a vessel's heading-elevation-bank rotation sequence that defines the orientation of the vessel at time $t(n)$

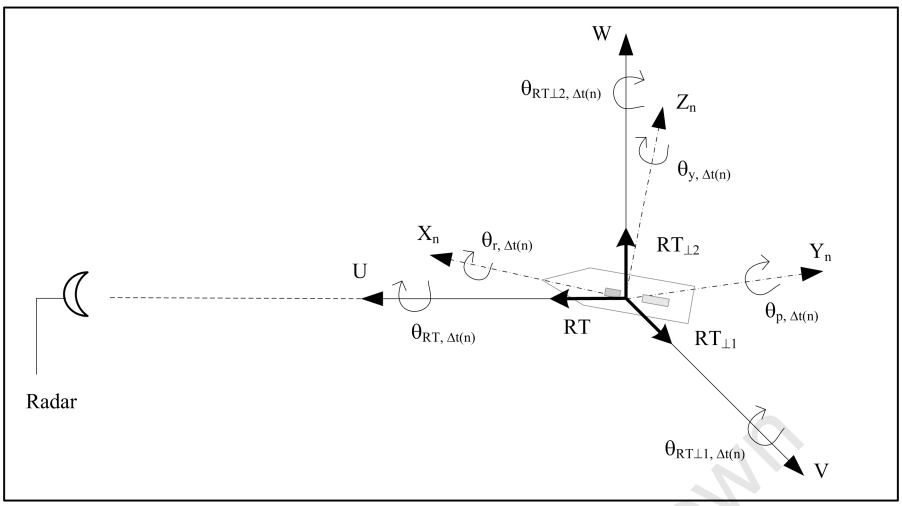

Figure 4.3: System model illustrating a vessel's yaw, pitch and roll angles as well as the effective yaw, effective pitch and effective roll angles

The system model is defined such that the heading of the vessel $\theta_{hs,t(n)}$ is zero when the vessel is sailing directly inbound with respect to the radar and such that it increases positively as the vessel rotates clockwise. As a result, the heading used in this system model can be obtained by using the heading measured from an INS $\theta_{h,t(n)}$ and the bearing $\theta_{br,t(n)}$ of the vessel, as follows:

$$\theta_{hs,t(n)} = \text{mod}\left(180^\circ + \theta_{h,t(n)} - \theta_{br,t(n)}, 360^\circ\right) \tag{4.8}$$

where $\text{mod}(a, b)$ is the modulus operation of a with b.

Assume that a vessel can be represented by K point scatterers. Then, the received signal at the radar is made up of the contributions from all the scatterers. The phase of the received signal at time $t(n)$ is dependent on the range of the k^{th} scatterer $R_{k,t(n)}$, which can be expressed in terms of the global coordinates $\mathbf{g}_{k,t(n)}$:

$$R_{k,t(n)} = \sqrt{(R_0 - u_{k,t(n)})^2 + (v_{k,t(n)})^2 + (w_{k,t(n)})^2} \tag{4.9}$$

Further assume that the radar transmits a stepped frequency waveform and that the motion of the vessel is stationary over the burst[3]. Then the signal received by the radar $\Phi_{n,m}$ is given by:

$$\Phi_{n,m} = \alpha_k \sum_{k=1}^{K} e^{\left(-j2\pi f_{c,m} \frac{2R_{k,t(n)}}{c}\right)} + e_{n,m} \tag{4.10}$$

where $f_{c,m}$ represents the centre frequency of the m^{th} transmitted pulse within a burst, where a burst of M pulses is compressed to form a high range resolution profile, n represents the burst number, α_k is the RCS of the k^{th} scatterer, c is the speed of light and $e_{n,m}$ denotes the clutter and noise.

The system model presented in this chapter is different to the other models found in the ISAR literature, and it is useful in the following ways:

- The vessel's current aspect, denoted by $\left(\mathbf{q}_{ins,t(n-1)}\mathbf{q}_{rk}(\mathbf{q}_{ins,t(n-1)})^*\right)$, and its incremental rotational motion over a discrete rotation, expressed by $\mathbf{q}_{tot,\Delta t(n)}$, are clearly expressed in (4.4). The variation of these two parameters over the CPI can be used to predict the presentation[4] of a vessel.

- The incremental rotational motion of a vessel between discrete rotations $\mathbf{q}_{tot,\Delta t(n)}$ can be used to calculate the vessel's image-generating Doppler components, which consist of the Doppler generating axis of rotation and the effective angular rotation rate, as shown in Section 4.3. This information can be used to explain the blurring caused by 3-D rotational motion as well as to assess the degree of 3-D rotational motion that exists in a CPI. Furthermore, it is an essential tool for the MACS algorithm, which is proposed in Chapter 5.

- The system model that is proposed is flexible enough to accept 3-D rotational motion measured from an attitude sensor. Thus, it can be used to

[3] This implies that the distance traversed by an object over an ISAR burst is much less than the down-range resolution of the high range resolution profile. This assumption is valid for imaging sailing yachts with a typical speed of 6 knots and a medium resolution of 0.5 m, when the burst repetition frequency is greater than 100 Hz.

[4] Presentation refers to the orientation of a vessel in an ISAR image, as defined by Musman *et al.* in [7].

develop an ISAR simulator for point-scatterer models that exhibit realistic motion.

4.3 The Proposed Quaternion Transformation

This section presents the quaternion-based transformation that calculates the image-generating Doppler components from measured attitude and GPS position data. The image-generating Doppler components consist of the Doppler generating axis of rotation and the effective angular rotation rate. It has been shown in Section 3.5 that the time-varying nature of these two parameters give rise to blurring in an ISAR image. Thus, these parameters provide detailed information about the amount of blurring that is exclusively caused by the 3-D rotational motion of an object (see Section 2.3 for other causes of blurring in ISAR).

Let $\mathbf{q}_{tot,\Delta t(n)}$ represent a vessel's incremental rotational motion over $\Delta t(n) = t(n) - t(n-1)$. The incremental rotational motion over the n^{th} discrete rotation $\Delta t(n)$ can be calculated from the attitude measurements (i.e. heading, elevation and bank) at time $t(n-1)$ and $t(n)$, as follows:

$$\begin{aligned}\mathbf{q}_{tot,\Delta t(n)} = \mathbf{q}_{b,t(n-1)}\Big(\mathbf{RT}, -\theta_{b,t(n-1)}\Big) \otimes \mathbf{q}_{e,t(n-1)}\Big(\mathbf{RT}_{\perp 1}, -\theta_{e,t(n-1)}\Big) \otimes \cdots \\ \cdots \mathbf{q}_{hs,t(n-1)}\Big(\mathbf{RT}_{\perp 2}, -\theta_{hs,t(n-1)}\Big) \otimes \mathbf{q}_{hs,t(n)}\Big(\mathbf{RT}_{\perp 2}, \theta_{hs,t(n)}\Big) \otimes \cdots \\ \cdots \mathbf{q}_{e,t(n)}\Big(\mathbf{RT}_{\perp 1}, \theta_{e,t(n)}\Big) \otimes \mathbf{q}_{b,t(n)}\Big(\mathbf{RT}, \theta_{b,t(n)}\Big) \qquad (4.11)\end{aligned}$$

where $\otimes$ represents the quaternion multiplication, $\theta_{b,t(n)}$ and $\theta_{e,t(n)}$ represent the bank and elevation measurements from an INS for time $t(n)$, and $\mathbf{RT} = [1 \;\; 0 \;\; 0]$, $\mathbf{RT}_{\perp 1} = [0 \;\; 1 \;\; 0]$ and $\mathbf{RT}_{\perp 2} = [0 \;\; 0 \;\; 1]$ are unit vectors about the U, V, W axes respectively. The calculation of $\mathbf{q}_{tot,\Delta t(n)}$ in (4.11) is accomplished by first reversing the rotation sequence at time $t(n-1)$ and then applying the rotation sequence at time $t(n)$.

The rotation motion $\mathbf{q}_{tot,\Delta t(n)}$ also represents the combined rotation due to the vessel's yaw, pitch and roll motion, which can be mathematically stated as:

$$\mathbf{q}_{tot,\Delta t(n)} = \mathbf{q}_{y,\Delta t(n)}\Big(\mathbf{z}_{n-1}, \theta_{y,\Delta t(n)}\Big) \otimes \mathbf{q}_{p,\Delta t(n)}\Big(\mathbf{y}_{n-1}, \theta_{p,\Delta t(n)}\Big) \otimes \cdots \\ \cdots \mathbf{q}_{r,\Delta t(n)}\Big(\mathbf{x}_{n-1}, \theta_{r,\Delta t(n)}\Big) \tag{4.12}$$

However, the vessel's Doppler generating axis of rotation that contributes to the ISAR image, lies in the VW plane, since the component of rotation about the U axis does not provide any Doppler component to the radar. Consequently, in order to obtain the image-generating Doppler components, the effective yaw, effective pitch and effective roll angles denoted by $\theta_{RT\perp 2,\Delta t(n)}$, $\theta_{RT\perp 1,\Delta t(n)}$ and $\theta_{RT,\Delta t(n)}$ respectively, need to be calculated such that:

$$\mathbf{q}_{tot,\Delta t(n)} = \mathbf{q}_{ey,\Delta t(n)}\Big(\mathbf{RT}_{\perp 2}, \theta_{RT\perp 2,\Delta t(n)}\Big) \otimes \mathbf{q}_{ep,\Delta t(n)}\Big(\mathbf{RT}_{\perp 1}, \theta_{RT\perp 1,\Delta t(n)}\Big) \otimes \cdots \\ \cdots \mathbf{q}_{er,\Delta t(n)}\Big(\mathbf{RT}, \theta_{RT,\Delta t(n)}\Big) \tag{4.13}$$

The rotation angles $\theta_{RT\perp 2,\Delta t(n)}$, $\theta_{RT\perp 1,\Delta t(n)}$ and $\theta_{RT,\Delta t(n)}$ can be calculated from the incremental rotation $\mathbf{q}_{tot,\Delta t(n)}$ over the n^{th} discrete rotation using the mathematical derivation is given in Kuipers [127]. A summary of the solution in terms of the notation defined in this chapter is presented below.

Define $A_{\Delta t(n)}$, $B_{\Delta t(n)}$ and $D_{\Delta t(n)}$ as follows:

$$A_{\Delta t(n)} = q^{\{1\}}_{tot,\Delta t(n)} q^{\{2\}}_{tot,\Delta t(n)} + q^{\{3\}}_{tot,\Delta t(n)} q^{\{4\}}_{tot,\Delta t(n)} \tag{4.14}$$

$$B_{\Delta t(n)} = -\Big(q^{\{1\}}_{tot,\Delta t(n)}\Big)^2 + \Big(q^{\{3\}}_{tot,\Delta t(n)}\Big)^2 \tag{4.15}$$

$$D_{\Delta t(n)} = \Big(q^{\{2\}}_{tot,\Delta t(n)}\Big)^2 - \Big(q^{\{4\}}_{tot,\Delta t(n)}\Big)^2 \tag{4.16}$$

then the effective roll angle $\theta_{RT,\Delta t(n)}$ can be calculated as:

$$\theta_{RT,\Delta t(n)} = \arctan\left(\frac{2A_{\Delta t(n)}}{-(B_{\Delta t(n)} + D_{\Delta t(n)})}\right) \tag{4.17}$$

Define the quaternion that represents the effective roll motion $\mathbf{q}_{er,\Delta t(n)}$ as well as $s_{1,\Delta t(n)}$, $s_{2,\Delta t(n)}$, $s_{3,\Delta t(n)}$ and $s_{4,\Delta t(n)}$, which are used to obtain the effective pitch $\theta_{RT\perp 1,\Delta t(n)}$ and the effective yaw $\theta_{RT\perp 2,\Delta t(n)}$ angles:

$$\mathbf{q}_{er,\Delta t(n)}\Big(\mathbf{RT},\theta_{RT,\Delta t(n)}\Big)=\left[\cos\left(\frac{\theta_{RT,\Delta t(n)}}{2}\right)\quad \mathbf{RT}\sin\left(\frac{\theta_{RT,\Delta t(n)}}{2}\right)\right] \tag{4.18}$$

$$s_{1,\Delta t(n)}=q^{\{1\}}_{tot,\Delta t(n)}q^{\{1\}}_{er,\Delta t(n)}+q^{\{2\}}_{tot,\Delta t(n)}q^{\{2\}}_{er,\Delta t(n)} \tag{4.19}$$

$$s_{2,\Delta t(n)}=q^{\{2\}}_{tot,\Delta t(n)}q^{\{1\}}_{er,\Delta t(n)}-q^{\{1\}}_{tot,\Delta t(n)}q^{\{2\}}_{er,\Delta t(n)} \tag{4.20}$$

$$s_{3,\Delta t(n)}=q^{\{3\}}_{tot,\Delta t(n)}q^{\{1\}}_{er,\Delta t(n)}-q^{\{4\}}_{tot,\Delta t(n)}q^{\{2\}}_{er,\Delta t(n)} \tag{4.21}$$

$$s_{4,\Delta t(n)}=q^{\{4\}}_{tot,\Delta t(n)}q^{\{1\}}_{er,\Delta t(n)}+q^{\{3\}}_{tot,\Delta t(n)}q^{\{2\}}_{er,\Delta t(n)} \tag{4.22}$$

Thereafter, $\theta_{RT\perp 1,\Delta t(n)}$ and $\theta_{RT\perp 2,\Delta t(n)}$ are given as:

$$\theta_{RT\perp 1,\Delta t(n)}=2\arctan\left(\frac{s_{3,\Delta t(n)}}{s_{1,\Delta t(n)}}\right) \tag{4.23}$$

$$\theta_{RT\perp 2,\Delta t(n)}=2\arctan\left(\frac{s_{4,\Delta t(n)}}{s_{1,\Delta t(n)}}\right) \tag{4.24}$$

The effective roll, effective pitch and effective yaw angles are used to obtain the Doppler generating motion, denoted by $\mathbf{q}_{eff,\Delta t(n)}$, which is later used to calculate the image-generating Doppler components. $\mathbf{q}_{eff,\Delta t(n)}$ is given by:

$$\begin{aligned}\mathbf{q}_{eff,\Delta t(n)}\Big(\mathbf{\Omega}_{eff,\Delta t(n)},\theta_{eff,\Delta t(n)}\Big)=\mathbf{q}_{ey,\Delta t(n)}\Big(\mathbf{RT}_{\perp 2},\theta_{RT\perp 2,\Delta t(n)}\Big)\otimes\cdots\\ \cdots\mathbf{q}_{ep,\Delta t(n)}\Big(\mathbf{RT}_{\perp 1},\theta_{RT\perp 1,\Delta t(n)}\Big)\end{aligned} \tag{4.25}$$

where $\mathbf{\Omega}_{eff,\Delta t(n)}$ and $\theta_{eff,\Delta t(n)}$ denote the Doppler generating axis of rotation and the effective rotation angle for $\Delta t(n)$ respectively.

Lastly, the effective angular rotation rate $\dot{\theta}_{eff,\Delta t(n)}$, the Doppler generating axis of rotation $\mathbf{\Omega}_{eff,\Delta t(n)}$ and the angle of the Doppler generating axis of rotation with respect to the W axis denoted by $\theta_{\Omega eff,\Delta t(n)}$ (see Figure 4.4) are calculated

by using the following equations:

$$\dot{\theta}_{eff,\Delta t(n)} = \frac{2\arccos\left(q^{\{1\}}_{eff,\Delta t(n)}\right)}{\Delta t(n)} \tag{4.26}$$

$$\mathbf{\Omega}_{eff,\Delta t(n)} = \frac{\left[q^{\{2\}}_{eff,\Delta t(n)} \quad q^{\{3\}}_{eff,\Delta t(n)} \quad q^{\{4\}}_{eff,\Delta t(n)}\right]}{\sin\left(\frac{\theta_{eff,\Delta t(n)}}{2}\right)} \tag{4.27}$$

$$\theta_{\Omega eff1,\Delta t(n)} = \arctan 2\left(q^{\{3\}}_{eff,\Delta t(n)}, q^{\{4\}}_{eff,\Delta t(n)}\right) \tag{4.28}$$

where $\arctan 2$ is a two-argument function that computes the arctangent with a range of $(-180°, 180°]$.

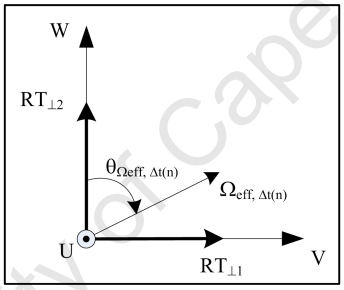

Figure 4.4: Illustration of the angle of the Doppler generating axis of rotation

4.4 Results

This section discusses the results that were obtained from applying the proposed transformation to the measured attitude and GPS position data of a yacht. The measurements were obtained during the Signal Hill 2007 trial (see Appendix A for more details). The measured rotational motion was smoothed by using a third order polynomial fit to reduce the measurement error.

The motion data was collected by using the Thales ADU5 INS/GPS sensor, which has update rates of 5 Hz and 1 Hz for attitude and GPS position data respectively. An experimental X-band radar with a stepped frequency waveform

was used to measure a yacht with the following radar parameters: a frequency step of 4 MHz, 64 pulses in an ISAR burst, and an effective BRF of 154 Hz. Radar measurements of a sphere suspended from a helicopter were used to compensate the measured HRR profiles for the radar's non-ideal response over the stepped frequency band.

A photograph of the Esperance yacht that was instrumented and its corresponding point-scatterer model, which was used for simulation purposes, are shown in Figure 4.5. In this model, scatterers were placed at key positions where substantial scattering was expected. The key positions were the metal railings at the back and front of the yacht and at the centre of the two spreaders along each mast. The (0, 0, 0) point of Figure 4.5(b) corresponds to the placement of the INS onboard the yacht.

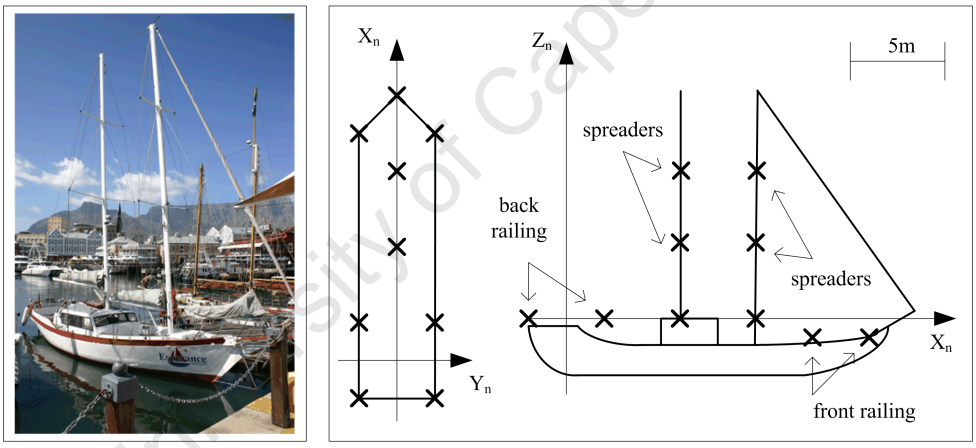

Figure 4.5: (a) Photo of the Esperance yacht and (b) the point scatterer model of the Esperance yacht

Figure 4.6 illustrates a smoothed motion dataset of 2 s. During this recording, the heading of the vessel θ_{hs} was between 2° and 4°, which confirms that the vessel was sailing inbound with respect to the radar. The proposed transformation was applied to the motion data set to extract the image-generating Doppler components (see Figure 4.7), the effective yaw $\theta_{RT\perp 2,\Delta t(n)}$ and the effective pitch $\theta_{RT\perp 1,\Delta t(n)}$ motion of the vessel (see Figure 4.8). Figure 4.7 clearly shows that both the angle of the Doppler generating axis of rotation and the effective angular

rotation rate vary over time. In addition, the effective yaw and the effective pitch motion of the vessel also varies over time.

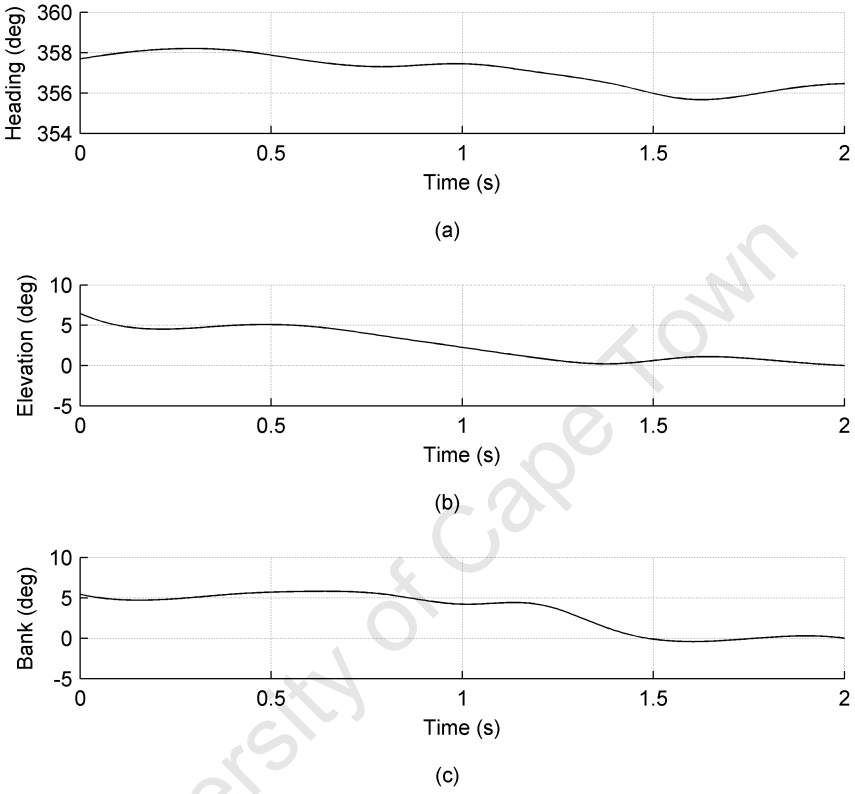

Figure 4.6: Measured motion data of the yacht, showing its heading, elevation and bank

In order to limit the blurring caused by 3-D rotational motion, the angle of the Doppler generating axis of rotation and the effective angular rotation rate need to be constant (see Section 3.5). From the data set, we observe that these conditions are mostly satisfied during the time interval 0.75 s $\leq t \leq$ 1.13 s. Moreover, during this time interval the effective yaw motion $\theta_{RT\perp 2,\Delta t(n)}$ is approximately zero and the effective pitch motion $\theta_{RT\perp 1,\Delta t(n)}$ is constant at approximately $-7°/s$. It should be noted that it is the dominant effective pitch motion that causes the Doppler generating axis of rotation to be approximately $-90°$. Since the vessel is

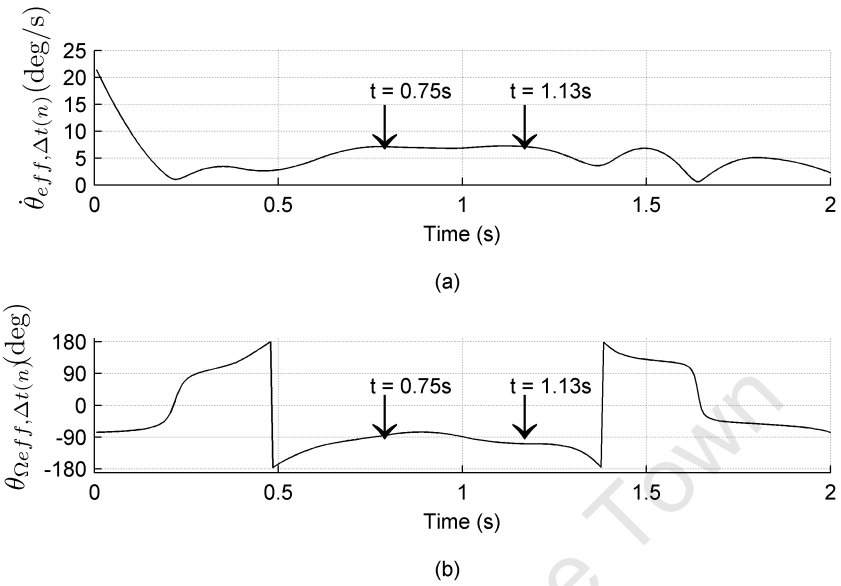

Figure 4.7: (a) Effective angular rotation rate and (b) the angle of the Doppler generating axis of rotation

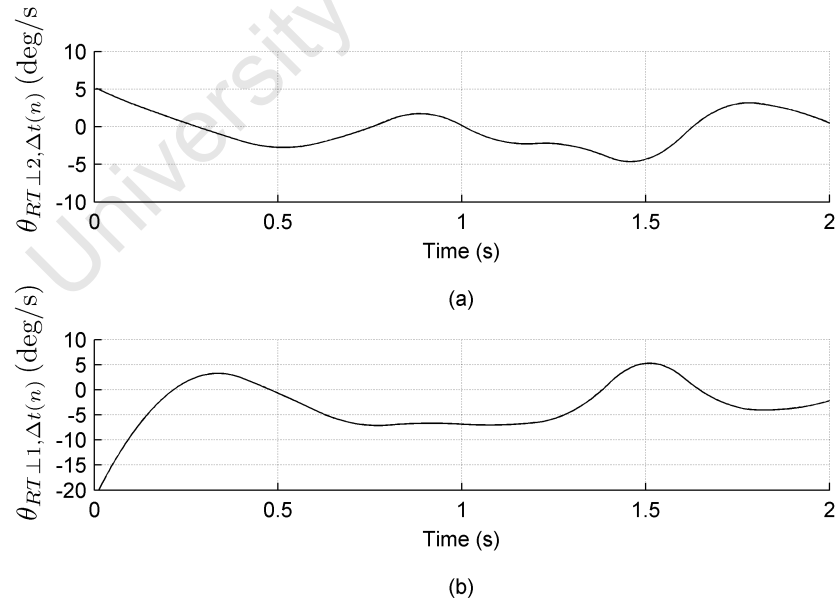

Figure 4.8: (a) The effective yaw and (b) the effective pitch motion of the vessel

sailing inbound with respect to the radar, the effective pitch motion will generate a side-view ISAR image. This is confirmed by the simulated and measured ISAR images shown in Figure 4.9(a) and 4.9(b) respectively.

The simulated ISAR image in Figure 4.9(b) was obtained by using the system model presented in Section 4.2. The signal-to-noise ratio was set to 15 dB (see Section 3.2.5 for more details), and the motion of the point-scatterer model corresponded to the measured motion of the yacht over the range of 0.75 s $\leq t \leq$ 1.13 s. In addition, the values of the simulated radar parameters were chosen to be equal to the radar parameters of the experimental X-band radar. Translation motion compensation of the measured vessel in Figure 4.9(b) was achieved by using the global range alignment algorithm in [29] and the autofocus algorithm proposed by Yuan and Casasent [30], which both assume that the vessel has pure 2-D rotational motion.

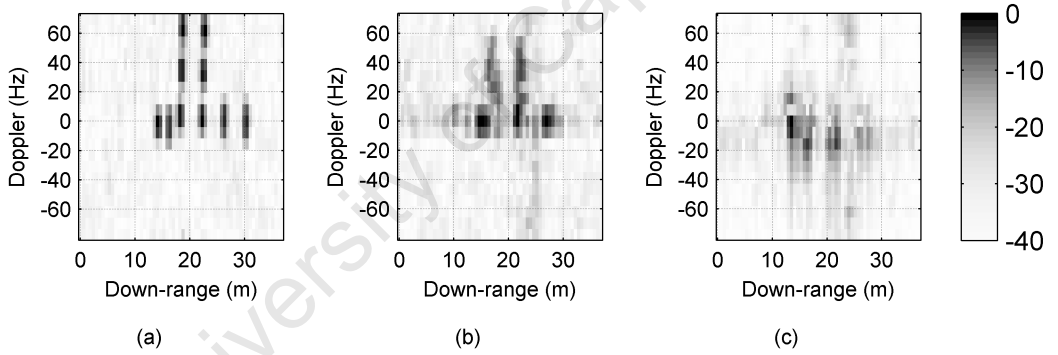

Figure 4.9: (a) Simulated ISAR image with measured motion data for CPI of 0.75 s $\leq t \leq$ 0.88 s, (b) measured ISAR image during the CPI of 0.75 s $\leq t \leq$ 0.88 s. and (c) measured ISAR image during 1.65 s $\leq t \leq$ 1.78 s.

The transformation can also be used to assess the degree of 3-D motion in a CPI for cooperative ISAR applications. This is shown by the measured ISAR images in Figure 4.9(b) and 4.9(c) for the time intervals 0.75 s $\leq t \leq$ 0.88 s and 1.65 s $\leq t \leq$ 1.78 s respectively. The ISAR image in Figure 4.9(b) shows a focused image of the yacht, in which its two masts can clearly be observed. A side-view ISAR image was produced because the angle of the Doppler-generating axis of rotation and the effective angular rotation rate are constant over the CPI.

In Figure 4.9(c), the image-generating Doppler components varied with time and this gave rise to an unfocused image since the vessel possesses 3-D motion, i.e. roll, pitch and yaw motion. In this way, suitable imaging intervals that produce focused ISAR images can be separated from poor intervals with 3-D motion that lead to unfocused images.

4.5 Conclusions

This chapter presented a new quaternion-based transformation that extracts the image-generating Doppler components, which consist of the Doppler generating axis of rotation and the effective angular rotation rate, from the measured motion data of an object. The proposed transformation is important and relevant to ISAR imaging of objects because it extracts the component of the 3-D rotational motion that contributes to Doppler or cross-range information.

The transformation was applied to the measured attitude and GPS position data of a yacht, and the results showed that both the Doppler generating axis of rotation and the effective angular rotation rate varied over time. However, there were intervals where the image-generating Doppler components did not vary significantly over time. By choosing subsets of radar data that correspond to these intervals, ISAR images with limited blurring can be obtained. This result was confirmed in simulations using a point-scatterer model of a yacht with 3-D rotational motion that corresponded to the measured motion data during the interval. In addition, the measured ISAR image over this interval also contained limited blurring. Thus, it was shown that the proposed transformation was able to assess the degree of 3-D rotational motion in a CPI for cooperative ISAR applications.

The transformation that was proposed in Chapter 4 showed that it is possible to extract the image-generating Doppler components from measured motion data of a sea vessel. Furthermore, results with measured radar data showed that, when the image-generating Doppler components vary over time, it causes blurring in ISAR imagery.

The next chapter presents a new algorithm that selects suitable CPTWLs for ISAR imaging of cooperative vessels. It makes use of the motion data of the vessel to select the length of imaging interval that limits the blurring caused by 3-D rotational motion.

Chapter 5

Selecting Suitable CPTWLs for Imaging Cooperative Sea Vessels

5.1 Introduction

Three-dimensional rotational motion of sea vessels is a major challenge for ISAR imaging of maritime vessels because it often leads to blurred images. A detailed discussion of this topic was given in Chapter 3. One way of limiting the blurring caused by 3-D rotation motion is to select carefully the duration of the CPI, which is referred to as CPTWL, so that the vessel exhibits approximately 2-D rotational motion. The CPTWL should be short enough to limit the blurring caused by 3-D rotational motion and long enough to ensure that the desired cross-range resolution is obtained.

The previous chapter presented a new transformation that extracts the image-generating Doppler components from the measured motion data of a sea vessel. Furthermore, the results showed that it was possible to limit the blurring in an ISAR image by selecting a processing interval where the image-generating Doppler components do not vary significantly over time. However, Chapter 4 does not address the selection of a suitable CPTWL that is short enough to limit the blurring in an ISAR image, and long enough to obtain the desired

cross-range resolution. This chapter proposes a new algorithm that uses the measured motion data of a vessel to select suitable CPTWLs for ISAR imaging of cooperative vessels.

Little work has been published on selecting suitable CPTWLs for ISAR imaging of vessels. In [40], it is reported that the optimum CPTWL for unfocused ISAR imagery lies between 0.025 s and 0.5 s for X-band measurements of ships. However, this work gives no information on how this suggested range of CPTWLs changes for different classes of sea vessels. In addition, the suggested range is too broad, as it spans more than an order of magnitude. An optimum imaging selection algorithm, referred to as the maximum-contrast-based automatic time Window selection (MC-ATWS) algorithm, was proposed by Martorella and Berizzi in [28] to estimate the optimum central time and the optimum CPTWL that together provide an ISAR image with the best focus. However, the MC-ATWS algorithm does not show how the initial CPTWL for a specific radar recording should be chosen, and the suitability of this technique for small ships with chaotic motion has not been investigated. Moreover, it does not take advantage of motion data from instrumented vessels that may be available during measurements trials for RCS measurement purposes.

This chapter proposes a new technique, referred to as the motion aided CPTWL selector (MACS) algorithm, which suggests suitable CPTWLs for ISAR imaging of cooperative sea vessels. The proposed algorithm uses the transformation proposed in Chapter 4 to extract the image-generating Doppler components from the measured motion data. Thereafter, the image-generating Doppler components are used to select suitable CPTWLs to obtain the desired cross-range resolution of ISAR image(s) as well as to limit the blurring caused by 3-D rotational motion.

ISAR imaging of cooperative vessels is a useful engineering problem since many Navies require their vessels to be measured, in order to minimize the effect of scattering hotspots. A good feature associated with the MACS algorithm is that the suggested range of suitable CPTWLs is much smaller than that reported in [40]. In addition, the proposed technique can be used to select an effective initial

CPTWL for the MC-ATWS algorithm, when it is applied to measured radar data of small vessels.

The system model that is considered is described in Section 5.2. Section 5.3 summarises the quaternion-based transformation that was proposed in Chapter 4. Thereafter, the cross-range resolution of an ISAR image together with the assumptions that are made in the mathematical derivation of the cross-range resolution are discussed in Section 5.4. The proposed MACS algorithm is described in Section 5.5. This algorithm was applied to the measured motion data of three different classes of vessels (a yacht, a fishing trawler and a survey vessel) and the results that were obtained are presented in Section 5.6. In addition, the effectiveness of the suggested CPTWL is demonstrated by using real radar measurements of a yacht. Lastly, conclusions are given in Section 5.7.

5.2 System Model

A rotation through an angle θ about an axis $\mathbf{h} = [h_1 \;\; h_2 \;\; h_3]$ is represented by a quaternion $\mathbf{q}_x(\mathbf{h}, \theta)$, arbitrarily labelled x, in vector form as:

$$\mathbf{q}_x(\mathbf{h}, \theta) = \left[\cos\left(\frac{\theta}{2}\right) \quad \mathbf{h}\sin\left(\frac{\theta}{2}\right)\right] \tag{5.1}$$

or in scalar form[1]:

$$\mathbf{q}_x(\mathbf{h}, \theta) = \left[q_x^{\{1\}} \quad q_x^{\{2\}} \quad q_x^{\{3\}} \quad q_x^{\{4\}}\right] \tag{5.2}$$

The system model, illustrated in Figure 5.1, considers a vessel with only rotational motion and assumes that any translation motion has been compensated for. Two coordinate axes are defined: the radar coordinate axes (U, V, W), which are fixed, and the local coordinate axes (X_n, Y_n, Z_n), which change as the vessel experiences 3-D rotational motion. In this diagram, R_0 represents the distance from the radar to the vessel's centre of rotation.

[1] It should be noted that the superscripts {1}, {2}, {3} and {4} are used to denote the respective scalar elements of the quaternion.

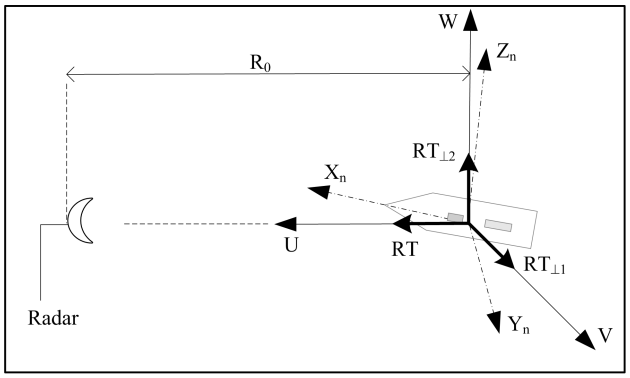

Figure 5.1: System model of the radar and the vessel showing the global and local coordinate axes

The system model assumes that the radar continuously tracks the vessel so that the vessel's centre of rotation always lies on the global U axis and the physical dimensions of the vessel are much less than R_0. The 4-D quaternion representation of the local coordinates of the k^{th} scatterer is expressed as $\mathbf{q}_{rk} = [0 \quad \mathbf{r}_k]$, where $\mathbf{r}_k = [x_k \quad y_k \quad z_k]$, and the global coordinates of the k^{th} scatterer are denoted by $\mathbf{g}_{k,t(n)} = \begin{bmatrix} u_{k,t(n)} & v_{k,t(n)} & w_{k,t(n)} \end{bmatrix}$. Thus, the global coordinates of the k^{th} scatterer at $t(n)$, which is represented by $\mathbf{q}_{gk,t(n)}$ in 4-D quaternion notation, can be expressed as:

$$\mathbf{q}_{gk,t(n)} = \left(\mathbf{q}_{tot,\Delta t(n)}\right)^* \otimes \left(\left(\mathbf{q}_{ins,t(n-1)}\right)^* \otimes \mathbf{q}_{rk} \otimes \left(\mathbf{q}_{ins,t(n-1)}\right) \right) \otimes \left(\mathbf{q}_{tot,\Delta t(n)}\right) \quad (5.3)$$

and

$$\mathbf{g}_{k,t(n)} = \begin{bmatrix} q_{gk,t(n)}^{\{2\}} & q_{gk,t(n)}^{\{3\}} & q_{gk,t(n)}^{\{4\}} \end{bmatrix} \quad (5.4)$$

where $*$ denotes the complex conjugate operation, $\otimes$ represents quaternion multiplication, $\mathbf{q}_{ins,t(n-1)}$ is the unit quaternion that represents the combined 3-D rotation of heading $\theta_{hs,t(n-1)}$, elevation $\theta_{e,t(n-1)}$ and bank $\theta_{b,t(n-1)}$ for time $t(n-1)$ and $\mathbf{q}_{tot,\Delta t(n)}$ is a unit quaternion that denotes the vessel's incremental rotational motion over $\Delta t(n)$. Stated mathematically:

$$\begin{aligned} \mathbf{q}_{ins,t(n-1)} = \mathbf{q}_{hs,t(n-1)} \left(\mathbf{RT}_{\perp 2}, \theta_{hs,t(n-1)}\right) \otimes \mathbf{q}_{e,t(n-1)} \left(\mathbf{RT}_{\perp 1}, \theta_{e,t(n-1)}\right) \otimes \cdots \\ \cdots \mathbf{q}_{b,t(n-1)} \left(\mathbf{RT}, \theta_{b,t(n-1)}\right) \end{aligned} \quad (5.5)$$

$$\mathbf{q}_{tot,\Delta t(n)} = \mathbf{q}_{y,\Delta t(n)}\left(\mathbf{z}_n, \theta_{y,\Delta t(n)}\right) \otimes \mathbf{q}_{p,\Delta t(n)}\left(\mathbf{y}_n, \theta_{p,\Delta t(n)}\right) \otimes \mathbf{q}_{r,\Delta t(n)}\left(\mathbf{x}_n, \theta_{r,\Delta t(n)}\right) \tag{5.6}$$

where the unit vectors $\mathbf{z}_n$, $\mathbf{y}_n$ and $\mathbf{x}_n$ are defined about the local coordinate axes X_n, Y_n and Z_n respectively, at time $t(n)$. The unit vectors $\mathbf{RT} = [1 \;\; 0 \;\; 0]$, $\mathbf{RT}_{\perp 1} = [0 \;\; 1 \;\; 0]$ and $\mathbf{RT}_{\perp 2} = [0 \;\; 0 \;\; 1]$ are unit vectors about the U, V, W axes respectively. The heading $\theta_{hs,t(n-1)}$, elevation $\theta_{e,t(n-1)}$ and bank $\theta_{b,t(n-1)}$ angles define the orientation of the vessel at $t(n-1)$. The yaw $\theta_{y,\Delta t(n)}$, pitch $\theta_{p,\Delta t(n)}$ and roll $\theta_{r,\Delta t(n)}$ angles represent the n^{th} incremental rotational motion about a vessel's local axes. This definition corresponds to the convention adopted by Kuipers in [127]. In this system model, the rotational sequence is assumed to be heading, elevation and then bank, since the INS measured motion data used this rotational sequence.

The heading in the system model, denoted by $\theta_{hs,t(n)}$, is defined such that it is zero when the vessel is sailing directly inbound with respect to the radar and it increases positively as the vessel rotates clockwise. As a result, the heading used in this system model can be obtained by using the heading measured from an INS $\theta_{h,t(n)}$ and the bearing $\theta_{br,t(n)}$ of the vessel, as follows:

$$\theta_{hs,t(n)} = \text{mod}\left(180^\circ + \theta_{h,t(n)} - \theta_{br,t(n)}, 360^\circ\right) \tag{5.7}$$

where $\text{mod}(a, b)$ is the modulus operation of a with b.

Since the proposed MACS algorithm makes use of the quaternion-based transformation that was proposed in Chapter 4, a summary of the transformation is given in the next section. The summary excludes detailed mathematical derivations and explanations, as these were already given in Section 4.3. As a result, the summary of the transformation concisely outlines the essential sequential processing that need to be applied to measured motion data in order to extract an object's image-generating Doppler components.

5.3 Summary of Quaternion-based Transformation

The transformation proposed in Chapter 4 extracts the image-generating Doppler components from measured motion data. The transformation consists of the following processing steps:

1. Obtain the heading $\theta_{hs,t(n)}$ used in the system model:

$$\theta_{hs,t(n)} = \text{mod}(180^\circ + \theta_{h,t(n)} - \theta_{b,t(n)}, 360^\circ) \tag{5.8}$$

where $\text{mod}(a, b)$ is the modulus operation of a with b, $\theta_{b,t(n)}$ denotes the bearing of the vessel obtained from GPS position data and $\theta_{h,t(n)}$ represents the heading measured from an INS. The heading that is used in the system model is defined such that $\theta_{hs,t(n)}$ is zero when the vessel is sailing directly inbound to the radar and that it increases positively as the vessel rotates clockwise.

2. Calculate the quaternion $\mathbf{q}_{tot,\Delta t(n)}$ that represents the vessel's incremental rotational motion over the discrete interval $\Delta t(n)$:

$$\begin{aligned}\mathbf{q}_{tot,\Delta t(n)} = \mathbf{q}_{b,t(n-1)}\Big(\mathbf{RT}, -\theta_{b,t(n-1)}\Big) \otimes \mathbf{q}_{e,t(n-1)}\Big(\mathbf{RT}_{\perp 1}, -\theta_{e,t(n-1)}\Big) \otimes \cdots \\ \cdots \mathbf{q}_{hs,t(n-1)}\Big(\mathbf{RT}_{\perp 2}, -\theta_{hs,t(n-1)}\Big) \otimes \mathbf{q}_{hs,t(n)}\Big(\mathbf{RT}_{\perp 2}, \theta_{hs,t(n)}\Big) \otimes \cdots \\ \cdots \mathbf{q}_{e,t(n)}\Big(\mathbf{RT}_{\perp 1}, \theta_{e,t(n)}\Big) \otimes \mathbf{q}_{b,t(n)}\Big(\mathbf{RT}, \theta_{b,t(n)}\Big)\end{aligned} \tag{5.9}$$

3. The quaternion $\mathbf{q}_{tot,\Delta t(n)}$ is used to obtain the effective roll angle $\theta_{RT,\Delta t(n)}$ using (5.10), (5.11), (5.12) and (5.13)

$$A_{\Delta t(n)} = q^{\{1\}}_{tot,\Delta t(n)} q^{\{2\}}_{tot,\Delta t(n)} + q^{\{3\}}_{tot,\Delta t(n)} q^{\{4\}}_{tot,\Delta t(n)} \tag{5.10}$$

$$B_{\Delta t(n)} = -\Big(q^{\{1\}}_{tot,\Delta t(n)}\Big)^2 + \Big(q^{\{3\}}_{tot,\Delta t(n)}\Big)^2 \tag{5.11}$$

$$D_{\Delta t(n)} = \left(q^{\{2\}}_{tot,\Delta t(n)}\right)^2 - \left(q^{\{4\}}_{tot,\Delta t(n)}\right)^2 \tag{5.12}$$

$$\theta_{RT,\Delta t(n)} = \arctan\left(\frac{2A_{\Delta t(n)}}{-(B_{\Delta t(n)} + D_{\Delta t(n)})}\right) \tag{5.13}$$

4. Define the quaternion that represents the effective roll motion $\mathbf{q}_{er,\Delta t(n)}$ as well as $s_{1,\Delta t(n)}$, $s_{2,\Delta t(n)}$, $s_{3,\Delta t(n)}$ and $s_{4,\Delta t(n)}$. Thereafter, these parameters are used to obtain the effective pitch $\theta_{RT\perp 1,\Delta t(n)}$ and the effective yaw $\theta_{RT\perp 2,\Delta t(n)}$ angles:

$$\mathbf{q}_{er,\Delta t(n)}\left(\mathbf{RT}, \theta_{RT,\Delta t(n)}\right) = \left[\cos\left(\frac{\theta_{RT,\Delta t(n)}}{2}\right) \quad \mathbf{RT}\sin\left(\frac{\theta_{RT,\Delta t(n)}}{2}\right)\right] \tag{5.14}$$

$$s_{1,\Delta t(n)} = q^{\{1\}}_{tot,\Delta t(n)} q^{\{1\}}_{er,\Delta t(n)} + q^{\{2\}}_{tot,\Delta t(n)} q^{\{2\}}_{er,\Delta t(n)} \tag{5.15}$$

$$s_{2,\Delta t(n)} = q^{\{2\}}_{tot,\Delta t(n)} q^{\{1\}}_{er,\Delta t(n)} - q^{\{1\}}_{tot,\Delta t(n)} q^{\{2\}}_{er,\Delta t(n)} \tag{5.16}$$

$$s_{3,\Delta t(n)} = q^{\{3\}}_{tot,\Delta t(n)} q^{\{1\}}_{er,\Delta t(n)} - q^{\{4\}}_{tot,\Delta t(n)} q^{\{2\}}_{er,\Delta t(n)} \tag{5.17}$$

$$s_{4,\Delta t(n)} = q^{\{4\}}_{tot,\Delta t(n)} q^{\{1\}}_{er,\Delta t(n)} + q^{\{3\}}_{tot,\Delta t(n)} q^{\{2\}}_{er,\Delta t(n)} \tag{5.18}$$

Calculate $\theta_{RT\perp 1,\Delta t(n)}$ and $\theta_{RT\perp 2,\Delta t(n)}$ angles as follows:

$$\theta_{RT\perp 1,\Delta t(n)} = 2\arctan\left(\frac{s_{3,\Delta t(n)}}{s_{1,\Delta t(n)}}\right) \tag{5.19}$$

$$\theta_{RT\perp 2,\Delta t(n)} = 2\arctan\left(\frac{s_{4,\Delta t(n)}}{s_{1,\Delta t(n)}}\right) \tag{5.20}$$

5. Obtain the Doppler generating motion represented by $\mathbf{q}_{eff,\Delta t(n)}$ using the effective pitch and yaw rotations:

$$\mathbf{q}_{eff,\Delta t(n)}\left(\mathbf{\Omega}_{eff,\Delta t(n)}, \theta_{eff,\Delta t(n)}\right) = \mathbf{q}_{ey,\Delta t(n)}\left(\mathbf{RT}_{\perp 2}, \theta_{RT\perp 2,\Delta t(n)}\right) \otimes \cdots \cdots \mathbf{q}_{ep,\Delta t(n)}\left(\mathbf{RT}_{\perp 1}, \theta_{RT\perp 1,\Delta t(n)}\right) \tag{5.21}$$

where $\mathbf{\Omega}_{eff,\Delta t(n)}$ and $\theta_{eff,\Delta t(n)}$ denotes the Doppler generating axis of rotation and the effective rotation angle respectively.

6. Lastly, the effective angular rotation rate $\dot{\theta}_{eff,\Delta t(n)}$, the Doppler generating axis of rotation $\mathbf{\Omega}_{eff,\Delta t(n)}$ and the angle of the Doppler generating axis of rotation with respect to the V axis denoted by $\theta_{\Omega eff1,\Delta t(n)}$ can be obtained using the following equations:

$$\dot{\theta}_{eff,\Delta t(n)} = \frac{2\arccos\left(q^{\{1\}}_{eff,\Delta t(n)}\right)}{\Delta t(n)} \tag{5.22}$$

$$\mathbf{\Omega}_{eff,\Delta t(n)} = \frac{\left[q^{\{2\}}_{eff,\Delta t(n)} \quad q^{\{3\}}_{eff,\Delta t(n)} \quad q^{\{4\}}_{eff,\Delta t(n)}\right]}{\sin\left(\frac{\theta_{eff,\Delta t(n)}}{2}\right)} \tag{5.23}$$

$$\theta_{\Omega eff1,\Delta t(n)} = \arctan 2\left(q^{\{4\}}_{eff,\Delta t(n)}, q^{\{3\}}_{eff,\Delta t(n)}\right) \tag{5.24}$$

where $\arctan 2$ is a two-argument function that computes the arctangent with a range of $(-180°, 180°]$.

The proposed MACS algorithm makes use of the transform described in this section to extract the angle of the Doppler generating axis of rotation $\theta_{\Omega eff1,\Delta t(n)}$ and the effective angular rotation rate $\dot{\theta}_{eff,\Delta t(n)}$ from the measured motion data. It also considers the cross-range resolution error and the blurring that is induced by the time-varying nature of the image-generating Doppler components. The next section discusses this in more detail.

5.4 Cross-range Resolution

Cross-range resolution refers to the spatial length of each cross-range cell of an ISAR image after it has been transformed from Doppler to distance. The cross-range dimension of an ISAR image fundamentally represents Doppler frequency, and it can be transformed to distance under certain conditions as explained in

[40]. This section presents the derivation of the cross-range resolution, in order to highlight the assumptions that are made about the motion of an object.

Figure 5.2 considers an object that has two scatterers of length l_1 and l_2 along the $\mathbf{RT}_{\perp 2}$ axis. In this diagram, the Doppler generating axis of rotation $\mathbf{\Omega}_{eff}$ is along the $\mathbf{RT}_{\perp 1}$ axis and the effective rotation rate is given by $\dot{\theta}_{eff,\Delta t(n)}$. The rotational motion of the object causes the two scatterers to have a non-zero radial velocity with respect to the radar given by v_1 and v_2.

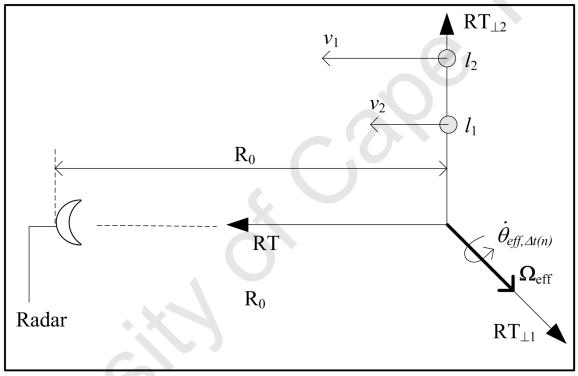

Figure 5.2: Diagram used to derive the mathematical expression of the cross-range resolution of an ISAR image

Assume that the radar illuminates the two scatterers for a CPI with a CPTWL of $\Delta\tau = \sum_{n=1}^{N-1} \Delta t(n)$, where $N-1$ is the number of discrete rotations over the CPI. At the cross-range resolution limit, given by $\Delta r_c = (l_2 - l_1)$, the radial velocities of the scatterers are such that their difference in Doppler is equal to the Doppler resolution. Stated mathematically:

$$\frac{2v_2}{\lambda} - \frac{2v_1}{\lambda} = \frac{1}{\Delta\tau} \tag{5.25}$$

Rearranging (5.25) to solve for the cross-range resolution gives:

$$\begin{aligned} \frac{2l_2\dot{\theta}_{eff,\Delta t(n)}}{\lambda} - \frac{2l_1\dot{\theta}_{eff,\Delta t(n)}}{\lambda} &= \frac{1}{\Delta\tau} \\ \frac{2\dot{\theta}_{eff,\Delta t(n)}}{\lambda}(l_1 - l_2) &= \frac{1}{\Delta\tau} \\ \Rightarrow \quad \Delta r_c &= \frac{\lambda}{2\Delta\theta_{eff}} \end{aligned} \tag{5.26}$$

where $\Delta\theta_{eff} = \sum_{n=1}^{N-1} \dot{\theta}_{eff,\Delta t(n)}\Delta t(n)$ and λ is the wavelength of the transmitted signal. The following assumptions are made about the motion of the object in the mathematical derivation of the cross-range resolution:

- **Assumption 1:** The Doppler generating axis of rotation does not change with time and it is aligned to the $\mathbf{RT}_{\perp 1}$ axis throughout the CPI
- **Assumption 2:** The effective rotation rate $\dot{\theta}_{eff,\Delta t(n)}$ is constant over the CPI

Chapter 4 analysed the motion data of a yacht, and it was observed that the image-generating Doppler components of measured motion data varies over time (see Figure 4.7 in Section 4.4). Thus, the motion of real vessels fails to satisfy the assumptions that are made in the derivation of the cross-range resolution. As a result, it is inaccurate to apply (5.26) to transform the cross-range dimension from Doppler to distance. For objects with 3-D rotational motion, it is necessary to relax the assumptions that are made in the derivation of the cross-range resolution. The errors that are made by relaxing these assumptions need to be understood and suitable CPTWLs should be chosen to minimize these errors.

5.4.1 Relaxing assumption 1

Consider the case where the Doppler generating axis of rotation $\mathbf{\Omega}_{eff}$ is not aligned to the $\mathbf{RT}_{\perp 1}$ axis as shown in Figure 5.3. Scatterer 1 and scatterer 2 are located at lengths l_1 and l_2 along the $\mathbf{RT}_{\perp 2}$ axis respectively. Since $\mathbf{\Omega}_{eff}$

is offset from the $\mathbf{RT}_{\perp 1}$ axis by an angle of $\theta_{\Omega eff1}$, the two scatterers appear along the cross-range axis at distances of $l_1 \cos(\theta_{\Omega eff1})$ and $l_2 \cos(\theta_{\Omega eff1})$. The cross-range resolution that is required to separate scatterer 1 and scatterer 2 into two different cross-range cells for a CPTWL of $\Delta\tau$ is given by:

$$\frac{2l_2\dot{\theta}_{eff,\Delta t(n)}\cos(\theta_{\Omega eff1})}{\lambda} - \frac{2l_1\dot{\theta}_{eff,\Delta t(n)}\cos(\theta_{\Omega eff1})}{\lambda} = \frac{1}{\Delta\tau}$$

$$\Rightarrow \quad \Delta r_{c1} = \frac{\lambda}{2\Delta\theta_{eff}\cos(\theta_{\Omega eff1})} \tag{5.27}$$

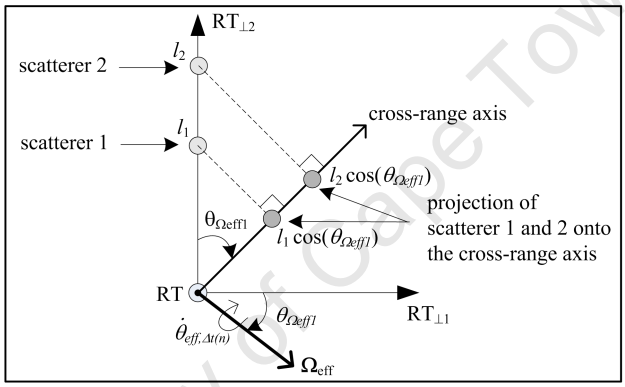

Figure 5.3: Diagram illustrating the error e_Ω when $\theta_{\Omega eff1}$ is not aligned to $\mathbf{RT}_{\perp 1}$ for side-view ISAR imaging

The cross-range resolution error e_Ω that is made by assuming that $\mathbf{\Omega}_{eff}$ was aligned to the $\mathbf{RT}_{\perp 1}$ axis is given by:

$$e_\Omega = \frac{\Delta r_{c1} - \Delta r_c}{\Delta r_{c1}}$$

$$e_\Omega = \frac{\Delta r_{c1} - \Delta r_{c1}\left|\cos\left(\theta_{\Omega eff1}\right)\right|}{\Delta r_{c1}}$$

$$e_\Omega = 1 - \left|\cos\left(\theta_{\Omega eff1}\right)\right| \tag{5.28}$$

For objects that possess 3-D rotational motion, the angle of the Doppler generating axis of rotation changes over the CPI. In cases where the angle of the Doppler generating axis of rotation does not change significantly over the CPI,

an upper bound for the maximum cross-range resolution error e_Ω that is made can be expressed as:

$$e_\Omega = \max_{n\in\{1,N-1\}} \left(1 - \left|\cos\left(\theta_{\Omega eff1,\Delta t(n)}\right)\right|\right) \tag{5.29}$$

5.4.2 Relaxing assumption 2

The formula of the cross-range resolution in (5.26) assumes that the angular rotation rate of the object $\dot{\theta}_{eff,\Delta t(n)}$ is constant over the CPI. In this case, the cross-range resolution Δr_c may be written in terms of the change in the object's aspect angle over the CPI, denoted by $\Delta\theta_{eff}$. When $\dot{\theta}_{eff,\Delta t(n)}$ varies over the CPI, it causes the Doppler frequency of a scatterer to migrate through the Doppler cells in the ISAR image. For example, consider the system model shown in Figure 5.2, which has a time-varying effective angular rotation rate. The scatterer located at length l_1 experiences d_b Doppler cells of migration, given by:

$$d_{b,1} = \max_{n\in\{1,N-1\}} \left(\frac{2l_1\dot{\theta}_{eff,\Delta t(n)}}{\lambda}\right)\Delta\tau \quad - \min_{n\in\{1,N-1\}} \left(\frac{2l_1\dot{\theta}_{eff,\Delta t(n)}}{\lambda}\right)\Delta\tau \tag{5.30}$$

If d_b Doppler cells of migration are allowed in the ISAR image, (5.30) can be rearranged to express the allowable change in the effective angular rotation rate, denoted by $\Delta\dot{\theta}_{eff}$, over the CPI:

$$\underbrace{\left(\max_{n\in\{1,N-1\}} \left(\dot{\theta}_{eff,\Delta t(n)}\right) \quad - \min_{n\in\{1,N-1\}} \left(\dot{\theta}_{eff,\Delta t(n)}\right)\right)}_{\Delta\dot{\theta}_{eff}} = \frac{\lambda d_b}{2l_{cr}\Delta\tau} \tag{5.31}$$

where l_{cr} is the cross-range extent of the object. It can be observed from (5.31) that $\Delta\dot{\theta}_{eff}$ is inversely proportional to the cross-range extent of the object l_{cr}. Thus, for the same λ and $\Delta\tau$, if l_{cr} increases, the variation in the effective angular rotation rate $\Delta\dot{\theta}_{eff}$ needs to decrease by the same factor in order for d_b to remain the same. This has an impact on ISAR imaging of sea vessels, since the scatterer that experiences the most migration is located at the maximum cross-

range extent of the vessel. This corresponds to the height of the tallest mast for the side-view ISAR imaging case. Therefore, the variation of the effective angular rotation rate needs to be smaller for vessels with longer masts for the same allowable Doppler cells of migration.

5.5 The Motion-aided CPTWL Selection Algorithm

The first step of the proposed MACS algorithm involves the extraction of the image-generating Doppler components from measured motion data (see Section 5.3). Thereafter, the MACS algorithm uses the image-generating Doppler components to select suitable CPTWLs for the ISAR imaging process. In this chapter, a suitable CPTWL is defined as a processing length that may be applied to a specific radar recording in order to obtain motion compensated ISAR image(s) with limited blurring due to 3-D motion. In addition, the ISAR image(s) should have the desired cross-range resolution with an acceptable error e_Ω as explained in Section 5.4.

The MACS algorithm is made up of the following processing steps:

1. Specify appropriate values for the allowable cross-range resolution error, denoted by e_Ω, and the allowable number of Doppler cells of migration, expressed as d_b, and a set of initial CPTWLs, where a single initial CPTWL value is denoted by $\Delta\tau^{(in)}$. Thereafter, specify an overlap factor between two successive CPIs, denoted by γ, and the desired cross-range resolution Δr_{cd}. Begin the algorithm with the initial value of the CPTWL range.

2. Apply the quaternion-based transformation described in Section 5.3 to a vessel's measured motion data in order to extract its image-generating Doppler components.

3. For each CPI, using (5.29), calculate the cross-range resolution error e_Ω that is made due to the time-varying Doppler generating axis of rotation.

In addition, using (5.30), calculate the maximum Doppler cells of migration d_b caused by non-uniform rotation where l_1 corresponds to the maximum cross-range extent. In the side-view ISAR imaging case, if k represents a scatterer at the top of the tallest mast and $t(n)$ is the average absolute time of the CPI, then l_1 is equal to the global coordinates of the k^{th} scatterer given by $w_{k,t(n)}$.

4. If e_Ω and d_b are less than the values allowed in Step 1, then a suitable CPI has been found. Calculate the cross-range resolution using (5.26) and, if it is better than the desired cross-range resolution, then a suitable CPTWL has been found.

5. Choose the next value in the initial CPTWL range and, if the maximum value has not been reached, go back to Step 2. Otherwise, the algorithm is terminated.

The range of initial CPTWLs that is chosen in Step 1 is dependent on the vessel of interest, and the next section provides guidelines for three different classes of vessels. If the chosen initial CPTWL range is not appropriate for a specific recording, it should be changed by the user until a satisfactory result is obtained.

5.6 Results

This section presents the results from applying the proposed MACS algorithm to measured motion data of three different classes of sea vessels: a yacht, a fishing trawler and a survey vessel with a weight of 25 tons, 450 tons and 2750 tons, a length of approximately 20 m, 60 m and 80 m and a maximum mast height of approximately 15 m, 20 m and 25 m respectively. Suitable CPTWLs are suggested for each type of vessel. The effectiveness of the suggested CPTWLs is demonstrated using measured radar data. Lastly, the significance of using the suggested CPTWL to select an effective initial CPTWL for the MC-ATWS algorithm is discussed.

The measured data that is used in this chapter was obtained from the Signal Hill 2007 trial (see Appendix A for more details). All three vessels were instrumented with the Thales ADU5 4-GPS antenna system, which measured each vessel's absolute GPS position, heading, elevation and bank. The measured rotational motion was smoothed using a third order polynomial fit to reduce the measurement error. An experimental X-band radar with a stepped frequency capability was used to obtain radar measurements of the vessels for ISAR imaging purposes. Radar measurements of a sphere suspended from a helicopter were used to compensate for the measured HRR profiles for the radar's non-ideal response over the stepped frequency band.

5.6.1 Selection of suitable CPTWLs

The proposed MACs algorithm was applied to the measured motion data of three vessels from different classes. The smoothed rotational motion of the three vessels is illustrated in Figure 5.4. Each recording is three minutes in duration. The heading measurements and the sailing profile indicate that the yacht and the fishing trawler are inbound, whereas the survey vessel is sailing outbound with respect to the radar. In all three cases, the pitch motion of the vessels is used to obtain a side-view ISAR image. The measurements show that the vessels also possessed roll and pitch motion as indicated by their bank and elevation angles respectively, and this causes each vessel's image-generating Doppler components to change with time. In addition, the period of the bank and elevation motion is observed to be longer for heavier vessels. Thus, for larger vessels the 3-D rotational motion is less chaotic; it is hypothesized that longer CPTWLs may be accommodated for larger vessels than for smaller vessels.

The proposed MACS algorithm was applied to the measured motion datasets shown in Figure 5.4, using the parameter values given in Table 5.1. Figure 5.5 and Figure 5.6 show the effect of the CPTWL on the percentage of CPIs for varying e_Ω and d_b respectively. The percentage of CPIs is given by the percentage of the number of suitable CPIs that are found over the total number of CPIs for

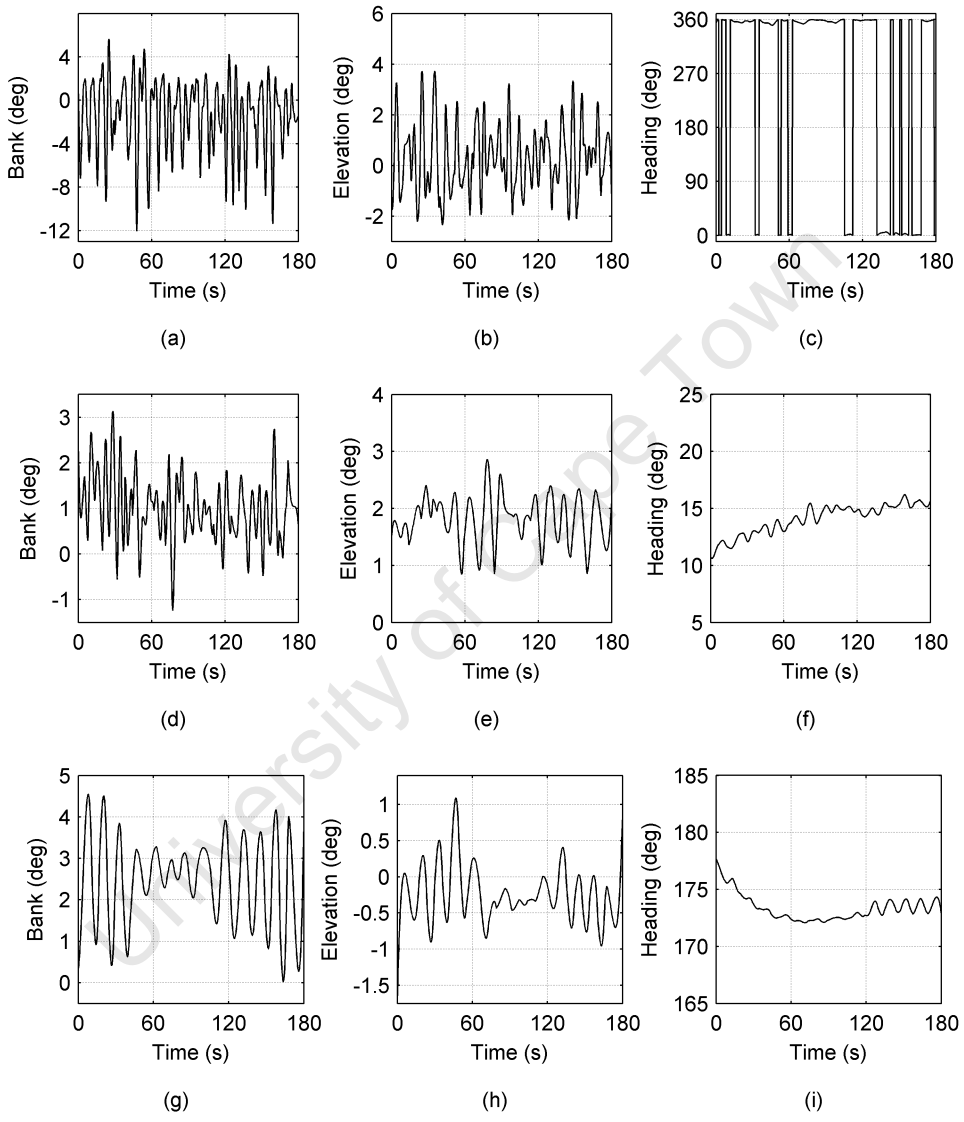

Figure 5.4: Measured 3-D rotational motion of (a)-(c) the yacht, (d)-(f) the fishing trawler and (g)-(i) the survey vessel

a specific initial CPTWL. It is mathematically expressed as:

$$\text{Percentage of CPIs} = \frac{\text{Number of suitable CPIs found}}{\text{Total number of CPIs}} \tag{5.32}$$

Table 5.1: Values of the parameters used in the MACS algorithm

Parameter description	Symbol	Value
Allowable cross-range resolution error	e_Ω	$\{1\%,\ 5\%,\ 10\%\}$
Allowable Doppler cells of migration	d_b	$\{2, 3, 4\}$
Initial CPTWLs for the yacht dataset	$\Delta\tau^{(in)}$	$\{0.10\text{ s},\ 0.25\text{ s},\ \cdots,\ 1.15\text{ s}\}$
Initial CPTWLs for the fishing trawler dataset	$\Delta\tau^{(in)}$	$\{0.2\text{ s},\ 0.4\text{ s},\ \cdots,\ 2.4\text{ s}\}$
Initial CPTWLs for the survey vessel dataset	$\Delta\tau^{(in)}$	$\{0.2\text{ s},\ 0.4\text{ s},\ \cdots,\ 2.8\text{ s}\}$
Overlap factor	γ	0.75
Desired Δr_c for the yacht	Δr_{cd}	0.75 m
Desired Δr_c for the fishing trawler	Δr_{cd}	1 m
Desired Δr_c for the survey vessel	Δr_{cd}	1.5 m

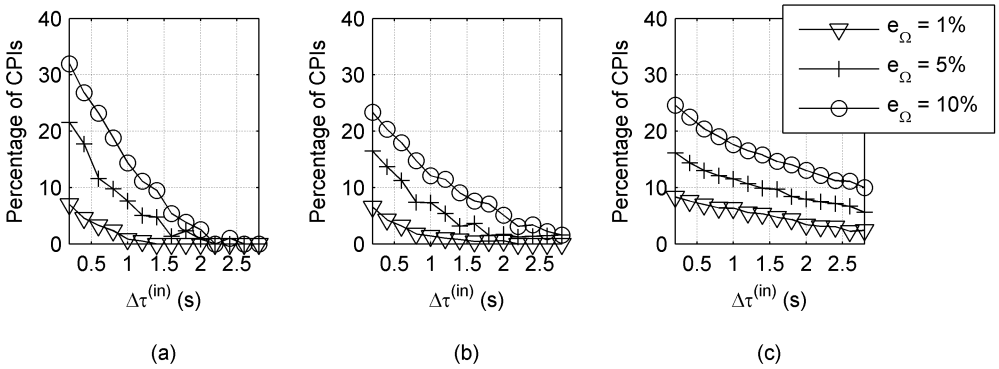

Figure 5.5: Diagram showing the effect of the initial CPTWL $\Delta\tau^{(in)}$ on the percentage of CPIs for various allowable errors e_Ω for (a) the yacht, (b) the fishing trawler and (c) the survey vessel

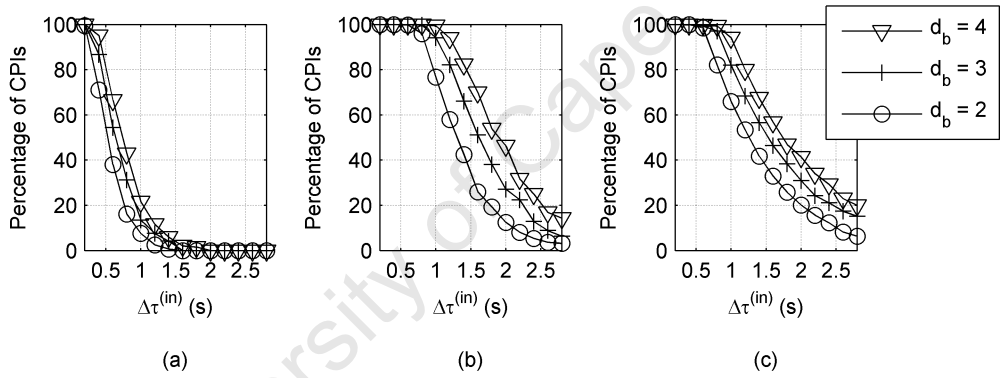

Figure 5.6: Diagram showing the effect of the initial CPTWL $\Delta\tau^{(in)}$ on the percentage of CPIs for various allowable Doppler cells of migration d_b for (a) the yacht, (b) the fishing trawler and (c) the survey vessel

Figure 5.5 shows that, as the allowable error e_Ω increases, the percentage of CPIs also increases. This result is expected because, for larger values of e_Ω, the angle of the Doppler generating axis of rotation is allowed to vary by a larger range over the CPI in order for it to be selected as a suitable CPI as indicated by (5.29). Thus, for larger e_Ω more suitable CPIs are found and this causes the percentage of CPIs to increase. Figure 5.5 also shows that, as the initial CPTWL increases, the percentage of CPIs decreases. This outcome is also expected since, for a longer initial CPTWL, there are more CPIs that possess significant 3-D rotational motion and fewer CPIs that satisfy the allowable error e_Ω caused by changes in the Doppler generating axis of rotation over the CPI. Similar trends can be observed in Figure 5.6, which illustrates the effects of different allowable Doppler cells of migration d_b and the range of initial CPTWLs on the percentage of CPIs.

Figure 5.7 shows histograms of the number of suitable CPIs that were found for an allowable error of $e_\Omega = 10\%$ and $d_b = 2$ for each vessel. The histogram shows the cross-range resolution of the suitable CPIs for different initial CPTWLs. For example: if the initial CPTWL is chosen to be 1 s for the fishing trawler dataset, then Figure 5.7(b) shows that there are 7 suitable CPIs that have a cross-range resolution of less than or equal to 2 m. These histograms show that, for large vessels such as the survey vessel, it is not practical to obtain focused ISAR images with a cross-range resolution of less than 1.5 m for the dataset under consideration. On the other hand, for small vessels such as the yacht, the fast pitch motion can be used to obtain focused ISAR images with a cross-range resolution of 0.75 m. These results apply to X-band measurements. One way of improving the cross-range resolution of ISAR images, without changing the motion of a vessel, is to increase the carrier frequency of the radar waveform.

The cumulative distribution shown in Figure 5.7 are used to select suitable CPTWLs that are able to produce motion compensated ISAR images with the desired cross-range resolution Δr_{cd} given in Table 5.1. The achievable cross-range resolution shown in the cumulative distribution suggests that suitable CPTWLs for the yacht, the fishing trawler and the survey vessel are $\{0.55\text{ s},\ 0.85\text{ s}\}$, $\{1.6\text{ s},\ 1.8\text{ s}\}$ and $\{1.2\text{ s},\ 2\text{ s}\}$ respectively. Note that this result confirms the hy-

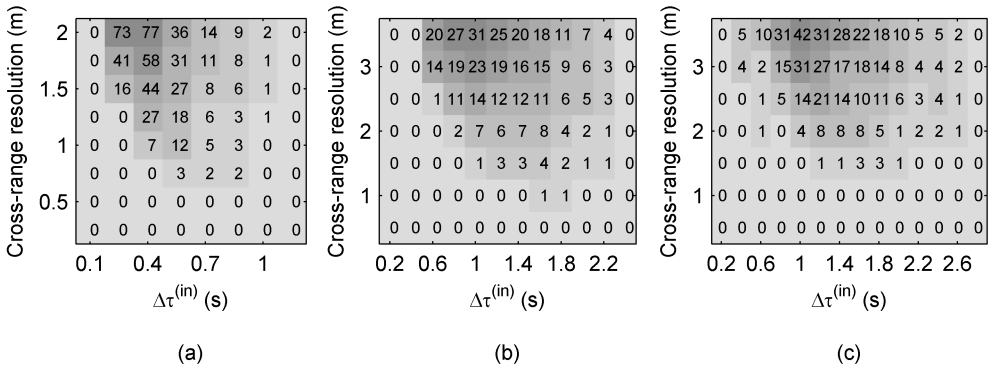

Figure 5.7: Diagram showing the histogram of the number of suitable CPIs and their respective cross-range resolution as a function of the initial CPTWL $\Delta\tau^{(in)}$ for (a) the yacht, (b) the fishing trawler and (c) the survey vessel

pothesis that longer CPTWLs may be accommodated for larger vessels in order to obtain motion compensated ISAR images with the desired medium cross-range resolution.

The effectiveness of the suggested CPTWL for the yacht was demonstrated using radar data that was measured during the same time period as the motion dataset. The radar recording was obtained with an experimental X-band radar that transmitted a stepped frequency waveform with the following radar parameters: a frequency step of 4 MHz, 64 pulses in an ISAR burst and a burst repetition frequency of 154 Hz. A photo of the instrumented yacht is shown in Figure 5.8. The motion data and the radar data were both time-stamped using a GPS receiver, which made it possible to extract useful radar data corresponding to the absolute time period of a suitable CPI for ISAR imaging purposes.

Figure 5.9 shows motion compensated ISAR images of the yacht for three different CPTWLs. Translation motion compensation was achieved by using the global range alignment algorithm [29] and the autofocus algorithm proposed by Yuan and Casasent [30]. Figure 5.9(a) shows the ISAR image of the yacht for a CPTWL of 0.2 s. The spreaders along the masts of the yacht can be observed; however, the image has a few undesirable characteristics: the cross-range resolution is poor because the change in aspect angle (or pitch motion) over the CPI is too small, the structure of the yacht's two masts is indiscernible and the front of

Figure 5.8: Photo of the Esperance yacht

the yacht is not clearly apparent. In this case, the CPTWL is too short. These limitations are overcome when the CPTWL is increased to 0.8 s, as shown by the ISAR image in 5.9(b). It should be noted that the CPTWL of 0.8 s corresponds to that suggested by the proposed MACS algorithm for the yacht dataset. Lastly, when the CPTWL is increased further to 1.6 s, it leads to a blurred ISAR image, as shown by Figure 5.9(c). In this case, the CPTWL is too long and blurring is caused by the yacht's 3-D rotational motion over the CPI.

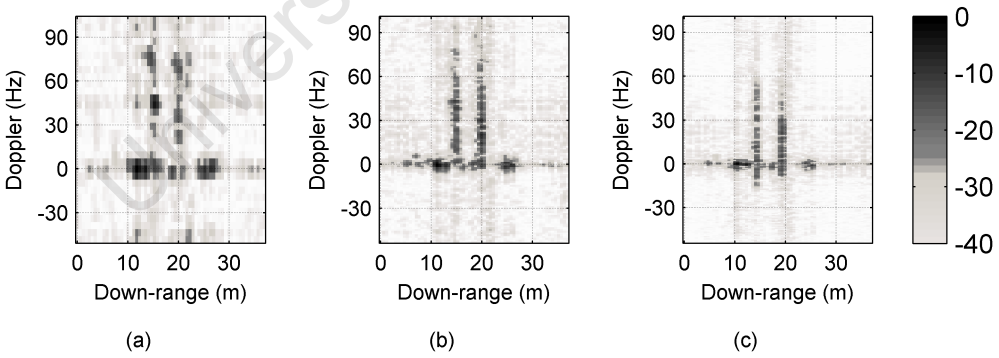

Figure 5.9: Motion compensated ISAR images of the yacht obtained using measured radar data for a CPTWL of (a) $\Delta\tau = 0.2$ s, (b) $\Delta\tau = 0.8$ s and (c) $\Delta\tau = 1.6$ s

As described previously, the absolute time of the suitable CPIs with the desired cross-range resolution may be used to extract useful subsets of radar data

for ISAR imaging purposes. This can be achieved when the motion data and the radar data are time-stamped by using the same time clock. This feature would provide significant computational savings for RCS measurement applications where long radar recordings are made and only a few high quality ISAR images are required. Lastly, the range of CPTWLs that is suggested by the MACS algorithm can be used to select an effective initial CPTWL for optimum imaging selection algorithms that operate on measured radar data. The value of using the suggested CPTWLs to choose an effective initial CPTWL value for the MC-ATWS algorithm is demonstrated in the next section.

5.6.2 Effectiveness of the suggested CPTWLs for the MC-ATWS algorithm

The MACS algorithm uses measured motion data to suggest a range of CPTWLs that is suitable for ISAR imaging. A range of suitable CPTWLs is suggested after assessing a range of initial CPTWLs. An improved or optimum CPTWL can be obtained by applying the MC-ATWS algorithm to the measured radar data. The MC-ATWS algorithm uses the contrast of the measured ISAR images to select the optimum imaging parameters for a particular radar recording. The MC-ATWS algorithm was applied to the measured radar recording with a sliding window of 8 HRR profiles, an initial window length increase, denoted as "2n" in [28] and 2p in Chapter 6, of 12 HRR profiles, and three different initial CPTWLs, denoted by $\Delta\tau^{(in)}$. The results obtained are shown in Figure 5.10 and Table 5.2.

Table 5.2: Summary of results obtained from applying the MC-ATWS algorithm to a subset of measured radar data

Initial CPTWL $\Delta\tau^{(in)}$	Optimum CPTWL $\Delta\tau_{opt}$	Optimum central instant τ_{opt}
0.2 s	0.34 s	-0.64 s
0.8 s	0.86 s	-0.34 s
1.6 s	1.64 s	-0.15 s

Figure 5.10 shows that the image contrast (IC) of ISAR images of small vessels are dependent on the initial CPTWL $\Delta\tau^{(in)}$. Furthermore, results in Table 5.2

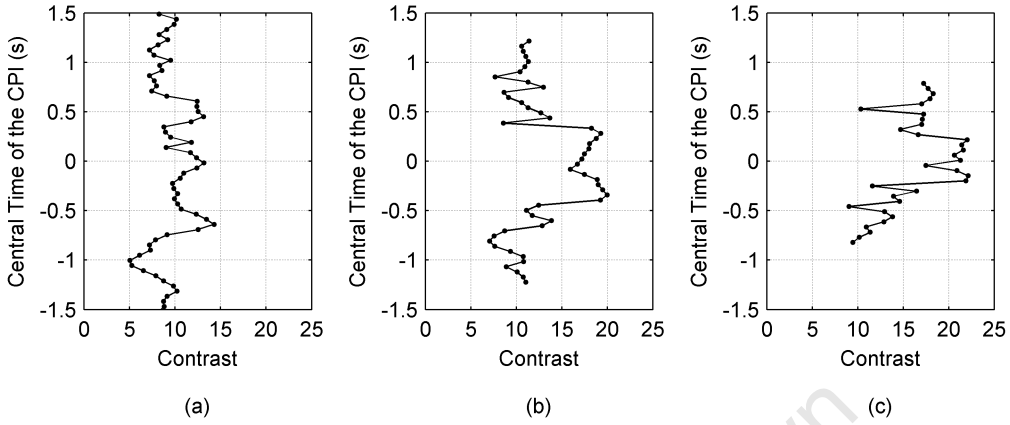

Figure 5.10: Image contrast plots for an initial CPTWL of (a) $\Delta\tau^{(in)} = 0.2$ s, (b) $\Delta\tau^{(in)} = 0.8$ s, and (c) $\Delta\tau^{(in)} = 1.6$ s

clearly shows that the optimum central instant τ_{opt} and the optimum CPTWL $\Delta\tau_{opt}$ are dependent on the intial CPTWL, for small vessels. It should be noted that the authors of [28] clearly mention that their proposed algorithm has not been tested on small ships, as this represented future work.

The optimum imaging parameters shown in Table 5.2 were applied to the radar recording and the ISAR images that were obtained are illustrated in Figure 5.11. The ISAR images shown in Figure 5.11 are very similar to the images illustrated in Figure 5.9. Thus, the comments that were made about Figure 5.9 apply to Figure 5.11 as well. It should be noted that it is only Figure 5.11 (b) that shows an image of the yacht with two equally long masts. Moreover, the optimum CPTWL of 0.86 s was obtained by using a good quality initial CPTWL value of $\Delta\tau^{(in)} = 0.8$ s, which was selected from the range of CPTWLs suggested by the MACS algorithm. This demonstrates the value of the MACS algorithm in providing a good quality initial CPTWL for the MC-ATWS algorithm when it is applied to radar measurements of small vessels.

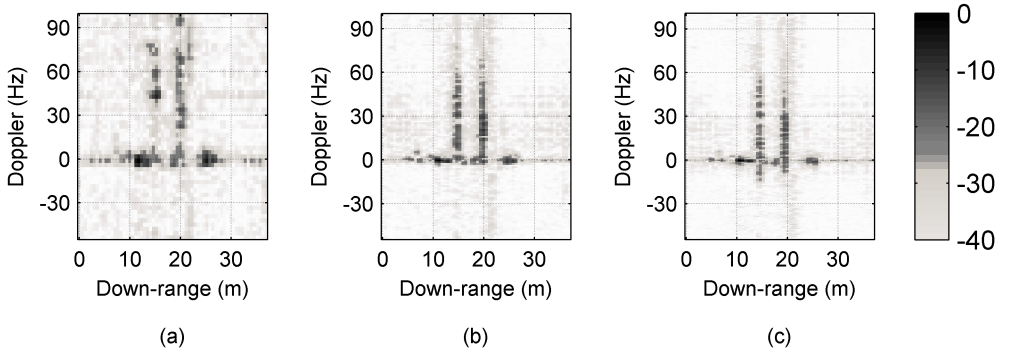

Figure 5.11: ISAR images obtained with the optimum imaging parameters of (a) $\Delta\tau_{opt} = 0.34$ s and $\tau_{opt} = 1$s, (b) $\Delta\tau_{opt} = 0.86$ s and $\tau_{opt} = 1.3$ s, and (c) $\Delta\tau_{opt} = 1.6$ s and $\tau_{opt} = 1.5$ s

5.7 Conclusions

This chapter presented a new technique, referred to as the MACS algorithm, which selects suitable CPTWLs for ISAR imaging of cooperative sea vessels. The proposed algorithm uses measured motion data of an instrumented vessel to extract the image-generating Doppler components, which consist of the Doppler generating axis of rotation and the effective angular rotation rate. Thereafter, the MACS algorithm uses the image-generating Doppler components to suggest suitable CPTWLs that may be used to obtain motion compensated ISAR images with limited blurring due to 3-D rotational motion. Furthermore, the suggested CPTWLs minimise the error in the predicted cross-range resolution due to changes in the Doppler generating axis of rotation over the CPI.

The MACS algorithm was applied to motion datasets of three different classes of sea vessels: a yacht, a fishing trawler and a survey vessel. The suggested CPTWLs indicate that a longer CPTWL is needed for larger vessels. Experimental results obtained using the measured radar data of a yacht show the effectiveness of the proposed algorithm.

The MACS algorithm showed that measured motion data of sea vessels can be used to select suitable CPTWLs that would limit blurring in ISAR imagery of

cooperative vessels. Moreover, it ensures that the CPTWLs are long enough to obtain ISAR images with the desired cross-range resolution.

The suggested CPTWL may be used to select an effective initial CPTWL for the MC-ATWS algorithm when it is applied to measured radar data of small vessels. Another good feature associated with the MACS algorithm is that, when the radar and motion data are time-stamped using the same time clock, the proposed MACS algorithm is able to identify subsets of radar data that are useful for cooperative ISAR imaging purposes. In this way significant computational savings may be achieved for RCS measurement applications, where long radar recordings are made and only a few high-quality ISAR images are required.

The next chapter presents a new technique that selects optimum imaging intervals for ISAR imaging of non-cooperative vessels. This technique only considers the measured radar data of a vessel and assumes that the corresponding motion data is not available.

Chapter 6

Selecting Optimum Imaging Intervals for Small Non-cooperative Sea Vessels

6.1 Introduction

In maritime surveillance applications, long HRR recordings of non-cooperative sea vessels are used to produce ISAR images that are useful for ship classification. The literature has demonstrated that 2-D ISAR images of sea vessels have the potential to aid classification, as shown in papers by Bon *et al.* [6] and Musman *et al.* [7]. Moreover, both [6] and [7] claim that side-view ISAR images contain discriminant information for ISAR-based ship classification, which is essential for peacetime applications, such as fishing monitoring, search and rescue and the prevention of poaching and terrorism at sea.

However, it is a challenging task to isolate focused side-view ISAR images of a non-cooperative vessel from a long radar recording, because a vessel's roll, pitch and yaw motion affects the presentation of the vessel in the ISAR image and because the 3-D rotational motion also causes blurring in many ISAR images, as shown in papers by Chen and Miceli [35] and Abdul Gaffar *et al.* [43].

Many algorithms have been proposed in the literature to identify optimum imaging intervals for ISAR imaging of non-cooperative sea vessels. These algorithms can be grouped into, firstly, frame selection techniques and, secondly, joint frame and optimum CPTWL selection techniques. Examples of the former include papers by Hajduch *et al.* [19], Rihaczek and Hershkowitz [32], Li *et al.* [34] and Pastina and Spina [41], whereas an example of the latter is the MC-ATWS algorithm proposed by Martorella and Berizzi [28]. Frame selection techniques use a single initial CPTWL to break up a long radar recording into many frames, and then use appropriate criteria to select frames that correspond to optimum imaging intervals. Similarly, the first step of joint frame and CPTWL selection techniques involves the selection of frames that correspond to optimum imaging intervals, whereas the next step addresses the optimisation of the CPTWLs of all the intervals that are found.

Frame selection techniques are limited because they do not show how an effective initial CPTWL should be chosen, and because they assume that the initial CPTWL is approximately equal to the duration of all the optimum ISAR imaging intervals in the radar recording. Furthermore, algorithms in [32], [34] and [41] are problematic to implement with real data, firstly, because they require accurate phase unwrapping and, secondly, because algorithms in [32] and [41] assume accurate tracking of a scatterer at the bow and the stern of the ship that are of the same width and at the same height position, which is difficult to achieve in practice.

The joint frame and optimum CPTWL selection technique proposed by Martorella and Berizzi in [28] addresses most of the limitations of existing frame selection techniques in the literature. The MC-ATWS algorithm estimates the optimum centre time position and the optimum CPTWL that provides the most focused ISAR image in the radar recording; this algorithm does not require problematic phase wrapping, nor does it assume any *a priori* knowledge of the non-cooperative sea vessel. However, MC-ATWS has several limitations: the algorithm only estimates the parameters of a single imaging interval and ignores other optimum imaging intervals that may exist in a long radar recording; when the algorithm is applied to radar recordings of small sea vessels, the algo-

rithm's performance is dependent on the value of the initial CPTWL, as shown by Abdul Gaffar *et al.* in [44]; furthermore, the highly focused ISAR image that corresponds to the optimum imaging interval does not always correspond to a side-view ISAR image, which is desired for ship classification.

This chapter proposes the extended maximum-contrast-based automatic time window selection (EMC-ATWS) algorithm; this identifies multiple optimum imaging intervals for small non-cooperative sea vessels, which possess prominent superstructures and are sailing inbound/outbound with respect to the radar. The proposed technique is superior to the original MC-ATWS algorithm because it uses a range of initial CPTWLs, which means that the proposed algorithm's performance is not dependent on a single initial CPTWL. Furthermore, the EMC-ATWS algorithm offers the advantage of extracting more than a single optimum imaging interval from a radar recording. Lastly, the imaging intervals that are found give rise to focused side-view ISAR images. These images are a rich source of information for operator assisted ship classification, where the user selects which ISAR images are used for classification.

The system model is described in Section 6.2. Section 6.3 summarises the relevant features of Martorella and Berizzi's MC-ATWS algorithm and highlights a few limitations of the existing technique. Thereafter, the proposed EMC-ATWS algorithm is presented in Section 6.4. This algorithm was applied to measured radar recordings of two non-cooperative sea vessels and the results obtained are shown in Section 6.5. Lastly, conclusions are given in Section 6.6.

6.2 System Model

The system model considers a monostatic ground-based radar that illuminates a vessel at sea. The mathematical description of the system model presented in this section is similar to the model described in [28], which expresses the complex baseband radar received signal in a time-frequency format, denoted by $S_R(f,t)$, as:

$$S_R(f,t) = W[f,t] \int \alpha(\mathbf{x})\, e^{-j(4\pi f/c)R(\mathbf{x},t)}\, \mathrm{d}\mathbf{x} \tag{6.1}$$

where $W[f,t] = \text{rect}((t-\tau)/\Delta\tau)\,\text{rect}((f-f_c)/B)$, f_c is the carrier frequency, B represents the effective transmit bandwidth over the CPI, τ is the central time of the CPI, $\Delta\tau$ is the CPTWL of the CPI, c is the speed of light, $R(\mathbf{x},t)$ is the distance between the radar and a generic point $\mathbf{x}$ that changes with time t due to a vessel's translation and 3-D rotational motion, and $\alpha(\mathbf{x})$ is the vessel's reflectivity function. The function $\text{rect}(x)$ equals to 1 when $|x| < \frac{1}{2}$, and 0 otherwise.

Assume that the radar transmits a stepped frequency waveform and the motion of the vessel is stationary over the burst. Then, the HRR profiles of the vessel may be obtained by applying the Inverse Fourier Transform (IFT) along the frequency dimension f of the received signal, as follows:

$$S_R(\eta,t) = IFT_{f\to\eta}[S_R(f,t)] \tag{6.2}$$

where η represents down-range.

Thereafter, an ISAR image of the vessel can be obtained by applying range alignment, autofocus and polar reformatting [40] to the HRR profiles. Assume that scatterers of the vessel do not migrate through cells in the ISAR image, i.e. the vessel's cross-range and down-range extent is smaller than the criteria defined in [23]. Then, the data measured in the polar grid is approximately equal to a regularly sampled rectangular grid. In this case, only range alignment and autofocus are needed obtain an ISAR image, and polar reformatting is not of great importance.

Let $\tilde{S}_R(\eta,t)$ represent the range aligned HRR profiles and let $\varphi(t)$ denote the phase history used to perform autofocus. Using this notation, the ISAR image intensity for a CPI with a central time of τ and a CPTWL of $\Delta\tau$, denoted by $I(\eta,\nu;\tau,\Delta\tau)$, can be obtained by applying the Fourier Transform (FT) along the time dimension t of the HRR profiles after range alignment and autofocus:

$$I(\eta,\nu;\tau,\Delta\tau) = \left| FT_{t\to\nu}\left[\tilde{S}_R(\eta,t)e^{(j\varphi(t))}\right]\right|^2 \tag{6.3}$$

where ν represents Doppler frequency in the cross-range dimension and (η, ν) are the two ISAR image coordinates.

In summary, a single 2-D ISAR image can be generated from many successive HRR profiles. The time interval of the set of HRR profiles is referred to as a CPI, which consists of a centre time τ and a CPTWL $\Delta\tau$. Since the cross-range dimension of an ISAR image fundamentally represents Doppler frequency, it is the rotation motion of the sea vessel over the CPI that affects the Doppler information in the ISAR image. Small sea vessels naturally possess 3-D rotation motion (roll, pitch and yaw) that changes rapidly over successive CPIs, and it is this chaotic motion that often produces blurry ISAR images and successive images with fast changing Doppler information. Thus, it is a challenging task to isolate the imaging intervals that give rise to focused ISAR images. The MC-ATWS algorithm is a technique, which estimates the optimum imaging interval that produces the most focused ISAR image from a long radar recording of a non-cooperative vessel.

6.3 Summary of the MC-ATWS Algorithm

The MC-ATWS algorithm proposed by Martorella and Berizzi in [28] measures the focus of ISAR images using the mathematical formulation of the normalised IC, and estimates the centre time and the CPTWL of a single CPI that gives rise to the most focused ISAR image. The algorithm is based on a double linear search strategy. Firstly, the long radar recording of HRR profiles is broken down into many overlapping frames, with equal CPTWLs given by $\Delta\tau^{(in)}$, and the algorithm calculates the IC of each frame. Then, the algorithm estimates the optimum centre time τ_{opt} that corresponds to the centre time of the frame with the highest IC. In the next step, the optimum CPTWL $\Delta\tau_{opt}$ is estimated by varying the length of the initial CPTWL $\Delta\tau^{(in)}$ to optimise the IC of the resulting ISAR image with a centre time of τ_{opt}. The MC-ATWS algorithm can be broken down into the following steps:

1. **Initialisation:** assign appropriate values to the initial CPTWL (s), denoted by $\Delta\tau^{(in)}$, the initial window length increase (in number of HRR profiles), denoted by $2p$, and the step size that the sliding window moves between two successive CPIs (in number of HRR profiles), which is denoted by s.

2. **Obtain the IC of all the frames:** break up the HRR radar recording of the sea vessel into many frames or CPIs. Each frame has a CPTWL of $\Delta\tau^{(in)}$ and the step size between two successive frames is given by s HRR profiles. Calculate the IC of all the frames using the following general formula:

$$IC\left(\tau,\Delta\tau\right)=\frac{\sqrt{A\left\{\left[I\left(\eta,\nu;\tau,\Delta\tau\right)-A\left\{I\left(\eta,\nu;\tau,\Delta\tau\right)\right\}\right]^{2}\right\}}}{A\left\{I\left(\eta,\nu;\tau,\Delta\tau\right)\right\}} \tag{6.4}$$

   where $A\left(\cdot\right)$ is the mean operator over the variables (η,ν).

3. **Estimate the optimum centre time** (τ_{opt})**:** the optimum centre time is given by the centre time of the frame with the highest contrast. Stated mathematically:

$$\tau_{opt}=\arg\left\{\max_{\tau}\left[IC\left(\tau,\Delta\tau^{(in)}\right)\right]\right\} \tag{6.5}$$

   This method is referred to as the maximum position locator (MPL) algorithm in [28].

4. **Estimate the optimum CPTWL** ($\Delta\tau_{opt}$)**:** in this step, the CPTWL of the frame with centre time τ_{opt} is iteratively adjusted to maximise the contrast of the resulting ISAR image. This technique is referred to as the window length estimator (WLE) algorithm in [28] and it can be summarised as follows:

(a) **Define relevant formulas and initialise variables:** Define the following formulas,

$$\Delta\tau_{inc}^{(k,h)} = \Delta\tau_{opt}^{(k-1)} + \left(2\left(p-k\right)h\right)\frac{1}{f_{BRF}} \tag{6.6}$$

$$\Delta\tau_{dec}^{(k,h)} = \Delta\tau_{opt}^{(k-1)} - \left(2\left(p-k\right)h\right)\frac{1}{f_{BRF}} \tag{6.7}$$

where f_{BRF} is the BRF of the radar given by $\frac{M}{f_{BRF}}$, M is the number of stepped frequency pulses that are used to form a HRR profile, and the variables $\Delta\tau_{inc}^{(k,h)}, \Delta\tau_{opt}^{(k-1)}, k, h$, are used in the WLE algorithm.

Initialise the variables: $k = 0$, $h = 1$ and $\Delta\tau_{opt}^{(-1)} = \Delta\tau^{(in)}$. Note that $k \in \{1, 2, \cdots, p\}$ and $h \in \mathbb{Z}^+$.

(b) **Vary the original CPTWL of $\Delta\tau^{(in)}$ to optimise IC:**

IF IC $\left(\tau_{opt}, \Delta\tau_{inc}^{(0,1)}\right) \leq$ IC $\left(\tau_{opt}, \Delta\tau^{(in)}\right)$:
  IF IC $\left(\tau_{opt}, \Delta\tau_{dec}^{(0,1)}\right) \leq$ IC $\left(\tau_{opt}, \Delta\tau^{(in)}\right)$:
    $\Delta\tau_{opt} = \Delta\tau^{(in)}$, algorithm terminates
  ELSE: go to step 4d
ELSE: go to step 4c

(c) **Increase the initial CPTWL to maximise IC:**

i. Increment h

ii. Evaluate the following condition

IF IC $\left(\tau_{opt}, \Delta\tau_{inc}^{(k,h)}\right) \leq$ IC $\left(\tau_{opt}, \Delta\tau_{inc}^{(k,h+1)}\right)$:
  go back to step 4(c)i
ELSE: $\tau_{opt}^{(k)} = \Delta\tau_{inc}^{(k,h)}$

where $\left(\text{IC}\left(\tau_{opt}, \Delta\tau_{inc}^{(k,h)}\right) \leq \text{IC}\left(\tau_{opt}, \Delta\tau_{inc}^{(k,h+1)}\right)\right)$ is referred to as the WLE_{inc} criteria.

iii. Increment k, initialise $h = 1$

IF $k \leq p$: go back to step 4(c)ii
ELSE: go to step 4e

(d) **Decrease the initial CPTWL to maximise IC:**

i. Increment h

ii. Evaluate the following condition

$$\text{IF IC}\left(\tau_{opt}, \Delta\tau_{dec}^{(k,h)}\right) \leq \text{IC}\left(\tau_{opt}, \Delta\tau_{dec}^{(k,h+1)}\right) : \text{ go back to step 4(d)i}$$
$$\text{ELSE: } \tau_{opt}^{(k)} = \Delta\tau_{dec}^{(k,h)}$$

where $\left(\text{IC}\left(\tau_{opt}, \Delta\tau_{dec}^{(k,h)}\right) \leq \text{IC}\left(\tau_{opt}, \Delta\tau_{dec}^{(k,h+1)}\right)\right)$ is referred to as the WLE_{dec} criteria.

iii. Increment k, initialise $h = 1$

IF $k \leq p$: go back to step 4(d)ii
ELSE: go to step 4e

(e) **Assign optimum CPTWL:** $\Delta\tau_{opt} = \Delta\tau_{opt}^{(k)}$

The MC-ATWS algorithm has been shown to be an effective technique for finding the parameters of the optimum imaging interval for ISAR imaging of large ships [28]. However, the MC-ATWS algorithm does not show how an effective value for the initial CPTWL should be chosen. Moreover, Abdul Gaffar *et al.* have shown that the initial CPTWL is critical to the algorithm's performance when it is applied to radar recordings of small sea vessels [44]. If the chosen initial CPTWL is much larger than the optimum CPTWL in the radar recording, then all the frames will possess significant 3-D rotation motion, and maximising the IC of blurry ISAR images would not identify the centre time of the optimum imaging interval. Conversely, if the chosen initial CPTWL is much smaller than the

optimum CPTWL, then successive frames around the optimum imaging interval will produce ISAR images with similar IC values and there would not be a single IC peak to ease the task of estimating the optimum centre time. In addition, long radar recordings typically have multiple optimum imaging intervals with varying optimum CPTWLs, and the current MC-ATWS algorithm is unable to estimate the parameters of multiple optimum intervals because the technique assumes that the initial CPTWL that is chosen is approximately equal to a single present optimum CPTWL.

The ISAR image corresponding to the estimated optimum imaging interval does not always correspond to a side-view ISAR image that is desired for operator assisted ship classification. This chapter proposes a new algorithm, referred to as the EMC-ATWS algorithm, which addresses these limitations of the current MC-ATWS algorithm.

6.4 The Proposed EMC-ATWS Algorithm

The proposed EMC-ATWS algorithm was developed to estimate the parameters of multiple optimum imaging intervals, which generate side-view ISAR images of a small non-cooperative vessel of interest from a long radar recording. In order to obtain a side-view ISAR image that contains significant Doppler information, a vessel with prominent superstructures should be sailing inbound/outbound with respect to the radar; when the vessel possesses dominant pitch motion, the cross-range dimension of the 2-D ISAR image is along the height of the vessel and a side-view ISAR image is generated. A side-view image is desired because it contains many features that may be used for classification: length, number of superstructure breaks, mast heights and distance between masts as described in references [6] and [7]. For this reason, the proposed EMC-ATWS algorithm assumes that the radar is tracking an inbound/outbound vessel with prominent superstructures; this makes it possible to obtain a side-view ISAR image with significant Doppler information so that important features may be extracted in the classification step.

The EMC-ATWS algorithm uses a modified calculation of the IC, referred to as the IC with zero Doppler masking (ZDM), which disregards the cross-range cells around zero Doppler in order to measure the focus of motion compensated ISAR images. Similar to the MC-ATWS algorithm, the calculated IC values are used to estimate the parameters of the optimum imaging intervals. The proposed technique uses a range of initial CPTWLs to search for multiple optimum intervals that may have different optimum CPTWLs. For each initial CPTWL, the radar recording is broken down into many frames, and each frame's CPTWL is equal to the initial CPTWL. Furthermore, the frames are separated so that successive frames have a fixed overlap factor. The EMC-ATWS technique then calculates the IC associated with all the frames, and candidate optimum centre times are estimated by identifying the existing local maxima. The estimated centre times are referred to as candidates because they require further assessment before they can be declared as optimum centre times. Note that each candidate optimum centre time has an associated initial CPTWL, which is given by the corresponding initial CPTWL used.

Thereafter, the candidate optimum centre times and the associated initial CPTWLs are used to generate candidate optimum ISAR images. This chapter also proposes the image test (IT) algorithm, which is used to reject candidate optimum intervals that generate undesirable ISAR images. More details of the undesirable characteristic are explained later in this section. The centre times of the accepted candidate optimum intervals are identified as the optimum centre times for the radar recording. Finally, a modified WLE algorithm is applied to the accepted candidate optimum intervals to obtain the associated optimum CPTWLs that produce highly focused side-view ISAR images.

The proposed EMC-ATWS algorithm can be broken down into the following steps:

1. **Initialisation:** assign values to a range of J initial CPTWLs (s), denoted by $\Delta\boldsymbol{\tau}^{(in)} = \left\{\Delta\tau^{(in)}(1), \quad \Delta\tau^{(in)}(2), \quad \cdots \quad \Delta\tau^{(in)}(j) \quad \cdots \quad \Delta\tau^{(in)}(J)\right\}$, the initial window length increase (in number of HRR profiles), denoted by $2p$, and the overlap factor between successive frames, denoted by γ.

Other variables, which are introduced later in this section, that also require initialisation are the following: the Doppler bandwidth about 0 Hz that is masked by IC with ZDM, which is denoted by B_{zdm}; the energy threshold (in Decibels), which is represented by ϵ_{thres}; and the Doppler bandwidth about 0 Hz that is used to test for undesirable characteristics in an ISAR image, which is denoted by B_{zdt}.

2. **For each initial CPTWL, break down the radar recording into many frames and calculate the IC with ZDM for each frame:** The IC calculation used in the MC-ATWS algorithm takes into account all Doppler cells of an ISAR image, as shown in (6.4). As a result, the MC-ATWS algorithm associates a high IC value with an ISAR image that possesses little Doppler energy and in certain radar recordings, the corresponding interval may be identified as the optimum imaging interval, i.e. the interval that produces the most focused ISAR image. However, ISAR images with little Doppler energy are undesirable because they do not possess the most discriminant information for ship classification. This chapter proposes a modified IC, referred to as the IC with ZDM, which does not associate a high IC value with ISAR images with little Doppler energy. The IC with ZDM, denoted by IC_{zdm}, measures the focus of an ISAR image by disregarding the Doppler cells around 0 Hz with a bandwidth of B_{zdm}. Stated mathematically, the IC_{zdm} value for an interval with a centre time of τ and a CPTWL of $\Delta\tau$ is given by:

$$\text{IC}_{\text{zdm}}\left(\tau, \Delta\tau, B_{\text{zdm}}\right) = \frac{\sqrt{A_{\text{zdm}}\left\{\left[I\left(\eta,\nu;\tau,\Delta\tau\right) - A_{\text{zdm}}\left\{I\left(\eta,\nu;\tau,\Delta\tau\right)\right\}\right]^2\right\}}}{A_{\text{zdm}}\left\{I\left(\eta,\nu;\tau,\Delta\tau\right)\right\}} \tag{6.8}$$

where A_{zdm} is the mean operator over the variables (η, ν), where $\nu \notin \left[-B_{zdt}/2 \;\; B_{zdt}/2\right]$.

3. **Estimate multiple candidate optimum centre times:** For each initial CPTWL, the corresponding IC with ZDM is used to estimate multiple candidate optimum centre times. The candidate optimum centre times

for the j^{th} initial CPTWL, denoted by $\Delta\tau^{(in)}$, are estimated by the local maxima of the corresponding $\mathrm{IC}_{\mathrm{zdm}}$, which is given by:

$$\boldsymbol{\tau}^{j}_{copt} = \arg\left\{\underset{\tau}{\mathrm{locmax}_2}\left[\mathrm{IC}_{\mathrm{zdm}}\left(\tau, \Delta\tau^{(in)}(j), B_{\mathrm{zdm}}\right)\right]\right\} \tag{6.9}$$

where locmax_2 represents the local maxima operator, which identifies local maxima as peak values that have two decreasing points on either side. The candidate optimum centre times corresponding to the j^{th} initial CPTWL are given by $\boldsymbol{\tau}^{j}_{copt}$, where $\boldsymbol{\tau}^{j}_{copt} = \left\{\tau^{j}_{copt}(1) \;\; \tau^{j}_{copt}(2) \;\; \cdots \;\; \tau^{j}_{copt}(i) \;\; \cdots \;\; \tau^{j}_{copt}(I_j)\right\}$ and I_j represents the number of optimum centre times that are estimated for the j^{th} initial CPTWL. Note that the i^{th} candidate optimum centre time $\tau^{j}_{copt}(i)$ has an associated initial CPTWL, denoted by $\Delta\tau^{(in)}(j)$, and these are parameters of a candidate optimum imaging interval. The HRR profiles corresponding to the candidate optimum imaging intervals are used to obtain the candidate optimum ISAR images.

In order to declare a local maximum, the number of decreasing points on either side was chosen to be two because it provides a suitable trade-off between having many false candidate optimum imaging interval alarms, when the number of decreasing points is set to one, and being to estimate close spaced optimum imaging intervals.

4. **Reject the candidate optimum intervals that produce undesirable ISAR images:** All the candidate optimum ISAR images have the good feature of possessing a relatively high IC. However, the proposed algorithm aims to select only the candidate optimum intervals that generate side-view ISAR images, which are desirable for operator assisted ship classification. Thus, it is important to assess each candidate optimum ISAR image and reject the undesirable images, i.e. side-view ISAR images with a long CPTWL that causes scatterers along a mast to possess both positive and negative Doppler frequencies.

   A side-view ISAR image is generated when an inbound sea vessel possesses pure uniform pitch motion over the imaging interval. Furthermore, the CPTWL of the imaging interval should be short enough so that the

Doppler frequency of scatterers along a vessel's masts is only positive or only negative, i.e. the Doppler frequency of the scatterers should not change from positive to negative Doppler over the CPI. When this condition is satisfied, Martorella's cross-range scaling algorithm [27] can be used to obtain cross-range scaled ISAR images, which is desirable for operator assisted classification.

This chapter proposes the IT algorithm that assesses the candidate optimum ISAR images and rejects the corresponding candidate optimum imaging intervals that produce side-view ISAR images with a long CPTWL, which causes scatterers along a mast to possess both positive and negative Doppler frequencies. The IT algorithm performs a long CPTWL side-view image test (LCSIT) to ensure that the optimum ISAR images have only positive or only negative Doppler, and this makes it possible to obtain cross-range scaled ISAR images with reasonable accuracy, as discussed in [27]. The IT of an interval with a centre time of τ and a CPTWL of $\Delta\tau$ is mathematically expressed as $\mathrm{IT}\left(\epsilon_{\mathrm{thres}}, B_{zdt}; \tau, \Delta\tau\right)$, where $\epsilon_{\mathrm{thres}}$ and B_{zdt} have been defined earlier in this section. Note that the IT algorithm assigns the value 1 to the imaging interval that produces a desirable side-view ISAR image. Otherwise, the value 0 is assigned.

The IT value of the candidate optimum ISAR image with a centre time of $\tau_{copt}^{j}\left(i\right)$ and a CPTWL of $\Delta\tau^{(in)(j)}$ is calculated using the following steps:

(a) For each down-range cell in the candidate optimum ISAR image, sum up the energy along the Doppler dimension and find the down-range cell with the most energy:

$$\eta_{max} = \arg\left\{\max_{\eta}\left[\operatorname*{sum}_{\nu}\left(I_{\mathrm{dB}}\left(\eta, \nu, \tau_{copt}^{j}\left(i\right), \Delta\tau^{(in)}\left(j\right)\right)\right)\right]\right\} \tag{6.10}$$

where η_{max} represents the down-range cell with the most energy, sum_{v} is the sum operator over the variable ν, and I_{dB} denotes the ISAR image in Decibels (dB).

(b) Apply the LCSIT to the candidate optimum ISAR image: When an inbound vessel possesses pure pitch motion over an imaging interval

and the CPTWL is kept short, then the Doppler frequencies of scatterers along the mast are either only positive or only negative and cross-range scaling can be achieved. However, when the CPTWL is increased, the ISAR image shows the scatterers along the mast possessing both positive and negative Doppler frequencies due to the velocity of the scatterers changing direction over the imaging interval. In this case, accurate cross-range scaling is difficult to achieve using conventional algorithms [23], and for this reason, such ISAR images are not desirable. The LCSIT algorithm assesses candidate optimum ISAR images for masts with positive and negative Doppler energy by finding the difference in energy between the sum of the positive Doppler cells from 0 Hz to $B_{zdt}/2$ and the sum of the negative Doppler cells from $-B_{zdt}/2$ to 0 Hz, for the η_{max} down-range cell. Stated mathematically:

$$\epsilon_{\text{LCSIT}} = \left| \underset{\nu_B^-}{\text{sum}} \left(I_{\text{dB}} \left(\eta_{max}, \nu, \tau_{copt}^{j} \left(i \right), \Delta\tau^{(in)} \left(j \right) \right) \right) - \underset{\nu_B^+}{\text{sum}} \left(I_{\text{dB}} \left(\eta_{max}, \nu, \tau_{copt}^{j} \left(i \right), \Delta\tau^{(in)} \left(j \right) \right) \right) \right| \tag{6.11}$$

where $\nu_B^- \in [-B_{zdt}/2 \;\; 0]$ and $\nu_B^+ \in [0 \;\; B_{zdt}/2]$. If $\epsilon_{\text{LCSIT}} < \epsilon_{\text{thres}}$, then the candidate optimum ISAR image may contain masts with positive and negative Doppler frequencies.

It should be noted that (6.10) and (6.11) assumes that the vessel of interest may be represented by point scatterers with equal reflectivity. Thus, the range bin with the greater energy would correspond to a mast of a vessel.

(c) If ϵ_{LCSIT} is less than the energy threshold ϵ_{thres}, then the candidate optimum ISAR image is rejected and the value of 0 is assigned to the IT. Otherwise, the candidate optimum interval is accepted and the

value 1 is assigned to the IT. Stated programmatically:

IF $(\epsilon_{\text{LCSIT}} < \epsilon_{\text{thres}})$: reject the candidate optimal interval, and assign an IT value of 0

$$\text{IT}\left(\epsilon_{\text{thres}}, B_{zdt}; \tau^{j}_{copt}(i), \Delta\tau^{(in)}(j)\right) = 0 \tag{6.12}$$

ELSE: accept the candidate optimum interval and assign an IT value of 1.

$$\text{IT}\left(\epsilon_{\text{thres}}, B_{zdt}; \tau^{j}_{copt}(i), \Delta\tau^{(in)}(j)\right) = 1 \tag{6.13}$$

Lastly, for all overlapping accepted candidate optimum intervals, only retain the interval with the longest CPTWL. Assign $\tau^{j}_{copt}(i)$ to the q^{th} optimum centre time and $\Delta\tau^{(in)}(j)$ to the q^{th} initial CPTWL

$$\tau_{opt}(q) = \tau^{j}_{copt}(i) \tag{6.14}$$

$$\Delta\tau^{(in)}(q) = \Delta\tau^{(in)}(j) \tag{6.15}$$

where $q \in \{1,\ 2,\ \cdots\ Q\}$, and Q is number of non-overlapping accepted candidate optimum intervals.

5. **Estimate the optimum CPTWLs associated with all Q optimum centre times:** This step involves iteratively adjusting the q^{th} initial CPTWL $\Delta\tau^{(in)}(q)$, to obtain the q^{th} optimum CPTWL, denoted by $\Delta\tau_{opt}(q)$. The iterative technique estimates the optimum CPTWL by satisfying two objectives: to maximise the IC of the resulting ISAR image and to ensure that the resulting ISAR image has an IT value of 1. The technique used to estimate the optimum CPTWL is referred to as the extended window length estimator (EWLE) algorithm, which is an extension of the existing WLE algorithm proposed in [28]. The processing steps of the EWLE algorithm are similar to the WLE algorithm, but there are two differences: the EWLE algorithm uses the IC with ZDM, formulated in (6.8), instead of the IC used in [28] (see (6.4)), and the EWLE techniques uses the new EWLE_{inc}/EWLE_{dec} criteria instead of the WLE_{inc}/WLE_{dec} criteria used in [28]. The new EWLE_{inc} and EWLE_{dec} criteria for the q^{th} accepted candi-

date optimum interval are mathematically given by:

$$\text{EWLE}_{\text{inc}} \text{ criteria} = \Bigg(\text{IC}\left(\tau_{opt}\left(q\right), \Delta\tau_{inc}^{(k,h)}\left(q\right)\right) \leq \text{IC}\left(\tau_{opt}\left(q\right), \Delta\tau_{inc}^{(k,h+1)}\left(q\right)\right) \text{ and IT}\Big(\epsilon_{\text{thres}}, B_{zdt}; \tau_{opt}\left(q\right), \Delta\tau_{copt}\left(q\right)\Big)\Bigg) \tag{6.16}$$

$$\text{EWLE}_{\text{dec}} \text{ criteria} = \Bigg(\text{IC}\left(\tau_{opt}\left(q\right), \Delta\tau_{dec}^{(k,h)}\left(q\right)\right) \leq \text{IC}\left(\tau_{opt}\left(q\right), \Delta\tau_{dec}^{(k,h+1)}\left(q\right)\right) \text{ and IT}\Big(\epsilon_{\text{thres}}, B_{zdt}; \tau_{opt}\left(q\right), \Delta\tau_{copt}\left(q\right)\Big)\Bigg) \tag{6.17}$$

The EWLE algorithm is applied to all Q initial CPTWLs to obtain Q optimum CPTWLs, denoted by $\Delta\boldsymbol{\tau}_{opt} = \{\Delta\tau_{opt}\left(1\right) \;\; \Delta\tau_{opt}\left(2\right) \;\; \cdots \;\; \Delta\tau_{opt}\left(Q\right)\}$. In summary, the proposed EMC-ATWS algorithm estimates Q optimum imaging intervals, where the parameters of the q^{th} optimum imaging interval are given by the optimum centre time $\tau_{opt}\left(q\right)$ and the optimum CPTWL of $\Delta\tau_{opt}\left(q\right)$.

6. **Reduce streaks from the optimum ISAR images:** ISAR images of vessels may contain streaks, which are caused by onboard rotating parts such as antennas. The streak reduction algorithm proposed in [7] is applied to all the optimum ISAR images so that the images shown to the user possess less prominent streaks. Another algorithm to remove streaks was proposed by Li and Ling in [128].

6.5 Results

The MC-ATWS algorithm and the proposed EMC-ATWS algorithm were applied to measured radar recordings of two non-cooperative yachts, and the results obtained are presented in this section. Radar recordings were obtained from the Signal Hill 2007 trial (see Appendix A for more information), where an

experimental X-band radar was used to obtain HRR profiles of the vessels using a stepped frequency waveform.

In both recordings, the following radar parameters were used: a frequency step of 4 MHz, 64 pulses in an ISAR burst and a burst repetition frequency of 154 Hz. Radar measurements of a sphere suspended from a helicopter were used to compensate the measured HRR profiles for the radar's non-ideal response over the stepped frequency band.

The two yachts used are illustrated in Figure 6.1. Separate radar recordings were made for each vessel and, in both recordings, the corresponding vessel was sailing inbound with respect to the radar. The Esperance and Tigresse radar recordings were approximately 23 s and 12 s in duration respectively. In both the MC-ATWS and the EMC-ATWS algorithms, translation motion compensation was achieved by using the range alignment and autofocus algorithm proposed by Haywood and Evans in [61]. The autofocus algorithm is commonly referred to as the dominant scatterer algorithm (DSA).

The proposed EMC-ATWS algorithm assumes that the autofocus algorithm accurately identifies zero-Doppler in the ISAR image. The DSA algorithm is an effective technique for identifying the zero-Doppler because it chooses a reference scatterer that has the least amplitude variance over the CPI. Range bins that correspond to masts are typically not chosen because there are many scatterers that sum up constructively and destructively over the CPI, leading to larger variance than a single scatterer on the vessel deck, which is at zero-Doppler.

Firstly, the MC-ATWS algorithm was applied to both recordings to estimate the parameters of the optimum imaging interval that produces the ISAR image with the highest IC. The following parameter values were used in the MC-ATWS algorithm: an initial CPTWL $\Delta\tau^{(in)}$ of 0.83 s, a sliding window of 32 HRR profiles and an initial window length increase $2p$ of 12 HRR profiles. Figure 6.2 illustrates the result obtained from the Esperance recording.

Figure 6.2(a) shows the IC versus time and Figure 6.2(b) shows the motion compensated ISAR image corresponding to the optimum imaging interval with

(a) (b)

Figure 6.1: Photos of the two non-cooperative yachts: (a) the Esperance yact, and (b) the Tigresse yacht

parameters $\tau_{opt} = 7.2$ s and $\Delta\tau_{opt} = 1.1$ s. The optimum ISAR has the good feature of possessing a high IC, but the image exhibits very little Doppler information, which is not desirable for ship classification. Similar trends can be seen in Figure 6.3, which shows the results obtained from the Tigresse recording.

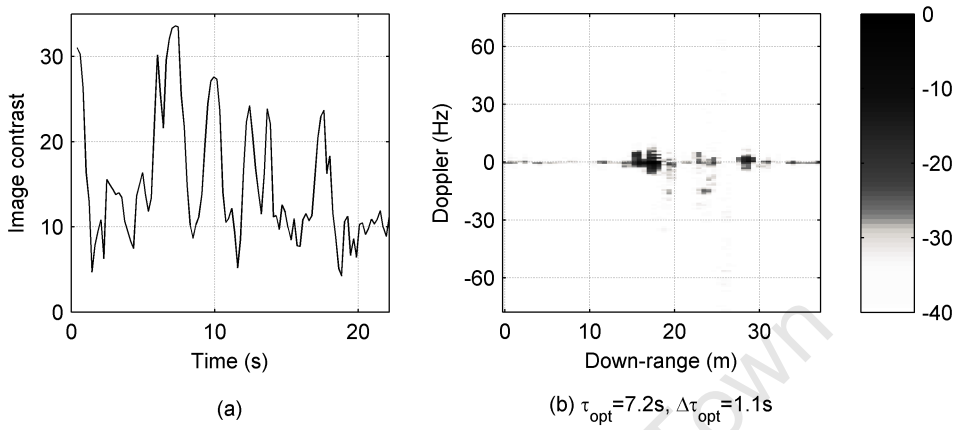

Figure 6.2: Results from applying the MC-ATWS algorithm to the radar recording of the Esperance: (a) IC versus time, (b) motion compensated ISAR image obtained from the optimum imaging interval with $\tau_{opt} = 7.2$ s and $\Delta\tau_{opt} = 1.1$ s

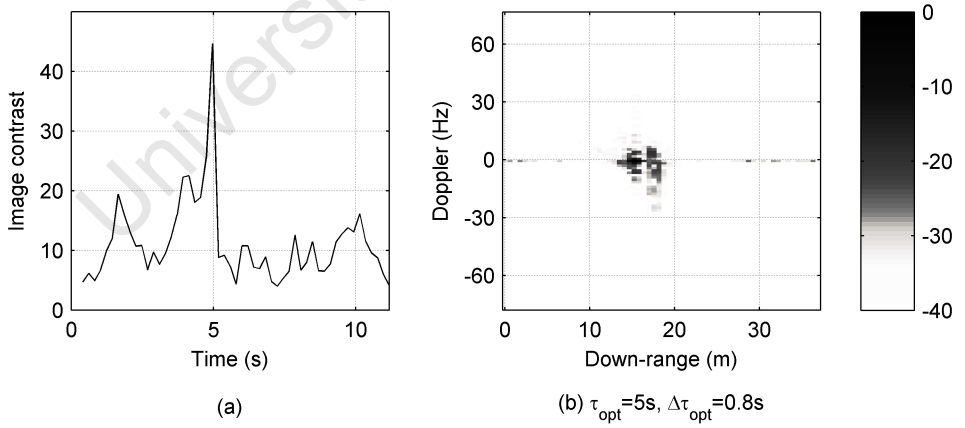

Figure 6.3: Results from applying the MC-ATWS algorithm to the radar recording of the Tigresse: (a) IC versus time, (b) motion compensated ISAR image obtained from the optimum imaging interval with $\tau_{opt} = 5$ s and $\Delta\tau_{opt} = 0.8$ s

Thereafter, the EMC-ATWS algorithm was applied to both radar recordings to estimate the parameters of multiple optimum imaging intervals that produce highly focused side-view ISAR images. The EMC-ATWS was initialised with the following parameters: a range of initial CPTWL given by $\Delta\boldsymbol{\tau}^{(in)} = \{0.5 \text{ s}, \ 0.7 \text{ s}, \ \cdots \ , 2.5 \text{ s}\}$, an overlap factor of $\gamma = 0.75$, an initial window length increase $2p$ of 12 HRR profiles. Suitable values for B_{zdm}, B_{zdt}, ϵ_{thres} are dependent on the sea state, the sailing profile of the vessel with respect to the wind direction, the size of the vessel of interest, the signal-to-noise ratio of the radar measurements and the side-lobe level achieved after calibration. In the dataset of the Esperance and the Tigresse, the radar data and the environmental conditions were analysed and the following parameter values were used: $B_{zdm} = 15$ Hz, $B_{zdt} = 60$ Hz and $\epsilon_{\text{thres}} = 8$ dB.

For each initial CPTWL, the recording was broken down into many frames and the IC with ZDM was calculated for each frame. Subsequently, multiple candidate optimum intervals are estimated from the local maxima of the IC with ZDM values associated with the frames. The IT was applied to the candidate optimum ISAR images and the candidate optimum intervals that produce ISAR images with undesirable characteristics were rejected. Lastly, the optimum CPTWL relating to each accepted candidate optimum interval was estimated by optimising the IC with ZDM of the corresponding ISAR image.

The EMC-ATWS algorithm was applied to the Esperance radar recording to extract multiple focused side-view ISAR images. Figure 6.4 illustrates the candidate optimum intervals and the accepted candidate optimum intervals that were identified.

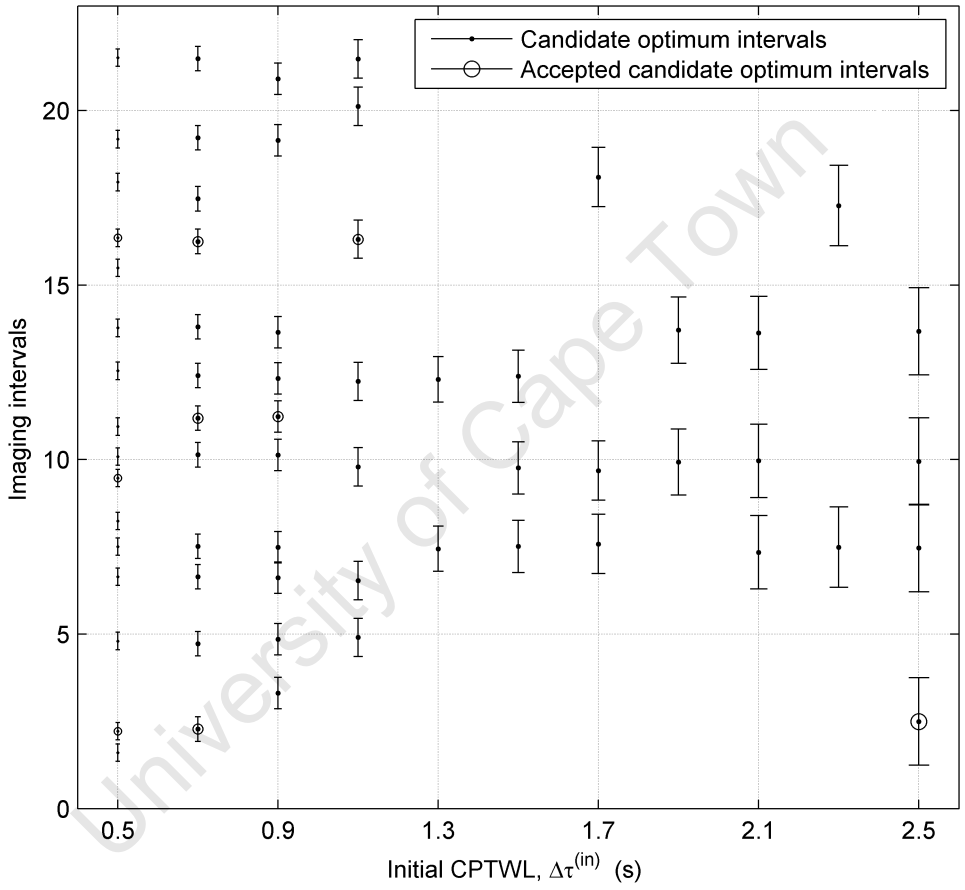

Figure 6.4: Diagram showing the candidate optimum intervals and the accepted candidate optimum intervals that were identified after applying the proposed EMC-ATWS algorithm to the Esperance radar recording

The candidate optimum ISAR images corresponding to the candidate optimum intervals for $\Delta\tau^{(in)} = 0.5$ s are shown in Figure 6.5. It is only Figure 6.5(a) that has an IT value of 1 and it is the only candidate optimum imaging interval that is accepted from the four available candidate optimum imaging intervals for $\Delta\tau^{(in)} = 0.5$ s.

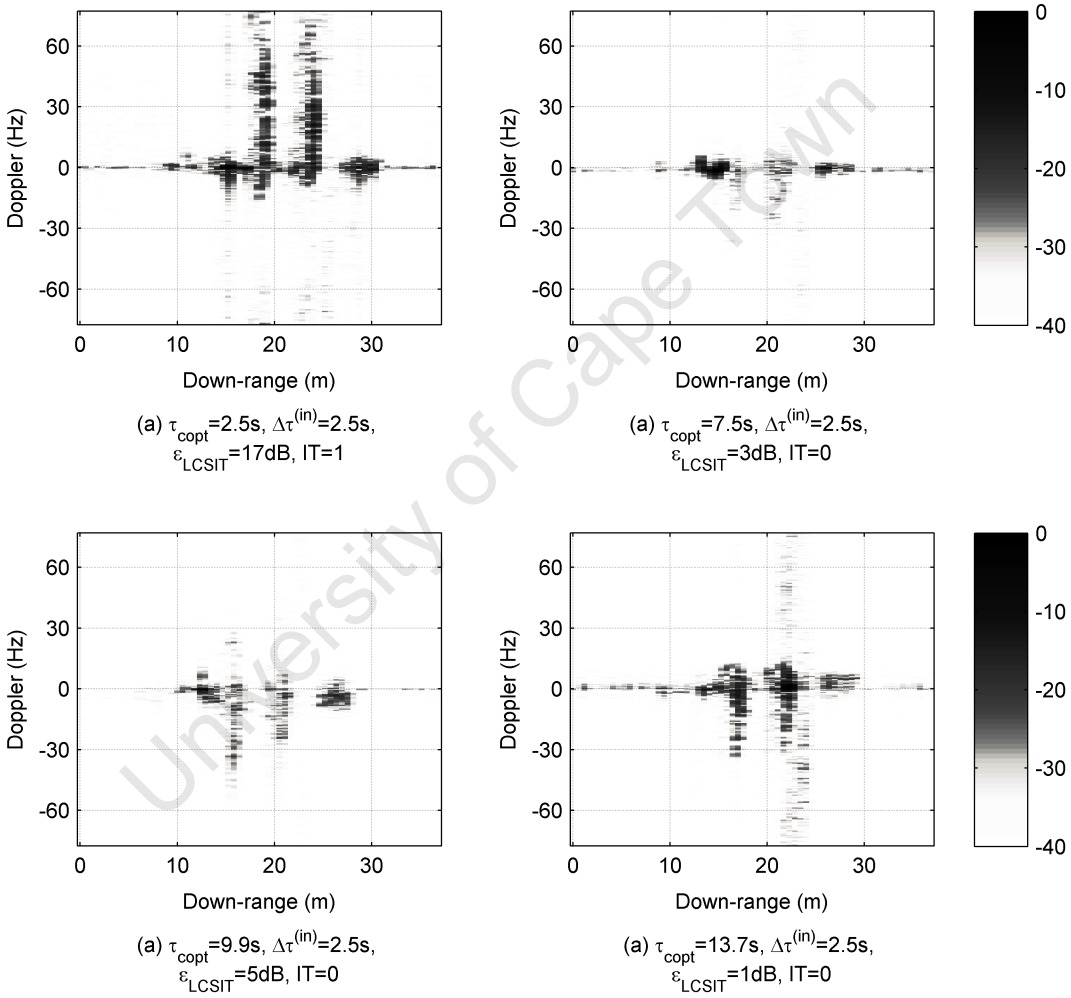

Figure 6.5: Candidate optimum ISAR images of the Esperance radar recording corresponding to the candidate optimum intervals for $\Delta\tau^{(in)} = 2.5$ s

Next, the overlapping accepted candidate optimum intervals are identified, and only the accepted candidate optimum interval with the longest initial CPTWL is retained. Thereafter, the EWLE algorithm is applied to the non-overlapping intervals that remain to estimate the optimum CPTWL associated with each interval. The optimum centre times and the optimum CPTWLs that are estimated correspond to the parameters of the optimum imaging intervals.

Figure 6.6 illustrates the non-overlapping accepted candidate optimum intervals and the optimum imaging intervals that were estimated from the Esperance recording. The motion compensated ISAR images corresponding to the optimum imaging intervals are shown in Figure 6.7. The results show that four optimum imaging intervals were estimated and that each interval produced a highly focused side-view ISAR image, which provides discriminant information for operator assisted ship classification.

Results from applying the EMC-ATWS algorithm to the Tigresse radar recording are shown in Figure 6.8, Figure 6.9, Figure 6.10 and Figure 6.11. In summary, the EMC-ATWS algorithm estimates four optimum imaging intervals that each produce highly focused side-view ISAR images of the Tigresse.

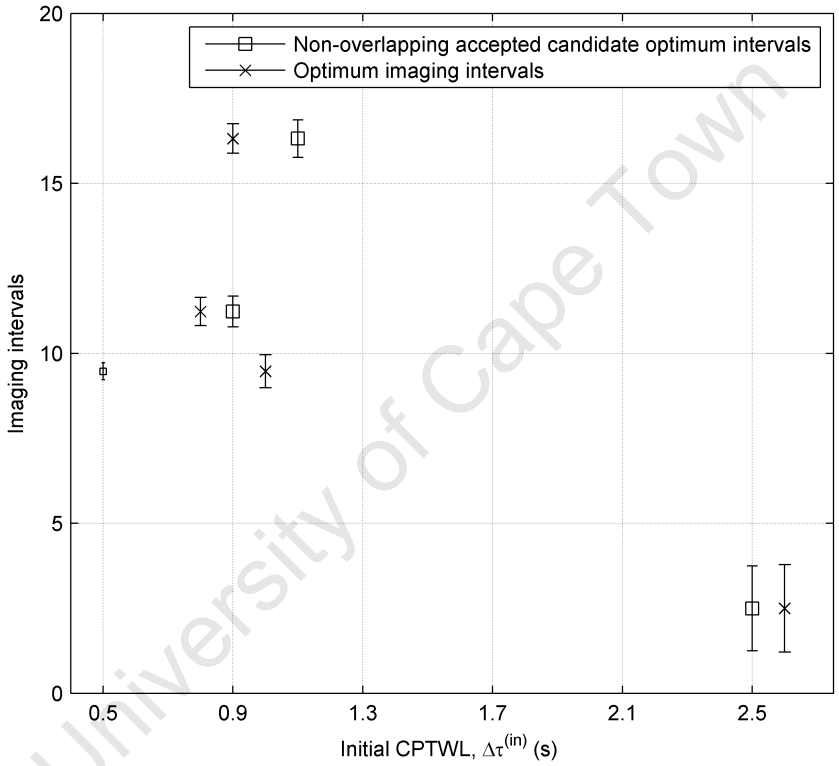

Figure 6.6: Diagram showing the non-overlapping accepted candidate optimum intervals and the optimum imaging intervals after applying the proposed EMC-ATWS algorithm to the Esperance radar recording

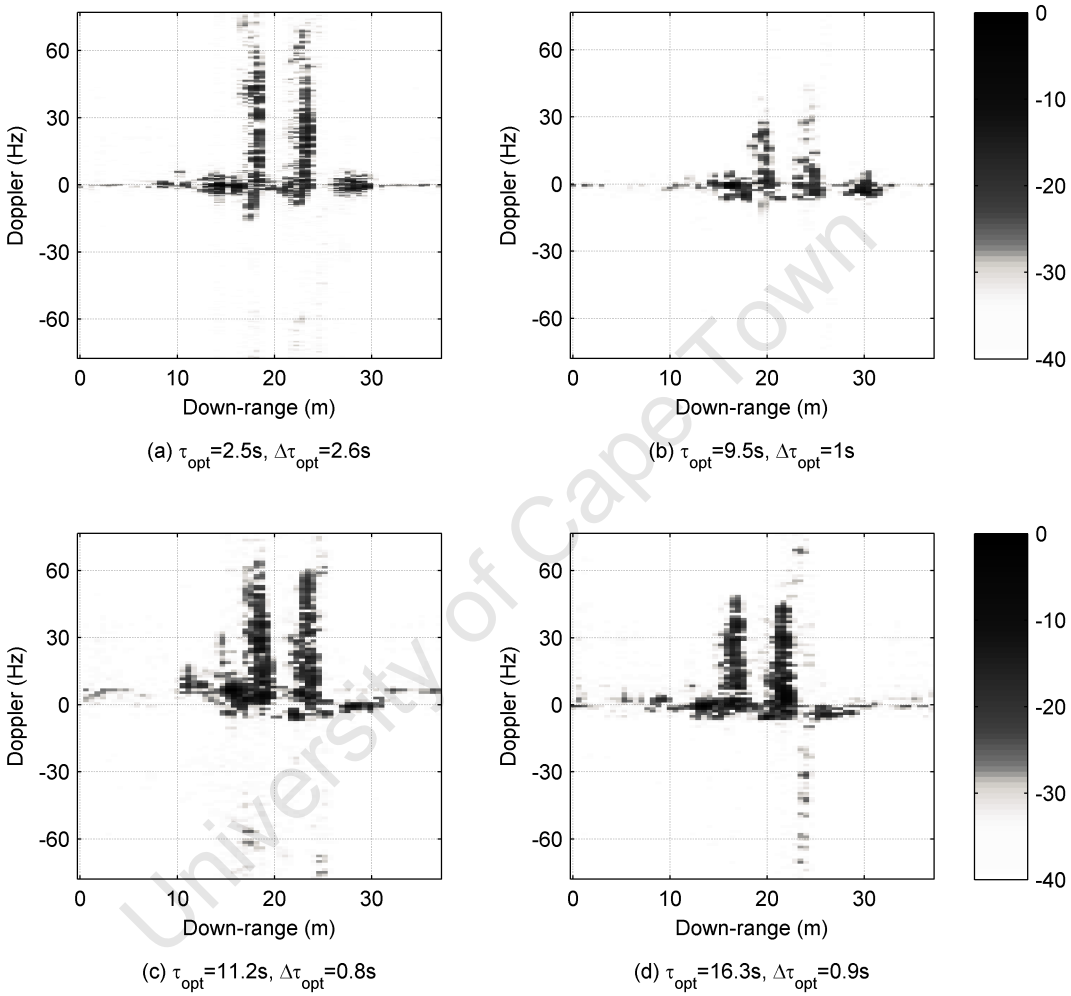

Figure 6.7: Results from applying the EMC-ATWS algorithm to the radar recording of the Esperance: motion compensated ISAR images obtained from the optimum imaging intervals with parameters (a) $\tau_{opt} = 2.5$ s and $\Delta\tau_{opt} = 2.6$ s , (b) $\tau_{opt} = 9.5$ s and $\Delta\tau_{opt} = 1$ s , (c) $\tau_{opt} = 11.2$ s and $\Delta\tau_{opt} = 0.8$ s , (d) $\tau_{opt} = 16.3$ s and $\Delta\tau_{opt} = 0.9$ s

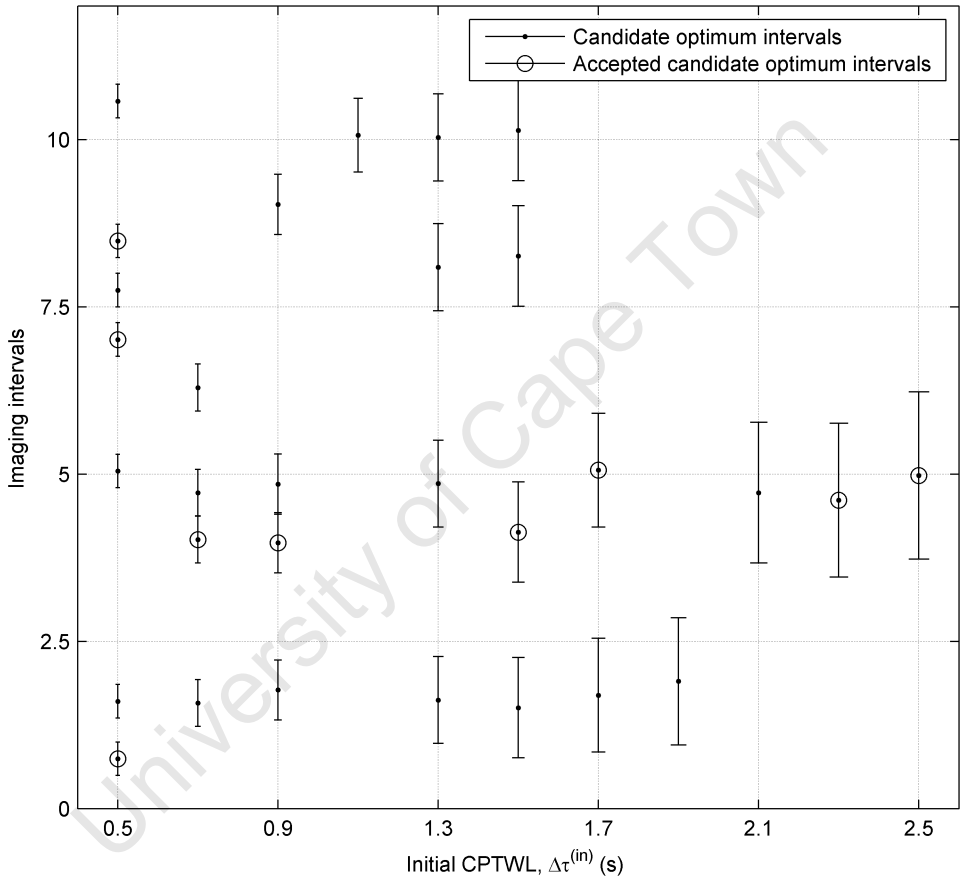

Figure 6.8: Diagram showing the candidate optimum intervals and the accepted candidate optimum intervals that are identified after applying the proposed EMC-ATWS algorithm to the Tigresse radar recording

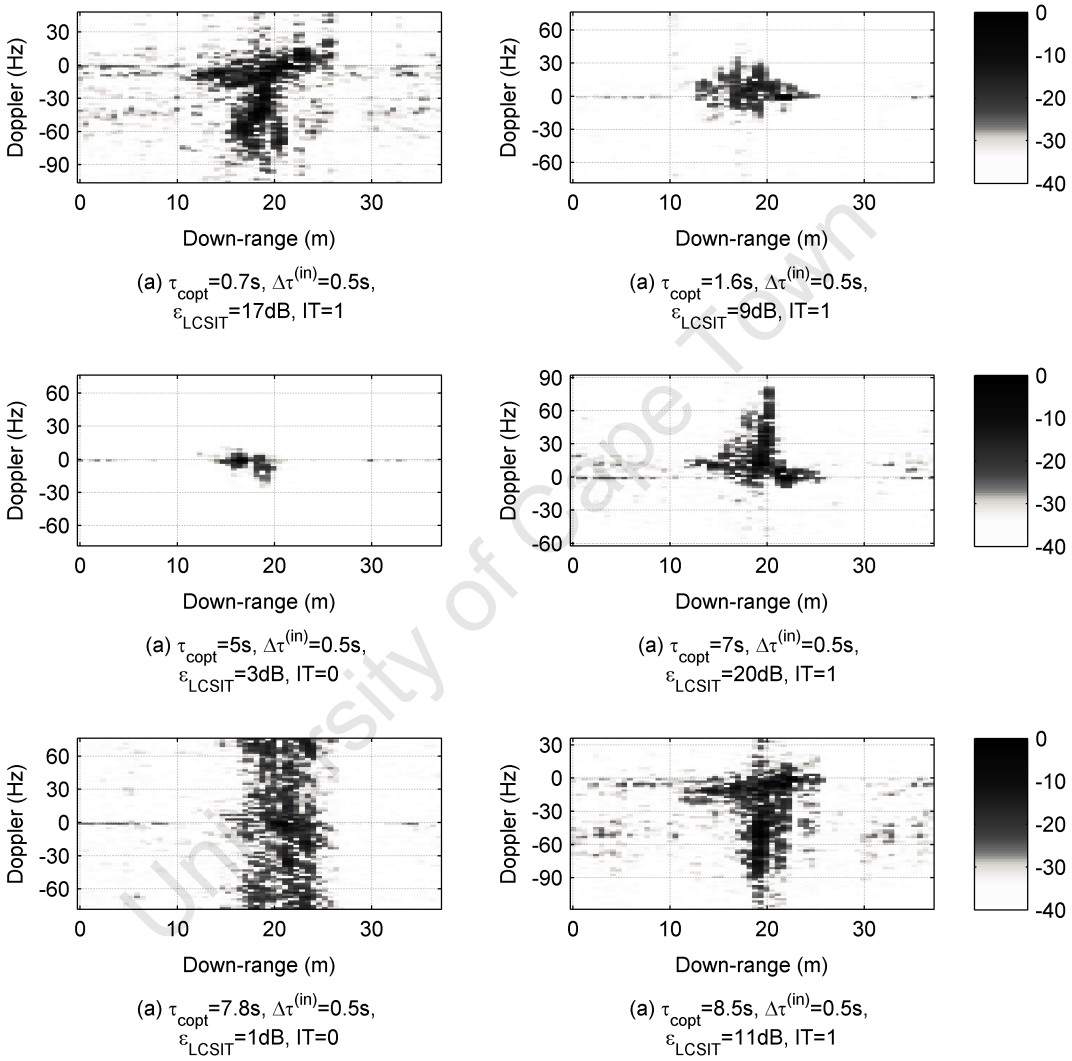

Figure 6.9: Candidate optimum ISAR images of the Tigresse radar recording corresponding to the candidate optimum intervals for $\Delta\tau^{(in)} = 0.5$ s

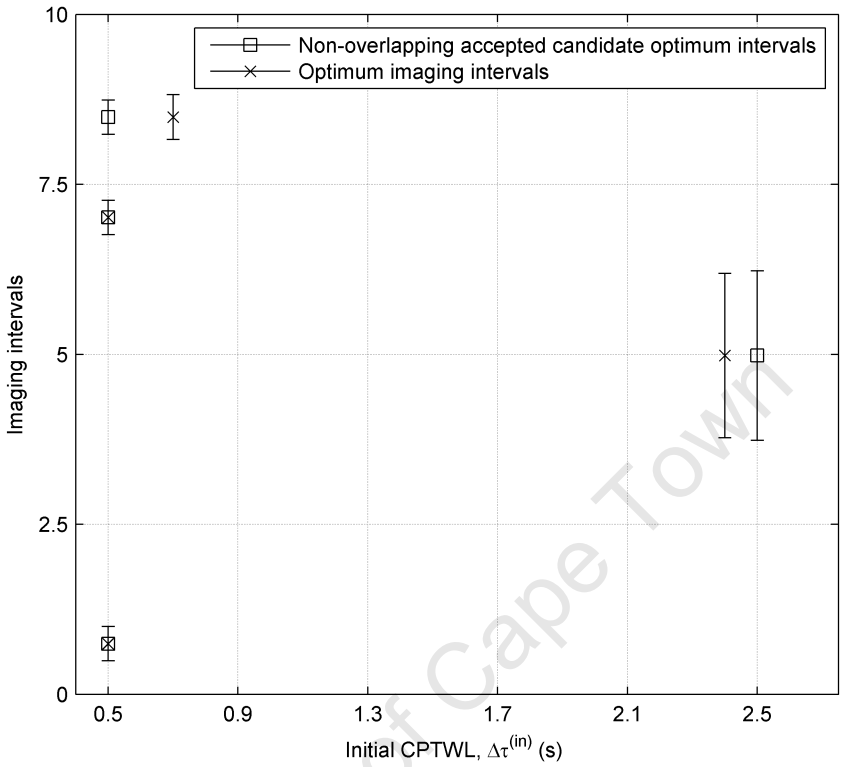

Figure 6.10: Diagram showing the non-overlapping accepted candidate optimum intervals and the optimum imaging intervals after applying the proposed EMC-ATWS algorithm to the Tigresse radar recording

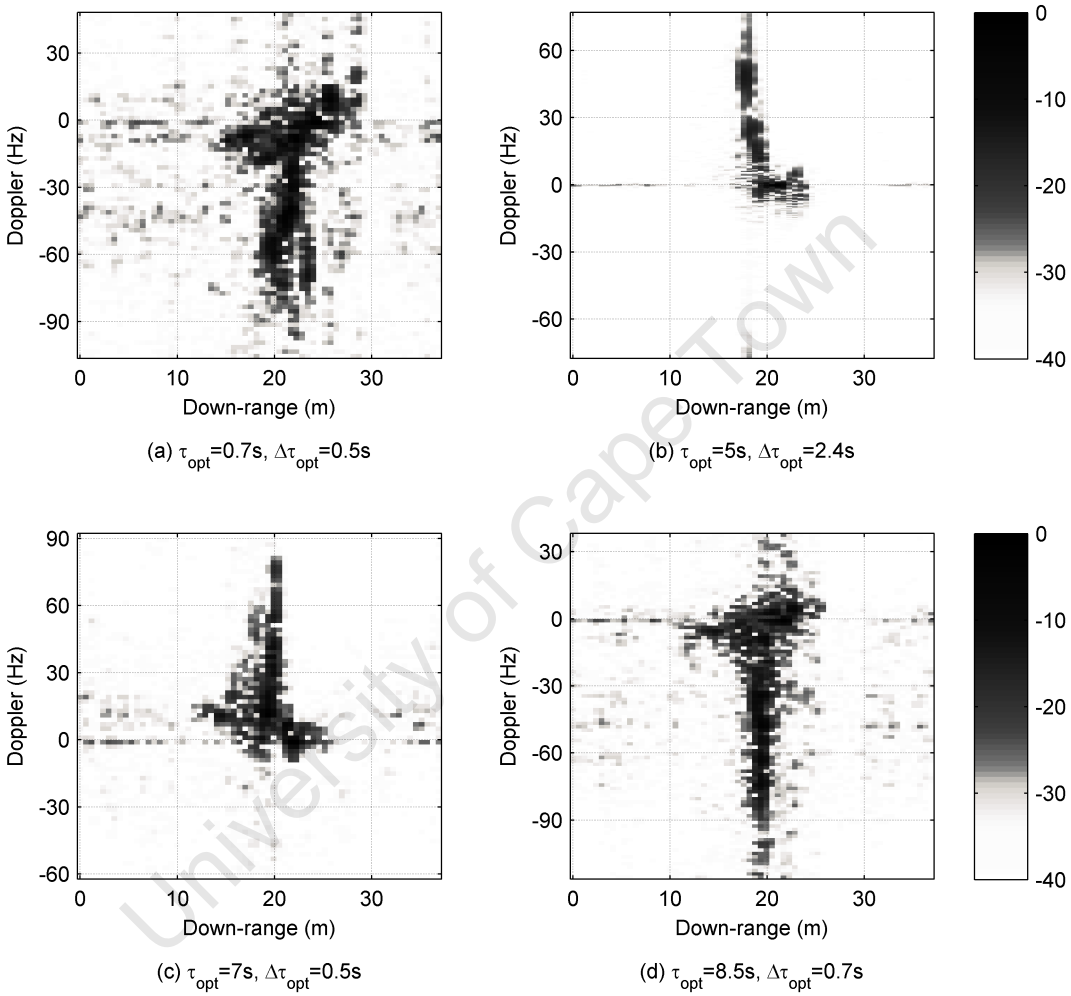

Figure 6.11: Results from applying the EMC-ATWS algorithm to the radar recording of the Tigresse: motion compensated ISAR images obtained from the optimum imaging intervals with parameters (a) $\tau_{opt} = 0.7$ s and $\Delta\tau_{opt} = 0.5$ s , (b) $\tau_{opt} = 5$ s and $\Delta\tau_{opt} = 2.4$ s , (c) $\tau_{opt} = 7$ s and $\Delta\tau_{opt} = 0.5$ s , (d) $\tau_{opt} = 8.5$ s and $\Delta\tau_{opt} = 0.7$ s

In conclusion, results from measured radar data show that the proposed EMC-ATWS algorithm is an effective technique for estimating multiple optimum imaging intervals that produce focused side-view ISAR images of small non-cooperative sea vessels.

6.6 Conclusions

This chapter proposed a new algorithm, referred to as the EMC-ATWS algorithm, for estimating multiple optimum imaging intervals for ISAR imaging of small non-cooperative sea vessels, which possess prominent superstructures and are sailing inbound/outbound with respect to the radar. The proposed algorithm uses a range of initial CPTWLs and a modified formulation of the IC to estimate the parameters of multiple optimum imaging intervals that produce side-view ISAR images.

Both the MC-ATWS and the EMC-ATWS algorithms were applied to measured radar recordings of two inbound non-cooperative yachts. Results showed that the MC-ATWS algorithm estimated the parameters of a single optimum imaging interval that produced a highly focused ISAR image with very little Doppler information, which is undesirable for operator assisted ship classification. Conversely, the EMC-ATWS algorithm estimated the parameters of multiple optimum imaging intervals that each generated a highly focused side-view ISAR image.

In summary, results from measured radar data showed that the proposed EMC-ATWS algoritm was an effective technique for estimating multiple optimum imaging intervals that produce focused side-view ISAR images of small non-cooperative vessels, which contain discriminant information for operator assisted ship classification

Chapter 7

Conclusions and Scope for Future Work

7.1 Conclusions

It has been shown in the literature that ISAR images of aircraft and sea vessels are a rich source of information for classification [7] and RCS measurement purposes [11], [12]. ISAR uses the 2-D rotational motion of an object to form a radar image. However, maritime objects possess 3-D rotational motion that often gives rise to blurry ISAR imagery, which is not desirable because blurry imagery reduces the probability of correct classification [31].

This thesis has focused on ISAR imaging of cooperative and non-cooperative sea vessels with 3-D rotational motion. The following aspects of ISAR imaging of sea vessels were addressed:

1. The effect of a vessel's 3-D rotational motion on ISAR imagery

2. Extraction of a vessel's image-generating Doppler components from measured motion data

3. Selection of suitable CPTWLs that limit the blurring in ISAR imagery of cooperative sea vessels

4. Selecting multiple optimum imaging intervals that produce side-view ISAR images of non-cooperative sea vessels

Chapter 3 investigated the effect of 3-D rotational motion on ISAR imaging. A new quaternion-based system model was proposed to represent the 3-D rotational motion of a sea vessel. The proposed system model provided the advantage of directly and independently modelling a vessel's image-generating Doppler components over the CPI. Furthermore, the model was flexible enough to incorporate measured motion data. Theory and simulations were used to show that, when a vessel's Doppler generating axis of rotation varies over time, it causes scatterers to migrate through cross-range cells. One of the simulations characterised the migration of a single scatterer through cross-range cells that was exclusively due to the time-varying nature of the Doppler generating axis of rotation, which has not been shown in the literature. In summary, results in Chapter 3 provided a detailed understanding of how 3-D rotational motion gives rise to blurring in ISAR imagery.

Chapter 4 proposed a new quaternion-based transformation that extracts the image-generating Doppler components from the measured attitude and GPS position data of an object. Furthermore, an improved quaternion-based system model was proposed that is computationally more efficient than the system model presented in Chapter 3. The proposed transformation was applied to measured motion data of a yacht, and the results showed that both the angle of the Doppler generating axis of rotation and the effective angular rotation rate varied over time. However, there were intervals where the image-generating Doppler components did not vary over time and by choosing radar data that corresponded to these intervals, ISAR images with limited blurring were obtained. Thus, the proposed transformation is a useful tool for assessing the degree of 3-D rotational motion that exists in a CPI for cooperative ISAR applications. In essence, the transformation provides the ability to gain an in-depth understanding of the time-varying nature of the image-generating Doppler components and it shows

that, when the image-generating Doppler components vary over time, it causes blurring in ISAR imagery.

In Chapter 5, a new technique was proposed, which is referred to as the MACS algorithm, that uses measured motion data to select suitable CPTWLs, which limits the blurring in ISAR images of cooperative vessels. The MACS algorithm was applied to motion datasets of three different classes of vessels: a yacht, a fishing trawler and a survey vessel. Results showed that longer CPTWLs are needed for larger vessels. The effectiveness of the suggested CPTWLs was demonstrated by using the measured radar data of a yacht. A good feature associated with the MACS algorithm is that the suggested range of suitable CPTWLs is much smaller than that reported in [40]. In addition, the proposed technique can be used to select an effective initial CPTWL for Martorella/Berrizi's optimum imaging selection algorithm, when it is applied to measured radar data of small vessels with chaotic motion. Lastly, when the radar and motion data are time-stamped using the same time clock, the MACS algorithm is able to offer significant computational savings by identifying subsets of radar data that would produce ISAR images with limited blurring for cooperative ISAR applications.

Chapter 6 proposed a new technique, referred to as the EMC-ATWS, that estimated the parameters of multiple optimum imaging intervals for generating focused side-view ISAR images of small non-cooperative sea vessels. The proposed algorithm uses a range of initial CPTWLs and a modified formulation of the IC to estimate the parameters of multiple optimum imaging intervals. The proposed EMC-ATWS algorithm was applied to radar recordings of two non-cooperative yachts. Results show that the EMC-ATWS algorithm estimated the parameters of multiple optimum imaging intervals that generated highly focused side-view ISAR images. Thus, the EMC-ATWS algorithm is an effective technique for identifying side-view ISAR images of small non-cooperative vessels, which contain discriminant information for operator assisted ship classification.

In summary, this thesis provided an in-depth understanding of how a vessels's 3-D rotational motion gives rise to blurring in ISAR imagery. A quaternion-based transformation was proposed to extract the image-generating Doppler compo-

nents from measured data, and the results showed that it is the time-varying nature of the image-generating Doppler components that causes blurring in measured ISAR imagery. The extracted time-varying image-generating Doppler components were used to develop a new technique, referred to as the MACS algorithm, which selected suitable CPTWLs to limit the blurring in ISAR imagery of cooperative vessels. Lastly, the EMC-ATWS algorithm was proposed for estimating the parameters of multiple optimum imaging intervals that produce side-view ISAR images of small non-cooperative sea vessels; these side-view ISAR images provide discriminant information for operator assisted ship classification.

7.2 Future Work

This section describes future directions for research into ISAR imaging of sea vessels. In maritime surveillance applications, ISAR images of vessels are used to provide a rich source of information for classification purposes. As a result, future work that needs to be done in order to develop an ISAR-based classification algorithm includes the following:

- **ISAR imaging of sea vessels from a non-stationary platform**: The proposed persistent maritime area surveillance system for the South African EEZ, referred to as Awarenet, requires classification of sea vessels in order to provide situational awarenss relating to activities of interest, such as illegal fishing and search and rescue. In the current Awarenet design, the primary radar will be located inside a high altitude airship to cover a large area of sea. The system is envisaged to operate in a wide range of environmental conditions, which include strong winds. As a result, the radar platform is non-stationary and the radar's received signal will include Doppler information due to the movement of the platform. Further research needs to be done into accurately measuring the motion of the non-stationary platform, and compensating for the platform's movement, in order to form focused ISAR images of vessels at sea.

- **Extending the point-scatterer model to obtain more realistic ISAR images of sea vessels**: The current point-scatterer model, which was used in Chapter 3 and Chapter 4, is limited because it assumes that a complex object can simply be represented by point-scatterers. The model ignores scattering phenonma such as diffraction and migration of a specular point of reflection for curved surfaces. A simple way of extending the simulation model is to use a physical optics (PO) facet model of sea vessels, which is discussed in papers by Garcia-Fernandez et al. [129]. Thereafter, existing electromagnetic simulation, such as CADRCS or SPECRAY EM, can be used to obtain more realistic EM backscatter of radar energy from a 3-D model of a vessel.

- **Generating focused and artefact-free ISAR images of sea vessels**: Focused and artefact-free ISAR images of sea vessels are desirable, because they provide a rich source of information for accurate extraction of features for ship classification purposes. Further research needs to be done to investigate the effect of multipath, realistic EM backscatter and sea clutter on ISAR images and to evaluate techniques that remove artefacts caused by these phenomena in ISAR images.

- **Classifying ships using ISAR imagery**: ISAR images of sea vessels are a rich source of information for ship classification. Further work needs to be done to extract discriminant features from ISAR images, which can be used for classification purposes.

- **Bi-static ISAR imaging of sea vessels**: Bi-static ISAR of sea vessels is another important area of future research.

Appendix A

Signal Hill 2007: Cooperative yacht measurements

This appendix provides an overview of the measurement trial performed at Signal Hill, Cape Town during November 2007, and it later focuses on the cooperative yacht measurements. During this measurement campaign, radar recordings were made of cooperative and non-cooperative sea vessels. Cooperative vessels were instrumented with the ADU5 system developed by Thales, which uses four GPS antennas to compute the attitude and position of an object. The trial lasted for two weeks and the key objectives were to obtain real world datasets for the detection of small boats at sea, which was the topic of research for Dr P. Herselman and R. de Wind, and ISAR imaging of sea vessels with 3-D rotational motion, which was researched by the candidate with support from his CSIR supervisor, W. A. J. Nel, and his UCT promoter, Prof M. R. Inggs.

During the trial, an experimental X-band radar was deployed at Signal Hill at a GPS location of $33°55'15.62''S$, $18°23'53.76''E$ at a height of 308 m above mean sea level. A plan view of the deployment site is illustrated in Figure A.1, with kind permission from Herselman *et al.* [130], and a photo of the experimental radar is shown in Figure A.2. The deployment site provided an azimuth coverage of 140° that spanned a large section of open sea. This made it possible to

measure non-cooperative vessels when they were approaching or leaving Cape Town harbour.

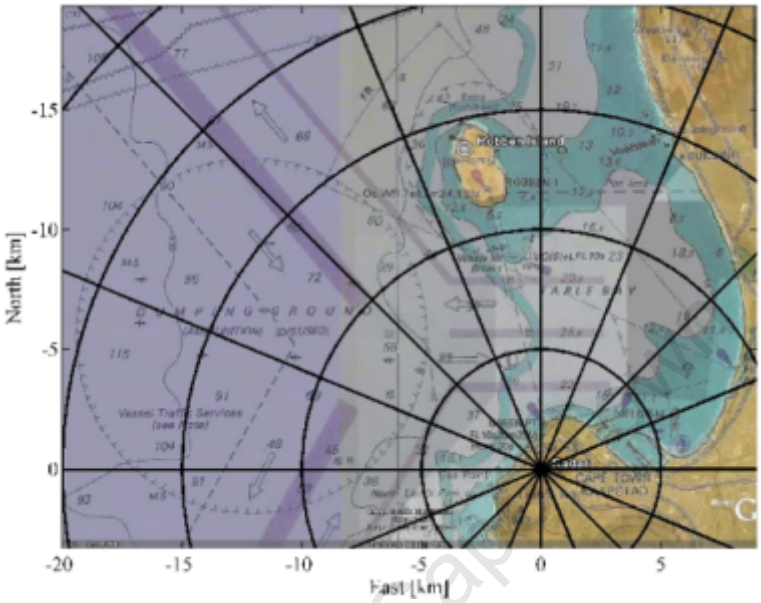

Figure A.1: Plan view of the deployment site

Stepped frequency waveforms were used to obtain radar recordings of the vessels. The measured HRR profiles were compensated for by using point scatterer test targets, which consisted of a sphere suspended by a helicopter (see Figure A.3). Recordings of the sphere were used to compensate for the measured HRR profiles of the vessel for the radar's non-linear and non-ideal response over the measurement band.

During the Signal Hill deployment, both radar and motion data were obtained from the Esperance, which is illustrated in Figure A.4. The rest of this appendix provides more details of the experiments involving the Esperance, since the related data recordings are used in Chapters 1, 4 and 5 of this thesis.

Figure A.5 illustrates how the four GPS antennas of the ADU5 system were mounted at the back of the Esperance during the cooperative experiment. The data processing and recording system, shown in Figure A.5, was placed in the hatch of the vessel to prevent it from coming into contact with water. A 12V battery was used to power the ADU5's data processing unit, which streamed the

Figure A.2: Photo of the experimental radar on Signal Hill

Figure A.3: The sphere test target

Figure A.4: Photo of the Esperance

processed data to a laptop. The system was developed to capture motion data continuously for up to six hours. Furthermore, it was designed to be mobile so that this measured system could be used for a variety of different cooperative vessels. The mobile measurement system was jointly developed by the candidate as well as W. A. J. Nel, P. Barlow, A. Cilliers and M. Goosen.

Since the ADU5 system is a joint INS/GPS system, it measured the heading, bank, elevation and GPS coordinates of the vessel. Before the start of the experiment, it was the responsibility of the candidate to instruct the captain of the vessel to perform two different sailing profiles: an inbound/outbound profile, where the change in the elevation of the vessel was used to generate a side-view ISAR image, and a turning/circular profile, where the change in heading of the vessel was used to produce a top-view ISAR image. Figure A.7 illustrates the sailing profile of the yacht through the entire experiment, which spanned approximately 2 hours and 12 minutes. The two sailing profiles that were requested are clearly illustrated in Figure A.8.

The raw motion data that was recorded by the ADU5 system throughout the experiment is shown in Figure A.9 and Figure A.10. The attitude measurements in Figure A.10 indicate that there are intervals when the heading of the vessel is inaccurate. For example, see recording at approximately 2400 s where the heading changes significantly over a short time. There are also intervals where

Figure A.5: ADU5 system instrumented on the Esperance

the elevation and bank measurements are incorrect because they do not vary over time (see recording between 5800 s and 5950 s). However, for most of the measurements, these inaccuracies are not present and care was taken only to process subsets of data where these inaccuraties were not present. Examples of such subsets of motion data are shown in Figure A.11 and Figure A.12. These motion datasets were smoothed by using a third order polynomial fit to reduce the measurement error before they were used in Chapter 4 and Chapter 5 of this thesis.

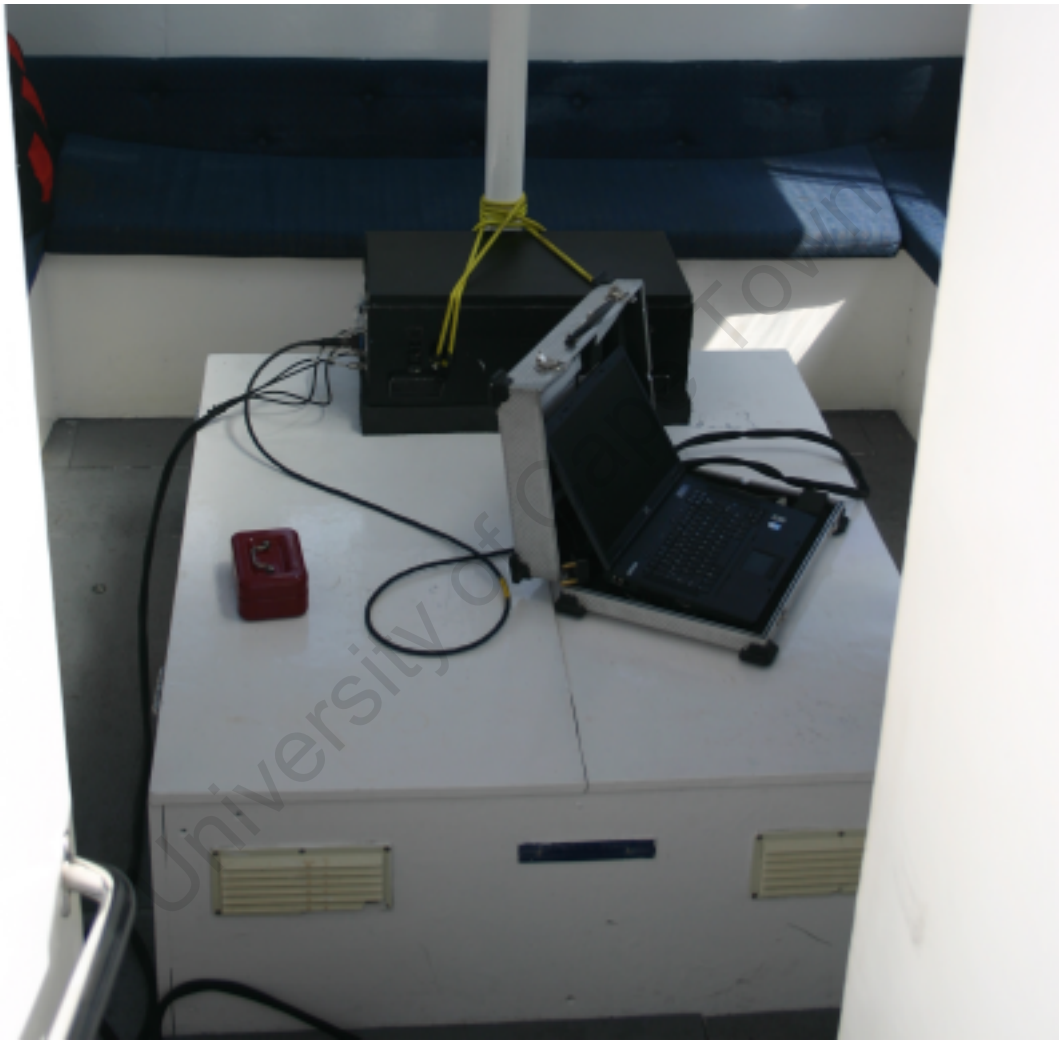

Figure A.6: Data processing and data capture unit

Figure A.7: Sailing profile of the yacht over the entire experiment

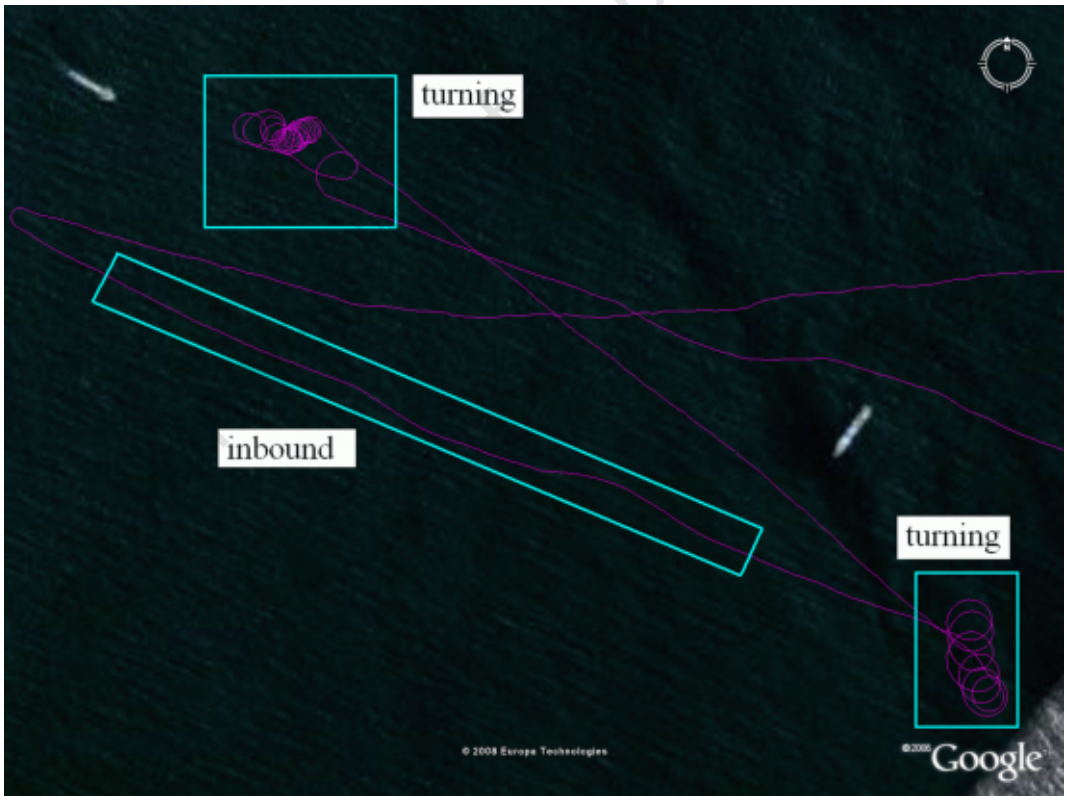

Figure A.8: Zoomed in diagram of the yacht's sailing profile, which clearly illustrates the requested inbound profile and the turning profile

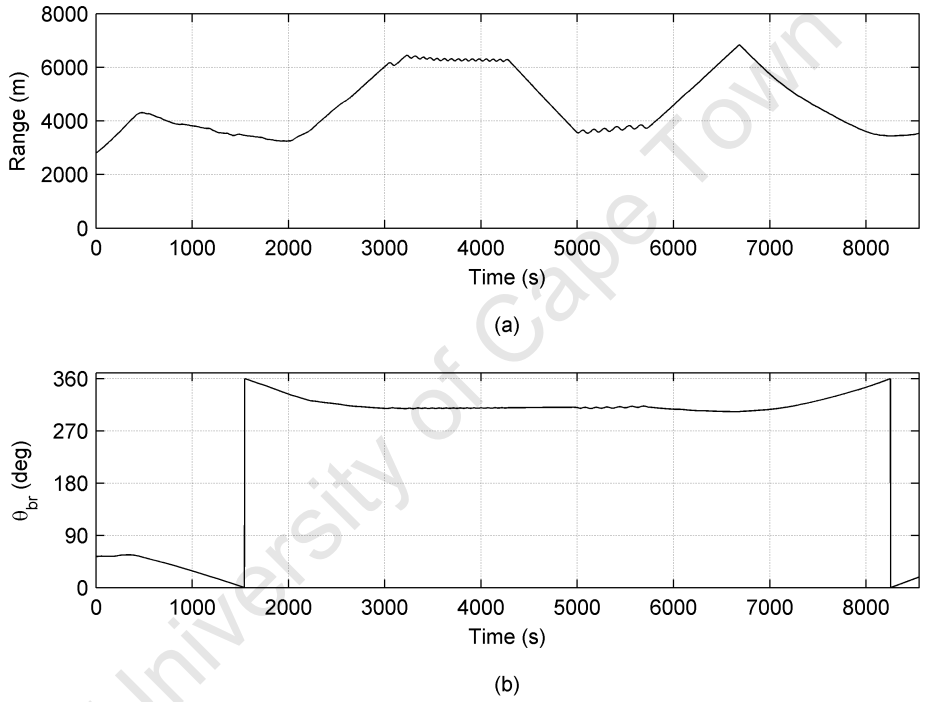

Figure A.9: (a) Range and (b) bearing measurement of the yacht during the entire experiment

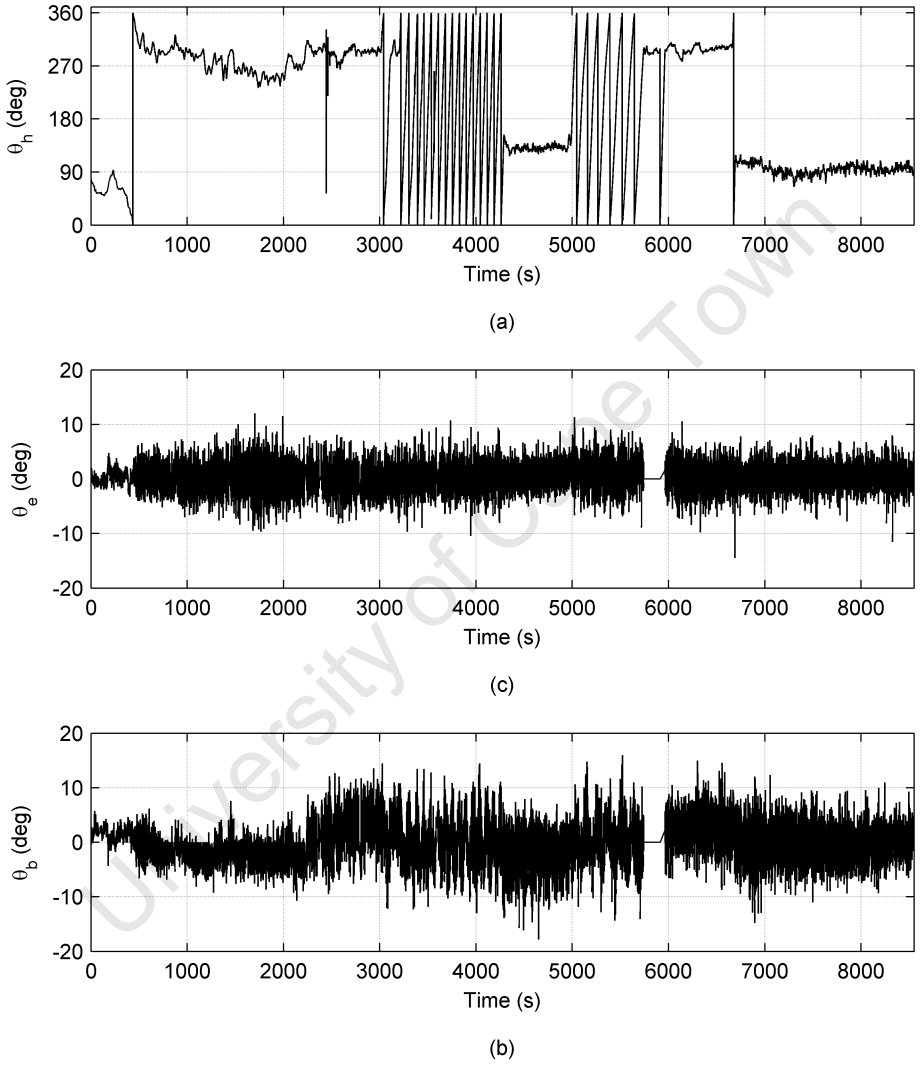

Figure A.10: (a) Heading, (b) elevation and (c) bank measurements of the yacht during the experiment

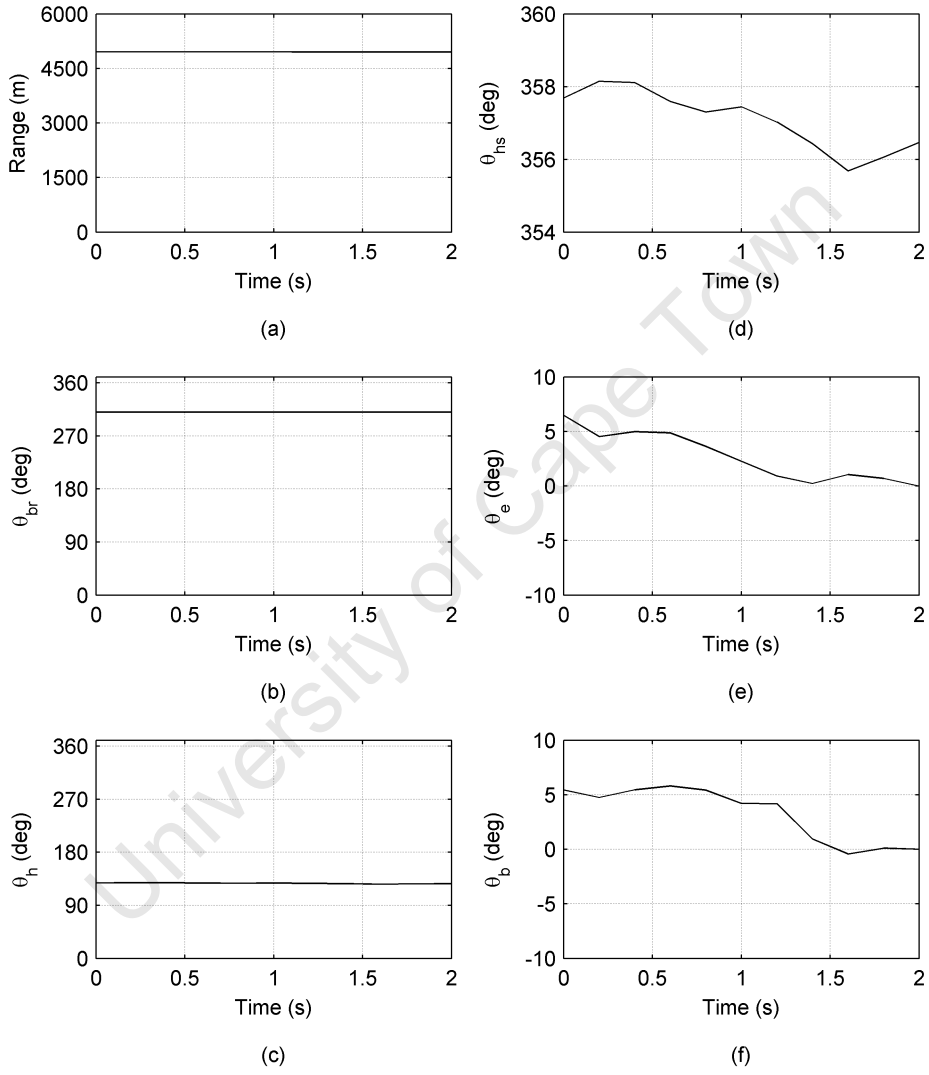

Figure A.11: Motion dataset of the Esperance yacht used in Chapter 4

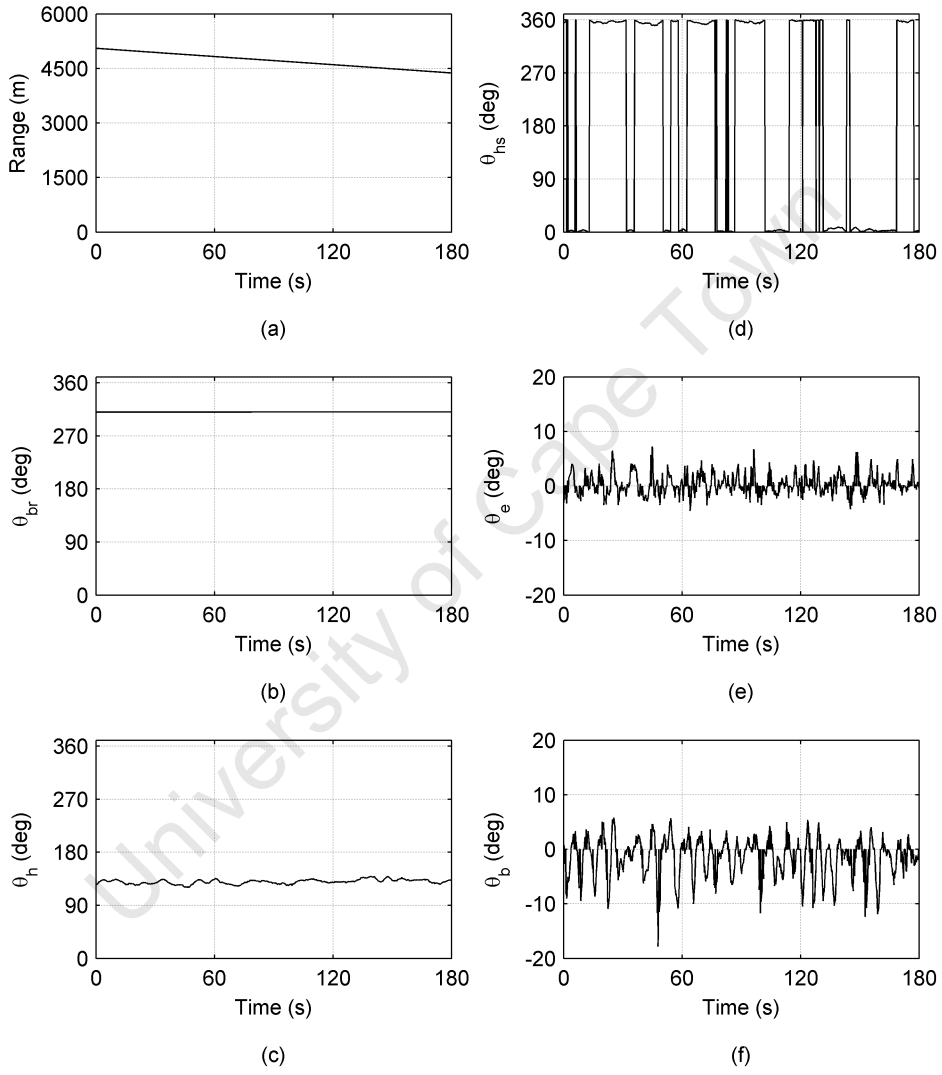

Figure A.12: Motion dataset of the Esperance yacht used in Chapter 5

Appendix B

Expressing the Doppler frequency of a scatter: comparison of two system models

This appendix provides a comparison of the quaternion-based system model proposed in this thesis with the system model originally proposed by Scaglione and Barbarossa [122], and later by Berizzi *et al.* in [1]. It is shown that under certain conditions, these two systems models equivalently express the Doppler frequency of a scatterer of interest.

The system model considered by Berizzi *et al.* in [1] is illustrated in Figure B.1. The global coordinates of the system are aligned with respect to the radar: the ξ_2 axis is aligned along the LOS and the target moves along the trajectory in the (ξ_1, ξ_2) plane. A target's translation and rotational motion give rise to the total angular rotation vector, denoted by $\mathbf{\Omega}_T(t)$. The projection of $\mathbf{\Omega}_T(t)$ on the plane orthogonal to the LOS is called the effective rotation vector $\mathbf{\Omega}_{eff}(t)$. The imaging plane (x_1, x_2) is orthogonal to the effective rotation vector, and x_3 is defined to be along the effective rotation vector. It should be noted that x_1 and x_2 axes are the cross-range and range coordinates of the imaging plane, respectively.

The reflectivity function of the target is defined by the introduction of a new reference system (y_1, y_2, y_3) that is embedded in the target and it is coincident that coordinate system of the reflectivity function is aligned to the coordinate system of the imaging plane.

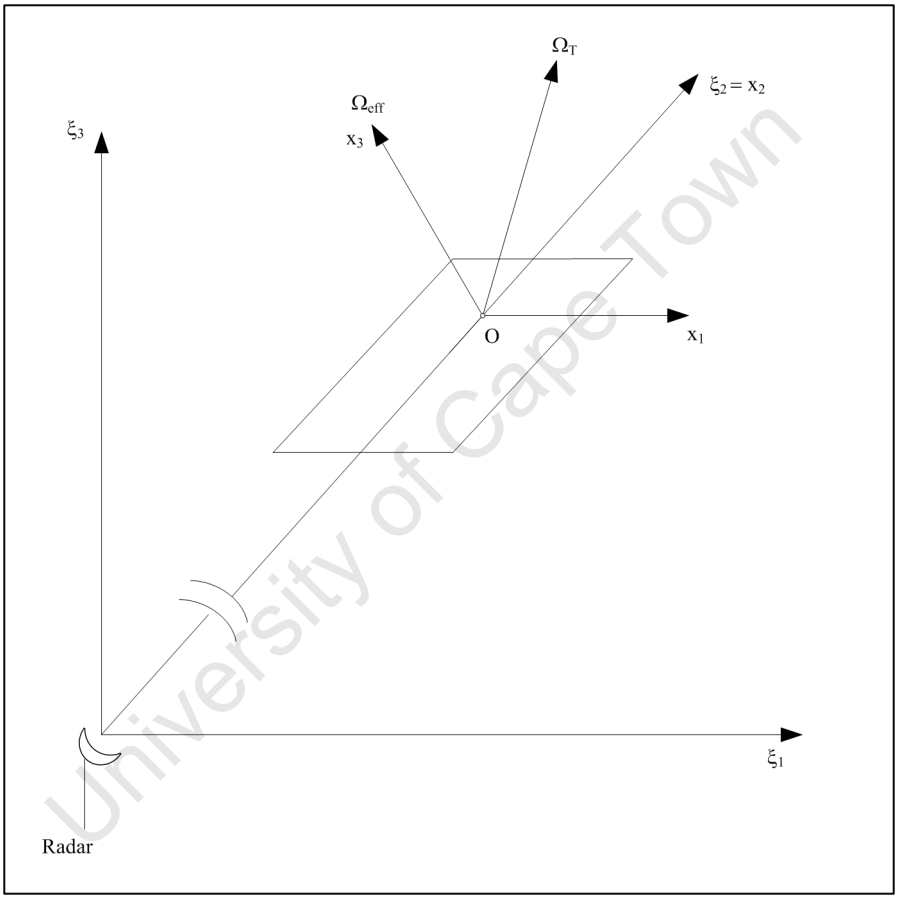

Figure B.1: System model proposed by Berizzi *et al.* in [1]

The received signal $S_R(f,t)$, after translation motion compensation, is written in the time-frequency format as:

$$S_R(f,t) = \int_V g(\mathbf{y})\, e^{-j(4\pi f/c)[\mathbf{y}.\mathbf{i}_{x2}(t)]}\, \mathrm{d}\mathbf{y} \;.\; \mathrm{rect}\left((t)/\Delta\tau\right) \quad \mathrm{rect}\left((f-f_0)/B\right) \quad \text{(B.1)}$$

where the symbols are defined as follows:

$$
\begin{aligned}
B &- \text{bandwidth of the transmitted signal} \\
f_0 &- \text{carrier frequency} \\
\Delta\tau &- \text{coherent processing time window length} \\
g(\mathbf{y}) &- \text{reflectivity function of the target} \\
V &- \text{volume where } g(\mathbf{y}) \text{ is defined} \\
\mathbf{i}_{x2}(t) &- \text{unit vector along the } x_2 \text{ axis}
\end{aligned}
$$

For small coherent processing time window lengths of less than 1 s, the total rotation vector is assumed to be constant over time:

$$\boldsymbol{\Omega}_T(t) \cong \boldsymbol{\Omega}_T \tag{B.2}$$

Under the assumption that the imaging plane remains constant over the CPTWL, the term $x_2(\mathbf{y}, t) = \mathbf{y} \cdot \mathbf{i}_{x2}(t)$ in B.1 can be expressed in closed form by solving the differential equation system $\dot{\mathbf{x}}(t) = \boldsymbol{\Omega}_T \times \mathbf{x}(t)$, with initial condition $\mathbf{x}(0) = \mathbf{y}$, that describes the target angular motions. The result is given by:

$$x_2(\mathbf{y}, t) = a_2(\mathbf{y}) + b_2(\mathbf{y}) \cos(\Omega_T t) + \frac{c_2(\mathbf{y})}{\Omega_T} \sin(\Omega_T t) \tag{B.3}$$

where

$$a_2(\mathbf{y}) = \frac{(\boldsymbol{\Omega}_T \cdot \mathbf{y})}{\Omega_T^2} \Omega_{T2} \tag{B.4}$$

$$b_2(\mathbf{y}) = y_2 - \frac{(\boldsymbol{\Omega}_y \cdot \mathbf{y})}{\Omega_T^2} \Omega_{T2} \tag{B.5}$$

$$c_2(\mathbf{y}) = \Omega_{eff} y_1 \tag{B.6}$$

Ω_T and Ω_{eff} denote the modulus of the vectors $\boldsymbol{\Omega}_\mathbf{T}$ and $\boldsymbol{\Omega}_\mathbf{eff}$ respectively. Ω_{T2} is the coordinate of $\boldsymbol{\Omega}_T$ along the x_2 axis. The authors of [1] state that when low spatial resolution is required, and by considering typical values of the angular velocity of ships, the term $\mathbf{x}_2(\mathbf{y}, t)$ can be reasonably approximated by its first-

order Taylor series around $t = 0$, which gives:

$$x_2(\mathbf{y}, t) = y_2 + \Omega_{eff} y_1 t \tag{B.7}$$

Thus, the Doppler frequency, $f_d(t)$ associated with a scatterer at position $\mathbf{y} = \{y_1, y_2\}$ is given by:

$$\begin{aligned} f_d(t) &= \frac{2}{\lambda}\frac{d}{dt}x_2 \\ &= \frac{2}{\lambda}\Omega_{eff} y_1 \end{aligned} \tag{B.8}$$

In the quaternion-based system model presented in Chapter 3, the Doppler frequency of the k^{th} scatterer is expressed in 3.50 as:

$$f_{d,k} = \frac{2}{\lambda}\left(\dot{\theta}_{eff} l_k\right) \tag{B.9}$$

where l_k is the distance of the scatterer from the Doppler generating axis of rotation and $\dot{\theta}_{eff}$ is the effective rotation rate.

It should be noted that these two system models both express the Doppler frequency of a scatterer in the same way. However, different notation is used in each case. In the quaternion-based system model l_k is used to denote the lever-arm distance, and Berizzi *et al.* use y_1 to denote this. Further, the quaternion-based system model uses $\dot{\theta}_{eff}$ to denote the modulus of the effective rotation rate and Berizzi *et al.* use Ω_{eff}.

Bibliography

[1] F. Berizzi, E. D. Mese, M. Diani, and M. Martorella, "High-resolution ISAR imaging of maneuvering targets by means of the range instantaneous doppler technique: Modeling and performance analysis," *IEEE Trans. Image Process.*, vol. 10, no. 12, pp. 1880–1890, Dec. 2001.

[2] C. Chen and H. C. Andrews, "Multifrequency imaging of radar turntable data," *IEEE Trans. Aerosp. Electron. Syst.*, vol. 16, no. 1, pp. 15–22, Jan. 1980.

[3] J. Walker, "Range-Doppler imaging of rotating objects," *IEEE Trans. Aerosp. Electron. Syst.*, vol. 16, no. 1, pp. 23–52, Jan. 1980.

[4] D. L. Mensa, *High Resolution Radar Imaging.* Dedham, MA: Artech House, 1981.

[5] C. Chen and H. C. Andrews, "Target-motion-induced radar imaging," *IEEE Trans. Aerosp. Electron. Syst.*, vol. 16, no. 1, pp. 2–14, Jan. 1980.

[6] N. Bon, G. Hajduch, A. Khenchaf, R. Garello, and J.-M. Quellec, "Recent developments in detection, imaging and classification for airborne maritime surveillance," *IET Signal Processing*, vol. 2, no. 3, pp. 192–203, Sep. 2008.

[7] S. Musman, D. Kerr, and C. Bachmann, "Automatic recognition of ISAR ship images," *IEEE Trans. Aerosp. Electron. Syst.*, vol. 32, no. 4, pp. 1392–1404, Oct. 1996.

[8] M. M. Menon, E. R. Boudreau, and P. J. Kolodzy, "An automatic ship classification system for ISAR imagery," *The MIT Lincoln Laboratory Journal*, vol. 6, no. 2, pp. 289–308, 1993.

[9] E. C. Botha, "Classification of aerospace targets using superresolution ISAR images," in *Proc. IEEE South African Symposium on Communications and Signal Processing COMSIG-94*, Oct. 1994, pp. 138–145.

[10] K. Kim, D. Seo, and H. Kim, "Efficient classification of ISAR images," *IEEE Trans. Antennas Propag.*, vol. 53, no. 5, pp. 1611–1621, May 2005.

[11] A. Jain and I. Patel, "Dynamic imaging and RCS measurements of aircraft," *IEEE Trans. Aerosp. Electron. Syst.*, vol. 31, no. 1, pp. 211–226, Jan. 1995.

[12] J. A. Given and W. R. Schmidt, "Generalized ISAR - part I: An optimal method for imaging large naval vessels," *IEEE Trans. Image Process.*, vol. 14, no. 11, pp. 1783–1791, Nov. 2005.

[13] M. T. Fennel and R. P. Wishner, "Battlefield awareness via synergistic SAR and MTI exploitation," *IEEE Aerosp. Electron. Syst. Mag.*, vol. 13, no. 2, pp. 39–45, Feb. 1998.

[14] T. Sauer, K. Bethke, F. Buettner, B. Roede, and A. Schroth, "Imaging of commercial aircraft by inverse synthetic aperture radar and their classification in a near-range radar network (NRN)," in *Proc. IEEE National Radar Conference*, May 1997, pp. 19–24.

[15] J. M. Munoz-Ferreras, J. Calvo-Gallego, and F. Perez-Martinez, "Monitoring road traffic with a high resolution LFMCW radar," in *Proc. IEEE Radar Conference RADAR '08*, May 2008, pp. 1–5.

[16] Y. Yoon and M. G. Amin, "High-resolution through-the-wall radar imaging using beamspace MUSIC," *IEEE Trans. Antennas Propag.*, vol. 56, no. 6, pp. 1763–1774, Jun. 2008.

[17] J. A. Trischman, J. R. Bennett, K. A. Melendez, B. F. Summers, J. Sorensen, K. B. Cooper, and P. H. Siegel, "Inverse synthetic aperture radar imaging at 580 GHz," in *Proc. 33rd International Conference on Infrared, Millimeter and Terahertz Waves IRMMW-THz 2008*, Sep. 2008, pp. 1–2.

[18] N. J. S. Stacy, D. P. Badger, A. S. Goh, M. Preiss, and M. L. Williams, "The DSTO Ingara airborne X-band SAR polarimetric upgrade: first results," in *Proc. 2003 IEEE International Geoscience and Remote Sensing Symposium (IGARSS)*, vol. 7, Jul. 2003, pp. 4474–4476.

[19] G. Hajduch, J. M. Le Caillec, and R. Garello, "Airborne high-resolution ISAR imaging of ship targets at sea," *IEEE Aerosp. Electron. Syst. Mag.*, vol. 40, no. 1, pp. 378–384, Jan. 2004.

[20] M. W. Barclay and N. K. Williams, "High resolution SAR/ISAR imaging from a helicopter platform," in *Proc. Radar 97 (Conf. Publ. No. 449)*, Oct. 1997, pp. 109–113.

[21] F. Anderson, "Persistent, ubiquitous surveillance technologies and system concepts for enhanced national safety and security," in *CSIR Conference 2008*, Pretoria, South Africa, Nov. 2008.

[22] J. Li, R. Wu, and V. C. Chen, "Robust autofocus algorithm for ISAR imaging of moving targets," *IEEE Trans. Aerosp. Electron. Syst.*, vol. 37, no. 3, pp. 1056–1069, Jul. 2001.

[23] J. M. Munoz-Ferreras and F. Perez-Martinez, "Uniform rotational motion compensation for inverse synthetic aperture radar with non-cooperative targets," *IET Radar Sonar Navig.*, vol. 2, no. 1, pp. 25–34, Feb. 2008.

[24] V. C. Chen and W. J. Miceli, "Simulation of ISAR imaging of moving targets," *IEE Proc. Radar, Sonar Navig.*, vol. 148, no. 3, pp. 160–166, Jun. 2001.

[25] F. Berizzi, "ISAR imaging of targets at low elevation angles," *IEEE Trans. Aerosp. Electron. Syst.*, vol. 37, no. 2, pp. 419–435, Apr. 2001.

[26] F. Prodi, "ISAR cross-range scaling using a correlation based functional," in *Proc. IEEE Radar Conference RADAR '08*, May 2008, pp. 1–6.

[27] M. Martorella, "Novel approach for ISAR image cross-range scaling," *IEEE Trans. Aerosp. Electron. Syst.*, vol. 44, no. 1, pp. 281–294, Jan. 2008.

[28] M. Martorella and F. Berizzi, "Time windowing for highly focused ISAR image reconstruction," *IEEE Trans. Aerosp. Electron. Syst.*, vol. 41, no. 3, pp. 992–1007, Jul. 2005.

[29] J. Wang and D. Kasilingam, "Global range alignment for ISAR," *IEEE Trans. Aerosp. Electron. Syst.*, vol. 39, no. 1, pp. 351–357, Jan. 2003.

[30] C. Yuan and D. Casasent, "Composite filters for inverse synthetic aperture radar," *Optical Engineering*, vol. 41, no. 1, pp. 94–104, Jan. 2002.

[31] F. E. McFadden and S. A. Musman, "Optimizing ship length estimates from ISAR images," in *Proceedings of the IEEE-INNS-ENNS International Joint Conference on Neural Networks*, vol. 1, Jul. 2000, pp. 163–168.

[32] A. Rihaczek and S. J. Hershkowitz, "Choosing imaging intervals for small ships," in *SPIE Proc. on Radar Processing, Technology, and Applications*, vol. 3810, Jul. 1999, pp. 139–148.

[33] V. C. Chen and R. Lipps, "ISAR imaging of small craft with roll, pitch and yaw analysis," in *Radar Conference, 2000. The Record of the IEEE 2000 International*, May 2000, pp. 493–498.

[34] J. Li, H. Ling, and V. C. Chen, "An algorithm to detect the presence of 3D target motion from ISAR data," *Multidimensional Systems and Signal Processing*, vol. 14, no. 1-3, pp. 223–240, Jan. 2003.

[35] V. C. Chen and W. J. Miceli, "Effect of roll, pitch and yaw motions on ISAR imaging," in *SPIE Proc. on Radar Processing, Technology, and Applications*, vol. 3810, Jul. 1999.

[36] ——, "Time-varying spectral analysis for radar imaging of manoeuvring targets," *IEE Proc. Radar, Sonar Navig.*, vol. 145, no. 5, pp. 262–268, Oct. 1998.

[37] F. Berizzi and M. Diani, "Target angular motion effects on ISAR imaging," *IEE Proc. Radar, Sonar Navig.*, vol. 144, no. 2, pp. 87–95, Apr. 1997.

[38] Z. Bao, G. Wang, and L. Luo, "Inverse synthetic aperture radar imaging of maneuvering targets," *Optical Engineering*, vol. 37, no. 5, pp. 1582–1588, May 1998.

[39] S. Wong, G. Duff, and E. Riseborough, "ISAR image distortion due to small perturbed motion and restoration of distorted images by time-frequency analysis," *Proceedings of the SPIE*, vol. 5102, pp. 200–212, Apr. 2003.

[40] D. R. Wehner, *High-Resolution Radar*, 2nd ed. Norwood, MA: Artech House, 1995.

[41] D. Pastina and C. Spina, "Slope-based frame selection and scaling technique for ship ISAR imaging," *IET Signal Processing*, vol. 2, no. 3, pp. 265–276, Sep. 2008.

[42] M. Y. Abdul Gaffar and W. A. J. Nel, "Investigating the effect of a target's time-varying Doppler generating axis of rotation on ISAR image distortion," in *Proc. IET International Conference on Radar Systems*, Session 5b, No 4, Oct. 2007, pp. 1–5.

[43] M. Y. Abdul Gaffar, W. A. J. Nel, and M. R. Inggs, "Quaternion-based transformation for extraction of image-generating Doppler for ISAR," *IEEE Geosci. Remote Sens. Lett.*, vol. 5, no. 4, pp. 560–563, Oct. 2008.

[44] ——, "Selecting suitable coherent processing time window lengths for ground-based ISAR imaging of cooperative sea vessels," *IEEE Trans. Geosci. Remote Sens.*, vol. 47, no. 9, pp. 3231–3240, Sept. 2009.

[45] ——, "Selecting optimum imaging intervals for side-view ISAR imaging of small non-cooperative sea vessels," *submitted to IEEE Geosci. Remote Sens. Lett.*, 2009.

[46] A. Aprile, D. Meledandri, T. M. Pellizzeri, and A. Mauri, "Translational rotational motion compensation: A single algorithm for different radar imaging applications," *IET Signal Processing*, vol. 2, no. 3, pp. 204–215, Sep. 2008.

[47] V. C. Chen and S. Qian, "Joint time-frequency transform for radar range-Doppler imaging," *IEEE Trans. Aerosp. Electron. Syst.*, vol. 34, no. 2, pp. 486–499, Apr. 1998.

[48] B. R. Mahafza, *Radar Systems Analysis and Design using Matlab.* Boca Raton, Florida: CRC Press, 2000.

[49] T. Berger, S. E. Hamran, and T. Sparr, "Estimation of rotation in ISAR imaging based on local sharpness measure," in *Proc. IEEE Radar Conference RADAR '08*, May 2008, pp. 1–6.

[50] R. T. Lord and M. R. Inggs, "High resolution SAR processing using stepped-frequencies," in *Proc. IEEE International Geoscience and Remote Sensing IGARSS '97. Remote Sensing - A Scientific Vision for Sustainable Development*, vol. 1, Aug. 1997, pp. 490–492.

[51] A. J. Wilkinson, R. T. Lord, and M. R. Inggs, "Stepped-frequency processing by reconstruction of target reflectivity spectrum," in *Proc. South African Symposium on Communications and Signal Processing COMSIG '98*, Sep. 1998, pp. 101–104.

[52] A. French, "Improved high range resolution profiling of aircraft using stepped-frequency waveforms with an S-band phased array radar," in *Proc. IEEE Conference on Radar*, Apr. 2006, pp. 69–75.

[53] Z. Gao, M. Xing, S. Zhang, and Z. Bao, "Experimental results on ISAR imaging with stepped-frequency waveforms," *Electronics Letters*, vol. 45, no. 1, pp. 77–79, Jan. 2009.

[54] H. Jeong, H. Kim, and K. Kim, "Application of subarray averaging and entropy minimization algorithm to stepped-frequency ISAR autofocus," *IEEE Trans. Antennas Propag.*, vol. 56, no. 4, pp. 1144–1154, Apr. 2008.

[55] M. Martorella, N. Acito, and F. Berizzi, "Statistical CLEAN technique for ISAR imaging," *IEEE Trans. Geosci. Remote Sens.*, vol. 45, no. 11, pp. 3552–3560, Nov. 2007.

[56] T. K. Moon and W. C. Stirling, *Mathematical Methods and Algorithms for Signal Processing*. Upper Saddle River, NJ: Prentice Hall, 2000.

[57] G. Thomas, F. C. Benjamin, and A. Martinez, "ISAR imaging of moving targets via the Gabor wavelet transform," *Proceedings of the SPIE*, vol. 3161, pp. 90–101, 1997.

[58] J. Odendaal, , E. Barnard, and C. Pistorius, "Two-dimensional superresolution radar imaging using the MUSIC algorithm," *IEEE Trans. Antennas Propag.*, vol. 42, no. 10, pp. 1386–1391, Oct. 1994.

[59] D. Zhu, L. Wang, Y. Yu, Q. Tao, and Z. Zhu, "Robust ISAR range alignment via minimizing the entropy of the average range profile," *IEEE Geosci. Remote Sens. Lett.*, vol. 6, no. 2, pp. 204–208, Apr. 2009.

[60] J. M. Munoz-Ferreras and F. Perez-Martinez, "Extended envelope correlation for range bin alignment in ISAR," in *Proc. IET International Conference on Radar Systems*, Session 2d, No 1, Oct. 2007, pp. 1–5.

[61] B. Haywood and R. J. Evans, "Motion compensation for ISAR imaging," in *Australian Symposium on Signal Processing and Applications*, Apr. 1989, pp. 112–117.

[62] L. Xi, L. Guosui, and J. Ni, "Autofocusing of ISAR images based on entropy minimization," *IEEE Trans. Aerosp. Electron. Syst.*, vol. 35, no. 4, pp. 1240–1252, Oct. 1999.

[63] Z. She and Y. Liu, "Autofocus for ISAR imaging using higher order statistics," *IEEE Geosci. Remote Sens. Lett.*, vol. 5, no. 2, pp. 299–303, Apr. 2008.

[64] F. Berizzi and G. Corsini, "Autofocusing of inverse synthetic aperture radar images using contrast optimization," *IEEE Trans. Aerosp. Electron. Syst.*, vol. 32, no. 3, pp. 1185–1191, Jul. 1996.

[65] D. E. Wahl, P. H. Eihel, D. C. Ghiglia, and C. V. Jakowatz Jr, "Phase gradient autofocus a robust tool for high resolution SAR phase correction," *IEEE Trans. Aerosp. Electron. Syst.*, vol. 30, no. 3, pp. 827–835, Jul. 1994.

[66] B. D. Steinberg, "Microwave imaging of aircraft," *Proc. IEEE*, vol. 76, no. 12, pp. 1578–1592, Dec. 1988.

[67] M. Martorella, J. Palmer, F. Berizzi, B. Haywood, and B. Bates, "Polarimetric ISAR autofocusing," *IET Signal Processing*, vol. 2, no. 3, pp. 312–324, Sep. 2008.

[68] T. Thayaparan, L. Stankovic, C. Wernik, and M. Dakovic, "Real-time motion compensation, image formation and image enhancement of moving targets in ISAR and SAR using S-method based approach," *IET Signal Processing*, vol. 2, no. 3, pp. 247–264, Aug. 2008.

[69] Y. Wang and Y. Jiang, "Modified adaptive chirplet decomposition with applications in ISAR imaging of maneuvering targets," *EURASIP Journal on Advances in Signal Processing*, pp. 1–8 (Article ID 456 598), Jan. 2008.

[70] Y. Li, R. Wu, M. Xing, and Z. Bao, "Inverse synthetic aperture radar imaging of ship target with complex motion," *IET Radar Sonar Navig.*, vol. 2, no. 6, pp. 395–403, Dec. 2008.

[71] A. Aprile, D. Meledandri, T. M. Pellizzeri, and A. Mauri, "A new approach for estimation and compensation of target translational motion in ISAR imaging," in *Proc. IEEE Radar Conference RADAR '08*, May 2008, pp. 1–6.

[72] A. Aprile, A. Mauri, and D. Pastina, "Real time rotational motion compensation algorithm for focusing Spot-SAR / ISAR images in case of variable rotation-rate," in *Proc. EURAD First European Radar Conference*, 2004, pp. 141–144.

[73] K. K. Kong and J. A. Edwards, "Slant range and cross range correction for polar format distortion in ISAR imaging," *IEE Proc. Radar, Sonar Navig.*, vol. 147, no. 1, pp. 2–8, Feb. 2000.

[74] G. Lu and Z. Bao, "Analysis of MTRC compensation algorithm in ISAR," in *Proc. Record of the 1999 IEEE Radar Conference*, Apr. 1999, pp. 242–245.

[75] D. Pastina, "Rotation motion estimation for high resolution ISAR and hybrid SAR/ISAR target imaging," in *Proc. IEEE Radar Conference RADAR '08*, May 2008, pp. 1–6.

[76] Y. Wang and Y. Jiang, "A novel algorithm for estimating the rotation angle in ISAR imaging," *IEEE Geosci. Remote Sens. Lett.*, vol. 5, no. 4, pp. 608–609, Oct. 2008.

[77] M. Xing, R. Wu, J. Lan, and Z. Bao, "Migration through resolution cell compensation in ISAR imaging," *IEEE Geosci. Remote Sens. Lett.*, vol. 1, no. 2, pp. 141–144, Apr. 2004.

[78] R. Lipps and D. Kerr, "Polar reformatting for ISAR imaging," in *Radar Conference, 1998. RADARCON 98. Proceedings of the 1998 IEEE*, May 1998, pp. 275–280.

[79] M. Xing, R. Wu, Y. Li, and Z. Bao, "New ISAR imaging algorithm based on modified wigner-ville distribution," *IET Radar Sonar Navig.*, vol. 3, no. 1, pp. 70–80, Feb. 2009.

[80] M. Zhu, J. Wang, and X. Liu, "An improved time-frequency phase adjustment technique for ISAR," in *Proc. IEEE International Geoscience and Remote Sensing Symposium IGARSS 2007*, Jul. 2007, pp. 5170–5173.

[81] J. A. Trischman, "Real-time motion compensation algorithms for ISAR imaging of aircraft," in *SPIE Proc. on Radar Processing, Technology, and Applications*, vol. 2845, Aug. 1996, pp. 110–119.

[82] F. Berizzi, M. Martorella, B. Haywood, E. Dalle Mese, and S. Bruscoli, "A survey on ISAR autofocusing techniques," in *Proc. International Conference on Image Processing ICIP '04*, vol. 1, Oct. 2004, pp. 9–12.

[83] S. Qian and D. Chen, "Joint time-frequency analysis," *IEEE Signal Process. Mag.*, vol. 16, no. 2, pp. 52–67, Mar. 1999.

[84] V. C. Chen and H. Ling, "Joint time-frequency analysis for radar signal and image processing," *IEEE Signal Process. Mag.*, vol. 16, no. 2, pp. 81–93, Mar. 1999.

[85] M. J. Prickett and C. C. Chen, "Principle of inverse synthetic aperture radar (ISAR) imaging," in *EASCON Record*, vol. 14, no. 6, 1980, pp. 340–345.

[86] A. W. Rihaczek and S. J. Hershkowitz, *Radar resolution and complex-image analysis*. Norwood MA: Artech House, 1996.

[87] B. Borden, "Mathematical problems in radar inverse scattering," *Inverse Problems*, vol. 18, no. 1, pp. R1–R28, Feb. 2002.

[88] D. A. Ausherman, A. Kozma, J. L. Waker, H. M. Jones, and E. C. Poggio, "Developments in radar imaging," *IEEE Trans. Aerosp. Electron. Syst.*, vol. 20, no. 4, pp. 363–400, Jul. 1984.

[89] J. Son, B. Flores, and G. Thomas, *Range-Doppler Radar Imaging and Motion Compensation*. Norwood, MA: Artech House, 2001.

[90] V. C. Chen and H. Ling, *Time-frequency Transforms for Radar Imaging and Signal Analysis*. Artech House, 2002.

[91] W. G. Carrara, R. S. Goodman, and R. M. Majewski, *Spotlight Synthetic Aperture Radar: Signal Processing Algorithms*. Boston: Artech House, 1995.

[92] B. Borden, *Radar Imaging of Airborne Targets*. Taylor & Francis, 1999.

[93] D. Pastina, A. Montanari, and A. Aprile, "Motion estimation and optimum time selection for ship ISAR imaging," in *Radar Conference, 2003. Proceedings of the 2003 IEEE*, May 2003, pp. 7–14.

[94] J. Gao, F. Su, X. Cao, and G. Xu, "Simulation of ISAR imaging of ships with multipath effects," in *Proc. 2nd IEEE Conference on Industrial Electronics and Applications ICIEA 2007*, May 2007, pp. 1484–1488.

[95] F. Berizzi and M. Diani, "Multipath effects on ISAR image reconstruction," *IEEE Trans. Aerosp. Electron. Syst.*, vol. 34, no. 2, pp. 645–653, Apr. 1998.

[96] R. T. Lord, W. A. J. Nel, and M. Y. Abdul Gaffar, "Investigation of 3-D RCS image formation of ships using ISAR," in *Proc. European Conference on Synthetic Aperture Radar, EUSAR 2006*, May 2006.

[97] J. Gao, F. Su, and G. Xu, "Multipath effects cancellation in ISAR image reconstruction," in *Microwave and Millimeter Wave Technology, 2007. ICMMT '07. International Conference on*, Apr. 2007, pp. 1–4.

[98] C. L. Trintinalia and H. Ling, "Joint time-frequency ISAR using adaptive processing," *IEEE Trans. Aerosp. Electron. Syst.*, vol. 45, no. 2, pp. 221–227, Feb. 1997.

[99] B. Borden, "Reduction of radar image artifacts caused by target inlets," *IEEE Trans. Antennas Propag.*, vol. 47, no. 5, pp. 898–901, May 1999.

[100] J. Li, "Model-based signal processing for radar imaging of targets with complex motions," Ph.D. dissertation, University of Texas at Austin, 2002.

[101] A. Ghaleb, L. Vignaud, and J. M. Nicolas, "Micro-Doppler analysis of wheels and pedestrians in ISAR imaging," *IET Signal Processing*, vol. 2, no. 3, pp. 301–311, 2008.

[102] R. Jonsson, A. Genell, D. Losaus, and F. F. Dicander, "Scattering center parameter estimation using a polynomial model for the amplitude aspect dependence," *Proceedings of the SPIE*, vol. 4727, pp. 46–57, Apr. 2002.

[103] J. Chadwick and G. L. Williams, "Air target identification - concept to reality," in *IET Radar Conference 2007*, session 9a, No 2, Oct. 2007, pp. 1–5.

[104] A. Karakasiliotis, A. Lazarov, and P. Frangos, "ISAR imaging based on two-dimensional GTD scattering model," in *Proc. European Radar Conference EuRAD 2008*, Oct. 2008, pp. 388–391.

[105] T. G. Kostis, "Simulator implementation of an inverse synthetic aperture radar system for an extended naval target in a three dimensional synthetic environment," in *Proc. Tenth International Conference on Computer Modeling and Simulation UKSIM 2008*, 2008, pp. 366–371.

[106] B. Haywood, W. C. Anderson, J. T. Morris, and R. Kyprianou, "Generation of point scatterer models for simulating ISAR images of ships," in *Proc. Radar 97 (Conf. Publ. No. 449)*, Oct. 1997, pp. 700–704.

[107] M. Martorella, J. Homer, J. Palmer, V. C. Chen, F. Berizzi, B. Littleton, and D. Longstaff, "Inverse synthetic aperture radar," *Editorial of Journal on Applied Signal Processing, Special Issue on Inverse Synthetic Aperture Radar*, pp. 1–4, 2006.

[108] T. Cooke, M. Martorella, B. Haywood, and D. Gibbins, "Use of 3D ship scatterer models from ISAR image sequences for target recognition," *Digital Signal Processing*, vol. 16, no. 5, pp. 523–532, Sep. 2006.

[109] A. Maki, K. Fukui, K. Onoguchi, and K. Maeda, "ISAR image analysis by subspace method: automatic extraction and identification of ship profile," in *Proc. 11th International Conference on Image Analysis and Processing*, Sep. 2001, pp. 523–528.

[110] K. A. Melendez and J. R. Bennett, "ISAR target parameter estimation with application for automatic target recognition," in *SPIE Proc. on Radar Processing, Technology, and Applications*, vol. 3462, Jul. 1998, pp. 2–13.

[111] D. Pastina and C. Spina, "Multi-feature based automatic recognition of ship targets in ISAR images," in *Proc. IEEE Radar Conference RADAR '08*, May 2008, pp. 1–6.

[112] S. Y. Shin and N. H. Myung, "Efficient technique for two-dimensional scattering center extraction and ISAR image formation," *Microwave and Optical Technology Letters*, vol. 50, no. 8, pp. 2173–2178, Aug. 2008.

[113] A. Maki, K. Fukui, Y. Kawawada, and M. Kiya, "Automatic ship identification in ISAR imagery: An on-line system using CMSM," in *Radar Conference, 2002. Proceedings of the IEEE*, Apr. 2002, pp. 206–211.

[114] M. Martorella, E. Giusti, A. Capria, F. Berizzi, and B. Bates, "Automatic target recognition by means of polarimetric ISAR images and neural networks," in *Proc. IEEE International Geoscience and Remote Sensing Symposium IGARSS 2008*, vol. 4, Jul. 2008, pp. IV – 1249–IV – 1252.

[115] F. Rice, T. Cooke, and D. Gibbins, "Model based ISAR ship classification," *Digital Signal Processing*, vol. 16, no. 5, pp. 628–637, Sep. 2006.

[116] X. Qiu and Y. Zhao, "Maximum likelihood-based range alignment for ISAR imaging," in *Proc. IEEE Antennas and Propagation Society International Symposium*, vol. 2, Jun. 2004, pp. 2103–2106.

[117] C. V. Jackowats and D. E. Wahl, "Eigenvector method for maximum-likelihood of phase errors in synthetic-aperture-radar imagery," *Journal of the Optical Society of America*, vol. 10, no. 12, pp. 2539–2546, Dec. 1993.

[118] Y. Wang, H. Ling, and V. C. Chen, "ISAR motion compensation via adaptive joint time-frequency technique," *IEEE Trans. Aerosp. Electron. Syst.*, vol. 34, no. 2, pp. 670–677, Apr. 1998.

[119] Z. Zhaoda, Q. Xiaohui, and S. Zhishun, "Modified Doppler centroid tracking method for phase compensation in ISAR," in *Radar, 1996. Proceedings., CIE International Conference of*, Oct. 1996, pp. 751–754.

[120] Z. Liu and S. Zhang, "A novel method of translation motion compensation for hopped-frequency ISAR imaging," in *Proceedings of the IEEE 2000 International Radar Conference*, May 2000, pp. 255–260.

[121] G. Y. Lu and Z. Bao, "Compensation of scatterer migration through resolution cell in inverse synthetic aperture radar imaging," *IEE Proc. Radar, Sonar Navig.*, vol. 147, no. 2, pp. 80–85, Apr. 2000.

[122] A. Scaglione and S. Barbarossa, "Estimating motion parameters using parametric modeling based on time-frequency representations," in *Proc. IEE Radar*, Oct. 1997, pp. 280–284.

[123] Z. She, D. A. Gray, and R. E. Bogner, "Autofocus for inverse synthetic aperture radar (ISAR) imaging," *Signal Processing*, vol. 81, no. 2, pp. 275–291, Feb. 2001.

[124] W. R. Hamilton, *Elements of Quaternions*. London: Longmar and Co., 1866.

[125] P. Daniel, "Quaternion calculus as a basic tool in computer graphics," *The Visual Computer*, vol. 5, no. 1-2, pp. 2–13, Jan. 1989.

[126] J. Funda and R. Paul, "A comparison of transforms and quaternions in robotics," in *Proc. IEEE International Conference on Robotics and Automation*, vol. 2, Apr. 1988, pp. 886–891.

[127] J. Kuipers, *Quaternions and Rotation Sequences: A Primer with Applications to Orbits, Aerospace and Virtual Reality*. Princeton, NJ: Princeton Univ. Press, 1999.

[128] J. Li and H. Ling, "Application of adaptive chirplet representation for ISAR feature extraction from targets with rotating part," *IEE Proc. Radar, Sonar Navig.*, vol. 150, no. 4, pp. 284–291, Aug. 2003.

[129] A. F. Garcia-Fernandez, J. Grajal, and O. A. Yeste-Ojeda, "Analysis of ISAR images of a helicopter by a facet model," in *International Conference on Radar 2008*, Sept. 2008, pp. 32–37.

[130] P. L. Herselman, C. J. Baker, and H. J. de Wind, "An analysis of X-band calibrated sea clutter and small boat reflectivity at medium-to-low grazing angles," *International Journal of Navigation and Observation*, pp. 1–14, 2008.